UNIVERSITY OF SOUTHAMPTON

Tracing seawater evaporation and its role in the formation of sediment-hosted stratiform copper deposits

by

James Philip Nowecki

A thesis submitted in partial fulfillment for the degree of Doctor of Philosophy

in the

Faculty of Natural and Environmental Sciences

Ocean and Earth Science

May 2014

Declaration of Authorship

I, James Philip Nowecki, declare that this thesis titled, 'Tracing seawater evaporation and its role in the formation of sediment hosted stratiform copper deposits' and the work presented in it are my own. I confirm that:

- This work was done wholly or mainly while in candidature for a research degree at this University.
- Where any part of this thesis has previously been submitted for a degree or any other qualification at this University or any other institution, this has been clearly stated.
- Where I have consulted the published work of others, this is always clearly attributed.
- Where I have quoted from the work of others, the source is always given. With the exception of such quotations, this thesis is entirely my own work.
- I have acknowledged all main sources of help.
- Where the thesis is based on work done by myself jointly with others, I have made clear exactly what was done by others and what I have contributed myself.

Signed: _____

Date: _____

"Face the facts. Then act on them. It's the only mantra I know, the only doctrine I have to offer you, and it's harder than you'd think, because I swear humans seem hardwired to do anything but. Face the facts. Don't pray, don't wish, don't buy into centuries-old dogma and dead rhetoric. Don't give in to your conditioning or your visions or your fucked-up sense of... whatever. FACE THE FACTS. THEN act."

— Quellcrist Falconer

UNIVERSITY OF SOUTHAMPTON

Abstract

Faculty of Natural and Environmental Sciences
Ocean and Earth Science

Doctor of Philosophy

by James Philip Nowecki

This study investigates the preserved fluid contents of different generations of mineralised and unmineralised vein minerals from multiple different deposits across the Zambian Copperbelt to define the fluid physicochemical characteristics of the fluids and investigate the importance of fluid processes through the basin history. An investigation into REE and trace element and sulphur isotope signatures of sulphides was conducted to investigate sulphide formation mechanisms. Re-Os dating of sulphides from the Domes Region to provide temporal constraints on mineralisation processes in this area. A textural study on uranium mineralisation at the Lumwana deposit was undertaken to understand the relationships between uranium and sulphide mineralisation.

Variable Cl/Br of fluids indicates they were derived from evaporation of seawater, deposition of evaporite sequences and the subsequent dissolution of these evaporite sequences, with bittern brines dominant earlier in the basin history, and dissolution of halite more important during compression and orogenesis. Cation contents of fluids record the development of alteration assemblages caused by the movement of these brines at temperatures typically >200 ℃ and salinities >30 wt% NaCl equiv. Stable isotope data records the role of organic reductants and fluid-host rock equilibration through basin history. Rare earth element signatures of sulphides further record the importance of the development of the alteration assemblage on the changing chemistry of the hydrothermal fluids, whilst trace element concentrations suggest the metal budget in the fluids reflects source rock variation. Sulphur isotope data suggests the main mechanism of sulphide formation was thermochemical sulphate reduction of seawater sulphate, consistent with the temperatures of the fluids reported here. Re-Os dating records the importance of orogenesis on the timing of mineralisation in the Domes Region, and are consistent with published Re-Os dating of sulphides and U-Pb dating of uranium minerals. Textural relationships indicate initial uranium mineralisation at the Lumwana deposit pre dates sulphide mineralisation, and final movement on the shear zone, but has undergone a remobilisation event later in the deposit history.

Acknowledgements

This is about as close to an Oscar acceptance speech as I'm ever likely to get, so you'll have to be indulgent as it'll go on a bit. I promised myself I wouldn't cry, but...

Many people have contributed to this thesis and my life while undertaking my Doctoral studies, in both a direct and indirect manner.

Great thanks go to my supervisor Stephen Roberts for years of support and putting together a great project, which allowed me to travel to some exciting, far-flung places like Zambia, Turkey, Alberta and East Kilbride. I had the great fortune to learn a lot, not just about geology and geochemistry, but also about being a scientist, the world, and life in general. If I am being fair, I also learned an awful lot about myself too. Additionally, Ross McGowan, Robin Bernau and Matt McGloin were critical in providing the framework of this project, which built upon the results of their own studies.

Within the department at the NOC, many thanks are due to a number of other people. Ian Harding and Sam Gibbs provided excellent guidance during my formative years as an undergraduate, and without that, I would not be where I am now. During my time as a postgraduate, I also received great help (and in many cases friendship) from Martin Palmer, Clive Trueman and Tom Gernon. Clive's influence with R and statistics in general has been invaluable. Andy Milton, Matt Cooper and Agnes Michalik provided technical assistance with labwork and ICP-MS. Richard Pearce aided SEM work, and Mike Bolshaw provided support for carbonate isotope analyses. Bob Jones and John Ford were consistently excellent with sample preparation, and certainly helped keep me in my place by showing me my shortcomings with a rock saw.

At SUERC, I received training and assistance in both obtaining and interpreting stable isotope data from Craig Barrie, Alison MacDonald, Terry Donnelly and Adrian Boyce, who were all a pleasure to work with. Similarly, I received excellent supervision while at the University of Alberta from Sarah Gleeson, as well as assistance and access to samples from Jeremy Richards, and Rob Creaser, who ran sulphides for Re-Os dating. Set and Saulo Castro are warmly thanked for accommodation and entertainment whilst in Edmonton. Richard Herrington and John Spratt are thanked for access and aid with the microprobe at the Natural History Museum, and discussion of data. Dan Sykes was a great help with processing computed tomography data. Philippe Muchez and Dave Broughton are thanked for numerous discussions about the Copperbelt in general at conferences.

This project could not have been undertaken without the support of numerous industrial partners, who kindly provided both access to the samples upon this project was based,

as well as expertise and accommodation whilst on fieldwork. I owe a great debt of gratitude to geologists and other staff at all the mines and exploration sites I spent time. Particularly of note are Bob Foster at Stratex, who facilitated fieldwork, Doug Jack and Dave Wood at First Quantum Minerals, Dave Armstrong (TEAL), but by far the largest thanks are due to the geologists at Equinox and Lumwana Mine (now Barrick) with whom I spent the longest period of time, and which was used as a base camp in Zambia. Shonny Jackson-Hicks, Finton Lehane, Reuben Morrison, Robbie Sparrow and Cain Fogarty were excellent company and incredibly helpful, and Mike Richards was critical in so many aspects of this study that his contribution to the project is, frankly, immeasurable.

Outside of the ivory tower of academic research, the greatest thanks are due to my parents, since without their unwavering love and support throughout this process, and all the steps and years leading up to it, this document would not exist. All this support, despite the fact that my sister has long eclipsed me in terms of achievement and success in life! Thank you.

On a personal level, Alex Carpel, Alex Hazeldean, Paul Marshall, Clare Sangster, and Sam and Talya Bradley-Dosaj kept me partially sane during this undertaking, and the previous years. They kept me entertained, gave me a boost when asked (and when not) and a slap when necessary and deserved. As a geologist, I'd like to think I know a little something about rocks, and these people define the word. Within the Ph.D community at the Oceanography Centre, the utmost thanks are due to Steve Hollis, Catriona Menzies, Alex Webber, Jen Rutter and Cristina Sghibartz. Some of you got the blunt end of science problems; some of you enjoyed the misfortune of my misanthropic social inadequacies; most of you unfortunates got both, and I'm very lucky to count you all as friends.

Anything written by me wouldn't be believable as my writing without a few well-targeted complaints, and this is no different. This thesis was completed with NO THANKS WHATSOEVER to Australia, for taking Steve and Rob Thorne to the dark side of the globe; Talya, for providing only rabbit pictures and not cat pictures (as specifically requested) for inspiration; fluid inclusions (for obvious reasons), and the designers of Blood Bowl and DOTA2 for distractions when none were necessary.

Finally, great thanks to all the undergraduates I had the pleasure of demonstrating for, in the field and the laboratory. It was with great enjoyment I watched you develop as scientists and people, and I'm very grateful and proud for the opportunity I had to contribute to this in my own, small way. Particularly of note are Edward Inglis, Izzy Marchant and Ryan Barr, who I'm fortunate enough to now count among my close friends. On a more abstract note, the writing of Garth Ennis, the music and lyrics of

Nick Cave and the Bad Seeds, and RC all meant an awful lot to me during the time it took to produce this piece of work, and I sincerely love you all, despite the fact that none of you will ever know.

Contents

List of Figures

List of Tables

Abbreviations

CAC	**C**entral **A**frican **C**opperbelt
SHSC	**S**ediment–**H**osted **S**tratiform **C**opper
SET	**S**eawater **E**vaporation **T**rajectory
LREE	**L**ight **R**are **E**arth **E**lements
MREE	**M**iddle **R**are **E**arth **E**lements
HREE	**H**eavy **R**are **E**arth **E**lements
TSR	**T**hermochemical **S**ulphate **R**eduction
BSR	**B**acterial **S**ulphate **R**eduction

A small contribution to human knowledge...

Chapter 1

Introduction

1.1 Project rationale and aims

Sediment-hosted stratiform copper deposits (SHSCs) are economically important sources of Cu, Co and Ag, which constitute ∼23 % of the world's Cu production and known reserves (Hitzman et al., 2005; Singer, 1995). The Central African Copperbelt is one of the largest examples of a basin containing SHSC mineralisation, containing super-giant deposits, defined as the largest 1 % of deposits containing >24 million tons of Cu; (Singer, 1995) and is also the world's largest cobalt supplier and repository (USGS Mineral Commodities Summaries). Historically, the Central African Copperbelt has been an important producer of copper since the early 1900s (Mendelsohn, 1961a), with numerous mines with long operational histories. The mine facilities and associated core repositories provide an excellent level of access for sampling and identifying and interpreting field relationships, making the Central African Copperbelt an ideal locality for the study of Cu and Co mineralisation. The broad aims of this project were to investigate fluid chemistries in the Zambian basin as a whole by comparing and contrasting samples from different mines and exploration projects, different generations of fluids, and build a picture of the fluid history of the basin through basin inversion and orogenesis. Basin brines are now generally regarded as playing critical roles in generating SHSC mineralisation by scavenging and transporting metals (Hitzman et al., 2005; Rose, 1976; Rose and Bianchi-Mosquera, 1993; Sverjensky, 1987), however there has been very little research done into fluid chemistries in the Copperbelt beyond basic fluid inclusion studies. Similarly, these authors regard the role of evaporite sequences to be critical in generating these brines, yet much of the evidence for this, while intuitive, is empirical in nature. Bulk fluid inclusion leachate studies are becoming a novel and important

tool in assessing anion and cation chemistries of fluids, and with this information, reconstructing halogen ratios, which can provide insights into sources of salinity and the fingerprinting of different fluids. The only previous such study the author is aware of for this class of deposit is that of Heijlen et al. (2008) undertaken on the Kipushi deposit. Whilst a useful study, the Kipushi deposit is very much unique, and is not representative of mineralisation styles in the Copperbelt or in SHSC deposits. The broad suite of samples available for this study provides an excellent opportunity to characterise the Copperbelt palaeofluids using this technique and attempt to understand and qualify the roles of seawater and evaporite formations. This information is supplemented by a regional study of isotopes on these vein and inclusion samples, including the first examples of δ^{37}Cl and δD generated from Copperbelt samples, allowing for interpretations about sources of chlorine, and fluid interactions. Similarly, whilst the pioneering study of Dechow and Jensen (1965) provides an excellent regional overview of the sulphur isotope systematics, most work has focussed on individual deposits. This study aims to utilise the broad suite of samples available to study the trace and rare earth element signatures of different sulphide minerals, different deposits and different generations of sulphides, as well as presenting a new perspective on sulphur isotope signatures within the Zambian Copperbelt. Re-Os dating provides a method capable of directly dating the formation of sulphides, potentially helping to constrain timing of mineralisation during the evolution of the Katangan basin.

This thesis also presents the findings of another study. Research on uranium mineralisation at Lumwana builds upon previous studies on the deposit conducted at the University of Southampton, improving understanding on the minor components of the mineralised assemblage. It also provides an interesting investigation into mineralisation within the basement rocks of Zambia, complementing the work on deposits hosted within the overlying sedimentary packages.

1.2 Sediment-hosted stratiform copper deposits: An overview

Sediment-hosted stratiform copper deposits (SHSCs) are an economically important source of Cu, Co and Ag, and can also commonly contain Pb, Zn, and U. Rare examples may also contain Au and PGE mineralisation. Their excellent grades, deposit geometry and long strike lengths make them worthwhile exploration targets and straightforward to mine.

Below is a summary of their key characteristics compiled from Cailteux et al. (2005a); Haynes (1986a,b); Hitzman et al. (2005); Jowett (1992); Kirkham (1989); Mendelsohn

(1961a); Oszczepalski (1999); Rose (1976, 1989); Rose and Bianchi-Mosquera (1993); Zielinski et al. (1983) and references therein:

- Deposits are hosted in siliciclastic or carbonate (typically dolomite) sedimentary rocks deposited within 20 to 30° of the palaeoequator.
- Mineralisation typically consists of iron and copper-iron sulphides, with supergene alteration common near the surface expressions of orebodies.
- Sulphide mineralisation conforms closely with the stratification of host sediments, but is often discordant at both a fine and orebody scale, resulting in thin mineralised zones generally <30 m thick and commonly only a few metres.
- Mineralogical zoning is common from a red bed contact into the reduced mineralised sediments, typically haematite-chalcocite-bornite-chalcopyrite-pyrite. Galena and sphalerite may form alongside chalcopyrite, or between the chalcopyrite and pyrite zones.
- The deposits are associated with basins containing immature continental red bed sediments, typically overlain by regionally important marine or lacustrine units such as a shales with evaporites also contained within the sequence.
- Metals are considered to be sourced from red bed lithologies containing labile minerals and iron oxyhydroxides capable of binding metals, as well as from basement lithologies.
- Metals are transported by moderate to highly saline brines at low to moderate temperatures, mostly as chloride complexes.
- Sulphur is sourced from evaporite sequences, seawater, H_2S-bearing petroleum or pre-existing sulphide phases (e.g. pyrite) in the host rocks.
- Metalliferous fluids are transported via basin architecture to sites of deposition by thinning and pinch out of porous lithologies, faults, palaeotopography of the basin, variable permeabilities of host rocks or basin inversion structures.
- Metal deposition is controlled by reduction, typically in the form of a carbonaceous shale or dolomite sequence acting as a reductant immediately overlying the oxidised red bed facies.

SHSCs are common in basins satisfying the above characteristics, but economic deposits are rare. Only 3 basins contain supergiant deposits, The Neoproterozoic Katangan basin Central African Copperbelt, the Palaeoproterozoic Kodaro-Udokan basin in Siberia,

and the Permian Kupferschiefer of central Europe. These basins also contain giant deposits (largest 10 % of deposits, containing >2 million tons of Cu), along with the Devonian to Carboniferous Chu-Sarysu basin in Kazakhstan, the Middle Proterozoic Mid Continental Rift of the USA (White Pine), and a Neoproterozoic to Cambrian age basin in Afghanistan. The timing of deposit formation is fundamentally controlled by the development of an oxidised atmosphere at ~2.3 Ga allowing for the development of contrasting oxidised and reduced lithologies, and no deposits formed before this time (Fig. 1.1), with SHSC development linked to the supercontinent cycle, particularly the break up of these large landmasses.

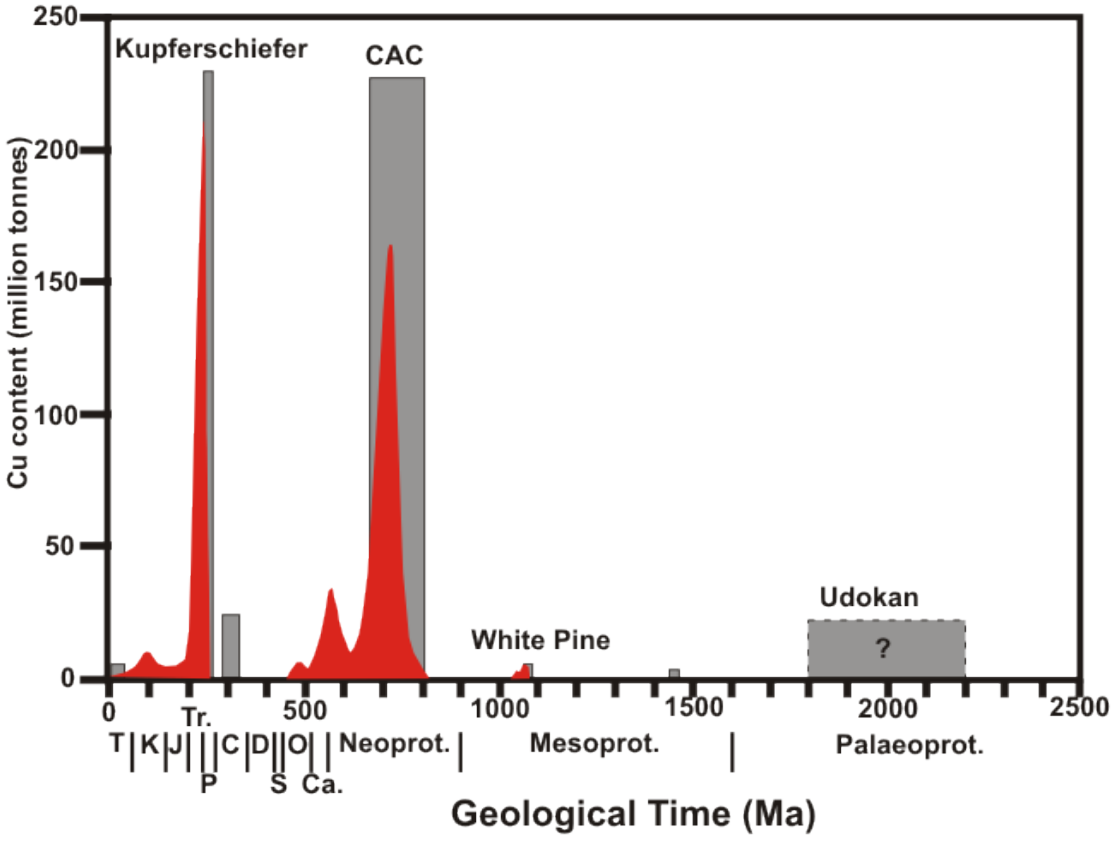

FIGURE 1.1: Temporal distribution of SHSC mineralisation. Grey bars show tonnage by the age of the host sediments, with red fields showing tonnage by estimates on timing of sulphide precipitation (adapted from Hitzman et al., 2010).

The origin of SHSCs has been particularly controversial, owing to their close spatial and geometrical correlations with host sediment packages. For a long period of time, the prevailing theory suggested that these deposits formed syngenetically, with mineralisation forming through synsedimentary deposition of sulphides with increased distance from a palaeoshoreline accounting for the sulphide mineral zonation (Mendelsohn, 1961a). Careful studies of the White Pine deposit showed mineralisation cross cutting lithological layering (Brown, 1971; White and Wright, 1966), whilst chemical modelling indicated that the mineralogical zonation was generated as a result of redox geochemistry

of sulphide minerals (Sverjensky, 1987). These key observations lead to rejection of the syngenetic model, and the adoption of the widely recognised interpretation that mineralisation post-dates sedimentation (Jowett, 1991). However, identifying the absolute age of mineralisation relative to sediment deposition and diagenesis has proved challenging due to the difficulty in applying absolute dating techniques to sulphide minerals, the lack of suitable alteration phases to date using conventional techniques, and the uncertainty in the temporal relationship between different hydrothermal alteration types and sulphide mineralisation, often due to metamorphism and subsequent recrystallisation.

Sulphur isotope ratios of sulphides can provide information on the origin of sulphur and any fractionation processes that sulphur may have undergone (Faure, 1986). This information can indirectly help to constrain the relative timing of sulphide formation. SHSCs show wide ranges in sulphur isotope signatures both across the deposit class (Dechow and Jensen, 1965; Hitzman et al., 2005), and frequently in individual deposits, e.g. White Pine (Hoy and Ohmoto, 1989) and Nchanga (McGowan et al., 2006). Examples exhibiting relatively depleted δ^{34}S indicate formation via bacterial sulphate reduction (BSR), suggesting that at least some sulphides may have formed before the completion of diagenesis in the shallow subsurface (e.g. Sawlowicz and Wedepohl, 1992). Signatures enriched in ^{34}S are generally thought represent a system where sulphides formed via thermochemical sulphate reduction (TSR) at higher temperatures, (e.g. Hoy and Ohmoto, 1989; McGowan et al., 2006), or through closed system fractionation.

Uncertainties in the timing of mineralisation relative to the formation of host sediments are compounded by other factors such as metamorphic overprinting, causing textural relationships between sulphides and host sediments to become less clear. Whilst there is evidence that sulphide mineralisation may in many cases postdate diagenesis, our understanding of sediment properties and how they affect fluid migration, during evolution from burial and diagenesis to orogenesis is not well constrained (Haynes, 1986a; Hitzman et al., 2005). Additionally, it is increasingly clear that both individual deposits and the basins as a whole show prolonged fluid histories with evidence of multiple stages of mineralisation and fluid flow (Hitzman et al., 2005; Jowett, 1986, 1987; Large et al., 1995; McGowan et al., 2006; Muchez et al., 2010; Selley et al., 2005). Recent work regards SHSCs as a common product of normal basinal processes and evolution, but with long basin histories, large scale and significant amount of fluid flow and circulation important for forming economic deposits. Mineralisation occurs at the first suitable reductant trap the fluids intersect, what is generally termed the 'first reductant model'.

1.3 An overview of the geology of the Central African Copperbelt

1.3.1 Geology and regional geotectonics

The Central African Copperbelt is hosted within the Neoproterozoic rocks of the Lufilian Arc, which streches across Northwest Zambia and the pedicle of the Democratic Republic of Congo. The Lufilian Arc is one of a number of Pan-African orogenic belts preserving sutures between the Congolese and Kalahari cratons formed as a result of the breakup of the Mesoproterozoic supercontinent Rodinia (Kampunzu et al., 2000), and the metamorphism and orogeny generated by the aggregation of Gondwana during the late Neoproterozoic and early Phanerozoic (Kampunzu and Cailteux, 1999; Selley et al., 2005). More recent work suggests the break up of Rodinia initiated after ~880 Ma separating the Congo-Tanzania plate from the Angola-Kalahari plate, forming an ocean basin and a passive continental margin on the southern edge of the Congolese Craton (John et al., 2003; Porada and Berhorst, 2000). This basin closed subducting oceanic lithosphere and forming eclogites around ~600 Ma, with the final convergence and continent-continent collision overriding the passive continental margin of the Congolese Craton at ~530 Ma (John et al., 2003). This event is interpreted to be responsible for the formation of the talc-kyanite 'whiteschist' assemblages in the Domes Region (John et al., 2004), followed by rapid uplift, erosion and cooling in order to preserve these assemblages.

Basement rocks in the region are pre-Neoproterozoic in age, comprising Archaean to Mesoproterozoic metagranites, migmatites, metavolcanics and metasediments which are exposed in the northwest and southeast of the Lufilian arc, as well as in the form of a number of basement inliers in the Domes Region of northern Zambia (Johnson et al., 2005). The oldest recorded rocks in the Copperbelt are the Lufubu Schists, consisting of a metamorphosed Palaeoproterozoic magmatic arc terrain of sedimentary and volcanic rocks and intrusive granitoids. The granites show an age of ~1994-1873 Ma, with the Lufubu Metamorphic Complex showing U-Pb SHRIMP zircon ages of 1980–1874 Ma (John et al., 2004; Rainaud et al., 2005). These are unconformably overlain by a laterally extensive series of quartzites and metapelites forming the Muva group (~1300-1100 Ma; Mendelsohn, 1961a). Whiteschist assemblages in the Domes Region (Mwombezhi Dome) give peak metamorphic ages from U-Pb dating of monazite of 532 ± 2 Ma to 524 ± 2 Ma (John et al., 2004) and suggest peak metamorphic conditions of up to 750 ± 25 °C and 13 ± 1 kilobars, equivalent to burial depths of ~ 50 km (Cosi et al., 1992; John et al., 2004). However, whether these rocks represent true whiteschist facies or a hydrothermal alteration assemblage is unclear.

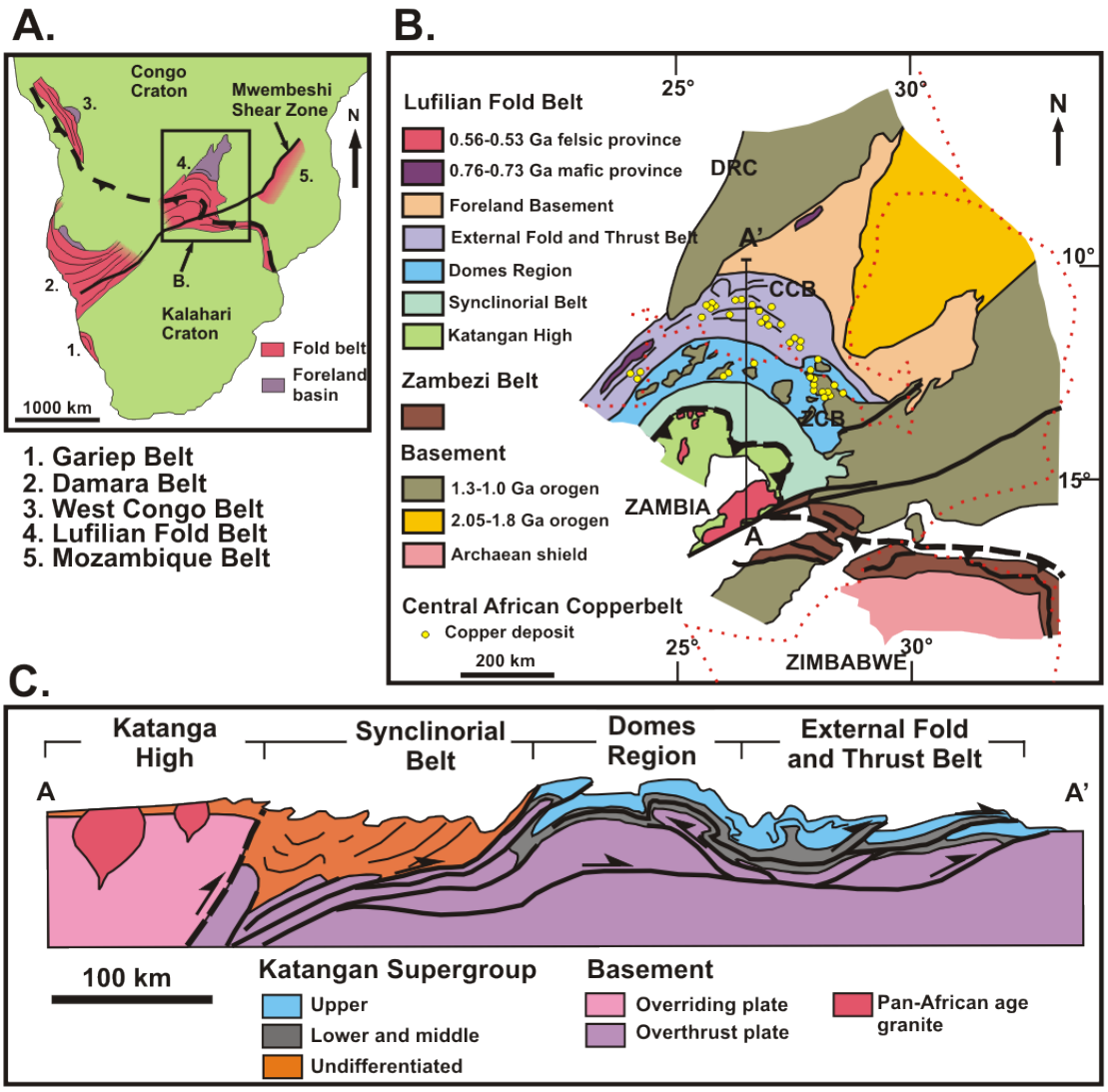

FIGURE 1.2: Tectonic setting of the Lufilian Arc. (a) Pan-African orogenic belts of central and southern Africa. (b) Tectonic zones of the Lufilian Arc and the distribution of the Zambian and Congolese Copperbelts (ZCB and CCB). (c) Cross-section of Lufilian Arc. (Adapted from Selley et al., 2005 and references therein).

The metasediments of the Katangan Supergroup which comprise much of the Lufilian Arc are the result of early Neoproterozoic extensional tectonics and basin development (Lefebvre, 1989). Initial basin fill is dominated by basal conglomerates and coarse terriginous sediments (red beds) deposited in fluvial or alluvial fan environments. These are overlain by a finer grained sequence of carbonates and evaporites which represent a transition to a restricted marine or lacustrine environment (Mendelsohn, 1961a; Selley et al., 2005). Stratigraphic and geochemical evidence suggests these sediments are characteristic of intracontinental rift basins (e.g. Munyanyiwa et al., 1997).

The Central African Copperbelt consists of a number of tectonic zones (Fig. 1.2). These are:

1. The Katangan High
2. The Synclinorial Belt
3. The Domes Region
4. The External Fold and Thrust Belt

The Lufilian Arc terminates in the north in the form of relatively undeformed Katangan Supergroup stratigraphy, with the south bounded by the east-northeast trending sinistral Mwembeshi shear zone. Regional kinematics suggest thrusting in a northerly direction, with northwest to northeast directions of thrusting dependent upon the trend of the Lufilian Arc as a whole (Kampunzu and Cailteux, 1999; Selley et al., 2005). Mineralisation is constrained to the Domes Region and External Fold and Thrust Belt tectonic zones, with the External Fold and Thrust Belt hosting the majority of Congolese deposits, and the Domes Region the host of the Zambian deposits. The majority of the Zambian deposits are clustered on the margins of the largest, easternmost basin inlier formed by the Kafue Anticline (Kampunzu and Cailteux, 1999; Mendelsohn, 1961a; Selley et al., 2005). The transition between the Domes Region and External Fold and Thrust Belt shows a distinct northward decrease in metamorphic grade (greenschist facies to prehnite-pumpellyite facies) into the fold and thrust belt, as well as a fundamental change in structural style from thick skinned to thin skinned tectonics, resulting in significant thrusting, fragmentation and repetition of Katangan stratigraphy further north (Key et al., 2001; Ramsay and Ridgway, 1977). Salt tectonics and dissolution of evaporite sequences is thought to have played a critical role in this change in structural style, with overpressured evaporites facilitating the movement of thrust sheets and allowing for decoupling of stratigraphy, as well as salt diapirism distorting and complicating stratigraphy and stratigraphic relationships (Jackson et al., 2003; Kampunzu and Cailteux, 1999).

In the Domes region of Zambia, Katangan stratigraphy is, in places, deformed along with the basement rocks, preserving the unconformable relationship between these units which was critical in rejecting early magmatic-hydrothermal models of ore formation. Upright and inclined high amplitude folds dominate structure, particularly in the eastern parts of this tectonic zone, resulting in greenschist to upper amphibolite metamorphic grades. Further west, decoupling between basement and sediment packages is observed, and thrust blocks containing different metamorphic grades are encountered in contact with each other (Cosi et al., 1992; Key et al., 2001). The basement inliers which define the Domes Region may have formed as antiformal stacks above mid to lower crustal ramps, providing evidence for thicker skinned tectonics than that responsible for the formation of the External Fold and Thrust Belt (Selley et al., 2005). There is still much work

to be done in understanding the tectonics in this area, as drilling results and mapping indicate that sheets of Katangan stratigraphy are repeated beneath basement lithologies. It remains unclear whether this represents multiple repeated thrusts, or regional scale recumbent folding and nappe formation as suggested by Cosi et al. (1992), but improving understanding of the western Domes region is becoming increasingly important as an exploration objective since the development of the Lumwana mine (Bernau et al., 2013).

The distinction between the outermost (mineralised) zones of the Lufilian Arc and the Katangan High and Synclinorial belt is poorly understood (Selley et al., 2005). The few models which exist suggest that this border represents a fundamental change in basin environment towards deeper water environments away from the shallow sedimentation which dominates the Katangan stratigraphy in the Domes Region and External fold and thrust belt (Cosi et al., 1992; Porada and Berhorst, 2000), however there is not currently enough evidence available to confirm these interpretations (Selley et al., 2005).

1.3.2 Stratigraphy

Stratigraphy and basin architecture play a fundamental role in controlling the formation and distribution of SHSCs. At a gross scale, the juxtaposition of oxidised lithologies with reduced facies is typically responsible for deposition of metals in the form of sulphides due to a sharp change in redox conditions forming a chemical trap. Additionally, the porosity and permeability of sediments exert a critical control on the distribution, transport and interaction of hydrothermal fluids, particularly early on in the history of basins. Juxtaposition of lithologies with different permeabilities may form physical traps for ore forming fluids. Understanding the stratigraphy, and the controls on stratigraphic development of the Katangan Supergroup sediments which host the majority of orebodies in the CAC is extremely important. The long mining history in the Copperbelt, the differences in mineralisation styles and host rocks between Zambian and Congolese deposits, different languages, and a variety of local mining nomenclature has resulted in an often confusing array of terminology for the stratigraphic package as a whole. A number of attempts to consolidate and reappraise the stratigraphy in a consistent manner have been applied (e.g. Cailteux et al., 1994, 2005a; Selley et al., 2005), with recent efforts using stable isotope and sequence stratigraphic methods (Bull et al., 2011). Different sedimentary facies at similar stratigraphic levels are preserved in the Congo relative to Zambia, suggesting some broad differences in depositional environment (Cailteux et al., 1994).

The Zambian Copperbelt preserves Katangan Supergroup rocks in a sequence ~1–3 km thick, with a likely pre-erosional thickness of ~5-7 km (Annels, 1989). These rocks

consist of metamorphosed continental and marine sediments overlying an unconformity with the basement. In the eastern part of the Domes Region where the majority of deposits are located (Fig. 1.3), the sedimentary packages are contained within a series of west-northwest to north-northwest trending synclines (typically termed 'basins') formed on the edges of the Kafue Anticline, formed by the largest of the basement domes (Mendelsohn, 1961a; Selley et al., 2005).

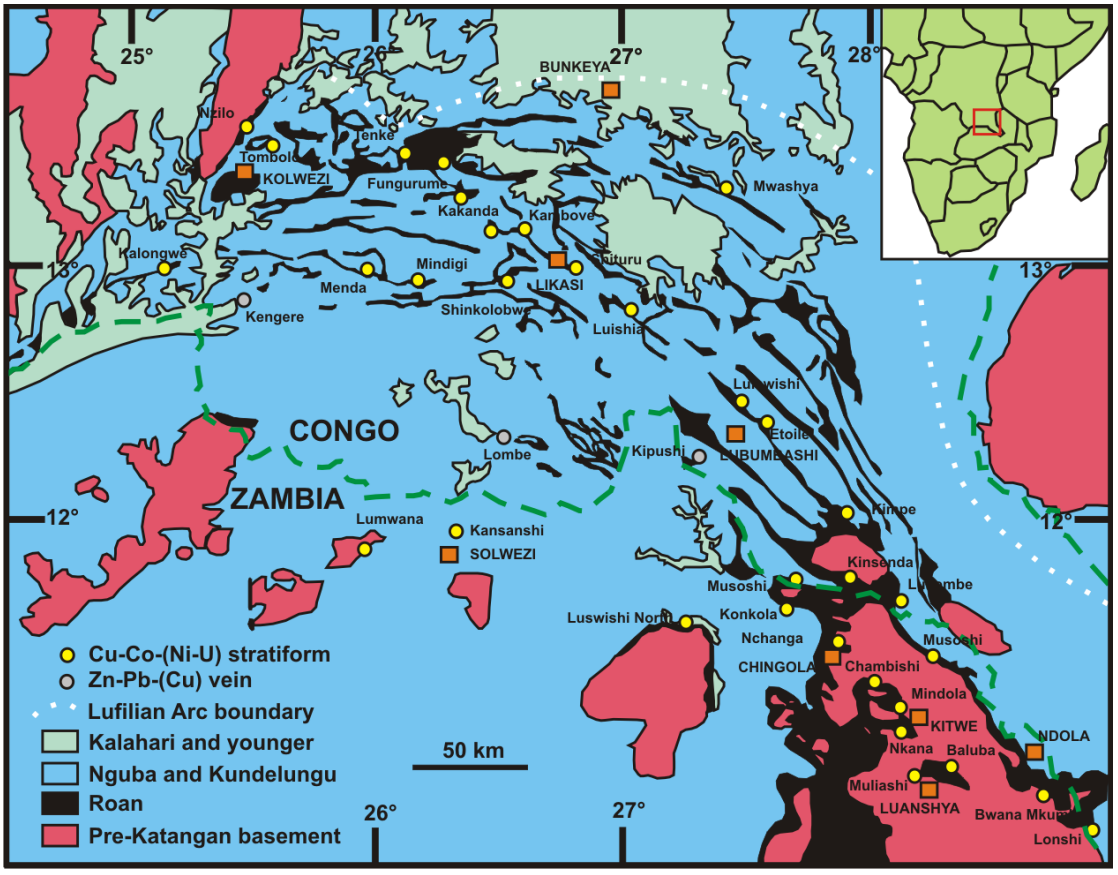

FIGURE 1.3: Geological map of the Central African Copperbelt, with geographic boundaries and ore deposits marked. (Adapted from Cailteux et al., 2005a).

There are various ways to divide the Katangan Supergroup, with recent works, e.g. Batumike et al. (2007) combining the Lower and Upper Roan and the Mwashia into one group (e.g. Fig. 1.4), giving a stratigraphy from base to top:

1. Roan Group
2. Nguba Group (previously Lower Kundelungu Group)
3. Kundelungu Group (previously Upper Kundelungu Group)

The Kundelungu Group is only locally preserved in the Zambian Copperbelt, but is relatively common in the Congolese Copperbelt. The Zambian part of the CAC preserves the stratigraphy in a consistent generally continuous manner. While differences

in stratigraphy between the two systems do occur, generally the key stratigraphic units can be correlated (Cailteux et al., 1994), this has been particularly important for interpretations of Congolese stratigraphy, which is tectonically disturbed. The majority of the ore bodies are located in lithologies which can be lithologically correlated between the Zambian and Congolese mining districts.

Age	Group	Subgroup	Lithologies
±500 Ma	Kundelungu (Ku)	Plateaux (Ku3)	Arkoses, conglomerates, sandstones and shales
		Kiubo (Ku2)	Sandstones, carbonate siltstones or shales, limestones
		Kalule (Ku1)	Ku1.3 Carbonate siltstones and shales, grey to pink oolitic limestone at base (Calcaire Rose Oolitique)
			Ku1.2 Carbonate siltstones and shales, pink to grey dolomite at base (Calcaire Rose)
±620 Ma			Ku1.1 Petit Conglomérat: Glacial diamictite
	Nguba (Ng)	Monwezi (Ng2)	Dolomitic sandstones, siltstones or shales
		Likasi (Ng1)	Ng1.3 Carbonate siltstones and shales
			Ng1.2 Dolomites, limestones, dolomitic shales and siltstones
±750 Ma			Ng1.1 Grand Conglomérat: Glacial diamictite

	Congo			Zambia		
Group	Subgroup	Formation	Lithologies	Subgroup	Formation	Lithologies
Roan (R)	Mwashia (R4)	Upper (R4.2)	Shales, carbonaceous shales, ssts	Mwashia		Dolomitic shales, grey-black carbonaceous shales, feldspathic sandstones
		Lower (R4.1)	Dolomites, jasper beds, pyroclastics, haematite, local Cu-Co			
	Dipeta (R3)	R3.2-3.4	Dolomites and interbedded argillaceous/dolomitic siltstones, feldspathic ssts, intrusic basic bodies	Kirilabombwe (RU1-2, RL3)	Kanwangungu	Dolomites and interbedded dolomitic shales, gabbros
		R3.1	Dolomitic siltstones			
	Mines (R2)	Kambove (R2.3)	Stromatolitic talc-dolomites/dolomitic siltstones minor Cu-Co	Kitwe (RL4-RL7)	Kibalongo	Shales with grit
		Dolomitic shale (R2.2)	Dolomitic, carbonaceous shales, dolomites, rare ssts. Stratiform Cu-Co, upper orebody.		Chingola	Dolomites/argillaceous dolomites, local Cu
		Kamoto (R2.1)	R2.1.3 Stromatolitic dolomite, interbedded siltstone, Cu-Co		Pelito-arkosic (inc. Copperbelt Orebody Member)	Arenites, argillites and dolomitic argillites, occasional dolomites at the base, main Cu-Co mineralisation in the lower part (Copperbelt Orebody Member)
			R2.1.2 Bedded dolomites and siltstones, silty dolomite base, Cu-Co (Lower Orebody)			
			R2.1.1 Dolomitic siltstone, Cu-Co at top			
	R.A.T. (R1) (base of R.A.T. unknown)	R.A.T. R1.3	Pink-lilac haematitic chloritic-dolomitic massive siltstones	Mindola clastics (RL7)	Mutonda	Conglomerates, coarse arkoses and argillaceous siltstones; occasional Cu-Co mineralisation
		R.A.T. R1.2	Pink-grey haematitic, chloritic siltstones with sandstones at base, stromatolitic dolomite at top		Kafufya	Quartzites
<877 Ma		R.A.T. R1.1	Purple haematitic dolomitic bedded siltstones		Chimfunsi	Pebble/cobble basal conglomerate

FIGURE 1.4: Lithostratigraphy of the Katangan Supergroup, showing the differences in the Roan Group between the Congolese and Zambian Copperbelts (adapted from Cailteux et al., 2005a).

1.3.2.1 Roan Group

The Roan Group is an amalgamation of the previous Lower Roan, Upper Roan and Mwashia stratigraphy.

The Lower Roan Subgroup is deposited upon a basement unconformity, comprising older Mindola Clastics Formation and the younger Kitwe Formation. The Mindola Clastics Formation is formed of texturally immature conglomerates and subarkosic sandstones deposited in fluvial, alluvial fan and fan delta environments (Selley et al., 2005). The formation exhibits significant lateral and vertical variations in sedimentary facies and represents the earliest rift fill, forming in narrow troughs and sub basins, controlled by half grabens, resulting in limited lateral extents bounded by basement topographic highs. This structural control on sedimentation resulted in variable thicknesses, from ∼1 km near the Konkola dome to pinching out completely, with average thicknesses of 200–300m (Selley et al., 2005). The Mindola Clastics are the 'red beds' in this system.

The Kitwe Formation hosts the majority of the Cu-Co mineralisation, and conformably overlies the Mindola Clastics. At the base of the Kitwe Formation lies the Copperbelt Orebody Member, or 'Ore Shale' as it is traditionally known. The Copperbelt Orebody Member is commonly a finely laminated dolomitic siltstone, typically 20–25m in thickness (Annels et al., 1983). Local dessication cracks in the silt and mudstone and variably replaced anhydrite nodules record periods of subaerial exposure and evaporitic conditions (Mendelsohn, 1961a; Muchez et al., 2008; Selley et al., 2005), while algal mat structures and local pyrite unrelated to mineralisation indicate deposition in intertidal to sub-tidal conditions (Bull et al., 2011). Geographical distribution of the Copperbelt Orebody Member is complicated, and west of the Kafue Anticline is where the most continuous thickness of the Copperbelt Orebody Member is preserved (Annels, 1984). The eastern margin of this section of outcrop shows an onlap surface between the Copperbelt Orebody Member and basement (Garlick, 1961). Lithostratigraphically equivalent units east of the Kafue Anticline indicate that the deposition of the Copperbelt Orebody Member occurred across much of the now elevated basement inlier, suggesting a regional sedimentary facies control and a likely transgressive event postdating the deposition of the Mindola Clastics (Binda, 1994). The western margin of Copperbelt Orebody Member outcrop is defined by abrupt pinch out, with sheared and brecciated gabbro, dolomites and dolomitic talc-chloritic schists overlying the Mindola Clastics (Selley et al., 2005).

Stratigraphically above the Copperbelt Orebody Member is a ∼200 m thick cyclical package of terrestrial conglomerates and subarkoses, and marginal marine evaporitic argillaceous sandstone, dolomitic siltstone and dolomites (Selley et al., 2005).

Correlations between the Lower Roan and equivalent rocks in the Congolese Copperbelt are critical. Most workers accept that the Copperbelt Orebody Member and the lower part of the Mines Group from the Congo are stratigraphically equivalent, though they show lithological variations, including significantly more dolomite in argillaceous sections in the Mines Group, and proportionally more distinct dolomite lithologies (Cailteux et al., 1994). The Red and Grey 'Roches-Argilo-Talqueuses' (RAT) of the Congo are thought to be statigraphically equivalent to the Lower Roan in Zambia, with the Red RAT the equivalent of the Mindola Clastics and the Grey RAT the equivalent of the Copperbelt Orebody Member in Zambia and the Mines Group in other parts of the Congolese Copperbelt (Cailteux et al., 2005b).

The Upper Roan Subgroup is traditionally distinguished from the Lower Roan by the dominance of carbonate strata over siliciclastics (Mendelsohn, 1961a), and Selley et al. (2005) suggest defining the base at the appearance of the first significant (e.g. ∼1 m thick) dolomite bed which is laterally extensive. The Upper Roan shows laterally extensive metre-scale fining upwards sequences of sandstone, siltstone, dolomite, algal dolomite and local anhydrite which are cyclical (Selley et al., 2005). Sediments in this sequence, but particularly the dolomites, show nodules and 'chicken wire' structures indicative of evaporitic processes in a subtidal environment (Selley et al., 2005). Thickness variations from <30 m to ∼800 m are common, and are typically associated with breccia bodies. These breccias vary in size from centimetres to tens of metres that can form laterally extensive complexes with thicknesses of hundreds of metres. They are usually locally stratabound, but on a regional scale can be present at different stratigraphic levels in the Upper Roan Subgroup (Selley et al., 2005). The breccias typically contain intraformational fragments of centimetre to metre scale supported by a matrix of crystalline carbonate, albite, quartz, anhydrite and chlorite, are usually internally structureless, and are thought to represent the dissolution of evaporite sequences (Selley et al., 2005).

Analogous breccia units occur in the Congolese Copperbelt, but they are larger, formed discordant to higher stratigraphic levels and contain carbonate-dominated megafragments hundreds of metres to kilometres in length in which significant swathes of stratigraphy are preserved. This tectonically mobilised, dislocated stratigraphy hosts the majority of mineralisation in the Congo (Jackson et al., 2003).

The stratigraphic equivalent to the Upper Roan in the Congo is the Dipeta Subgroup, with dolomites interbedded with shales that can be correlated with Zambian equivalents, with both groups showing evidence of evaporitic conditions during formation (Cailteux et al., 1994).

Mineralised discoveries at Frontier and Lonshi, as well as correlation of the host sediments of the Kansanshi deposit with the Mwashia Subgroup have highlighted the potential importance of the upper stratigraphy of the Katangan Supergroup (Broughton et al., 2002; Selley et al., 2005). In Zambia, the Mwashia Subgroup is traditionally recognised as a sequence of shale-dominated sediments overlying the carbonate dominated Upper Roan Subgroup (Mendelsohn, 1961a).

In the DRC, the Mwashia is formed of a lower dolomitic sequence containing minor volcanics overlain by a clastic sequence of carbonaceous shales grading upwards into sandstones or interbedded siltstones and shales (Cailteux et al., 1994, 2007). In the Congolese Copperbelt, it is normally defined at the base by tectonic breccias, making stratigraphic correlation difficult. These breccias are also present at the base of the Mwashia at Konkola and Mufulira (Cailteux et al., 1994; Selley et al., 2005).

Bull et al. (2011) recognise 6 main sedimentary sequences in the Roan Group, defined by lowstand (LST), transgressive (TST) and highstand (HST) system tracts and attempted to relate these to the isotopic signatures of carbonate horizons. These sequences are segregated with transgressive events at their bases. The base of the Copperbelt Orebody Member regionally defines one of these transgressive sequences. The carbon and oxygen isotope curves for the Roan Group carbonates broadly mirror each other, with the exception of the brecciated zones in the upper stratigraphy (Bull et al., 2011). The brecciated zones show anomalously light $\delta^{18}O$ interpreted to be the result of alteration by fluid flow (Bull et al., 2011). Three negative isotope excursions are recorded, with the most significant well recognised and associated with ore formation in the Copperbelt Orebody Member (e.g. Selley et al., 2005). The other two are not associated with mineralisation or alteration and have magnitudes consistent with potential secular variation in seawater values. One of these excursions shows its lightest values in carbonates at the base of the Upper Roan and the other begins at the base of the Mwashia and becomes progressively lighter (Bull et al., 2011). Bull et al. (2011) tentatively correlate the lower of the 2 secular isotope excusions to the Bitter Springs Stage isotope excursion, suggesting a ~811 Ma age for this part of the Katangan Supergroup (Macdonald et al., 2010), and providing further constraints on the timing of Lower Roan deposition.

1.3.2.2 Nguba Group

The base of the Nguba (previously Lower Kundelungu) is defined by the base of the Grand Conglomérat, which preserves a series of debris flows and diamictites with interbedded laminated siltstone and coarse sandstones (Binda and Van Eden, 1972). The thickness of this unit is variable in the Zambian Copperbelt, from ~10–100 m, but is

significantly thicker in the Congo (up to ∼1300 m). The clasts within the diamictite are predominantly Mwashia and Upper Roan, but basement lithologies are also observed. This important marker horizon is correlated with Sturtian diamictites deposited globally at ∼740 Ma in the 'Snowball Earth' event (Bodiselitsch et al., 2005; Key et al., 2001).

The upper stratigraphy of the Nguba Group is poorly constrained in the Zambian Copperbelt, thought to consist of 400–500 m thick sequence of carbonates, siltstones and mudstones (Selley et al., 2005).

In the Congo, the Nguba Group is well recognised, and is defined by deposition of the Grand Conglomérat. Overlying the basal diamictite is a series of carbonate shales and siltstones, transitioning upwards into dolomites with dolomitic sandstones and siltstones and rare sandstones (Batumike et al., 2007). The Monwezi Sandstone occurs at the top of this group, representing a prograding transgressive clastic sequence (Batumike et al., 2007), and in the Kundelungu Plateau is known to host mineralisation thought to be much younger (post-orogenic) than that of the traditional Copperbelt orebodies (El Desouky et al., 2008a). The carbonate formations above the Grand Conglomérat are regarded as cap carbonates formed after glaciation (Batumike et al., 2007).

1.3.2.3 Kundelungu Group

The Kundelungu Group (formerly Upper Kundelungu) is rarely preserved in Zambian successions, and where present, contains the Petit Conglomérat diamictite and a series of carbonates, siltstones and mudstones (Selley et al., 2005).

In the Congo, the Kundelungu Group is much more commonly preserved, and is defined at the base by the presence of the Petit Conglomérat glacial diamictite layer thought to be formed during the Marinoan (∼620 Ma; Batumike et al., 2007). The Petit Conglomérat contains clasts of Mwashia and Nguba rocks, indicating erosion of the stratigraphy prior or during its deposition and potentially the development of a foreland basin (Batumike et al., 2007). Stratigraphically above this horizon lie more cap carbonates in the form of dolomites, carbonate siltstones and shales, eventually transitioning to dolomitic sandstones and siltstones then finally into arkoses, argillaceous siltstones and conglomerates (Batumike et al., 2007). These rocks represent deposition in glacial to glacio-marine conditions (Batumike et al., 2007), and this group broadly represents the change from extensional to compressional tectonics in the CAC (Batumike et al., 2006; John et al., 2004).

1.3.3 Basin development

Whilst the stratigraphy of the Copperbelt is well studied and generally accepted, aside from naming conventions and correlation between the Congolese and Zambian stratigraphy, the understanding of basin development is weaker (Selley et al., 2005), particularly the influence of rifting as an active process in basin growth. The classic view involves passive basin development without rifting playing a significant role, evidenced by a lack of magmatism, volcanism, deep water rift sedimentary facies and lack of recorded syn-depositional faulting (Binda, 1994; Mendelsohn, 1961a), suggesting instead that eustacy was more important than slow subsidence rates. In contrast, the frequent half-graben morphologies and facies and thickness variations are regarded by Selley et al. (2005) as rift-formed geometries, similar to tectonostratigraphic models of modern Phanerozoic intracontinental rifts. Selley et al. (2005) regard the compartmentalised sub-basin geometry and depositional environment of the Mindola Clastics as typical of rift initiation and early development of fault growth systems. In this model, the transgression forming the Copperbelt Orebody Member represents a transition to a system controlled by a number of master faults, rather than small individual faults and basins. The cyclic sediments (including carbonates) in the Upper Roan and Mwashia record a shift to a stable, platform environment with accomodation space formed by gradual regional subsidence (Selley et al., 2005). Gabbro intrusives and rare mafic extrusives in the Mwashia and Nguba formed during a period of extensional tectonism (Kampunzu et al., 2000; Key et al., 2001; Porada and Berhorst, 2000), with the diamictites of the Grand Conglomérat and associated volcanism related to extension and the breakup of Rodinia (Hoffman, 1999).

Whilst most workers regard the formation of the polylithic breccia units which are common across much of the CAC as resulting from evaporite dissolution and halokinesis, the timing of their formation and role in terms of basin evolution is still contentious. Most workers agree that these horizons represented planes of weakness and lubrication during basin inversion, causing the fragmentation of stratigraphy at multiple scales and aiding significant northward transport, particularly in the Congolese Copperbelt (Porada and Berhorst, 2000; Selley et al., 2005). Other workers also recognise the potential impact of salt tectonics during basin extension (Jackson et al., 2003). Difference in available salt thickness between Zambian and Congolese successions, and the associated lack of widespread salt diapirism in Zambian successions may play a role in why Zambian stratigraphy is more intact than that in the Congo, and why thrusting is less prevalent (Selley et al., 2005).

1.3.4 Temporal constraints

The earliest temporal constraint on sedimentation is the Nchanga Red Granite (883 ± 10 Ma; Armstrong et al., 2005), which is uncomformably overlain by the Katangan Supergroup, indicating significant uplift and erosion occurred before the formation of the Katangan Basin. Recent isotopic evidence and chemostratigraphy (Bull et al., 2011) indicates the Lower Roan formed before ∼811 Ma. Small but common mafic to intermediate igneous intrusions (primarily gabbros and diorites) occur within the middle part of the Katangan Supergroup dated at ∼765 to 735 Ma (Key et al., 2001). Main stage orogenesis occurred between ∼560 and ∼530 Ma based on U-Pb zircon dating of syntectonic to postectonic granites and rhyolites intruding Upper Katangan strata (Hanson et al., 1993), supported by U-Pb monazite ages (peak metamorphism; ∼530 Ma) from whiteschist assemblages from the Domes region (John et al., 2004). Examples of ages between 512–465 Ma (Cosi et al., 1992; John et al., 2004; Torrealday et al., 2000) likely represent postorogenic cooling (Selley et al., 2005).

1.3.5 Mineralisation

The Central African Copperbelt is the world's largest SHSC province, hosting at least 14 deposits containing >2 Mt Cu, with combined production and reserves totalling ∼190 Mt Cu with Zambia containing ∼88 Mt, as well as being the world's richest cobalt repository (Hitzman et al., 2005; Selley et al., 2005). The Zambian Copperbelt contains seven deposits with > 2 Mt Cu: Konkola, Nchanga, Nkana, Mufilira, Luanshya, Chambishi and Musoshi (Fig. 1.3). Whilst Musoshi is located across the Congolese border, its characteristics are most similar to Zambian-style deposits (Selley et al., 2005).

1.3.5.1 Stratigraphic and host rock relationships

The traditional exploration paradigm focussed on the Copperbelt Orebody Member in the Lower Roan, since most Copperbelt deposits in Zambia occur within an interval ∼100 m either side of this key formation (Fig. 1.5). However, other parts of the stratigraphy are recognised as increasingly important, hosting deposits such as Kansanshi, Frontier, Lonshi and Kamoa (Broughton et al., 2002; Selley et al., 2005). Mineralisation is also present in basement lithologies (Bernau et al., 2013; Wakefield, 1978). Many deposits, particularly volumetrically major ones contain multiple orebodies, sometimes in the form of stacked mineralised horizons with barren stratigraphy between (e.g. Nchanga and Mufulira; McGowan et al., 2006; Brandt et al., 1961). Other deposits show multiple orebodies in the same stratigraphic interval, but separated by barren gaps (e.g. Konkola;

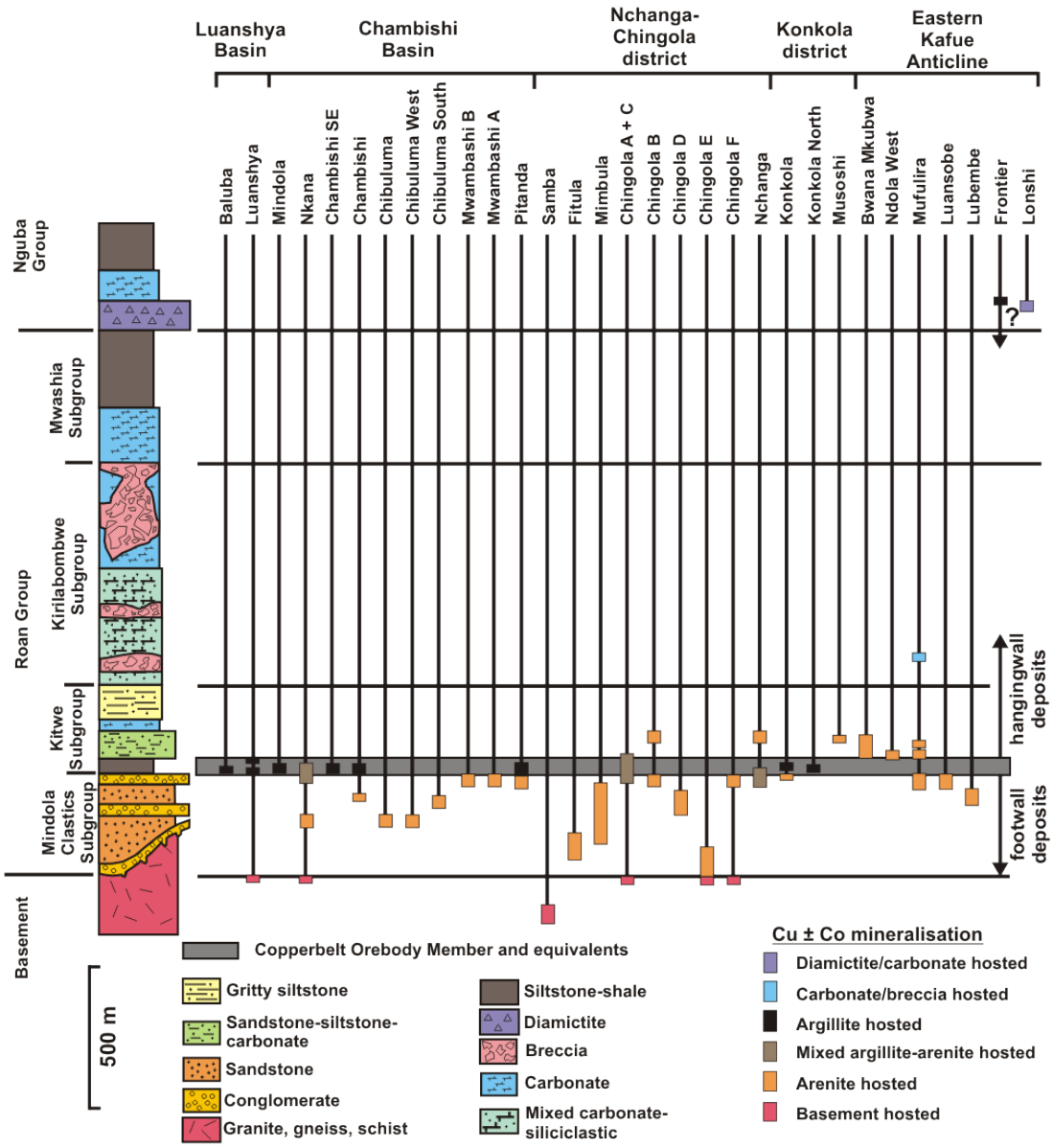

FIGURE 1.5: Stratigraphic distribution of Zambian Copperbelt mineralisation. Thicknesses of mineralised intervals not to scale due to variable thickness of the Lower Roan Subgroup. Most major orebodies located within a ~200 m interval centred on the Copperbelt Orebody Member (Adapted from Selley et al., 2005).

Sweeney et al., 1986). In Zambia, deposits are typically hosted in either argillaceous rocks or arenites (Selley et al., 2005). Some rare deposits contain orebodies in both argillites and arenites, and again, typically tend to be the larger deposits containing multiple stacked ore lenses (Selley et al., 2005). Economic mineralisation in argillites occurs at the base of the Copperbelt Orebody Member, and tends to show long strike lengths. While mineralisation is observed in the upper parts of the Copperbelt Orebody Member, it is generally uneconomic (Selley et al., 2005). In contrast, arenite-hosted orebodies may form both below (footwall) and above (hanging-wall) the Copperbelt Orebody Member, with footwall orebodies formed either directly below the Copperbelt

Orebody Member, or in stratigraphy separated by barren units (Selley et al., 2005). Hanging-wall orebodies are stratigraphically segregated from the Copperbelt Orebody Member and typically form as parts of the larger deposits with multiple stacked lenses, (e.g. Nchanga; McGowan et al., 2006). Most basement-hosted mineralisation is uneconomic and is located immediately below the basal Katangan Supergroup unconformity (Selley et al., 2005) and is mostly spatially associated with significant mineralisation in the Lower Roan. However, occurrences of mineralisation within the basement distinct from Lower Roan mineralisation are recognised (e.g. Samba; Wakefield, 1978) and may form economic deposits (e.g. Lumwana, Bernau et al., 2013). Geometries and characteristics of arenite-hosted deposits are comparable to hydrocarbon traps, and many workers suggest this relationship may explain the formation of sulphides within the ostensibly reductant-poor arenites (McGowan et al., 2006; Selley et al., 2005).

Where multiple orebodies are present in the same stratigraphic horizon, they tend to be separated by barren gaps (Mendelsohn, 1961a). These zones can vary from hundreds to thousands of metres along strike, typically containing pyrite and haematite along with uneconomic copper sulphide grades. Barren gaps are often associated with structural and thickness variations in the Mindola Clastics, and lateral facies changes in the Copperbelt Orebody Member, transitioning away from argillite into microbially laminated dolomite or arenites (Selley et al., 2005). The lack of mineralisation in these zones may reflect lack of available reductant, or significant changes in porosity and permeabilities altering the transport of mineralising fluids.

1.3.5.2 Styles of mineralisation and minor metals

At the deposit scale, similar to most SHSCs, mineralisation can be hosted in a variety of different styles, from disseminated, to vein-hosted, both pre- and post-kinematic veins, and shear zone hosted, with oxidised supergene mineralisation commonly overprinting parts of orebodies. The majority of most orebodies is comprised of hypogene sulphide mineralisation consisting of a mix of chalcocite (Cu_2S), bornite (Cu_5FeS_4), chalcopyrite ($CuFeS_2$) and pyrite (FeS_2), with Co mineralisation typically formed as carrolite ($CuCo_2S_4$). Most veining, particularly pre-kinematic veins, show identical sulphide mineralogy to the disseminated mineralisation, though post-kinematic veins may be dominated by chalcopyrite. Mineralised post-kinematic veins commonly contain uraninite and other uranium phases, rutile, specular haematite and molybdenite as accessory phases. Barren post-kinematic veins, common in many deposits, are typically quartz, carbonate or quartz-carbonate. Gangue minerals in hypogene mineralisation commonly contain phlogopite, potassic feldspars, sericite and muscovite, albite, calcite and dolomite, quartz, rutile, specular haematite, and anhydrite. Supergene overprinting

of the hypogene assemblage typically occurs within ~30–70 m of the present day surface (Mendelsohn, 1961a), but in certain areas may reach significant depths (e.g. Konkola and Nchanga; McGowan et al., 2006). At Konkola, the supergene alteration reaches a depth of over 1300 m, occurring at the base of the Copperbelt Orebody Member and in an underlying conglomerate, which acts as an aquifer transporting oxidised waters into contact with the orebody. Supergene alteration typically occurs in the form of malachite ($Cu_2CO_3[OH]_2$) and chrysocolla ($[Cu,Al]_2H_2Si_2O_5[OH]_4.nH_2O$), but commonly supergene alteration progresses from the hypogene assemblage to a chalcocite ± malachite ± chrysocolla assemblage to a final supergene oxidised assemblage, which may lead to complications in recognising primary chalcocite.

Many deposits in the Copperbelt exhibit sulphide zonation which is common in SHSCs, both in a lateral and vertical direction, particularly those deposits hosted within the Copperbelt Orebody Member (Mendelsohn, 1961a). The zonation forms as a function of varying relative solubilities in sulphide minerals during precipitation due to changing redox conditions (Rose, 1989). The zonation is typically bornite (± chalcocite) to chalcopyrite (± carrolite) to pyrite (± pyrrhotite with rare sphalerite), with the pyritic zone typically marking the end of economic mineralisation (Mendelsohn, 1961a). Locally, the zonation may be more complicated and less obvious, with barren gaps in particular causing breaks in the zonation pattern with unmineralised pyrite zones. The CAC is notable in its lack of significant galena and sphalerite mineralisation, as well as being depleted in Ag, and enriched in Co over other SHSC districts (Hitzman et al., 2005). It is unclear what causes the difference in secondary metal characteristics in SHSCs, with metal transport and deposition mechanisms perhaps being factors, but it seems highly likely that metal budget is controlled by the source rocks. Hitzman (2000) suggests that there is not a sufficiently high enough volume of red beds in the CAC to account for the copper endowment, assuming metal concentrations in Copperbelt red beds were the same as other examples. This then requires that either Copperbelt red bed metal concentrations were anomalously high compared to similar successions elsewhere, that there is a set of missing red bed stratigraphy somewhere in the Copperbelt that the known stratigraphy is displaced from (Hitzman, 2000), or that there has been a significant contribution of metals from the basement lithologies. The contribution of basement lithologies to the metal budget seems by far the most realistic, since there is ample evidence for mineralisation in the basement (Bernau et al., 2013; Selley et al., 2005; Wakefield, 1978), suggesting ore forming fluids were capable of circulating at depth, and this empirical evidence is supported by numerical modelling (Koziy et al., 2009).

Understanding of the controls on cobalt mineralisation and distribution in the CAC is poor. Deposits which show economic cobalt mineralisation in Zambia are confined to a restricted area on the western side of the Kafue Anticline, and show some spatial

relationships with a broadly equivalent area where gabbros intrude into the Upper Roan Group (Annels, 1984). However, this does not explain the wide distribution of economic cobalt mineralisation in deposits in the Congolese Copperbelt, where mafic rocks are rare. Additionally, it is difficult to reconcile the relative age of the gabbroic intrusions with an early diagenetic timing for Cu mineralisation which many authors prefer. Much work is yet to be done in order to improve understanding of Co mineralisation, though some recent work has suggested a relationship between Co mineralisation and heavier $\delta^{34}S$ signatures of sulphides (Bernau et al., 2013; McGowan et al., 2006).

Uranium mineralisation in the CAC generally forms in post-kinematic veins, though can also form as disseminations as pitchblende, uraninite, brannerite, coffinite and secondary oxides (Selley et al., 2005). In most cases uranium mineralisation is subeconomic and not exploited. Uranium enriched zones may occur stratigraphically below or adjacent to main copper orebodies (Mendelsohn, 1961a; Selley et al., 2005).

Whilst Pb and Zn mineralisation is uncommon in typical Copperbelt orebodies, discrete bodies of Pb–Zn mineralisation are present in the Copperbelt as a whole, typically associated with shallow marine platformal carbonates of the Katangan Supergroup (Kampunzu et al., 2009). These deposits comprise Zn–Pb mineralisation with some copper, as well as minor Cd, Co, Ge, Ag, Re, As, Mo, Ga and V, and are typically small, with only a few thousand tons of ore, and are exploited on a minor scale, if at all (Kampunzu et al., 2009). The exceptions are the Kabwe and Kipushi deposits, which are much larger in size and economic. Most Zn–Pb–Cu mineralisation is hosted within carbonates in the Nguba Group. Whilst some deposits may show stratiform control on mineralisation, the largest, economic deposits are associated with thrust zones, breccias, faults and karstic structures providing fluid conduits for mineralisation, forming irregular pipe-like structures (Kampunzu et al., 2009). Age constraints on mineralisation range from 680 ± 13 Ma for Kabwe based on Pb isotopes (Kamona et al., 1999), with Kipushi dated at 451.1 ± 6 Ma and 450.5 ± 3.4 Ma by Rb-Sr and Re-Os of sulphides (Schneider et al., 2007). These ages indicate that, like traditional SHSC deposits in the Copperbelt, Zn-Pb mineralisation may have spanned a long time period, and in some cases postdates orogenesis.

1.3.5.3 Textures and relative timing

Sulphide paragenesis is similar across many deposits, and is a function of sulphide solubility, similar to the sulphide zonation (Mendelsohn, 1961a; Rose, 1989), with pyrite on the edge of the zonation pattern forming earliest and the copper mineralisation paragenetically later. Multiple types of pyrite can be present in Copperbelt orebodies however.

Some pyrite formed in the Copperbelt Orebody Member at Nchanga shows isotopic signatures, forming from bacterial sulphate reduction, indicative of formation during diagenesis, and these signatures are distinct compared to those of sulphides forming the mineralisation (McGowan et al., 2006, 2003).

Many of the textures interpreted as forming through diagenesis simply reflect the control of porosity and permeability on mineralisation. Assuming porosity and permeabilities are maintained, or secondary porosity developed as suggested by Selley et al. (2005), these textures may form at a wide variety of times in the basin, up until orogenesis. Replacement textures of nodules and other minerals could also occur over a wide time scale in the basin, although evidence in the Congo in the form of sulphur isotope signatures indicative of BSR suggest a diagenetic time of formation (Muchez et al., 2008); and textures and geometries of orebodies indicative of the presence of hydrocarbons acting as reductants also suggest a later period of mineralisation after hydrocarbon maturation and migration. Much of the interpretation of textures is hindered by the local remobilisation of sulphides during basin inversion and deformation into foliation planes and veins. Modern workers generally recognise that mineralisation probably occurred over a variety of stages, from late diagenesis to basin inversion (e.g. Nchanga; McGowan et al., 2006) all the way through to mineralisation formed by post-orogenic veins (e.g. Kansanshi; Broughton et al., 2002; Torrealday et al., 2000). Many deposits exhibit evidence of multiple stages of mineralisation and remobilisation (e.g. Nkana; Muchez et al., 2010). It seems likely that the long basin history and repeated episodes of mineralisation, as well as the scale of the CAC are a major factor in why the district is so well endowed with a great number and size of deposits.

Absolute controls on timing of mineralisation in the Copperbelt are poor. Mineralisation is present within the Lower Roan sediments, and so must post-date the Nchanga granite (883 $\pm$ 10 Ma; Armstrong et al., 2005) which forms the basement unconformably below the Katangan succession. Mineralisation at Musoshi is cut by late veins which locally remobilise sulphides but also contain rutile, which has been dated at 514 $\pm$ 2 Ma (Richards et al., 1988a). Similarly, the vein hosted mineralisation at Kansanshi has been dated with the Re-Os method at 512 $\pm$ 1.2 Ma and 502 $\pm$ 1.2 Ma (Torrealday et al., 2000).

1.3.6 Alteration

The mineralised stratigraphy in the CAC are visibly altered, with the earliest workers suggesting the influence of magmatic derived hydrothermal fluids (e.g. Bateman, 1930). Once the unconformity between the basement and the Katangan Supergroup

was identified, the syngeneticists attributed the formation of the alteration assemblage to post-mineralisation processes (Mendelsohn, 1961a). Currently, most workers view the alteration as being formed from the transport and interaction of basin brines with the host rocks, which circulated through much of the stratigraphy in the lower part of the Katangan Supergroup, as well as the upper basement and probably deeper basement as well (Koziy et al., 2009; Selley et al., 2005).

There are three main types of alteration in the Zambian Copperbelt (Selley et al., 2005):

- Calcium and magnesium
- Potassic
- Sodic

Ca and Mg-rich phases in the Copperbelt are typically calcite, dolomite and phlogopite, with phlogopite typically ubiquitous. Phlogopite is common in argillaceous rocks in the lower parts of the Katangan Supergroup, as well as being formed in carbonates and in the basement lithologies (Selley et al., 2005). It occurs as discrete laths, disseminations and porphyroblasts, and as an accessory in veins, or as an alteration product around their edges (Selley et al., 2005). Phlogopite commonly aligns within the foliation and forms in the pressure shadows of porphyroblasts indicating formation and recrystallisation during deformation (Selley et al., 2005). Anhydrite, dolomite and calcite typically form as nodules, cements, replacements and in veins in the lower Katangan, as well as in the basement. Much of the magnesian alteration in terms of texture and mineralogy is indicative of sabkha environments, and sulphur isotope signatures of sulphate from anhydrite is similar to that of Neoproterozoic seawater, reflecting an evaporitic origin (Muchez et al., 2008; Selley et al., 2005). Anomalously light carbon isotope signatures for much carbonate related to ore formation indicate oxidation of organic matter and sulphate reduction (Machel, 2001, 1987; Machel et al., 1995; McGowan et al., 2006; Muchez et al., 2008; Selley et al., 2005). Ore sulphides typically show an antithetic relationship with anhydrite, where progressive replacement of anhydrite by sulphide minerals indicates the importance of pre-ore evaporitic anhydrite in providing an in-situ oxidised sulphur source for reduction (Selley et al., 2005; Sweeney and Binda, 1989). Paragenetic relationships between alteration phases suggest that the calcium-magnesium alteration stage postdates the earliest stage of potassic alteration, but predates a later stage of replacive potassium feldspar formation (Selley et al., 2005)

Common potassic phases in the Copperbelt in the lower Katangan Supergroup include potassium feldspar, phlogopite, muscovite and phengite (Selley et al., 2005). Detrital K-feldspar is a common component of coarser beds in the lower Katangan Supergroup,

comprising up to 20 % of the detrital grains. This is in stark contrast to plagioclase, which is a common component in the basement lithologies but is typically absent in the sediments derived from erosion of the basement. Petrographic analysis indicates the replacement of plagioclase by K-feldspar and muscovite, with secondary K-feldspar overgrowths occuring on detrital K-feldspar as an early (pre-carbonate) alteration phase (Selley et al., 2005; Sweeney and Binda, 1989). Most K-feldspar alteration occurs in the form of micro to coarsely crystalline matrices formed in both argillites and arenites. Volumetrically less significant K-feldspar alteration forms along fractures and in veins. Secondary K-feldspar often contains inclusions of tourmaline, helping distinguish it from detrital examples, and is formed as rims on detrital feldspar and in post-kinematic veins. This indicates a long pervasive, multi-stage period of potassic alteration (Selley et al., 2005; Sutton and Maynard, 2005). Secondary K-feldspar alteration is a common gangue product in many deposits (Mendelsohn, 1961a), commonly intergrown with sulphide mineralisation, and there is typically a concomitant increase in Cu content and K_2O/Al_2O_3 in the Copperbelt Orebody Member (Selley et al., 2005). However, high K_2O/Al_2O_3 ratios and the presence of secondary K-feldspar occur at all levels of Lower Roan stratigraphy, indicating the presence of potassic alteration hundreds to thousands of metres beyond the mineralised zone (Selley et al., 2005). Sericite is a common alteration mineral, particularly in arenite-hosted deposits, replacing detrital and secondary K-feldspar and often forms on shear zones and mineralised faults (e.g. Nchanga; McGowan et al., 2006, 2003), and may represent changing conditions during ore formation causing K-feldspar to become unstable (Selley et al., 2005).

Secondary albite is the principal component of the sodic alteration phase, typically forming after secondary K-feldspar and sericite as overgrowths, with scapolite locally an important component (Selley et al., 2005). Zones of albite alteration typically show association with carbonate minerals and often show phlogopite enrichment compared to nearby K-feldspar altered zones (Annels, 1989). Sodic alteration is more common in the Upper Roan than the Lower Roan (Selley et al., 2005). In the Upper Roan, intense albitisation occurs in breccias, forming matrices of coarsely crystalline albite, along with dolomite, anhydrite, talc, tremolite, phlogopite and minor rutile and haematite (Selley et al., 2005). Breccia clasts are also strongly albitised, but this albitisation replaces earlier K-feldspar alteration. Post-kinematic veins at Kansanshi show albite alteration halos (Broughton et al., 2002; Torrealday et al., 2000) suggesting albite formation and sodic alteration occurred throughout orogenesis. The strong association of sodic alteration with brecciation and fracture zones suggests an important role for fracture-induced permeability (Selley et al., 2005). Albite is a common gangue mineral in many deposits, but its relationship with sulphides is less clear. In many cases, albite appears to have

replaced the K-feldspar in a pre-existing sulphide-K-feldspar assemblage, only locally overprinting pre-existing mineralisation (Selley et al., 2005).

Locally, evidence of carbonaceous alteration can be observed in arenites, particularly within and near the Mufulira deposit (Brandt et al., 1961). These zones are not confined to bedding, with carbonaceous material finely disseminated throughout the arenites. These zones are often associated with high ore grades, and have been proposed to represent the remains of hydrocarbons within arenite reservoirs (Selley et al., 2005).

1.3.7 The 'First reductant model'

The significant research into SHSCs over the past century has led to the development of an interpretation for the formation of these deposits, loosely termed here 'The first reductant model'. In this model, metals are released from basement rocks or labile detrital minerals in immature sediments deposited during basin formation and rifting by the formation of iron oxides and oxyhydroxides during the 'reddening' process of red bed formation. These metals are weakly bound to the iron oxides and oxyhydroxides, and readily mobilised, predominantly as chloride complexes in basin brines, either seawater or evaporite derived. These oxidised fluids then deposit sulphide mineralisation at the first available chemical trap, typically a reductant in the form of a shale. This process may be aided by varying factors such as geometries of the stratigraphy, in the form of traps such as folds or pinch out structures on basin highs. This process is not necessarily confined to either diagenetic, late-diagenetic or post diagenetic timing, with timing of deposit formation likely controlled by the development of the basin and associated fluid expulsion/mobilisation events. In the case of the Central African Copperbelt, the Copperbelt Orebody Member in the Lower Roan is exceptionally mineralised compared to the rest of the stratigraphy because it formed the first reductant, and at the same time a seal for hydrocarbons above the red bed succession of the Mindola Clastics that is present over a great lateral extent in the basin. Deposits present in upper parts of stratigraphy likely represent areas where mineralising fluids did not intersect the Copperbelt Orebody Member, allowing them to contact another reducing horizon and deposit mineralisation higher up the stratigraphy. This may be due to lack of Copperbelt Orebody Member in the underlying succession or breaching of the Copperbelt Orebody Member allowing mineralising fluids to move through without a significant mineralisation event occurring.

1.4 Thesis outline

Chapter 2

This chapter details the methodologies used to acquire the data presented in this thesis.

Chapter 3

This chapter describes the process of categorising the veins used in this project to estimate the characteristics of preserved palaeofluids. The results of a regional fluid inclusion study are presented, giving estimates on fluid temperature, salinity and chemistry. The results of a crush leach bulk fluid inclusion study are presented, giving anion and cation chemistries. This allows for a reconstruction of seawater evaporation processes and a broad characterisation of fluid halogen chemistry through basin history. Stable isotope data are presented in the form of δ^{37}Cl of fluid inclusion leachates, δD of fluid inclusions and δ^{18}O and δ^{13}C of vein quartz and carbonates. The stable isotope data are used to constrain fluid sources and interactions over the basin history.

Chapter 4

This chapter presents trace and rare earth element chemistry of sulphide minerals from across the Zambian Copperbelt. Normalised REE profiles are generated to assess the distribution of LREEs and HREEs and identify Eu and Ce anomalies. Relationships between trace elements are investigated to assess distributions of common minor components in SHSCs such as Co, Ag, Au, Pb, Zn, Ni and U. The effect of different sulphide mineralogy on trace and REE contents is investigated. The trace and REE concentrations of these sulphides are compared to other published data for sulphides. Stable isotope data is presented in the form of δ^{34}S in order to investigate signatures of mineralisation and mechanisms of sulphate reduction. The secular variation in δ^{34}S of seawater sulphate is described, and the impact of this variation on the Copperbelt dataset is discussed. The results of Re-Os dating of Copperbelt sulphides are presented, and the importance of these new data in understanding and constraining the temporal history of the Copperbelt region is assessed.

Chapter 5

A summary of uranium mineralisation and prospects within the Copperbelt area is

presented in this chapter. The mineralogy, structure and textures of uranium mineralisation at the Lumwana deposits is described at mine, hand specimen, thin section and SEM scale. The remobilisation of uranium mineralisation is detailed, discussed and interpreted. The results of a uranium-lead dating program are presented. Comparisons are made with other uranium occurrences in the Copperbelt, and with other uranium ores worldwide.

Chapter 6

This chapter summarises the conclusions of the project and presents avenues for further research in light of these conclusions.

Chapter 2

Methodology

The main aims of this project are to investigate the nature of palaeofluids preserved within the Zambian basin and their role in the formation of mineralisation in order to test the hypothesis that fluids were generated via basin processes such as evaporation of seawater and evaporite generation. In order to establish the nature of these palaeofluids a variety of standard techniques were applied, such as fluid inclusion microthermometry, analysis of fluid inclusion leachates for anion and cation contents and stable isotope studies. Fluid inclusion microthermometry is the standard basic technique for investigating palaeofluid temperatures and salinities, as well as providing information on salt chemistry (e.g. Roedder, 1984; Shepherd et al., 1985), whilst micro computed tomography is a recent development in imaging which presents a novel tool for mapping fluid inclusions in 3D. Analysis of fluid inclusion leachates is a tool frequently used to differentiate fluids and investigate fluid chemistries, including sources of salinity and fluid interactions within geological and hydrological systems (e.g. Gleeson and Turner, 2007; Grandia et al., 2003). Studies of stable isotopes of sulphur, oxygen, hydrogen and carbon are classic techniques used to investigate mineralisation processes, fluid-fluid and fluid-rock interactions, and differentiate between sources of fluids (Ohmoto and Goldhaber, 1997; Taylor, 1997). Stable chlorine isotope studies are a relatively recent technique used to investigate sources of chlorine and physicochemical processes affecting this common fluid component (eg. Eastoe et al., 2001). Solution ICP-MS provides a mechanism to investigate chemistry of minerals, in this case to obtain trace and rare earth element data on sulphide mineral grains. the U-Pb and Re-Os radiogenic dating techniques are standard tools for the dating of minerals and have been used in previous studies on the Copperbelt (eg. Torrealday et al., 2000), used here to attempt to constrain the age of mineralisation for a variety of uranium and sulphide mineral samples.

2.1 Sample collection and preparation

This study involved the analysis of rocks, mineral veins, their hosted palaeofluids and separate mineral phases. The majority of samples collected for this study were obtained from field sampling in Zambia during the period of October to November 2009 and 2010. Sampling was conducted at both active mines and exploration prospects. Hand specimen samples were obtained from the open pits of the Lumwana and Kansanshi copper mines, and from diamond drill core from Lumwana, Kansanshi, Konkola, Konkola North. Diamond drill core was also sampled from the Kalumbila-Sentinel, Enterprise, and Samba exploration prospects (Fig. 2.1). The ore deposits of the Konkola district are essentially a single broadly continuous orebody, including extensive mineralisation at Chililabombwe, Konkola North and Musoshi. The orebody is mined at several places on the edges of basement highs, giving rise to the different deposit names. For this study, 'Konkola' refers to the samples obtained from the Chililabombwe part of the orebody, with Konkola North referred to separately (Fig. 2.2). Other samples were held over from previous projects by Ross McGowan (Nchanga), Robin Bernau and Matt McGloin (Lumwana). Samples for Musoshi were kindly supplied by JP Richards. A summary of the deposits sampled is provided in Table 2.1.

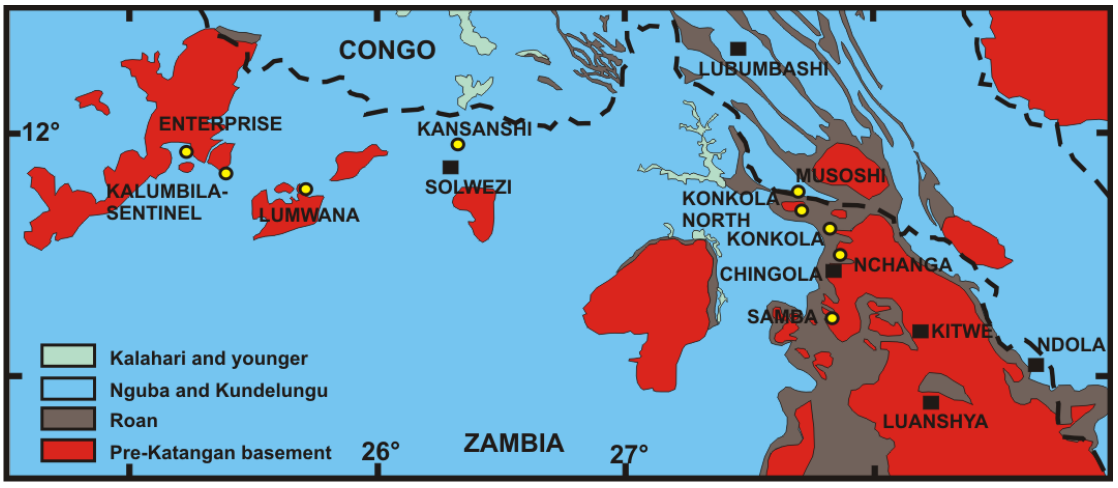

FIGURE 2.1: Map of deposits sampled in the Zambian Copperbelt (adapted from Cailteux et al., 2005a).

Samples were photographed and sub-sampled for suitability for the production of polished thin sections, doubly-polished wafers for microthermometry and the picking of mineral separates. Samples were then cut for sub-sampling using a diamond saw and crushed using a fly press, taking care not to contact the metal of the press. Samples were subsequently washed, sonicated and sieved in order to provide size fractions for the picking of mineral separates.

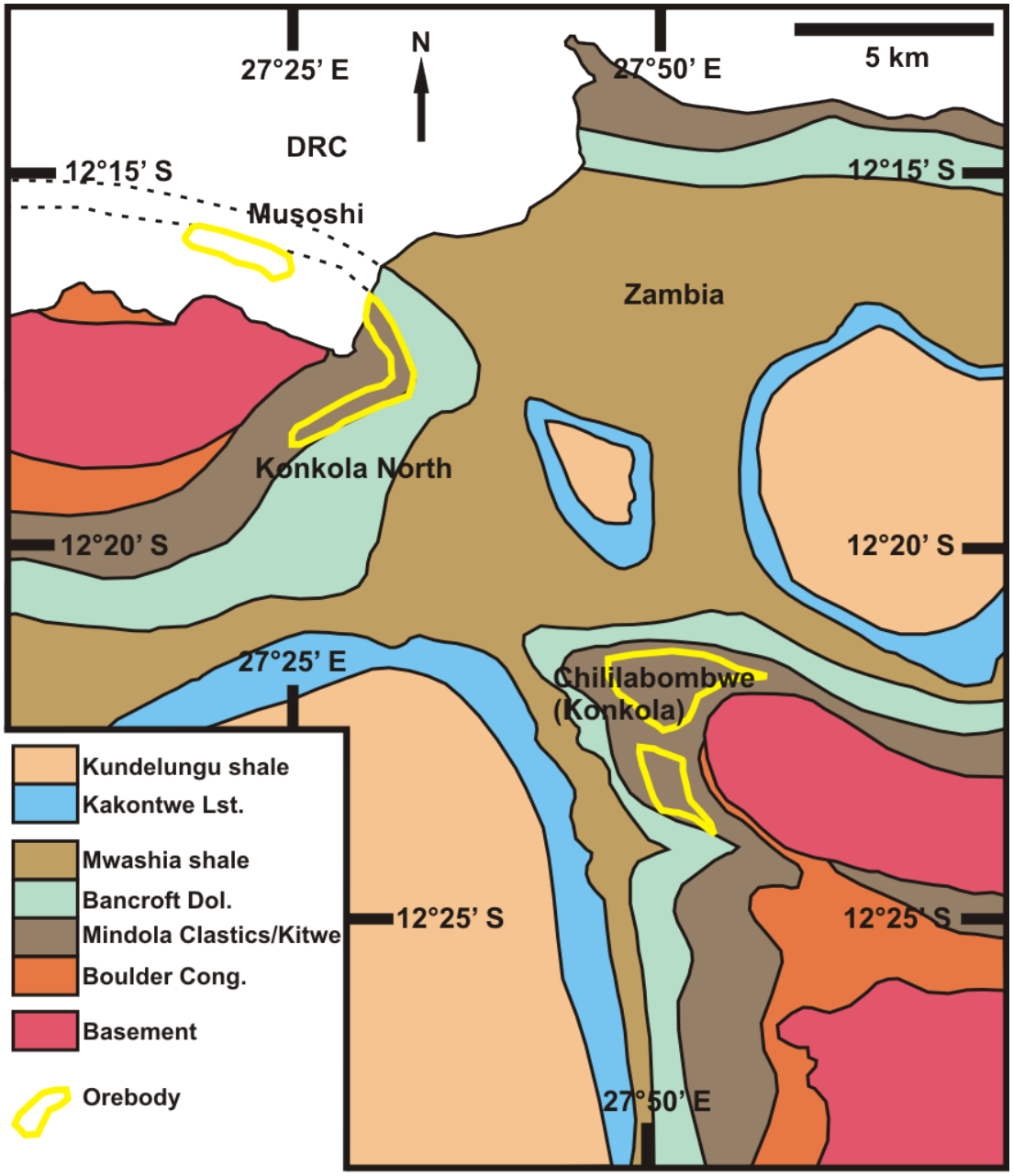

FIGURE 2.2: Map of geology and orebodies of the Konkola region of the Zambian Copperbelt (adapted from Selley et al., 2005; Sweeney et al., 1986).

TABLE 2.1: Summary of deposits sampled

Deposit	Location	Stratigraphy	Mineralisation	Veining	Tectonic Setting	Reference
Lumwana	Mwombezhi Dome	Granite gneisses and qtz-bt-musc-ky schist	Cpy-bn (±U ±Co)	Pre kinematic boudinaged qtz veins, pre-syn kinematic veins remobilising sulphides within ore schist, post-kinematic veins	Basement shear zones	Bernau et al. (2013)
Kansanshi	Solwezi Dome	Qtz-carb veins hosted in Kundelungu phyllites, marbles and schists	Cpy-pyrr-py (±Mo ±Au)	Post kinematic qtz-carb veins	Post kinematic veins host mineralisation	Broughton et al. (2002)
Enterprise	Kabompo Dome	Phyllite—metamorphosed Mwashia sediments?	Nickeliferous py, vaesite, millerite	Post kinematic qtz-talc-kyanite veining	Post kinematic veins host mineralisation	
Kalumbila-Sentinel	Kabompo Dome	Phyllite - metamorphosed Mwashia sediments?	Cpy-pyrr-py (±Ni)	Pre-syn kinematic carbonate-qtz veins, later quartz-carb veins	Stratiform and vein remobilised sulphides	Steven and Armstrong (2003)
Konkola	Classic mining district	Lower Roan Ore Shale	Py-cpy-bn-ccc-carrolite	Pre-syn kinematic quartz carbonate veins in Ore Shale	Stratiform mineralisation	Sweeney et al. (1986)
Konkola North	Classic mining district	Lower Roan Ore Shale	Ccc-cpy-py-bn-tenorite-carrolite	Pre-syn kinematic quartz carbonate veins in Ore Shale	Stratiform mineralisation	Sutton and Maynard (2005)
Nchanga	Classic mining district	Lower Roan Ore Shale and sandstones	Py-bn-cpy-ccc-carrolite	Veining contained within basement and multiple levels of host stratigraphy	Mineralisation associated with basin inversion structures	McGowan et al. (2006)
Samba	Classic mining district	Qtz-musc schists in porphyry intrusives and volcanics	Py-cpy-bn	Pre kinematic boudinaged quartz veins	Basement shear zone	Wakefield (1978)
Musoshi	Classic mining district	Lower Roan Ore Shale	Cpy-bn-py (±carrolite)	Post kinematic quartz-haematite veins	Stratiform and vein remobilised sulphides	Richards et al. (1988a)

2.2 Petrography

Petrographic descriptions of rocks, minerals and fluid inclusion assemblages were undertaken using a Leitz optical microscope under plane-polarised, cross-polarised and reflected light.

2.3 Scanning Electron Microscopy

Scanning electron microscopy (SEM) was conducted at the University of Southampton on thin sections, thin section offcuts and polished sample blocks coated in 20 nm of carbon using the Carl Zeiss SMT Ltd. LEO1450VP (variable pressure) Scanning Electron

Microscope in back scattered electron mode to analyse mineralogy and composition of samples, as well as textures. Elemental spot analyses were acquired using a PGT energy dispersive, light element X-ray microanalysis system.

2.4 U-Pb dating

Samples containing uranium mineralisation were identified using a scintillometer. SEM was used to identify uraninite, brannerite and other uranium phases, and locate and demarcate suitable samples and sample zones for a LA-ICP-MS U-Pb dating study. Uranium samples were either mounted in polished resin blocks or as offcuts of thin section blocks. Zircon samples were mounted on glass cover slips to keep them at a single horizon, then encased in resin to form a polished block. The cover slip was then polished through to get the small zircon crystals to the surface of the block, suitable for ablation.

Laser ablation was undertaken at the University of Southampton using a New Wave Research U-P-193 excimer Laser Ablation System coupled to a Thermo X-series II Quadrupole ICP-MS. Uraninite standards were not available, and so zircon standards 91500 and PMA-7 were used, along with standard G42728A and the glasses NIST 610 and 612 to calibrate the analyses. Since the zircons and glass contained much lower levels of U and Pb than the uranium phases, this was partially compensated for by using different spot sizes, ablation frequencies and laser power for the zircons compared to the uranium phases. In the case of the glass and the 91500 zircon, a spot size of 150 μm, a frequency of 8 Hz and 100 % power was used. The PMA-7 crystals were much smaller and required a 35 μm spot size. For the uranium phases, both 10 μm and 20 μm spot sizes were used, with repetition rates of 2 Hz and 60 % power. The reason for the different spot sizes was that some of the material was locally heterogeneous with non-uranium-rich impurities, and with the smaller spot size these impurities caused significant variability in the signal when unavoidably ablated. Using a larger spot size allowed for more ablation of the uranium phase and higher U and Pb beam voltages. In most cases, a raster path of ablation was used to minimise the role of downhole fractionation of isotope ratios, as well as to avoid impurities as much as possible in the uranium samples. The PMA-7 grains were too small for this, and so repeated ablation of a single spot was undertaken. Analyses times were 30 seconds of reference gas to form a baseline reference blank, followed by 90 seconds of sample ablation. Sample analyses were bracketed before and after by analyses of 91500 reference zircon. Data were collected using the Thermo Plasmalab software.

Data reduction was performed using the U-Pb data reduction scheme in the Iolite software package for Igor Pro (Paton et al., 2011), and where necessary, correction for downhole fractionation was applied. This method resulted in a $^{206}Pb/^{238}U$ age of 1063 Ma ± 1.6 Ma (2σ) for 91500 zircon. Published analyses of the 91500 zircon give a mean $^{206}Pb/^{238}U$ age of 1062 Ma and a mean $^{207}Pb/^{235}U$ age of 1065 Ma (Wiedenbeck et al., 1995), suggesting that the LA-ICP-MS method established here gives acceptable reproducibility of the zircon standard.

2.5 Fluid inclusion microthermometry

Doubly polished wafers of vein quartz and carbonate of ~250 μm thickness were prepared for fluid inclusion microthermometry. Fluid inclusion populations were identified, located and categorised using optical microscopy. Microthermometry was conducted using a Linkham THMS 600 heating and cooling stage and a Leitz optical microscope at the University of Southampton.

2.5.1 Calibration

The heating and cooling stage was calibrated at low temperatures using a synthetic chip containing CO_2-rich inclusions. Repeated measurements of the CO_2 melting point at a rate of 0.1 ℃/min give a reproducibility of ± 0.4 ℃ (2σ). At high temperatures, the melting point of sodium nitrate (+306.8 ℃) was used for calibration giving a reproducibility better than ± 5 ℃ (2σ).

2.5.2 Cooling and heating

Since microthermometry is often a destructive process, sample wafers were broken up into smaller, millimetre scale chips in order to prevent destruction of the fluid population of the whole chip. Samples were initially heated to 110 ℃ and held there for 4 minutes in order to drive off water vapour from the chamber, preventing the formation of ice crystals on the sample surface during the cooling leg, which reduce visibility.

Test runs were made at relatively rapid heating rates (typically 5-10 ℃/min) in order to determine the general temperature ranges for first melting and T_MICE. For the actual measurement runs, samples were cooled using liquid nitrogen to -140 ℃ at a rate of 50 ℃/min and held there for 6 minutes to allow inclusions to freeze. They were then heated at a rate of 10 ℃/min until -57 ℃. At this point the rate was reduced to 0.1 ℃/min over the CO_2 melting point interval until -56 ℃. After this, the rate was increased to 5

℃/min until close to the range where T_{FM} was expected, where the rate was reduced to 0.5 ℃/min until T_{FM}, T_MICE, T_HCLATH (where present) were recorded. The rate was then increased back to 10 ℃/min until close to 30 ℃ where rates were slowed to 1 ℃/min to measure the CO_2 homogenisation point. This heating and cooling ramp was repeated for all inclusions, with slight modifications, when heating rates were changed to account for different melting temperatures.

Heating runs proceeded at 50 ℃/min until vapour bubbles in inclusions began to become agitated, indicating the onset of T_HVAP. Heating rate was slowed to 5 ℃/min and 1 ℃/min where necessary to record homogenisation temperatures of vapour, and halite daughters.

2.6 Bulk fluid analyses

The crush-leach study to sample fluid inclusion leachates for anion and cation chemistry was undertaken at the Department of Earth and Atmospheric Sciences at the University of Alberta under the supervision of Sarah Gleeson.

2.6.1 Sample preparation

Vein samples were targeted for quartz and carbonate and cut from hand specimens or drill core using a rock saw. Care was taken to select samples suitable for the study. Crush-leach is a bulk process and samples all fluid inclusions held within the mineral phases. As such, the best samples are ones which are volumetrically dominated by only one fluid inclusion assemblage. Samples were crushed, rinsed in 18.2 mΩ water and sonicated to remove fine dust from the crushing process, and then sieved to extract a 1-2 mm size fraction. This size fraction was then hand picked under a binocular microscope to obtain ∼3 g of clean mineral separate for as many samples as possible. The samples from Konkola and Konkola North were small (quarter diamond drill core) and showed fine intergrowth between quartz and carbonate, and in the case of Konkola North, sulphide minerals, and so these were crushed without mineral phase separation (except a small amount for isotope work), and in the case of Konkola North, with impurities.

Handpicked clean vein quartz was soaked in 10 % concentrated nitric acid at 70 ℃ on a hot plate for one hour to remove any remaining surface impurities. This process was repeated twice more with 18.2 mΩ water to remove any trace of the acid from the samples. For carbonate samples this process was used without any acid. Samples were left to dry down overnight in an oven at 70 ℃.

~1 g of sample was then crushed under clean and controlled conditions using an agate mortar and pestle to facilitate the precipitation of salts from the inclusions. This powder was transferred to an unreactive vial, and 5 ml of clean water added. These vials were then shaken, and the solution then filtered through 0.2 μm filters to give a clean leachate. This process is a variation on that described by Gleeson and Turner (2007).

2.6.2 Anion and cation analysis

Anions (Cl^-, Br^-, F^-, ${SO_4}^{2-}$, ${PO_4}^{3-}$) were analysed from the leachate using a Dionex DX600 ion chromatograph (IC) fitted with an AS-14 analytical column at the University of Alberta. Na^+, K^+ and Li^+ were analysed for the leachate using atomic adsorption spectroscopy (AAS).

2.7 Stable isotopes

2.7.1 Chlorine

Leachate remaining from the initial crush leach process was reacted with $AgNO_3$ to precipitate AgCl as described by Long et al. (1993) and Wassenaar and Koehler (2004). Quantitative conversion of AgCl to CH_3Cl gas was conducted at the Stable Isotope Hydrology and Ecology Laboratory of Environment Canada in Saskatoon, Saskatchewan using the Iodomethane reaction of Wassenaar and Koehler (2004). A multicollector GV Instruments Isoprime IRMS was used to obtain δ^{37}Cl values. δ^{37}Cl analyses of multiple injections of 100 % CH_3Cl were repeatable within 0.06 ‰ ($\pm$ SD) for analysis of δ^{37}Cl. To correct values relative to Standard Mean Ocean Chloride (SMOC) standards of Ocean Scientific Internal Stock Atlantic Seawater were used.

2.7.2 Carbonates

Oxygen and carbon isotope analyses on handpicked vein carbonate minerals were obtained at the National Oceanography Centre, Southampton. Samples were crushed in an agate mortar and pestle, and analysed using a Europa Scientific GEO dual inlet Stable Isotope Ratio Mass Spectrometer (SIRMS) fitted with a CAPS CO_3 automated preparation system. External precision using repeated analyses of in house standards calibrated to NBS-19 are better than $\pm$ 0.1 ‰ (2σ) for δ^{18}O and δ^{13}C. Carbonate data are reported relative to V-PDB, oxygen data relative to V-SMOW.

2.7.3 Oxygen (Quartz)

Oxygen isotope values of vein quartz was obtained via laser fluorination conducted at SUERC following the process of Sharp (1990). ~2 mg of hand-picked quartz separates were loaded into a stainless steel holding rack and placed into an evacuated chamber. Samples were then fluorinated overnight by gaseous ClF_3. O_2 gas is released by heating the sample with a laser to react with the ClF_3, and subsequently reacted with a heated platinised graphite rod to generate CO_2. The CO_2 is purified on a vacuum line to remove any non-condensables. Sample gas was then analysed on a VG SIRA 10 mass spectrometer. Results were calibrated against NBS-28 and an in-house standard SES-QTZ, with a reproducibility better than ± 0.8 ‰ (2σ). Results are reported in standard notation $\delta^{18}O$ as per mil (‰) deviation from Standard Mean Ocean Water (V-SMOW).

2.7.4 Hydrogen

~1g of clean hand-picked quartz and carbonate mineral separates hosting fluid inclusions were required for hydrogen isotope analysis at SUERC. Samples were loaded into platinum crucibles (previously degassed under vacuum) within glass tubes, placed under vacuum and heated at 140 ℃ overnight to remove any further volatiles. Samples were then heated in a furnace (700 ℃ for pure quartz, 400 ℃ for samples containing carbonate) to drive off water vapour from fluid inclusions for analysis. Hydrogen gas was obtained by reduction of H_2O via a chromium furnace (Donnelly et al., 2001), captured using a Toepler pump, and analysed using a VG-Micromass 602D mass spectrometer. GISP, SLAP, V-SMOW and an internal standard were used for calibration, showing a reproducibility of ± 6 ‰ (2σ). Reproducibility for individual samples is likely to be lower than this however, due to heterogeneity within fluid inclusion populations within the samples. Results are reported in standard notation δD relative to the Standard Mean Ocean Water standard V-SMOW.

2.7.5 Sulphur

Individual mineral separates of pyrite, pyrrhotite, chalcopyrite, bornite, chalcocite, carrolite and vaesite were hand-picked for analyses at SUERC using minor modification from the technique of Robinson and Kusakabe (1975). ~6 mg of sulphide mineral separates were ground in an agate mortar and pestle with ~200 mg of cuprous oxide (Cu_2O), loaded into a glass tube with silica wool, and reacted in vacuo at 850 ℃ for 25 minutes to obtain SO_2 gas. SO_2 gas was analysed for $\delta^{34}S$ on a Thermo Fisher MAT 253 dual inlet mass spectrometer. Data were calibrated against NBS-123 sphalerite, IAEA S-3

silver sulphide, and in-house standard CPY-1, resulting in a reproducibility better than ± 0.3 ‰ (2σ). Data are reported in standard notation (δ^{34}S) relative to Canyon Diablo Troilite (V-CDT).

2.8 Micro Computed Tomography

Micro CT scanning of an individual carbonate crystal from quartz-carbonate veins at Kansanshi was conducted using the Metris X-Tek HMX ST 225 CT Scanner at the mineralogy department of the Natural History Museum, London. Processing of data was also conducted at the NHM using the software package Drishti (Limaye, 2012).

2.9 Trace and Rare Earth Elements in sulphides

2.9.1 Sample preparation

Hand-picked clean sulphide mineral separates were weighed, placed in teflon vials and dissolved in ∼4 ml concentrated aqua regia on a hot plate overnight along with procedural blanks. Samples which did not dissolve fully were redissolved with more acid until complete dissolution was achieved. For the few samples that did not fully dissolve, the residue of non-sulphide minerals (mostly a small amount of clays and micas) was weighed and subtracted from the initial sample weight. Once samples were dissolved in concentrated aqua regia, they were dried down to a residue on the hot plate, and taken up in 6M HCl to form mother solutions. Procedural blanks were created following the same process. This gave a bulk sample and does not account for any zonation within sulphide minerals.

Daughter solutions for ICP-MS analysis were sub-sampled from their mother solutions and made up with 3 % sub-boiled HNO_3 to achieve a dilution factor of ∼1000. They were then spiked to produce 20 ppb Be, 5 ppb In and 5 ppb Tm to act as internal standards.

2.9.2 ICP-MS

Daughter solutions were analysed for a selection of major, trace and rare earth elements on a Thermo X-series II Quadrupole ICP-MS in solution mode at the University of

Southampton. The instrument was calibrated using synthetic multi-element calibration standards with the instrument drift and matrix effects corrected using the internal standards.

2.10 Re-Os dating

Rhenium-osmium dating was conducted on sulphide minerals, primarily molybdenite, by Dr. Robert Creaser at the Department of Earth and Atmospheric Sciences, University of Alberta. Full analytical procedures for Re-Os dating at the University of Alberta Radiogenic Isotope Facility are detailed in Selby and Creaser (2004), and Markey et al. (2007), and are summarised here.

Molybdenite samples were dissolved and equilibrated with a known amount of ^{185}Re and isotopically normal Os in 3 ml of 2:1 16 N HNO_3 and 12 N HCl at 240 °C in a Carius tube for 24 hours. Re and Os were extracted and isolated using solvent extraction, microdistillation and anion exchange chromatography. Analyses were made by negative thermal ionisation mass spectrometry (NTIMS) using a Micromass Sector 54 mass spectrometer using Faraday collectors (Selby and Creaser, 2004).

Re and Os concentrations and Re-Os dating uncertainties are presented at the 2σ level. This includes the uncertainties in mass spectrometer measurements for Re and Os, spike and standard Re and Os isotopic compositions. The use of a mixed ^{185}Re and Os tracer solution ensures uncertainties in the weight of sample and tracer solution do not affect the calculated age. These weight uncertainties are taken into account when calculating the uncertainty in Re and ^{187}Os concentrations. Final weighted average ages are given at 95 % confidence level (2σ; Selby and Creaser 2004).

Chapter 3

The geochemistry of fluids in the Zambian Copperbelt

3.1 Abstract

The Central African Copperbelt is the world's largest sediment-hosted stratiform copper deposit district, preserving regional and basinal-scale evidence of fluid flow. Investigations of vein samples from eight deposits identified different vein generations formed throughout basin evolution. Microthermomentric studies show that the paleofluids preserved in copper deposits were chemically complex Na ± K ± Ca ± Mg brines with salinities typically between ∼14 to 39 wt% NaCl equivalent, frequently containing trace amounts of CO_2. Total homogenisation generally occurred via halite dissolution at temperatures >200 ℃.

Analysis of fluid inclusion leachates revealed a range of sources of salinity. Samples with Cl/Br <658 suggest salinity mainly developed from residual fluids formed by evaporation of seawater beyond the halite precipitation point (bittern brines). Samples with Cl/Br >658 (the Cl/Br of modern seawater) indicate a fluid with an increasing component of salinity supplied by the dissolution of halite from evaporite sequences. Samples from pre kinematic veins show Cl/Br <658, in contrast, post kinematic veins typically show Cl/Br >658. These data suggests that there is a temporal control over the sources of salinity within fluids, with initial basinal fluids comprising bittern brines formed after deposition of evaporite sequences, followed by a shift towards fluids dominated by the dissolution of halite, probably during basin inversion and orogenesis. A seawater, evaporitic origin of the salinity is supported by chlorine isotope data from leachates, where $\delta^{37}\mathrm{Cl} = 0 \pm 1$ ‰ (V-SMOW), typical values for Phanerozoic seawater, evaporites and evaporite-derived brines.

Cation ratios from fluid inclusion leachates reflect widespread water-rock interaction and alteration, with significant Na loss, consistent with basin scale alteration assemblages and the formation of albite and scapolite. The fluids are K-enriched, supporting evidence for K-rich fluids in the form of widespread potassic alteration in the stratigraphy. Sulphate concentrations are typically much greater than modern seawater values (up to ~43,000 ppm), likely obtaining the sulphate from local dissolution of anhydrite nodules.

δ^{18}O signatures of quartz and carbonate vein material vary between +7 to +26 ‰ (V-SMOW), with $\delta^{18}O_{Fluid}$ from ~-1.5 to +11.5, indicating some equilibration and buffering by country rocks. δ^{13}C in carbonate samples varies between -1.5 to -19 ‰ (V-PDB). δD signatures from fluid inclusions are highly variable, and generally isotopically light; i.e. -116.6 to -16.9 ‰ relative to V-SMOW. Samples from post kinematic veins at Kansanshi and the late fluid overprint at Lumwana show striking trends with similar $\delta^{18}O_{Fluid}$ values, but wide variation in δD values. $\delta^{18}O_{Fluid}$ exhibits a negative relationship with Cl/Br and suggests that fluids developed early in the basin history have undergone more oxygen equilibration with host rocks than later fluids.

3.2 Fluids in the Copperbelt

Fluid inclusion studies of individual deposits have previously been completed for Chambishi (Annels, 1989; Greyling et al., 2005), Nchanga (McGowan et al., 2006), Kansanshi (Speiser et al., 1995) and Nkana (Muchez et al., 2010). Furthermore, although the Musoshi deposit (Richards et al., 1988a) resides on the Congolese side of the border, it shares more characteristics similar to Zambian-type deposits rather than the classic Congolese-type. Annels (1989) reported homogenisation temperatures (T_HTOT) and salinities from inclusions in nodules and subconcordant veins within the ore shale at Chambishi and Chambishi South-East. T_HTOT ranged from ~110 to 180 ℃ with a mean of ~147 ℃ and salinities from 9-22 (wt% NaCl equiv.). Chambishi South-East shows very similar salinities, with slightly lower T_HTOT values (100-155 ℃, mean of 130 ℃). Late stage veins at Chambishi show T_HTOT from 197-425 ℃. Greyling et al. (2005) present data from a lateral secretion vein at Chambishi, interpreted to have formed post-sulphide mineralisation, but early on in the basin history. Primary inclusions are aqueous and aqueo-carbonic, and show salinities 11.9-23.1 wt% NaCl equiv., T_HTOT 86-129 ℃ and a complex salt chemistry, containing NaCl + $CaCl_2$ ± $MgCl_2$ with minor N_2 and CH_4. Secondary inclusions, probably formed during early metamorphism of the basin, comprise aqueous, aqueo-carbonic and pure methane inclusions. These fluids also contain multiple salts (NaCl ± $CaCl_2$ ± $MgCl_2$ ± KCl) as well as N_2, CH_4 and H_2S (Greyling et al., 2005). The aqueous and aqueo-carbonic secondary assemblages show two end

members, a higher salinity (18-23 wt % NaCl equiv.) lower temperature (∼130-160 ℃) fluid, and a low salinity (∼6 wt% NaCl equiv.) higher temperature fluid (140-210 ℃), interpreted as late diagenetic fluids and early methane productive metamorphic fluids (Greyling et al., 2005).

Vein generations and fluid inclusion assemblages at Nkana show similar salt chemistries (NaCl/KCl + $MgCl_2$) and salinities to those at Chambishi, ranging from 10.2 - >23.2 wt% NaCl equiv., with the majority >17.8 wt% NaCl equiv. (Muchez et al., 2010). T_HTOT at Nkana describe two main events, a fluid at 450 ℃ present in layer parallel veins which is interpreted to form during peak burial conditions, and a lower temperature fluid, T_HTOT 100-250 ℃ interpreted to have formed during retrograde metamorphism (Muchez et al., 2010).

Subconcordant veins from the upper and lower orebodies at Nchanga contain a saline Na-Mg-Ca-Fe brine with 31-38 wt% NaCl equiv. which show T_HTOT between 105-300 ℃ (McGowan et al., 2006). Post kinematic veins at Musoshi which redistribute the pre-existing ore assemblage show highest T_HTOT values near a proposed 'influx zone', with lower temperatures away from this conduit (Richards et al., 1988a). Inclusions homogenised via halite dissolution, giving T_HTOT of ∼400 ℃ and ∼39 wt% NaCl equiv.. The fluids also contained ∼15 wt% KCl, $FeCl_2$, as well as minor CO_2 (Richards et al., 1988a). Dating of rutile from these veins gives an age of 514 ± 2 Ma, indicating the fluid event was related to compressional deformation as part of the Lufilian Orogeny (Richards et al., 1988a). High-angle discordant quartz carbonate veins which host mineralisation at the Kansanshi deposit near the Solwezi dome, west of the traditional Copperbelt mining district show complex salt compositions, with NaCl, $CaCl_2$, KCl and $MgCl_2$, as well as CO_2 and CH_4. Aqueous inclusion assemblages record T_HTOT data 230-310 ℃, and initial salinities 30-43 wt% NaCl equiv. (Speiser et al., 1995).

These data show that saline brines are evident in veins from all the Zambian deposits investigated to date, with an underlying trend from lower salinity, lower temperature often aqueo-carbonic fluids early in the basin history e.g. Chambishi, towards hotter more saline fluids associated with kinematic and post kinematic veins at Nchanga, Musoshi and Kansanshi.

In the Democratic Republic of Congo detailed fluid inclusion studies at Musonoi, Kamoto, Kipushi and Luiswishi reveal two main types of fluid: a moderate salinity-moderate temperature fluid of ∼10-20 wt% NaCl equiv. and T_HTOT ∼80-220 ℃, and a high salinity-high temperature fluid with >∼30 wt% NaCl equiv. and T_HTOT >∼200 ℃. (Dewaele et al., 2006; El Desouky et al., 2009; Heijlen et al., 2008). Inclusions within authigenic quartz from Musonoi and Kamoto orebodies suggest that mineralising fluids consisted of H_2O + NaCl with salinity 8.4-18.4 wt% NaCl equiv. and T_HTOT from

80-195 ℃ (Dewaele et al., 2006). Mainstage mineralisation at Kipushi was accompanied by a fluid event within multiple phases of dolomite and quartz which exhibit salinities from 30-43 wt% NaCl equiv. and T_HTOT ∼150-360 ℃. Secondary inclusions, and inclusions within paragenetically later phases exhibit significantly lower temperatures and salinities. Some aqueo-carbonic inclusions were noted, with the vapour phase noted to be impure, likely a mixture of CO_2 and CH_4 (Heijlen et al., 2008).

Studies of Kamoto and Luiswishi reveal the presence of two main fluid types (El Desouky et al., 2009). The first fluid, 'type-I', is associated with an early diagenetic stratiform phase and exhibits T_HTOT 115-220 ℃ and salinities 11.3-20.9 wt% NaCl equivalent, similar to that described by Dewaele et al. (2006). The second fluid, 'type-II', occurs within stratiform nodules, stratabound veins and tectonic breccia cements and is characterized by much higher T_HTOT (270-385 ℃) and salinities (35-45.5 wt% NaCl equiv.). El Desouky et al. (2009) suggest that their 'type-I' fluid is characteristic of early diagenesis across the Copperbelt and can be correlated with that at Chambishi (Greyling et al., 2005) and that their 'type-II' is representative of orogenesis (similar to Nchanga and Musoshi; McGowan et al., 2006; Richards et al., 1988a).

Fluid inclusion studies on prospects and deposits in the Kundelungu Plateau region, north of the traditional Lufilian Arc mining region of the Katanga province of the DRC, include Lufukwe (El Desouky et al., 2008a), Mwitapile (El Desouky et al., 2008b) and Dikilushi (Haest et al., 2009). At Lufukwe, an inclusion assemblage formed within authigenic quartz overgrowths prior to the mineralisation event, exhibits salinities from 18.8-23.4 wt% $CaCl_2$ equiv. and T_HTOT 80-130 ℃. A second assemblage, interpreted to be representative of a mineralising fluid, is weakly saline 1.9-7.7 wt% NaCl equiv. with NaCl the dominant salt and T_HTOT of 120-180 ℃ (El Desouky et al., 2008a). At Mwitapile a NaCl-$CaCl_2$ fluid, exhibits salinities ∼24 wt% $CaCl_2$ equiv. with T_HTOT from 111-182 ℃. A second fluid, related to the sulphide mineralisation phase, showed variable salinities, 2.4-19.8 wt% NaCl equiv. and higher T_HTOT, 120-280 ℃ (El Desouky et al., 2008b).

The Dikulushi deposit contains two stages of mineralisation, the first a Cu-Pb-Zn-Fe stage aqueous fluid which contains NaCl and $CaCl_2$, with salinities 16-25 wt% CaCl equiv., and T_HTOT ∼60-160 ℃. A second Cu-Ag stage of mineralisation formed from different a aqueous fluid characterised by NaCl-KCl content, salinities 3-19 wt% NaCl equiv., and T_HTOT ∼65 ℃ (Haest et al., 2009). Overall, fluids within the Lufilian foreland appear to be cooler and less saline than most Copperbelt deposits.

TABLE 3.1: Summary table of the available fluid inclusion data for the Central African Copperbelt

Deposit	Chemistry	Salinity (wt% NaCl. equiv)	Temperature (°C)	Reference
Chambishi	NaCl ± CO_2 ± N_2	9–22	110–180, mean 147	Annels (1989)
Chambishi late veins	NaCl ± CO_2 ± N_2	9–22	197–425	Annels (1989)
Chambishi SE	NaCl ± CO_2 ± N_2	9–22	100–155, mean 130	Annels (1989)
Chambishi lateral secretion primary	NaCl + $CaCl_2$ ± $MgCl_2$, minor CO_2, N_2	11.9–23.1	86–129	Greyling et al. (2005)
Chambishi lateral secretion high sal. low temp.	NaCl + $CaCl_2$ ± $MgCl_2$, minor CO_2, N_2	18–23.1	130-160	Greyling et al. (2005)
Chambishi lateral secretion low sal. high temp.	NaCl + $CaCl_2$ ± $MgCl_2$, minor CO_2, N_2	6	140-210	Greyling et al. (2005)
Nkana peak metamorphism	NaCl/KCl + $MgCl_2$	10.2–>23.2	450	Muchez et al. (2010)
Nkana retrograde	NaCl/KCl + $MgCl_2$	10.2–>23.2	100–250	Muchez et al. (2010)
Nchanga	NaCl + $MgCl_2$ + $CaCl_2$ + $FeCl_2$	31-38	105-300	McGowan et al. (2006)
Musoshi post-kinematic	NaCl + KCl + $FeCl_2$ + CO_2	39 wt% NaCl equiv., 15 wt% KCl equiv.	400	Richards et al. (1988a)
Kansanshi aqueous	NaCl + $CaCl_2$ + KCl + $MgCl_2$ + CO_2 + CH_4	30–43	230–310	Speiser et al. (1995)
Musonoi, Kamoto	NaCl	8.4–18.4	80–195	Dewaele et al. (2006)
Kipushi	NaCl ± CO_2	30–43	150–360	Heijlen et al. (2008)
Kamoto, Luiswishi 'Type-I' (diagenetic)	NaCl	11.3–20.9	115–220	El Desouky et al. (2009)
Kamoto, Luiswishi 'Type-II' (veins, breccias)	NaCl	35–45.5	270–385	El Desouky et al. (2009)
Lufukwe pre mineralisation	NaCl + $CaCl_2$	18.8–23.4 wt% $CaCl_2$ equiv.	80–130	El Desouky et al. (2008a)
Lufukwe mineralisation	NaCl	1.9–7.7	120–180	El Desouky et al. (2008a)
Mwitapile	NaCl + $CaCl_2$	24 wt% $CaCl_2$ equiv.	111–182	El Desouky et al. (2008b)
Mwitapile mineralisation	NaCl	2.4–19.8	120–280	El Desouky et al. (2008b)
Dikilushi Cu-Pb-Zn-Fe stage	NaCl + $CaCl_2$	16–25 wt% $CaCl_2$ equiv.	60–160	Haest et al. (2009)
Dikilushi Cu-Ag stage	NaCl + KCl	3–19	65	Haest et al. (2009)

3.3 Vein categorisation and sampling

Vein samples were obtained from open pit and drill core at Lumwana, Kansanshi, Konkola and Konkola North, as well as from prospects at Kalumbila-Sentinel, Enterprise and Samba. Samples from Nchanga and Musoshi were collected from the archive of McGowan et al. (2006) and provided by JP Richards (Richards et al., 1988a). Sampling locations are illustrated in Fig. 2.1. Vein samples were collected from open pits where relationships to kinematic indicators could be well constrained. However, where access was limited to drill core, the exact spatial and temporal relationship of veins with the

host rocks was less clear. Generally the veins in the deposits sampled were divided into two end members:

1. Pre- and syn-kinematic veins. These veins have been subjected to all, or some of the same kinematic processes as the host rocks, including folding and shearing and the development of compressional tectonic fabrics (Fig. 3.1; 3.2). These veins record an earlier stage of fluid flow.

2. Post-kinematic veins. These veins cross-cut prevailing host rock foliations and fabrics such as bedding, laminations, schistosity and cleavage, gneissose banding, and deformation structures where present. They can typically be observed at multiple levels of the stratigraphy (Fig. 3.1; 3.2). These veins represent a later stage of fluid flow, at peak or post-peak metamorphism.

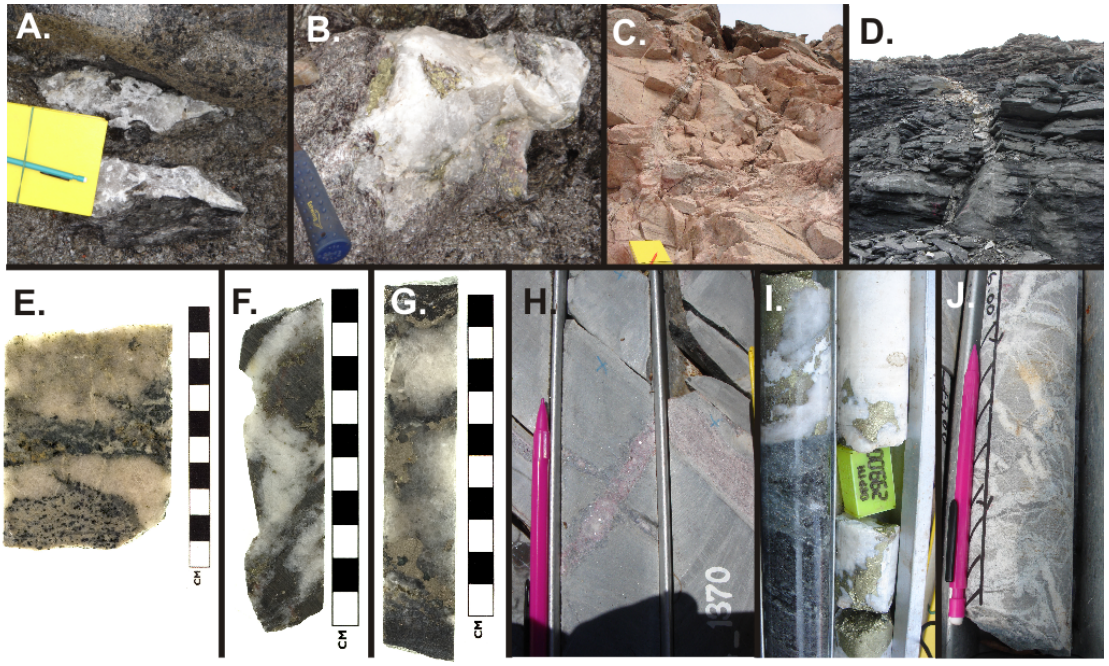

FIGURE 3.1: Vein generations in the Copperbelt. A) Pre-kinematic boudinaged quartz vein, Malundwe open pit, Lumwana. B) Pre-syn-kinematic quartz vein remobilising sulphide mineralisation, Malundwe open pit, Lumwana. C) Post-kinematic quartz veins cut hanging wall gneiss at Malundwe open pit, Lumwana. D) Post-kinematic quartz veins cut footwall gneisses and schists at Malundwe open pit, Lumwana. E) Pre-kinematic quartz vein in drill core from Samba prospect. F) Pre-syn-kinematic quartz-carbonate (+py) vein in ore shale, Konkola. G) Pre-syn-kinematic quartz-carbonate (+sulphides) vein in phyllite, Kalumbila-Sentinel. H) Pre-syn-kinematic cobalt rich quartz-carbonate-chlacocite vein cuts and exploits stratigraphy in ore shale Konkola North. I) Post-kinematic quartz-carbonate-chalcopyrite veins at Kansanshi. J) Post-kinematic quartz-kyanite-talc veins cut phyllite at Enterprise.

The majority of inclusions within the veins sampled are either aqueous 2-phase (L + V) or multiphase aqueous (L + V + halite ± secondary daughter minerals) occasionally

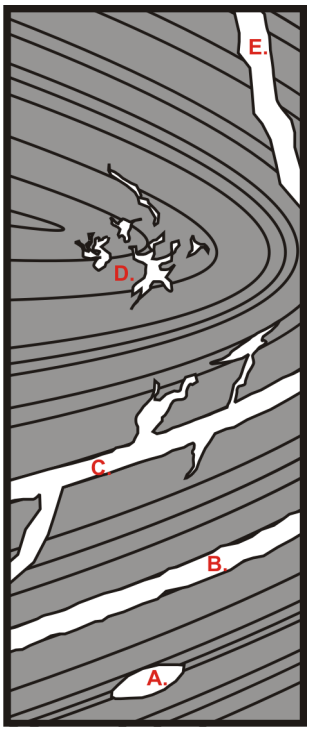

FIGURE 3.2: Schematic of types of veins sampled in this study from the Copperbelt. A) Pre-kinematic boudinaged veins (common within sheared basement rocks). B) Pre-kinematic layer parallel veins. C) Pre-syn kinematic veins which both exploit foliation and cut it. D) Syn-kinematic veins formed in noses of folds. E) Post-kinematic cutting foliation.

containing CO_2, either visible as a distinct vapour phase, or identified upon freezing/-formation of clathrate. Table 3.2 summarises the different types of fluid inclusions and assemblages identified in the vein samples in this study, illustrated in figure 3.3. In addition, most veins contain one dominant fluid inclusion assemblage, making them ideal candidates for crush leach analysis.

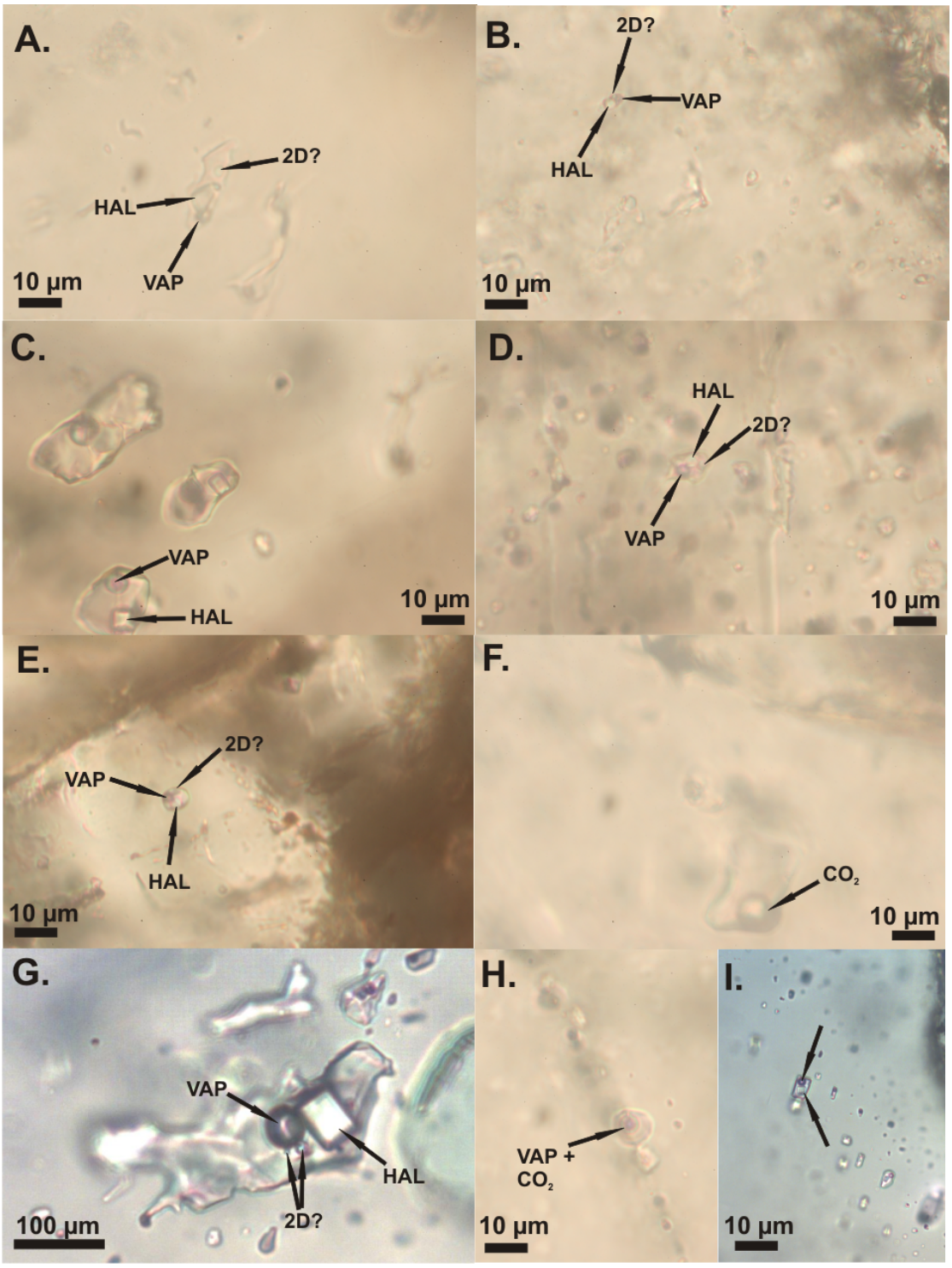

FIGURE 3.3: Fluid inclusion assemblages at A) Enterprise; B) Kalumbila-Sentinel; C) Kansanshi; D) Konkola; E) Konkola North; F) Samba; G) Lumwana type-1; H) Lumwana Type-3; I) Lumwana Type-2. HAL = Halite daughter, 2D = Secondary daughter, VAP = Vapour bubble.

3.4 Fluid inclusion microthermometry

CO_2 was common in the inclusion assemblage at Samba, some of the inclusions at Kansanshi (Type D; Speiser et al. 1995), and at Lumwana. At Samba, T_MCO_2 varied between ∼-58.1 and -56.6 ℃ with a mode of -57 ℃ (n=35) suggesting a CO_2 vapour phase with some other gaseous components. At Kansanshi, Type D inclusions show T_MCO_2 in a broad range from -84.8 to -72.2 ℃ (n=29). This large depression of the CO_2 melting point suggests a significant component of other gaseous phases, probably methane, which is reported from other inclusion assemblages at Kansanshi (Speiser et al., 1995). T_MCO_2 for Lumwana inclusions which showed visible CO_2 generally occurred at ∼-56.6 ℃ (n=45), indicating a relatively pure CO_2 gaseous phase.

First melting temperatures (T_{FM}) were difficult to establish due to the size of inclusions, and no estimates on fluid chemistry via T_{FM} could be made for Kalumbila-Sentinel and Enterprise. Kansanshi Type-D inclusions record a wide range in T_{FM} from -72.8 to -35.6 ℃ with a mean of -57.9 ℃ and a mode of -57℃ (n=44), falling within the range reported by Speiser et al. (1995). The modal value falls close to that expected for an aqueous system containing NaCl + $CaCl_2$ (-55 ℃, Shepherd et al., 1985). Samba T_{FM} show a tight grouping with a mean of -25.6 ℃ and a mode of -27 ℃ (n=41), suggesting a multiple salt aqueous system with Na + K and additional divalent cation(s). Konkola T_{FM} also show a tight grouping between -49.3 and -39.2 ℃ with a mean of -44.1 ℃ and a mode of -44 ℃ (n=28), suggesting the presence of a divalent cation, potentially Ca, consistent with the presence of carbonate within the vein. Konkola North T_{FM} data show a wide range between -79.3 and -43.4 ℃, without a strong mode (n=26) making specific salt chemistry difficult to identify, but not indicative of a pure H_2O-NaCl fluid. The Type-2 and Type-3 inclusions at Lumwana convey a wide range of T_{FM} (-88.2 to -27.2 ℃) but with the vast majority of inclusions clustered around ∼-31 ℃ (n=83). There is no systematic difference in T_{FM} between the Type-2 and Type-3 fluid populations at Lumwana. The bulk of the data suggest an H_2O-NaCl-$MgCl_2$ system (Shepherd et al., 1985). The first melting temperatures from fluid inclusion assemblages across the Copperbelt and Domes regions reported in this study record the presence of saline aqueous fluids, with complex chemistries containing NaCl and additional salts.

Whilst clathrate formation could be observed in rare (often large >40 μm) inclusions in most of the assemblages, most likely reflecting the presence of minor CO_2, only at Samba and Lumwana was clathrate formation common enough for numerous readings. At Samba, clathrate melted between -3.6 and +8.3 ℃ with a mode of +4.3 ℃ (n=25). For Lumwana Type-2 and Type-3 inclusions, clathrate melted between -10.1 and 19.4 ℃ with a mode of -6 ℃ (n=33).

TABLE 3.2: Summary table of the physical characteristics of fluid inclusion assemblages

Deposit	Fluid inclusion assemblage	Type	Size (μm)	% Vapour	% Daughters	Notes
Lumwana Type-1	L+V+HAL; decrepitated	Primary	Up to 400	N/A	N/A	Large, decrepitated saline fluid phase. Normally only visible in pre-kinematic boudins. Difficult to determine between Type-1 and decrepitated Type-2 inclusions in pre-syn kinematic veins. Not present in post-kinematic veins.
Lumwana Type-2	L+V+HAL (± secondary daughters; $\pm CO_2$)	Pseudosecondary, secondary	2 to 10	2 to 25	2 to 25	More common in pre-kinematic boudins and pre-syn kinematic veins than post-kinematic veins
Lumwana Type-3	L+V+CO_2	Primary, pseudosecondary, secondary	5 to 50	1 to 30	N/A	Primary in post-kinematic veins
Kansanshi Type-D	L+V+HAL ($\pm CO_2$)	Primary, pseudosecondary	5 to 45	2.5 to 15	2.5 to 10	Type D volumetrically dominant (>95 %), see Speiser et al. (1995) for breakdown of other inclusion types
Enterprise	L+V+HAL (± secondary daughters; $\pm CO_2$)	Primary, pseudosecondary	2 to 13	15 to 40	15 to 40	Volumetrically dominant, some unidentifiable second daughters
Enterprise	L	Secondary	<2	N/A	N/A	Volumetrically minor; commonly necked down and decrepitated
Kalumbila-Sentinel	L+V+HAL ($\pm CO_2$)	Primary, secondary	5 to 15	15 to 40	15 to 40	No difference in microthermometry between primary and secondary versions
Kalumbila-Sentinel	L	Secondary	<2	N/A	N/A	Volumetrically minor; commonly necked down and decrepitated
Konkola	L+V+HAL ($\pm CO_2$)	Primary, pseudosecondary	2 to 13	10 to 30	10 to 20	Volumetrically dominent, exhibit negative crystal shapes in carbonate
Konkola	L	Secondary	<2	N/A	N/A	Volumetrically minor; too small for microthermometry
Konkola North	L+V+HAL ($\pm CO_2$)	Primary, pseudosecondary	2 to 15	5 to 25	5 to 25	Volumetrically dominent, exhibit negative crystal shapes in carbonate, rare unidentifiable second daughter phase
Konkola North	L	Secondary	<2	N/A	N/A	Volumetrically minor; too small for microthermometry

Samba	L+V+CO_2	Primary, secondary	5 to 50	10 to 50	N/A	Volumetrically dominant; visible bubble-in-bubble CO_2
Samba	L	Secondary	<2	N/A	N/A	Form along grain boundaries and fractures. Volumetrically minor overprint

Within this study, the majority of larger inclusions (>20 μm) decrepitated or visibly leaked before homogenisation at temperatures >200 ℃. L+V inclusions homogenised into the liquid phase. In most L+V+Halite (± secondary daughter products) inclusions, the vapour phase tended to homogenise first (T_HVAP), and the inclusions finally homogenised via halite dissolution (HAL OUT; in this case HAL OUT also represents T_HTOT). Other inclusions followed a pattern of halite dissolution (HAL OUT), followed by final homogenisation of the vapour bubble into the aqueous phase (T_HVAP; in this case T_HVAP also represents T_HTOT; Fig. 3.4).

At Samba, inclusions contained no halite daughters and homogenised into the liquid phase. T_HTOT at Samba varied between 201 and 394 ℃ (Fig. 3.4D), with a mean of 287 ℃ and without a well-defined mode (n=16). Type 2 inclusions at Lumwana show T_HVAP values from 97 to 300 ℃ (Fig. 3.4F) with a mean of 182 ℃ and a mode of 185 ℃ (n=39). HAL OUT temperatures (n=49) show a slight bimodality (Fig. 3.4F) varying between 138 and 339 ℃ with a mean of 231 ℃ and with modes at 145 ℃ and 255 ℃, and the majority of data fall around the upper mode. The majority of inclusions homogenised via halite dissolution rather than vapour bubble homogenisation, resulting in T_HTOT varying between 141 and 382 ℃ (Fig. 3.4F), with a mean of 241 ℃ and a mode of 255 ℃ (n=38). T_HVAP and T_HTOT for the L+V Type-3 inclusions at Lumwana varies between 91 and 445 ℃ (Fig. 3.4F) with a mean of 220 ℃ and a mode of 235 ℃ (n=49).

Fluids at Enterprise show high temperatures and homogenise via halite dissolution, with mean T_HVAP of 218 ℃ and a mode of 205 ℃ (n=38). HAL OUT and T_HTOT occurred between 331 and 415 ℃ with a mean of 359 ℃ and a mode of 345 ℃ (n=16; Fig 3.4A). Kalumbila-Sentinel T_HVAP varied from 130 to 292 ℃ with a mean of 167 ℃ (Fig. 3.4B) and a well-defined mode of 155 ℃ (n=40). HAL OUT (n=37) at Kalumbila-Sentinel shows a slightly bimodal distribution of temperatures (Fig. 3.4B) with a lower temperature group of data with a mode of 175 ℃. The majority of the data however show higher temperatures, with a mode of 275 ℃, and this group is regarded as more representative for the inclusion assemblage as a whole.

Few homogenisation data from Konkola and Konkola North were achieved due to leaking and decrepitation, and so these have been combined into Fig. 3.4E, though the data for

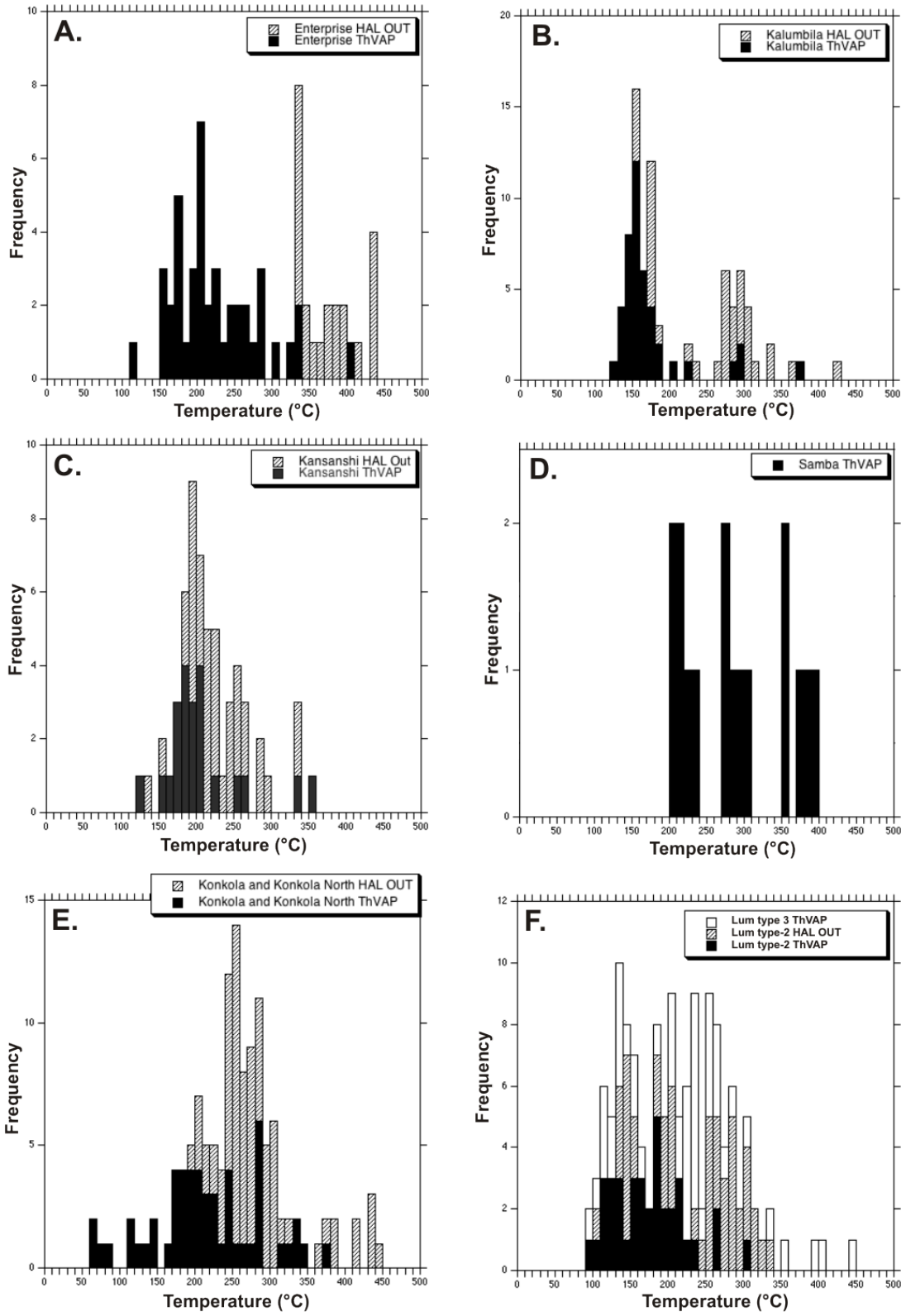

FIGURE 3.4: Halite dissolution temperatures (HAL OUT) and vapour homogenisation temperatures (T_HVAP)

the different deposits is also reported here. T_HVAP from Konkola inclusions vary from 110 to 339 ℃ with a mean of 218 ℃ (n=9; most inclusions leaked or decrepitated before vapour homogenisation was achieved). HAL OUT varied between 190 and 412 ℃, with a mean of 230 ℃ and a mode of 255 ℃ (n=30). Konkola T_HTOT showed a minimum of 277 ℃, a maximum of 378 ℃ and a mean of 323 ℃ and mode of 330 ℃ (n=5). T_HVAP from Konkola North inclusions varies from 66 to 379 ℃ with a mean of 217 ℃ and a mode of 275 ℃ (n=37). HAL OUT occurs from 231 to 440 ℃ with a mean of 306 ℃ and a mode of 285 ℃ (n=38). In the majority of cases, homogenisation occurred via halite dissolution, and T_HTOT measurements range from 231 to 440 ℃ with a mean of 321 ℃ and mode of 280 ℃ (n=26). Combining the data for Konkola and Konkola North, which are parts of the same orebody allows for a better overall dataset, and Figure 3.4E shows an overall normal distribution for T_HVAP and HAL OUT. Most of the combined T_HVAP data falls between 170 and 290 ℃, and HAL OUT (and T_HTOT, since most inclusions homogenised via halite dissolution) shows a strong mode at ∼255 ℃.

T_HVAP in Kansanshi Type D inclusions varies between 160 and 353 ℃ with a mean of 190 ℃ and mode of 200 ℃ (n=24). HAL OUT varies between 132 and 333 ℃, with a mean of 228 ℃ and a mode of 195 (n=36; Fig. 3.4C). Inclusions homogenised both by halite dissolution and by vapour homogenisation into the aqueous phase (as reported by Speiser et al. 1995). T_HTOT varies between 132 and 353 ℃ with a mean of 235 ℃ and a mode of 210 ℃ (n=20).

Most fluid assemblages identified and measured in this study homogenised via halite dissolution, giving typical T_HTOT values >200 ℃.

3.4.1 Salinities (wt% NaCl equiv.)

Inclusions at Samba and Type-3 inclusions at Lumwana did not contain halite daughter products, and thus final ice melting temperature (T_MICE) is used for salinity calculations for these assemblages. At Samba, T_MICE occurs between -22.1 and -0.9 ℃ with a mean of -11.0 ℃ and a mode of -7.5 ℃(n=42), indicating salinities between 1.5 and 23.8 wt% equiv. NaCl with a mean of 14.3 wt% equiv. NaCl. T_MICE for Lumwana Type-3 inclusions has a strong mode of ∼-10 ℃, and the salinities of these inclusions varied between 9.7 and 17.9 wt% equiv. NaCl with a mean of 13.8 wt% equiv. NaCl.

The majority of inclusion assemblages studied had much higher salinities, resulting in the formation of daughter products, and all other salinities could be estimated via dissolution temperatures. Unlike Type-3 inclusions, Lumwana Type-2 inclusions contained halite daughter products, and salinities could be measured via halite dissolution, recording salinities from 29.2 to 41.4 wt% equiv. NaCl with a mean of 34.2 wt% equiv. NaCl.

Type D inclusions at Kansanshi show salinities similar to the estimates of Speiser et al. (1995), from 29.9 to 40.9 wt% equiv. NaCl with a mean of 33.6 wt% equiv. NaCl. Salinities at Kalumbila-Sentinel vary from 29.7 to 53.0 wt% equiv. NaCl, with a mean of 36.3 wt% equiv. NaCl. Veins at Enterprise also contain highly saline fluids, from 40.6 to 51.8 wt% equiv. NaCl with a mean of 45.0 wt% equiv. NaCl, and this range may extend to much higher salinities since many inclusions decrepitated before dissolution of halite. Samples from Konkola record salinities of 31.4 to 48.8 wt% equiv. NaCl with a mean of 35.1 wt% equiv. NaCl, and those from Konkola North are very similar (between 33.5 and 52.0 wt% equiv. NaCl, with a mean of 39.0 wt% equiv. NaCl).

3.4.2 Summary

Whilst there are some significant variations between different deposits, the vast majority of fluid inclusion assemblages investigated in this study share some similar characteristics, summarised below, with data summarised in table 3.3. All fluid inclusion assemblages preserve brines ± CO_2 with the majority highly saline, >30 wt%. The majority contained large visible daughter crystals, typically homogenised via halite dissolution, and showed T_HTOT values generally >200 °C.

TABLE 3.3: Summary table of the results of fluid inclusion microthermometry

Fluid inclusion assemblage	$T_M CO_2$ (°C)	T_{FM} (°C)	T_MICE (°C)	T_MCLATH (°C)	T_HVAP (°C)	HAL OUT (°C)	T_HTOT (°C)	Salinity (wt% NaCl equiv.)
Lumwana Type-2	Mode at -56.6	Mode at -31		-10.1 to +19.4	97 to 300	138 to 339	141 to 382	29.2 to 41.4
Lumwana Type-3	Mode at -56.6	Mode at -31	Mode at -10	-10.1 to +19.4	91.4 to 445		91.4 to 445	9.7 to 17.9
Samba	-58.1 to -56.6	Mode at -27	-22.1 to -0.9	-3.6 to +8.3	201 to 394		201 to 394	1.5 to 23.8
Kalumbila-Sentinel					130 to 292	150.4 to 423	186 to 423	29.7 to 53.0
Enterprise					152 to 400	331 to 415	331 to 415	40.6 to 51.8
Kansanshi Type-D	-84.8 to -72.2	-72.8 to -35.6			160 to 353	132 to 333	132 to 353	29.9 to 40.9
Konkola		-49.3 to -39.2			110 to 339	190 to 412	277 to 378	31.4 to 48.8
Konkola North		-79.3 to -43.4			66 to 379	231 to 440	231 to 440	33.5 to 52.0

3.5 Bulk chemical analysis from crush-leach

The fluid inclusion populations analysed in this study show a range of Cl/Br ratios, both greater and less than the seawater Cl/Br of ~656 (Fig. 3.5A). If the samples are grouped by vein setting into the groups described earlier, samples grouped as pre-kinematic and most pre-syn kinematic veins show Cl/Br <656 whilst the majority of

post-kinematic veins show Cl/Br >656 (Fig. 3.5B). Where sampling could be conducted in greater detail for example at Lumwana, this pattern is further illustrated with pre and syn-kinematic veins showing Cl/Br <656, whilst the post-kinematic veins show Cl/Br >656 (Fig. 3.5C). Reconstructions of anion concentrations have been made using the salinities estimated from microthermometry, the crush leach values and the equation of Banks et al. (2000). For the Lumwana deposit, this splits the data into two groups based upon the predominant inclusion assemblage within the veins (Type-2 or Type-3). Measurements of chlorine and bromine concentrations indicate that for the majority of fluids, significant evaporation has occurred, beyond the halite and carnalite saturation points (Fig. 3.6A, B).

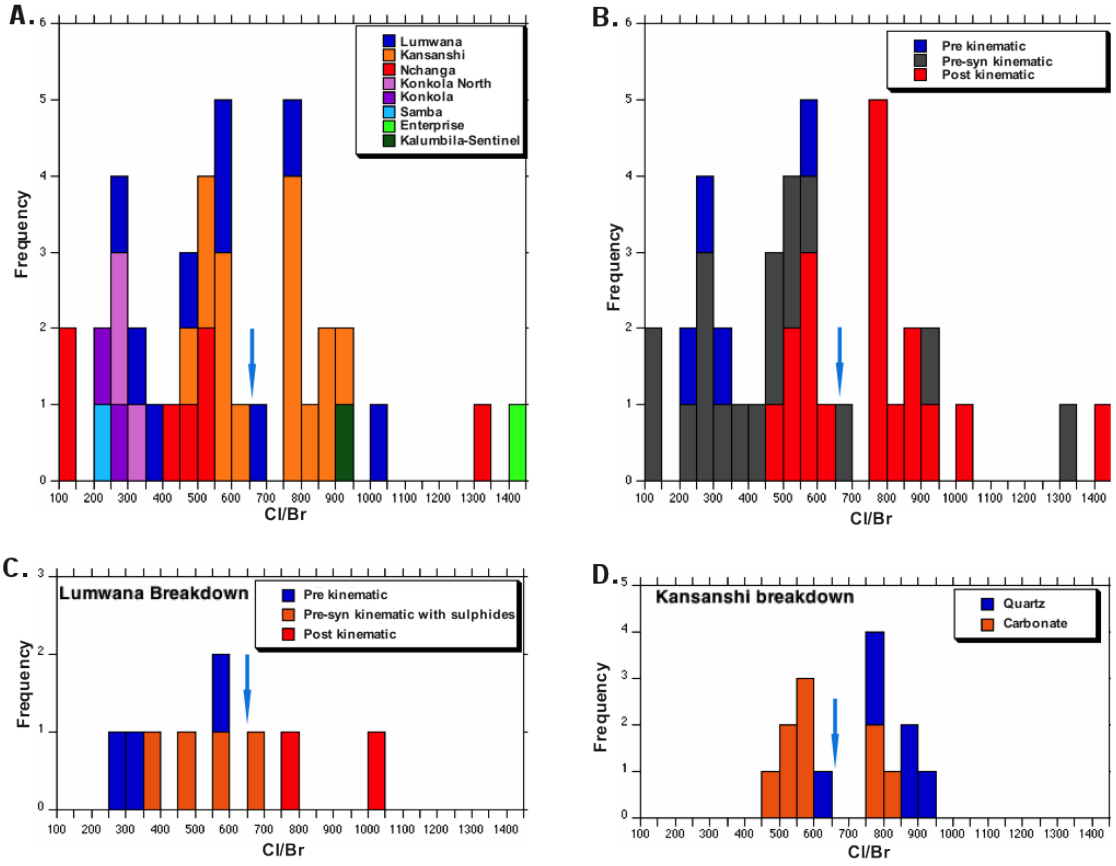

FIGURE 3.5: A) Chlorine-bromine ratios for veins from the different deposits studied. B) Cl/Br for the same group of data, grouped by textural and tectonic setting. C) Cl/Br for Lumwana samples. D) Cl/Br for Kansanshi samples. Blue arrow indicates Cl/Br of modern seawater.

K/Na ratios show a much greater spread of data at lower Cl/Br values and a slight negative trend (Fig. 3.8). Sodium-bromine ratios are variable but show a positive trend with Cl/Br, with most data suggesting depletion of sodium is occurring relative to the seawater evaporation trajectory (SET; Fig. 3.9). Few of the data fall near the SET. Much of the data for Nchanga, Konkola, Konkola North and Samba plot on the lower part of the graph, whilst other data (e.g. Kalumbila-Sentinel; Enterprise; parts of the

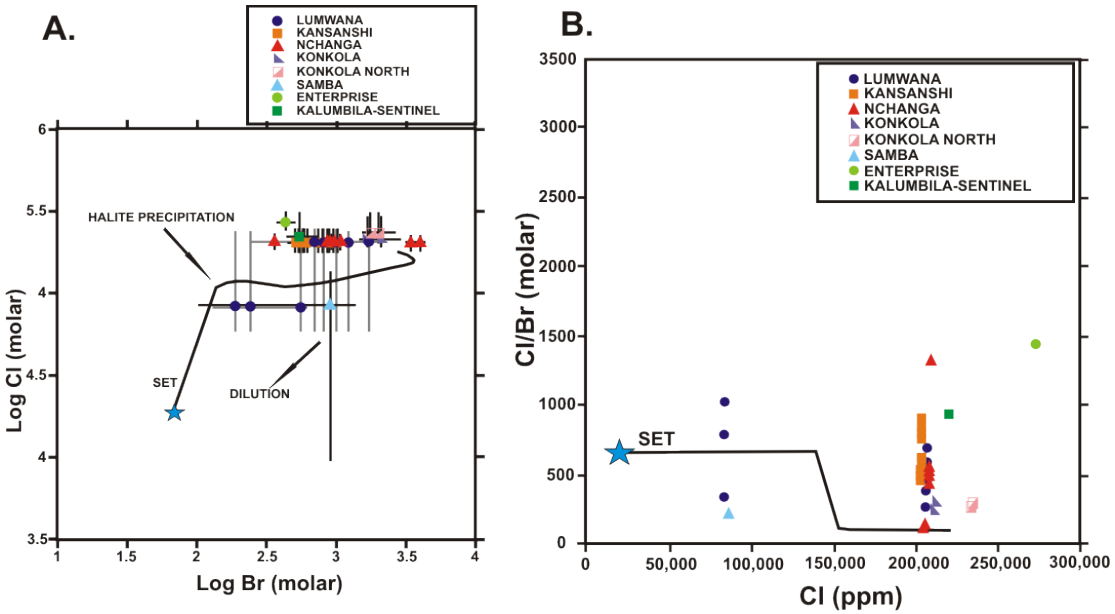

FIGURE 3.6: A) Calculated halogen compositions using salinities estimated by microthermometry. Points are based on the average salinity of the fluid inclusion assemblage, with error bars taking into account the full range of salinity measurements. Lumwana samples (grey error bars) contained multiple inclusion assemblages, and so mean salinity estimates were based on the more dominant assemblage in that sample, with the error bars showing the full range of salinities, accounting for both Type-2 and Type-3 assemblages. Modern seawater evaporation trajectory (SET) from Fontes and Matray (1993). Most data fall well above the SET. B) Variation of Cl/Br with chloride concentration, with modern SET from Fontes and Matray (1993).

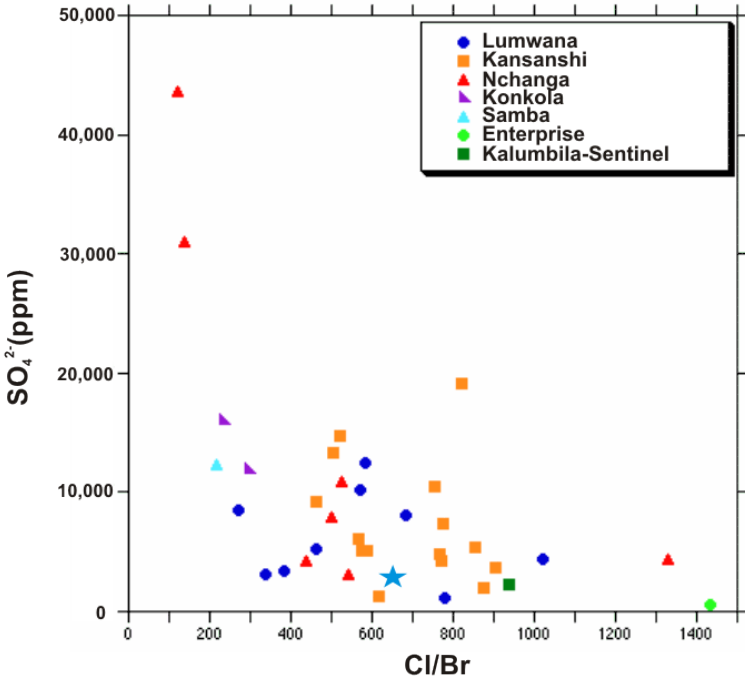

FIGURE 3.7: Calculated sulphate concentrations (back calculated from salinities estimated from microthermometry). Blue star is modern seawater. Konkola North not included due to finely intergrown chalcocite within the vein material.

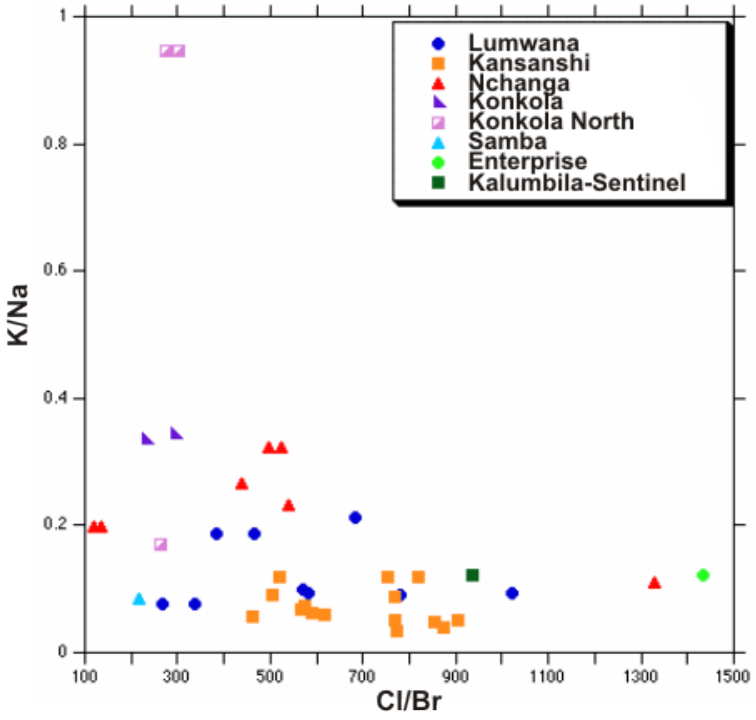

FIGURE 3.8: K-Na-Cl-Br systematics of inclusion leachates.

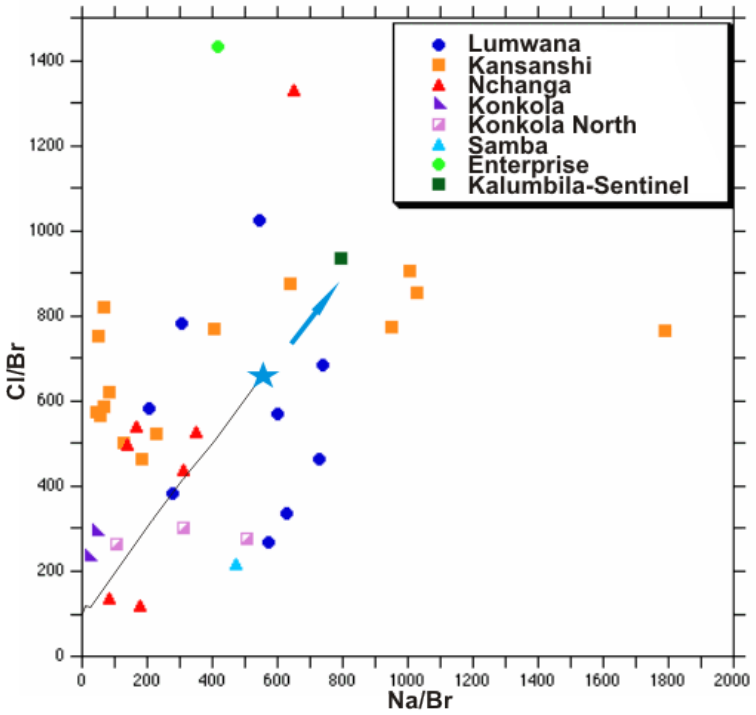

FIGURE 3.9: Na-Cl-Br systematics of fluid inclusion leachates. Line is seawater evaporation trajectory of Fontes and Matray (1993). Blue star is modern seawater value, and blue arrow represents the direction taken by adding a component of dissolved halite to a seawater-derived fluid. Most data fall away from SET, indicating both Na-enrichment and Na-depletion compared to initial seawater. Deposits which show low Cl/Br tend to also show low Na/Br.

Lumwana and Kansanshi datasets) plot above modern day seawater. Potassium-bromine ratios are highly variable, and also do not correlate particularly well with the modern day seawater evaporation trajectory (Fig. 3.10). The vast majority of data fall above the SET, indicating K-enrichment in the fluids. Only the Konkola data and part of the Kansanshi dataset plot close to the SET.

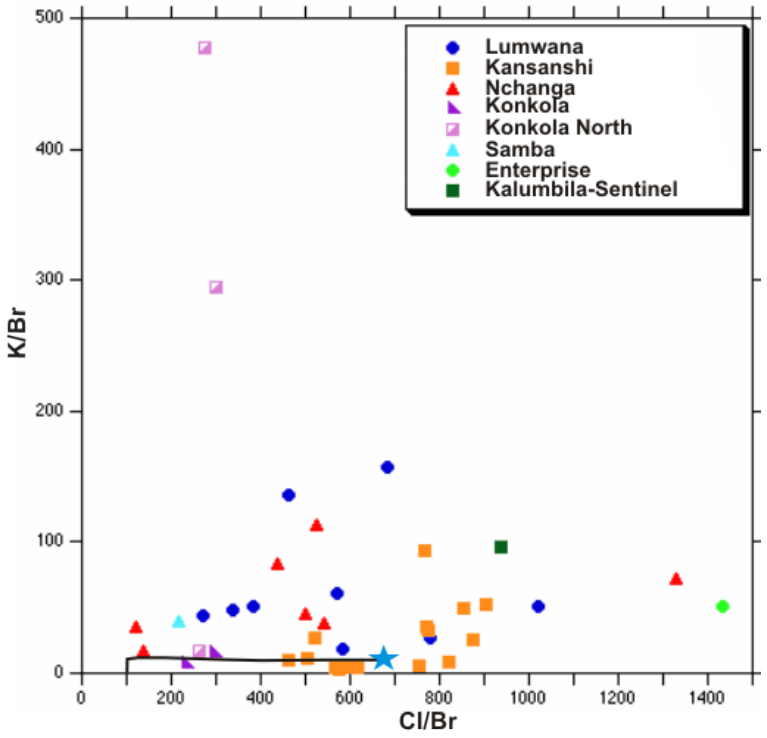

FIGURE 3.10: K-Cl-Br systematics of fluid inclusion leachates. K/Br (molar) ratios are extremely variable, and most fall well above the seawater evaporation (black line, blue star indicating modern seawater values) trajectory of Fontes and Matray (1993). Most fluids are K-enriched, with only a few depleted, falling below the SET.

3.6 Stable isotope analysis

3.6.1 Chlorine isotopes

The data obtained from chlorine isotope analyses on selected leachates recovered from the bulk chemical analysis process are presented in Table 3.4.

All leachates from this study show very consistent chlorine isotope values, with δ^{37}Cl between -0.72 and +0.43 ‰, and show no variability with Cl/Br ratios (Fig. 3.11).

TABLE 3.4: Chlorine isotope data from subsampled fluid inclusion leachates

Sample	Mineralogy	Deposit	Category	δ^{37}Cl ‰ (SMOC)
MLW0291 50.85	QTZ	Lumwana (Mal)	Post-kinematic	-0.54
EQMAL083 94.43	QTZ	Lumwana (Mal)	Pre-syn kinematic	-0.20
SP-005	QTZ	Lumwana (Mal)	Pre-kinematic boudin	-0.22
1E-008	QTZ	Lumwana (Mal)	Pre-kinematic boudin	-0.09
SAM001 64.30	QTZ	Samba	Pre-kinematic boudin	-0.22
NOP99 TFQ	QTZ	Nchanga	Pre-syn kinematic?	-0.04
NOP21 Arkose	QTZ	Nchanga	Pre-syn kinematic?	-0.72
NOP122	QTZ	Nchanga	Pre-syn kinematic?	+0.29
KON149A 1421.20	QTZ/CARB	Konkola	Pre-syn-kinematic	+0.02
KN54-191 1372.5	QTZ/CARB	Konkola North	Pre-syn kinematic	-0.08
KAL0200 160.35	QTZ	Kalumbila-Sentinel	Pre-syn kinematic?	+0.19
KAL23 445.8	QTZ	Kalumbila-Sentinel	Pre-syn kinematic?	-0.07
ENT0003 76.00	QTZ	Enterprise	Post-kinematic	+0.15
KAN 1-4	CARB	Kansanshi	Post-kinematic	+0.13
KAN 2-1	CARB	Kansanshi	Post-kinematic	+0.36
KAN 3-8	CARB	Kansanshi	Post-kinematic	+0.43
KAN 2-5	QTZ	Kansanshi	Post-kinematic	-0.39
KAN 3-8	QTZ	Kansanshi	Post-kinematic	+0.19

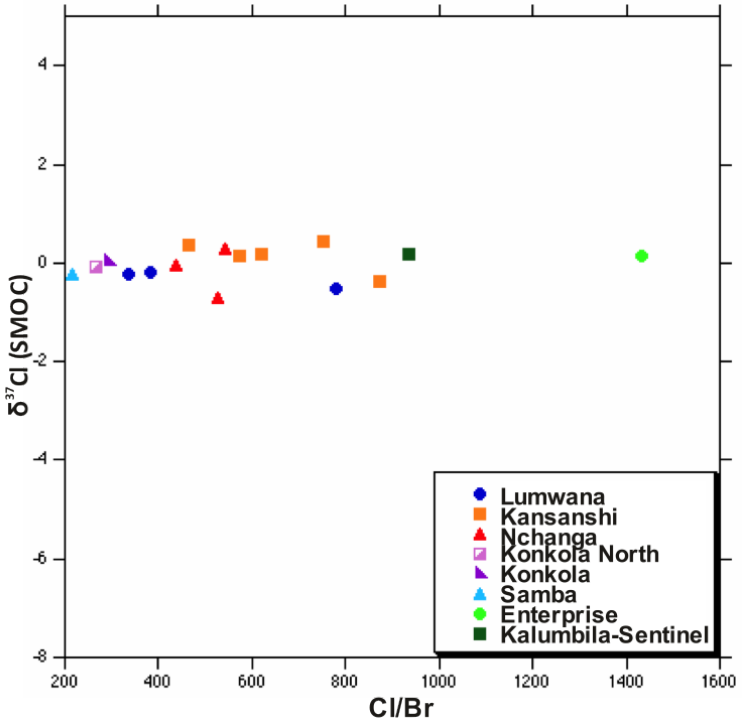

FIGURE 3.11: Stable chlorine isotope data from a subset of fluid inclusion leachates. Data fall very close to 0 ‰ (relative to Standard Mean Ocean Chloride) and show little or no variation with Cl/Br.

3.6.2 Oxygen isotopes

Table 3.5 shows the results of the analyses of quartz and carbonate vein material, and host rock carbonate for $\delta^{18}O$.

TABLE 3.5: Oxygen isotope data from quartz-carbonate veins and host rocks

Sample	Mineralogy	Deposit	Category	$\delta^{18}O$ ‰ (V-SMOW)
MLW0291 44.65	QTZ	Lumwana (Mal)	Post-kinematic	+10.0
1E-002	QTZ	Lumwana (Mal)	Post-kinematic	+8.4
1E-003	QTZ	Lumwana (Mal)	Post-kinematic	+8.6
MLW0291 50.85	QTZ	Lumwana (Mal)	Post-kinematic	+8.4
1E-008	QTZ	Lumwana (Mal)	Pre-kinematic boudin	+9.5
LUM0287 80.82	QTZ	Lumwana (Mal)	Pre-kinematic boudin	+9.5
EQMAL083 71.2	QTZ	Lumwana (Mal)	Pre-kinematic boudin	+8.7
SP-005	QTZ	Lumwana (Mal)	Pre-kinematic boudin	+9.9
LUM0287 59.75	QTZ	Lumwana (Mal)	Pre-syn kinematic	+10.4
EQMAL084 91.3	QTZ	Lumwana (Mal)	Pre-syn kinematic	+7.9
EQMAL083 94.43	QTZ	Lumwana (Mal)	Pre-syn kinematic	+8.3
SAM001 64.30	QTZ	Samba	Pre-kinematic boudin	+10.2
NOP41 GR	QTZ	Nchanga	Pre-syn kinematic?	+12.6
NOP122 GR	QTZ	Nchanga	Pre-syn kinematic?	+12.5
NOP96 BSSL	QTZ	Nchanga	Pre-syn kinematic?	+19.2
NOP96 BSSL	QTZ	Nchanga	Pre-syn kinematic?	+19.8
NOP21 ARKOSE	QTZ	Nchanga	Pre-syn kinematic?	+12.2
NOP99 TFQ	QTZ	Nchanga	Pre-syn kinematic?	+16.6
NOP81	QTZ	Nchanga	Pre-syn kinematic?	+26.8
NOP81	QTZ	Nchanga	Pre-syn kinematic?	+25.7
KON149A 1421.20	CARB	Konkola	Pre-syn kinematic	+16.7
KON149A 1421.20	QTZ	Konkola	Pre-syn kinematic	+14.8
KON149A 1421.30	CARB	Konkola	Pre-syn kinematic	+16.7
KON149A 1421.30	QTZ	Konkola	Pre-syn kinematic	+17.0
KN54-191 1361.7	QTZ	Konkola North	Pre-syn kinematic	+14.1
KN54-191 1368.7	CARB	Konkola North	Pre-syn kinematic	+17.5
KN54-191 1368.7	QTZ	Konkola North	Pre-syn kinematic	+17.4
KN54-191 1372.5	CARB	Konkola North	Pre-syn kinematic	+16.7
KN54-191 1372.5	QTZ	Konkola North	Pre-syn kinematic	+16.4
KAL23 309.8	CARB	Kalumbila	Pre-syn kinematic?	+7.5
KAL23 445.8	QTZ	Kalumbila	Pre-syn kinematic?	+12.4
KAL0200 160.35	QTZ	Kalumbila	Pre-syn kinematic?	12.0
ENT0003 74.22	QTZ	Enterprise	Post-kinematic	+15.1
ENT0003 76.00	QTZ	Enterprise	Post-kinematic	+14.7
KAN 1-3	CARB	Kansanshi	Post-kinematic	+13.8
KAN 1-3	QTZ	Kansanshi	Post-kinematic	+12.6
KAN 1-4	CARB	Kansanshi	Post-kinematic	+13.8
KAN 1-4	QTZ	Kansanshi	Post-kinematic	+13.2
KAN 1-7	CARB	Kansanshi	Post-kinematic	+13.5
KAN 2-1	CARB	Kansanshi	Post-kinematic	+15.1
KAN 2-2	CARB	Kansanshi	Post-kinematic	+15.7
KAN 2-5	QTZ	Kansanshi	Post-kinematic	+14.9
KAN 2-9	CARB	Kansanshi	Post-kinematic	+14.6
KAN 3-6	QTZ	Kansanshi	Post-kinematic	+14.9
KAN 3-8	CARB	Kansanshi	Post-kinematic	+12.8
KAN 3-8	QTZ	Kansanshi	Post-kinematic	+14.3
KAN 3-9	CARB	Kansanshi	Post-kinematic	+13.2
KAN 3-10	CARB	Kansanshi	Post-kinematic	+14.3
KAN 1-1	CARB	Kansanshi	Host marble	+22.2
KAN 1-1	CARB	Kansanshi	Host marble	+22.2
KAN 1-1	CARB	Kansanshi	Host marble	+22.1
KAN 1-1	CARB	Kansanshi	Host marble	+22.1
6. 350W 144 JPR	QTZ	Musoshi	Post-kinematic	+9.8
10. 375 R500 JPR	QTZ	Musoshi	Post-kinematic	+9.8

The oxygen isotope ratios from quartz across all deposits varies between +7 and +26 ‰ (V-SMOW; Fig. 3.12). All samples from Lumwana (pre-kinematic veins, pre-to syn-kinematic sulphide remobilising veins and post-kinematic veins) show similar values (between +7 and +11 ‰). Samples from Nchanga show a very similar range to that reported by McGowan et al. (2006). Vein samples from Konkola and Konkola North, and Enterprise and Kalumbila-Sentinel show similar values (Fig. 3.12A). Carbonates in

quartz-carbonate veins show δ^{18}O between +7 and +18 ‰ relative to V-SMOW (Fig. 3.12B).

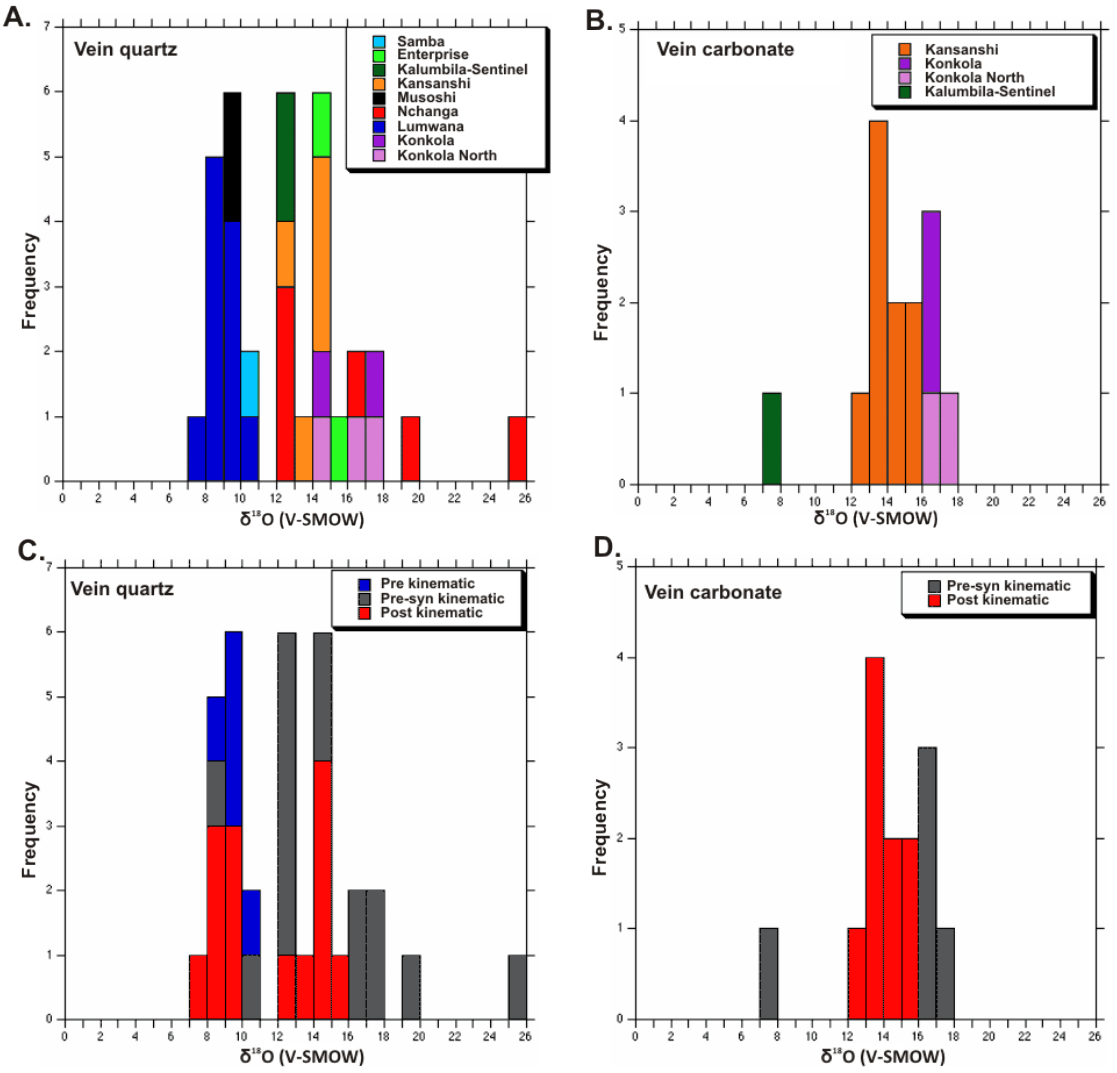

FIGURE 3.12: A) δ^{18}O data from vein quartz grouped by deposit. B) δ^{18}O from vein carbonates grouped by deposit. C) δ^{18}O data from vein quartz grouped by vein paragenesis. D) δ^{18}O from vein carbonates grouped by vein paragenesis. Data in permil (‰) relative to V-SMOW.

3.6.3 Carbon isotopes

Table 3.6 shows the results of analyses of vein carbonate material and host rocks for δ^{13}C.

δ^{13}C of vein carbonates varies from ∼-1.5 ‰ (Kalumbila-Sentinel) to -19 ‰ (Konkola). The Kansanshi data show very consistent δ^{13}C ∼-3 ‰ and there is good grouping in the data from Konkola and Konkola North (Fig. 3.14). The Kansanshi and Kalumbila-Sentinel vein data fall within the lower end of the range, and the Kansanshi Marble data

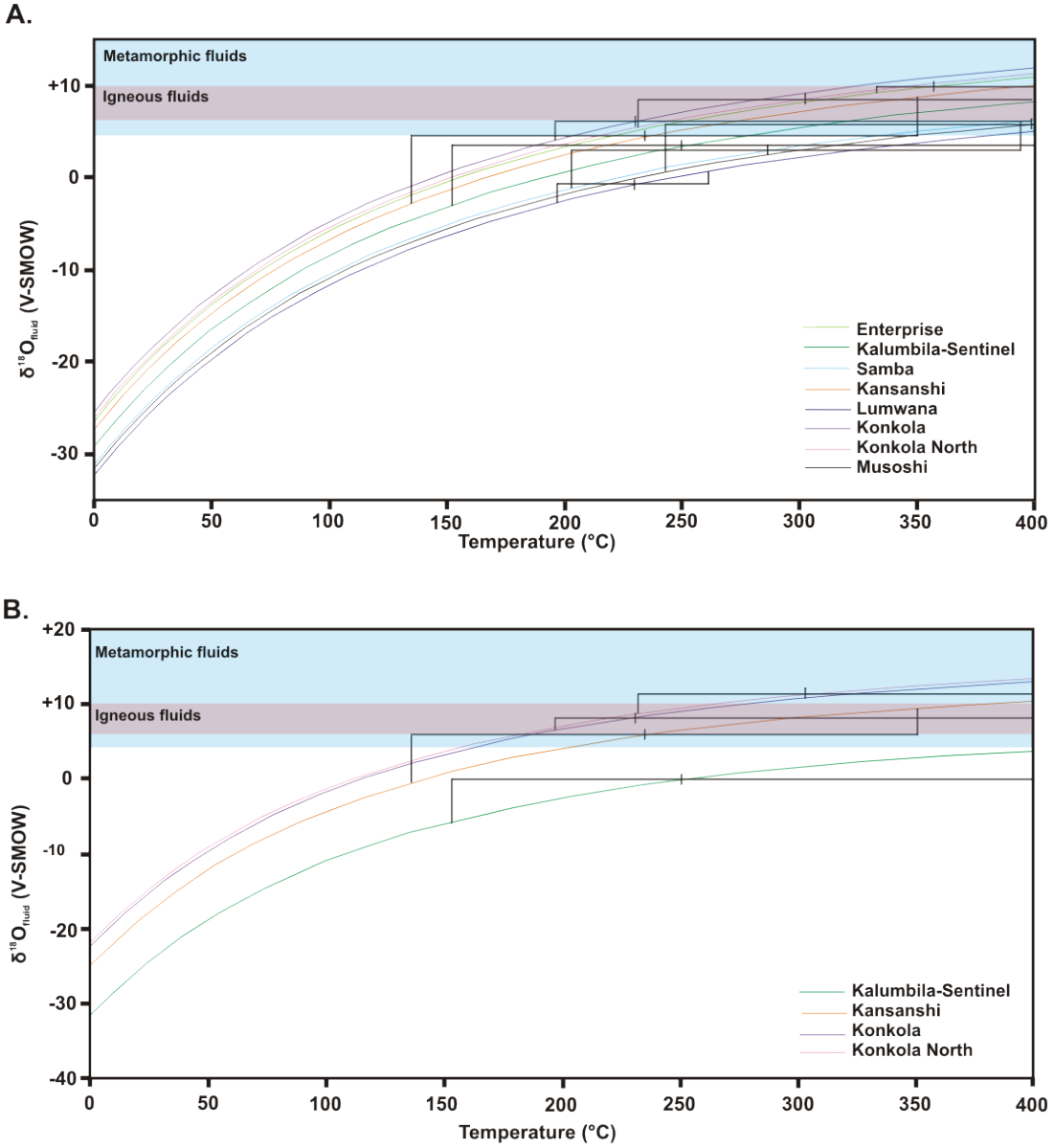

FIGURE 3.13: A) Calculated curves based on average δ^{18}O of vein quartz for each deposit. Black bars represent microthermometric constraints on temperature for each deposit including the range and mean, allowing for $\delta^{18}O_{fluid}$ to be estimated. Fractionation factor from Matsuhisa et al. (1979). B) As above, but for δ^{18}O of vein dolomite using the fractionation factor of Zheng (1999). Igneous and metamorphic fluid fields from Taylor (1997). Data in per mil (‰) relative to V-SMOW.

TABLE 3.6: Carbon isotope data from carbonate vein material and host rocks

Sample	Deposit	Category	δ^{13}C ‰ (V-PDB)
KON149A 1421.20	Konkola	Pre-syn kinematic	-18.9
KON149A 1421.30	Konkola	Pre-syn kinematic	-19.1
KN54-191 1368.7	Konkola North	Pre-syn kinematic	-14.2
KN54-191 1372.5	Konkola North	Pre-syn kinematic	-19.0
KAL23 309.8	Kalumbila	Pre-syn kinematic?	-1.5
KAN 1-3	Kansanshi	Post-kinematic	-3.2
KAN 1-4	Kansanshi	Post-kinematic	-3.3
KAN 1-7	Kansanshi	Post-kinematic	-2.8
KAN 2-1	Kansanshi	Post-kinematic	-3.3
KAN 2-2	Kansanshi	Post-kinematic	-2.9
KAN 2-9	Kansanshi	Post-kinematic	-3.2
KAN 3-8	Kansanshi	Post-kinematic	-3.0
KAN 3-9	Kansanshi	Post-kinematic	-3.0
KAN 3-10	Kansanshi	Post-kinematic	-3.2
KAN 1-1	Kansanshi	Host marble	+0.5
KAN 1-1	Kansanshi	Host marble	+0.5
KAN 1-1	Kansanshi	Host marble	+0.5
KAN 1-1	Kansanshi	Host marble	+0.5

falls well within the values for Neoproterozoic marine carbonates defined by Jacobsen and Kaufman (1999) for this time period. The δ^{13}C values for Konkola and Konkola North, in contrast, are much lighter.

3.6.4 Hydrogen isotopes

Table 3.7 shows the results of the analyses of vein material for δD.

Hydrogen isotope ratios from fluid inclusions within quartz and carbonate vein material from all deposits vary between -117 and -17 ‰, with a significant intra deposit range for deposits characterised by post-kinematic veins, e.g. Kansanshi and the fluid overprint at Lumwana (Fig. 3.15). Data from Nchanga show closely grouped δD compared to $\delta^{18}O_{mineral}$ and $\delta^{18}O_{fluid}$ in comparison to Kansanshi and Lumwana. Plotting δD against $\delta^{18}O_{fluid}$ shows that Copperbelt fluids plot away from the meteoric water line with a general trend towards and into the metamorphic water field (Fig. 3.16A), with a significant proportion of late discordant vein samples falling close to or within the metamorphic water field. The large variation in δD compared to $\delta^{18}O_{fluid}$ for fluids at Kansanshi and Lumwana result in sub-vertical linear trends away from the meteoric water line and the metamorphic water field, whilst data from Nchanga show a sub horizontal trend into the metamorphic water field.

3.7 Micro computed tomography

Optical examination of doubly polished wafers of both quartz and carbonate from vein material from Kansanshi was undertaken as part of the fluid inclusion study. However,

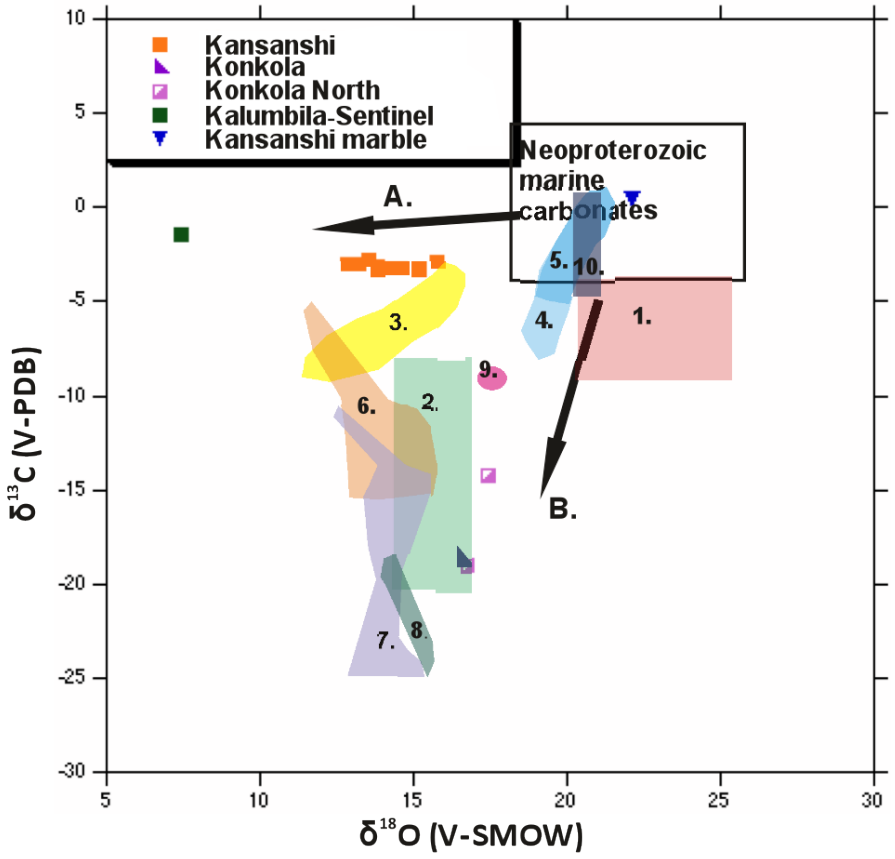

FIGURE 3.14: Vein carbonate stable isotope systematics. Two differing trends away from Neoproterozoic marine carbonates. A shows Significant variation in δ^{18}O with minimal variation in δ^{13}C. B shows significant variation in δ^{13}C away from Neoproterozoic marine carbonate with less variation in δ^{18}O. Data in permil (‰) relative to V-SMOW for oxygen, and V-PDB for carbon. Coloured fields denote data from: 1) Konkola Footwall. 2) Konkola Ore Shale (Sweeney et al., 1986). 3) Nchanga ore and shearzone dolomite (McGowan et al., 2006). 4) Dolomite pseudomorphs in Mines Subgroup 5) Fine grained dolomite in Mines Subgroup (Muchez et al., 2008). 6) Nkana vein carbonate. 7) Nkana nodule carbonate (Muchez et al., 2010). 8) Chambishi nodule dolomite. 9) Chambishi subconcordant vein dolomite. 10) Chambishi reef dolomite (Annels, 1989).

the transparency of the carbonate was found to be particularly poor, meaning fluid inclusions could not be identified. When undergoing the crush-leach process, the carbonate samples from Kansanshi were noted to give very concentrated leachates, which needed significant dilution, suggesting that they contained either a large volume of palaeofluids, very saline inclusions or both. Additionally, the carbonate shows different Cl/Br than the quartz samples (Fig. 3.5D). A pilot micro-CT study was conducted on a single carbonate crystal to attempt to image any fluid inclusions.

Six different density materials could be identified by this study. The majority of the material is made up of the host carbonate (Fig. 3.17A). Material with a density between that of the host carbonate and that of air was interpreted as the fluid inclusions (Figs. 3.17, 3.18). 4 materials denser than the host carbonate were also identified. These

TABLE 3.7: Hydrogen isotope data from fluids within quartz-carbonate veins

Sample	Mineralogy	Deposit	Category	δD ‰ (V-SMOW)
SP-005	QTZ	Lumwana (Mal)	Pre-kinematic boudin	-43
LUM0287 80.82	QTZ	Lumwana (Mal)	Pre-kinematic boudin	-117
MLW0291 28.00	QTZ	Lumwana (Mal)	Pre-syn kinematic	-17
EQMAL083 94.43	QTZ	Lumwana (Mal)	Pre-syn kinematic	-39
EQMAL084 91.3	QTZ	Lumwana (Mal)	Pre-syn kinematic	-96
MLW0291 50.85	QTZ	Lumwana (Mal)	Post-kinematic	-76
1E-002	QTZ	Lumwana (Mal)	Post-kinematic	-85
SAM001 64.30	QTZ	Samba	Pre-kinematic boudin	-85
NOP41 GR	QTZ	Nchanga	Pre-syn kinematic?	-67
NOP122 GR	QTZ	Nchanga	Pre-syn kinematic?	-71
NOP96 BSSL	QTZ	Nchanga	Pre-syn kinematic?	-62
NOP21 ARKOSE	QTZ	Nchanga	Pre-syn kinematic?	-81
NOP99 TFQ	QTZ	Nchanga	Pre-syn kinematic?	-69
KON149A 1421.20	QTZ/CARB	Konkola	Pre-syn kinematic	-95
KON149A 1421.30	QTZ/CARB	Konkola	Pre-syn kinematic	-93
KN54-191 1372.5	QTZ/CARB	Konkola North	Pre-syn kinematic	-94
KAL0200 160.35	QTZ	Kalumbila	Pre-syn kinematic?	-70
KAL23 309.8	CARB	Kalumbila	Pre-syn kinematic?	-99
ENT0003 74.22	QTZ	Enterprise	Post-kinematic	-74
KAN 1-3	QTZ	Kansanshi	Post-Kinematic	-98
KAN 1-3	CARB	Kansanshi	Post-kinematic	-71
KAN 1-4	QTZ	Kansanshi	Post-kinematic	-63
KAN 1-4	CARB	Kansanshi	Post-kinematic	-68
KAN 1-7	CARB	Kansanshi	Post-kinematic	-39
KAN 2-1	CARB	Kansanshi	Post-kinematic	-50
KAN 2-2	CARB	Kansanshi	Post-kinematic	-44
KAN 2-5	QTZ	Kansanshi	Post-kinematic	-72
KAN 2-9	CARB	Kansanshi	Post-kinematic	-67
KAN 3-6	QTZ	Kansanshi	Post-kinematic	-105
KAN 3-8	QTZ	Kansanshi	Post-kinematic	-36
KAN 3-8	CARB	Kansanshi	Post-kinematic	-94
KAN 3-9	CARB	Kansanshi	Post-kinematic	-100
KAN 3-10	CARB	Kansanshi	Post-kinematic	-90
2. 350W 72 JPR	QTZ	Musoshi	Post-kinematic	-105
6. 350W 144 JPR	QTZ	Musoshi	Post-kinematic	-88
10. 375 R500 JPR	QTZ	Musoshi	Post-kinematic	-89

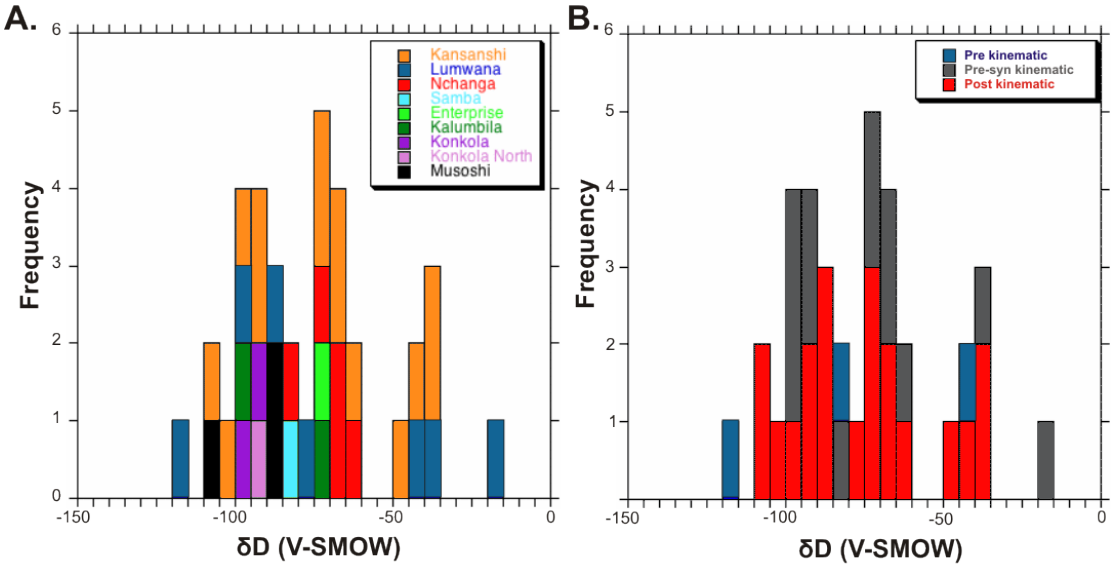

FIGURE 3.15: δD data from fluid inclusions in quartz and carbonate vein material. A) Grouped by deposit. B) Grouped by vein textural paragenesis. Data in permil (‰) relative to V-SMOW.

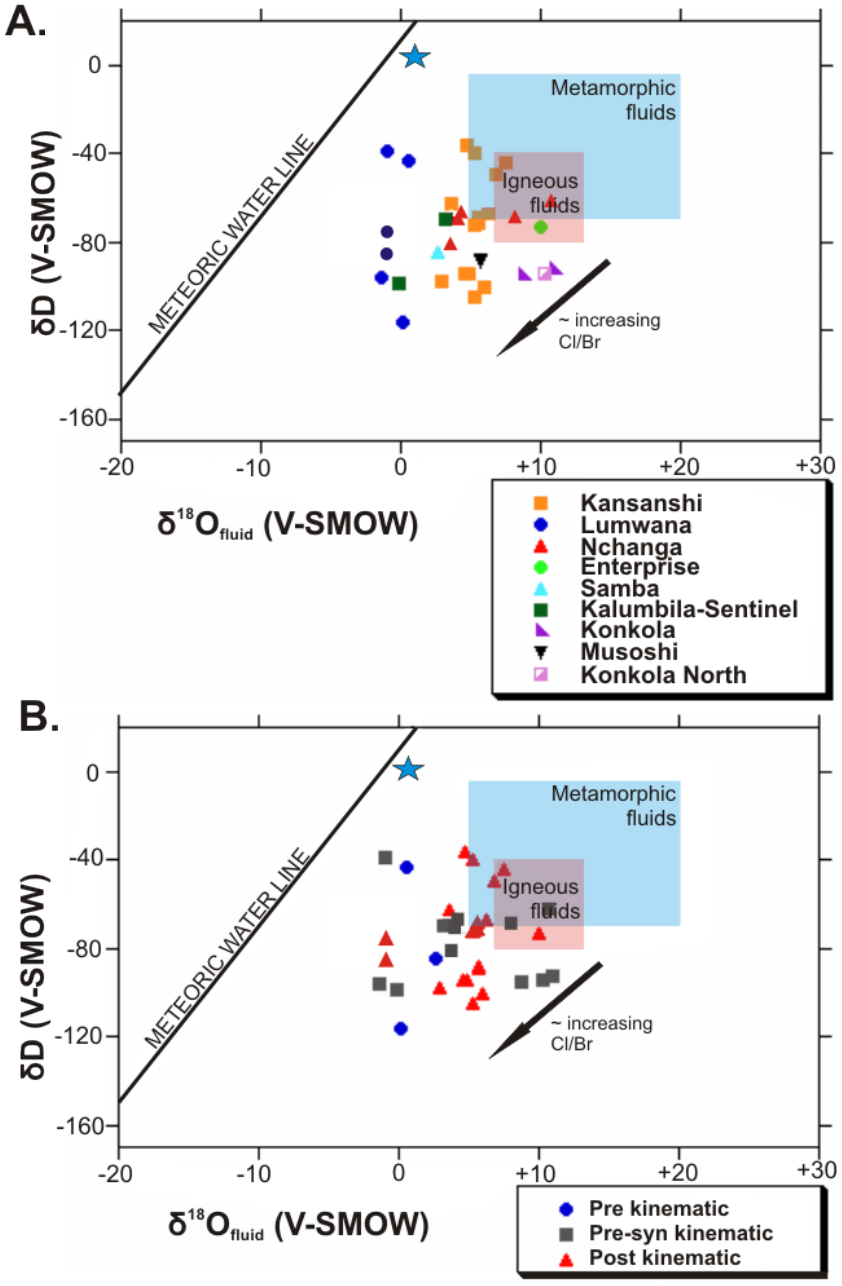

FIGURE 3.16: Isotopic composition of Copperbelt vein samples grouped by A) Deposit. B) Vein textural paragenesis. (Figure after Sheppard, 1986). $\delta^{18}O_{fluid}$ calculated for each sample based on mineral $\delta^{18}O_{mineral}$ value and average temperature of fluid inclusion assemblage for deposit using the fractionation factors of Matsuhisa et al. (1979) for quartz samples and Zheng (1999) for carbonates. Data in permil (‰) relative to V-SMOW.

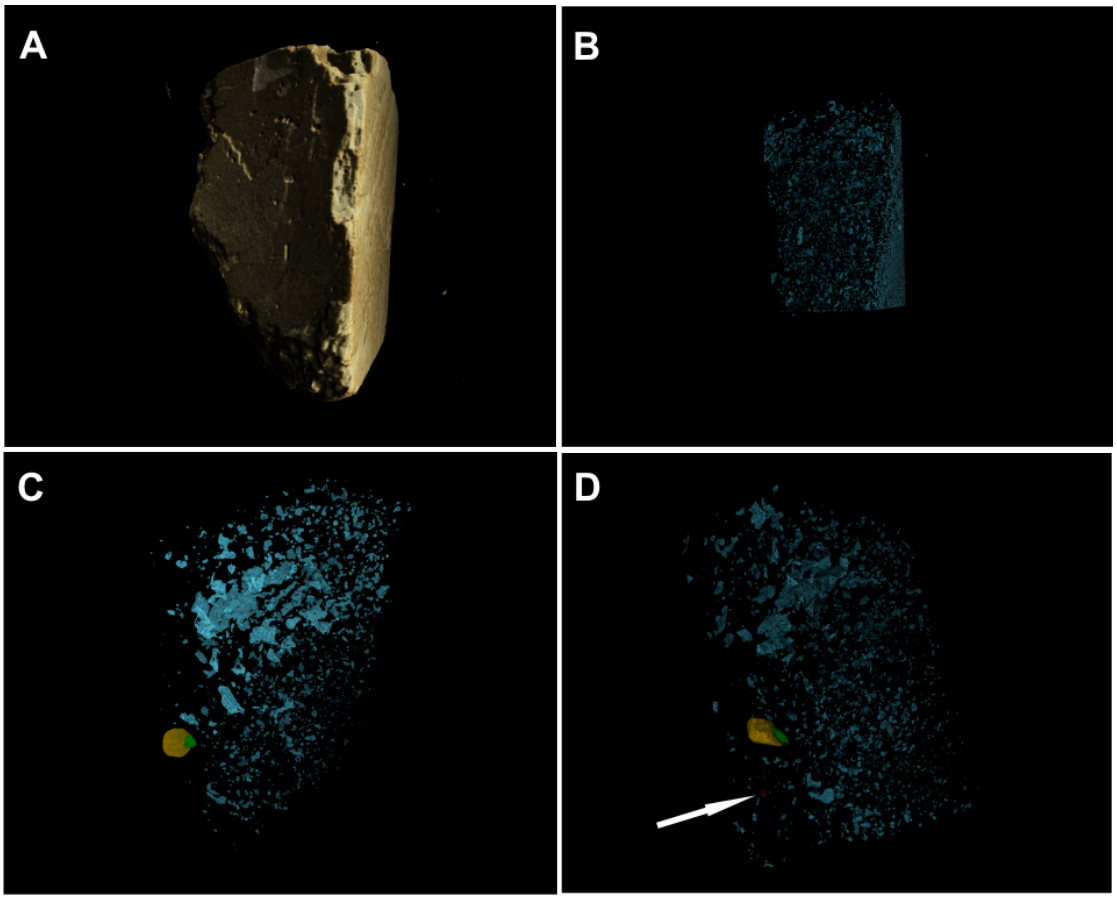

FIGURE 3.17: Micro computed tomography images. A) Carbonate crystal exterior, ~2 mm high. B) 3D section within the centre of the crystal cropped to remove edge effects, showing distribution of fluid inclusions (blue). C) Random distribution of fluid inclusions, and spatial association between chalcopyrite (yellow) and pyrite (green) mineralisation. D) Same image as C, but from a different angle, further illustrating the random orientation of inclusions, as well as minor, a more dense phase (red, shown by arrow, possibly gold or a uranium phase).

denser materials tend to show spatial correlation, particularly the two most volumetrically significant, interpreted as pyrite and chalcopyrite based on the common sulphide assemblage identified for the Kansanshi veins (Figs. 3.17C, D; 3.18A, C). Two of the phases are volumetrically minor, with one showing spatial correlation on the surface of pyrite and chalcopyrite, interpreted here as an iron oxide (Fig. 3.18B, D) . The other is the densest material identified, with a higher relative density than pyrite and chalcopyrite (Fig. 3.17A), potentially representing minor gold mineralisation, or a uranium phase (e.g. Broughton et al., 2002).

It is not possible to identify different types of fluid inclusion assemblage from this data, or discern any daughter salt phases within the inclusions. However, the random emplacement of inclusions within the crystal suggests that they are probably primary inclusions, consistent with the interpretation that the veins at Kansanshi were formed during a single mineralisation event (Broughton et al., 2002). This pilot study has been effective at

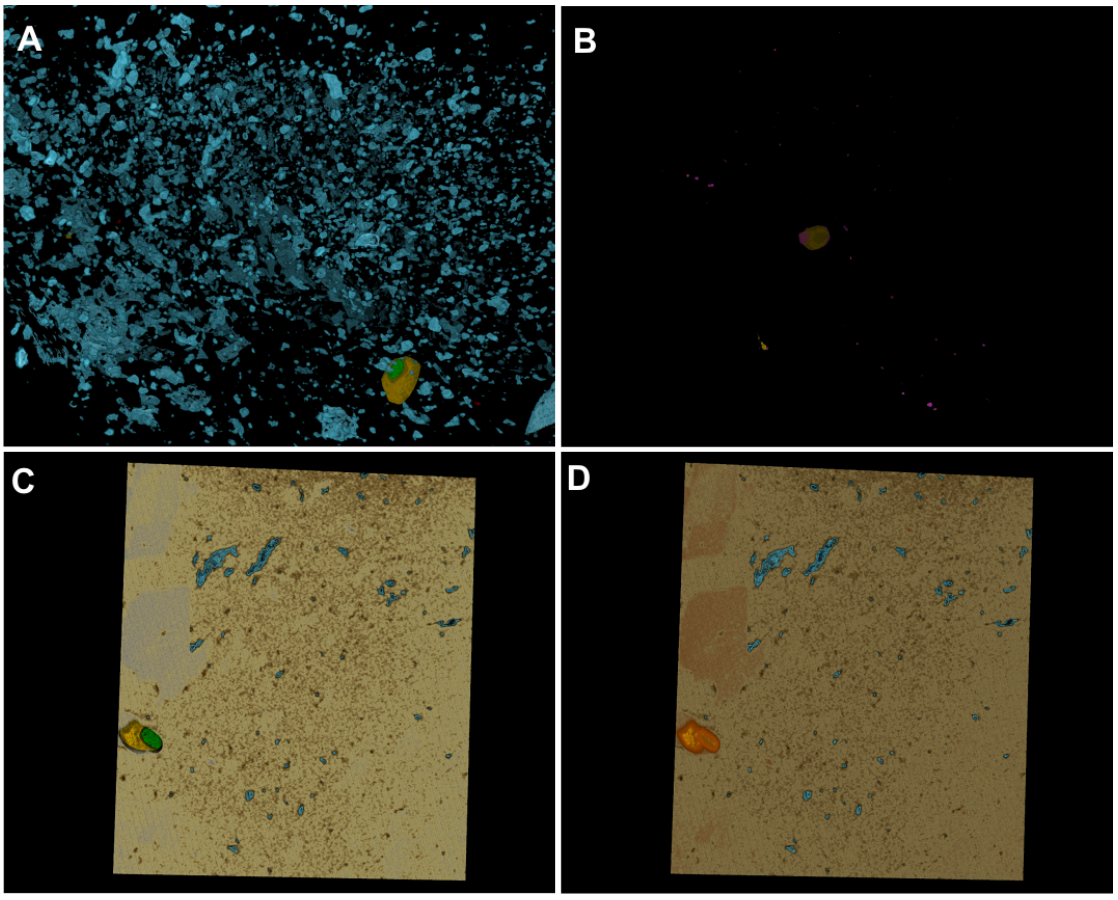

FIGURE 3.18: Micro computed tomography images. A) Close up of fluid inclusions, showing random orientations, spacing and shape. B) Spatial association between sulphide (yellow) and a phase interpreted as Fe oxides (pink). C) Section through crystal showing carbonate (beige), fluid inclusions (blue), and sulphides (yellow and green). Very large inclusions in top left may be decrepitated. D). Same section as C, but showing the presence of phase spatially associated with the surface of sulphides (orange), interpreted as Fe oxide.

revealing the significant volume of fluid inclusions within the Kansanshi vein carbonate. In future, more detailed studies could be conducted on fluid inclusion assemblages using this technique.

The presence of minor amounts of sulphides, and their subsequent oxidation products within Kansanshi vein material considered clean by hand picking techniques suggests that hand picking is not completely reliable for obtaining sulphide free material. The fine nature of the sulphides indicates that other techniques would be unlikely to be any more effective at screening for these inclusions, especially in opaque minerals. The presence of the sulphides suggests that the vein material from other deposits sampled in this project may also include fine sulphide inclusions, despite best practice during hand picking. Minor sulphide inclusions and their oxidation products are unlikely to affect the results for stable isotope studies, but may cause higher sulphate contents within the fluid inclusion bulk leachates (e.g. Fig. 3.7) and so these data must be treated with

caution. The leachates already contain much more SO_4^{2-} than seawater (Fig. 3.7), and the presence of sulphides within the crushed material may have contributed to those results.

3.8 Discussion

Evaporation of seawater beyond the point of halite precipitation is a fundamental way in which chlorine-bromine ratios of seawater can be altered (e.g. Carpenter, 1978). Fluids with Cl/Br <656 are bromine enriched, and may represent a component of residual seawater which has evaporated beyond the halite saturation point, forming halite and removing Cl from the fluid. Fluids with Cl/Br >656 are chlorine enriched, and may be interpreted as having a component derived from the dissolution of halite. The most likely source of fluid and halogens in the Copperbelt system is seawater, as there is little evidence for igneous contribution in the formation of these deposits.

The Cl/Br data presented here show a range, some with values lower than seawater, some with values higher, suggesting that these fluids represent modifications from an initial seawater source. This range of values likely suggests a mixture of fluid components involving residual bittern brines, halite dissolution fluids and seawater. It is common for fluid systems to comprise of a mixture of fluid components, and it can be difficult to differentiate between mixtures of fluids based on Cl/Br and Na/Br ratios alone (Chi and Savard, 1997). Pre-and syn-kinematic veins mostly show Cl/Br < seawater, indicating they are formed primarily from a residual fluid formed after the evaporation of seawater beyond the halite saturation point (Fig. 3.5). Concentrations of chlorine greater than 200,000 ppm in the majority of samples indicate strong evaporation beyond the carnalite saturation point and the dissolution of halite, incorporating this component into the system (Fig. 3.6). Post-kinematic veins from across the Copperbelt dominate the population which preserve Cl/Br ratios > seawater, and are likely to represent a fluid with an increasing component of halite dissolution. These data suggest that, fluids in the Copperbelt may have been initially dominated by residual brines formed after the deposition of the evaporite sequences in the Upper Roan. This stage may have lasted as long as early basin inversion, since this fluid dominates veins in the upper and lower orebodies at Nchanga, interpreted as forming during this tectonic setting (McGowan et al., 2006, 2003). Veins from within the ore shale at Konkola and Konkola North also record this fluid, and these deposits have been interpreted as forming during late diagenesis, relatively early on in the Copperbelts tectonic history (Sweeney et al., 1986). The post-kinematic veins with a Cl/Br ratio indicative of a major halite dissolution component suggest that later in the basin history, there was a successive fluid event where

the evaporite sequences were dissolved (represented by the formation of the collapse breccias; Selley et al., 2005).

Although petrographic work and the microthermometric study suggests that there has been a fluid overprint on the Lumwana samples, they preserve different chlorine-bromine signatures. The data from pre-kinematic samples at Lumwana are all bromine-enriched, suggesting they formed from residual seawater after evaporation has occurred beyond the halite saturation point. Post-kinematic veins at Lumwana, interpreted here to have formed from the fluid which has caused the overprint are Cl-enriched, suggesting late fluids contained a significant component of dissolved halite. This indicates that the component of residual seawater was volumetrically large enough to preserve a low Cl/Br ratio even with the presence of a Cl-enriched overprint. The large, saline, partially decrepitated Type-1 inclusions identified at Lumwana may be the reason that pre-kinematic veins preserve a lower Cl/Br ratio.

The fact that the range of brines is recorded at Lumwana (Fig. 3.5C) indicates that these fluids were capable of penetrating basement structures, as suggested by the modelling work of Koziy et al. (2009). Cl/Br data for chalcopyrite-rich veins at Kansanshi suggest that there are different fluids preserved within the quartz and carbonate sections of the veins, with the majority of the carbonate samples showing Cl/Br <seawater and the quartz with Cl/Br > seawater (Fig. 3.5D).

In summary there is a range of values in the Copperbelt samples suggesting that the evaporation of seawater was critical in all stages of the fluid history of the basin. Evaporation provided the halogens in the fluids, both in terms of creating evaporite sequences and residual Br-enriched fluids, and then dissolving these salt packages. The range of values indicates that unaltered seawater was likely not a common component in the fluid history of the Copperbelt, rather being present as a residual fluid after halite precipitation, or having mixed with other components. There is also an overall temporal control over these data, related to the tectonic history in the basin. Data from pre-kinematic veins provide the best estimates on potentially 'early' fluids.

Most of the Cl/Br data showing values >seawater fall within the range 800-1000. Typical fluids dissolving halite can reach Cl/Br values up to ~20,000 (Grandia et al., 2003), suggesting that only a small component of dissolved halite was required to generate these fluids, or that there has been mixing between low Cl/Br bittern brines and high Cl/Br halite dissolution fluids. Mixing is common in basin environments and mixed fluids cannot be easily differentiated using Cl/Br (e.g. Chi and Savard, 1997). Theoretical mixing of evaporated seawater and halite dissolution end members suggests that relatively small proportions of residual evaporated seawater compared to dissolved halite can still result in values less than that of seawater (Chi and Savard, 1997), and so fluid mixing is highly

likely to explain the range of values observed in this study. It is clear from the results of the crush-leach study that evaporation of seawater, the formation of evaporites and the subsequent dissolution of those evaporite sequences has played the key role in generating the saline brines present in the Copperbelt. Plate reconstructions suggest that the region was between the equator and ~30 °S during the period ~883 to ~740 Ma when Katangan sedimentation took place, suggesting good latitudinal conditions for evaporation (Armstrong et al., 2005; Key et al., 2001; Meert and Torsvik, 2004). Overall the Cl/Br data suggest a progression towards higher Cl/Br values through basin evolution indicating an increasing importance of halite dissolution late in the basin history.

Most of the fluid leachates sampled in this study were significantly enriched in sulphate in comparison to modern seawater (Fig. 3.7). Sulphate concentrations in seawater are thought to have been significantly lower in the past due to anoxic conditions (Foriel et al., 2004) and to have oscillated in the Phanerozoic (Lowenstein et al., 2003). However, modern seawater represents a period where sulphate concentrations are relatively high, in the $MgSO_4$-rich, Ca-poor 'aragonitic sea' configuration, possibly similar to that of the Neoproterozoic (Lowenstein et al., 2003). Using the sulphate concentration of modern seawater as a comparator, the fluids investigated in this study still contain up to an order of magnitude more sulphate. Many Copperbelt studies record the presence of former evaporite nodules (e.g. Muchez et al., 2008; Selley et al., 2005). Dissolution of these nodules would increase the sulphate content of fluids.

Seawater cation concentrations (Na^+, K^+, Mg^{2+}, Ca^{2+}) are known to have been variable through geological time (Brennan et al., 2004; De Ronde et al., 1997; Gutzmer et al., 2003; Hardie, 1996; Horita et al., 1996, 2002; Kovalevich et al., 1998; Lowenstein et al., 2003, 2001), however cation contents in fluids from this study are likely to represent ancient seawater values that have been significantly altered through water-rock reactions (Figs. 3.8, 3.9, 3.10). The relationships between K/Br and Na/Br with Cl/Br (Figs. 3.9 and 3.10) may reflect both initial evaporation of seawater beyond the halite dissolution point and water-rock interaction. The high K/Na ratio for two of the Konkola North samples (Fig. 3.8) stand out from the third, and from the rest of the dataset in general, and are consistent with the high bulk-K, K-feldspar alteration and multiple K-feldspar overgrowths reported by Sutton and Maynard (2005). This supports their interpretations of the presence of a K-rich fluid at the deposit. High K compared to Na at low Cl/Br also reflects the removal of Na as halite during evaporite formation (i.e. the presence of bittern brines). When Na/Br and Cl/Br are compared, few of the data fall close to the seawater evaporation trend (Fig. 3.9), with a large number indicating sodium depletion. Na-depletion may occur through fluid-rock interaction, and the common sodic alteration in the Copperbelt in the form of albite and scapolite (Selley et al., 2005) likely accounts for the Na-loss. K/Br ratios are highly variable and

indicate significant K-enrichment in the fluids (Fig. 3.10). Only the Konkola data and part of the Kansanshi dataset plot close to the seawater evaporation trajectory. It is clear there is a widespread enrichment of K in these fluids. Alteration and destruction of K-feldspars in basement lithologies and detrital red-bed arkoses of the Lower Roan are likely to account for the potassium enrichment, as hypothesised by Selley et al. (2005), who suggest that K-rich phlogopite formed after consumption of K-feldspar.

3.8.1 Chlorine isotopes

The consistency of the chlorine isotope data suggests that the Cl source was the same for all the fluids studied, almost certainly seawater. The crustal chlorine reservoir is dominated by the Cl content of the oceans, and δ^{37}Cl ~0 ‰ is typical of Phanerozoic ocean waters (Godon et al., 2004; Kaufmann et al., 1984). The vast majority of Phanerozoic evaporite sequences, shield brines and formation waters all show δ^{37}Cl = 0 ‰ ± 0.9 ‰ (Eastoe et al., 2001, 2007, 1999; Shouakar-Stash et al., 2007). The remarkable homogeneity of the dataset, along with strong empirical evidence from studies of sedimentary stratiform copper systems suggests that a crustal source is likely. Secular change in δ^{37}Cl through geological time is unlikely (Eastoe et al., 2007) and recirculation and convection of brines in restricted basins (Jowett, 1986) would likely encourage homogenisation of chlorine isotope signatures, supporting the interpretation that δ^{37}Cl values presented here are derived from seawater evaporation.

3.8.2 Oxygen, carbon and hydrogen isotopes

Carbon (and oxygen) isotope data in carbonates follow the broad trend of isotopically light carbonate minerals related to Copperbelt fluids and ore generation via oxidation of organic matter (Machel, 1987; McGowan et al., 2006; Muchez et al., 2008; Selley et al., 2005). Carbon isotope data generated in this study show two groups, one with δ^{13}C values comparable to Neoproterozoic sedimentary carbonates (trend A, Fig. 3.14), the other with much lighter δ^{13}C (Trend B, Fig. 3.14). Kansanshi vein carbonate shows very little variation in δ^{13}C values. The δ^{13}C signature is similar to Neoproterozoic marine carbonates, and may be caused by inheriting the carbon isotope signature of the carbonate units within the succession. Similarly, Kalumbila-Sentinel also contains local carbonate units within the sequence, and buffering of the carbon isotope signature may also have occurred here. Data from vein carbonate samples from Konkola and Konkola North fall within or close to the field defined for Konkola ore shale gangue carbonate by Sweeney et al. (1986), following the trend of isotopically light carbonate related to ore generation in the Copperbelt (Fig. 3.14). This suggests that the mechanisms and

isotopic sources of oxygen and carbon forming the vein carbonate were the same as those forming the disseminated gangue mineralisation, or alternatively that the carbonate in the veins was simply locally remobilised from the abundant disseminated and lenticular dolomite present in the ore body, preserving its isotopic signature. Overall, carbonate isotopic signatures in the Copperbelt reflect both the oxidation of organic matter, but in some cases also a component of the δ^{13}C signature of Neoproterozoic marine carbonates, particularly where they are present and volumetrically significant in the host sedimentary sequences.

Oxygen isotope data from vein quartz for all deposits show a range similar to that previously reported for the Nchanga deposit (McGowan et al., 2006). All samples from Lumwana (pre-kinematic boudins, pre-syn kinematic veins which remobilise sulphides, and post-kinematic veins) are tightly grouped with values between +7 and +11 ‰. Konkola and Konkola North share similar values between +14 and +18 ‰. Enterprise and Kalumbila-Sentinel also show similar values (Fig. 3.12). Using the fractionation factors of Matsuhisa et al. (1979) and Zheng (1999) combined with δ^{18}O values of quartz and carbonate with microthermometric data allows the δ^{18}O of fluid in equilibrium to be calculated (Fig. 3.13). Taking the mean homogenisation temperatures for each deposit shows that fluid in equilibrium with quartz veins at Samba, Kalumbila-Sentinel, Kansanshi, and higher temperature data at Lumwana had δ^{18}O ∼-1 to +4 ‰. This is similar to the estimates of McGowan et al. (2006) at Nchanga. This range of values expands to ∼-3 to +5 ‰ when minimum and maximum temperatures are included, along with the data for Musoshi. Data from Enterprise, and Konkola and Konkola North suggest an isotopically heavier fluid (∼+7 to +10 ‰). The carbonate data vary slightly from the fluid in equilibrium with quartz in the veins, but are generally very similar.

Much of the data generated in this study for Lumwana, Kalumbila-Sentinel, Samba, Kansanshi and Musoshi are similar to those of McGowan et al. (2006) for the Nchanga deposit, though slightly expanding their range to $\delta^{18}O_{fluid}$ ∼-3 to +5 ‰. In contrast, $\delta^{18}O_{fluid}$ for the samples from Enterprise, Konkola and Konkola North is significantly higher at ∼+8 to +11 ‰. These data sit within the range of metamorphic fluids. The veining at Enterprise occurred late in the basin history, and so equilibration of basin brines with the host rocks may be considered as a potential reason for the increased $\delta^{18}O_{fluid}$ values here. Oxygen and carbon isotope data for both quartz and carbonate in veins from Konkola and Konkola North fall within that generated from dolomite and calcite from within the Ore Shale at Konkola reported by Sweeney et al. (1986) interpreted as forming via oxidation of organic material. However, texturally these veins clearly postdate diagenesis. The heavier $\delta^{18}O_{fluid}$ at these deposits may then represent the beginning of equilibration between the fluids and sediments such as arkoses (common

in the Lower Roan sequence) or greywackes which fall in the lower part of the oxygen isotope range of metasediments (∼+10 to +30 ‰; Taylor, 1997).

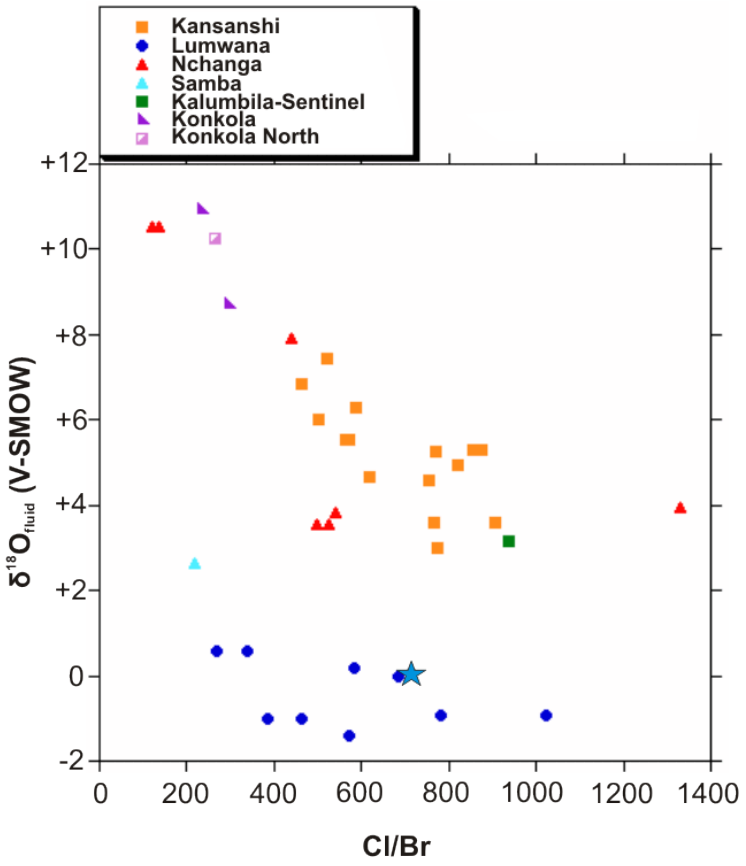

FIGURE 3.19: Paired calculated fluid oxygen isotope compositions and chlorine bromine ratios across the Copperbelt. Isotope data in permil (‰) relative to V-SMOW.

The oxygen isotope data presented here supports the conclusions of McGowan et al. (2006) that many of these fluids were initially isotopically lighter than would be expected for fluids that had equilibrated with igneous and metamorphic rocks (Taylor, 1997). The lack of any data significantly lighter than 0 ‰ suggests that the initial source of these fluids was seawater, supported by the results of the crush leach study and the chlorine isotope data. The combined oxygen and hydrogen data show a trend extending into the field of metamorphic fluids (Fig. 3.16). At face value, this might suggest that fluids were becoming increasingly equilibrated with the host rocks, leading to the generation of heavier $\delta^{18}O_{fluid}$ signatures. If this was the case, it could be expected that post-kinematic veins would show the most equilibration, and a more 'metamorphic' signature, which is not supported by the dataset (Fig. 3.15B). When chlorine-bromine data is combined with $\delta^{18}O_{fluid}$ there is a clear negative trend in the data from Nchanga, Konkola, Kansanshi and Konkola, particularly for values of Cl/Br indicative of a fluid primarily derived from residual evaporated seawater (Fig. 3.19). Other data presented in this study suggest that Cl/Br can be correlated with the timing of fluid events within

the basin, with 'earlier' fluids likely to show lower Cl/Br than 'late' fluids. The negative trend shown by Figure 3.19 suggests that earlier fluids have more positive oxygen isotope signatures than later fluids. This feature is also noted in late, massive veins at the Nkana deposit when compared to paragenetically earlier nodules and layer parallel veins (Muchez et al., 2010). During strong evaporation, the isotopic composition of seawater is thought to follow a 'hook' shaped pattern, where δ^{18}O first increases, then becomes lighter again with increasing evaporation (Holser, 1979). This potentially provides a mechanism to explain the lighter δ^{18}O values in fluids with higher Cl/Br ratios (Fig. 3.13). Equilibration with host rocks likely also plays a part in controlling $\delta^{18}O_{fluid}$. Fluids with low Cl/Br and heavier $\delta^{18}O_{fluid}$ probably formed relatively early in the basin history and had a long time to equilibrate with the host rocks. Additionally, low water-rock ratios were likely at this time period due to increased preservation of porosity within the host sedimentary packages. These factors may then allow for a greater degree of oxygen isotope equilibration between the brines and host rocks over a longer period of time than for fluids generated later in basin history. Post-kinematic veins preserve fluids generated later in basin history and typically show higher Cl/Br ratios indicative of dissolution of evaporite packages and lower $\delta^{18}O_{fluid}$ measurements. These fluids potentially had shorter residence times in the system during basin inversion and orogenesis, as well as probably greater water-rock ratios due to a shift from preserved porosity within sedimentary packages towards permeability controlled by fewer, larger scale structures such as faults and cavities caused by the dissolution of evaporite packages, resulting in a lower degree of fluid-rock equilibration, resulting in lower $\delta^{18}O_{fluid}$.

The broad spread of δD, particularly for samples from Kansanshi and Lumwana, when combined with fairly tight grouping of $\delta^{18}O_{fluid}$ suggests an isotopically heterogeneous hydrogen supply compared to that of oxygen. This is different from the situation encountered in modern oilfield basin brines where the majority of variation is controlled by heterogeneity of δ^{18}O, with limited variation in δD (Clayton et al., 1966), suggesting an additional, strong fractionation effect is required to explain the high variation in δD in the dataset presented here. Many basin brines show δD signatures lighter than would be expected for seawater derived fluids, and this has been attributed to flushing and expulsion of initial brines by fluids generated from locally derived, temporally recent meteoric waters (Clayton et al., 1966). As a result, the isotopic signatures for δD and $\delta^{18}O_{fluid}$ typically form linear arrays between the meteoric water line and the metamorphic water field, developed as the $\delta^{18}O_{fluid}$ equilibrates with the host rocks. However, it is difficult to reconcile this mechanism with the dataset presented here for the Zambian Copperbelt, since the δD signatures are too light for the palaeolatitudinal history of the region, based on plate reconstructions (e.g. Meert and Torsvik, 2004), and the modern latitude. Additionally, the linear trends of heterogeneous δD with little variation in

$\delta^{18}O_{fluid}$ do not support this interpretation. It has been proposed that anomalously light isotopic signatures in brines may be a function of colder climatic conditions at formation (Clayton et al., 1966). It cannot be discounted that isotopically light fluids generated in the colder conditions of the 'Snowball Earth' events in the Sturtian and Marinoan time periods (represented in the Copperbelt area by diamictite horizons in the Katangan Supergroup) may have contributed to the light δD signal. However, this would also concomitantly generate light $\delta^{18}O_{fluid}$ which does not support the linear trends of variable δD for little change in δ^{18}O presented in this study.

δD values may also be affected by the presence of structural hydrogen within the host mineral lattice in addition to that preserved in fluid inclusions, (Faure, 2003; Grant et al., 2003; Knauth and Epstein, 1975; Simon, 2001). Anomalously light δD values can be generated by samples giving low yields, or those derived from high temperature (>750 ℃) heating of the samples (Gleeson et al., 2008). No samples in this study were heated above 700 ℃ and there is no correlation between yield and δD value, suggesting that any effect of structural hydrogen is likely to be negligible. The studies of Simon (2001) and Faure (2003) suggest that even at temperatures as low as 500 ℃ thermal decrepitation of hydrothermal quartz may result in anomalously low δD values by between 10-30 ‰ compared to the initial hydrothermal fluid. Faure (2003) suggests calcite preserves the δD value of the initial fluid. Samples from Kansanshi quartz-carbonate veins allow for interrogation of pairs of δD values from both quartz and carbonate from within the same hand specimen. In the three sets of paired data available, one pair shows a much lighter δD value in the quartz than the carbonate, another pair shows a much lighter δD value in the carbonate than the quartz, and the third shows similar values (KAN 1-3: quartz = -97.6, carbonate = -71.1; KAN 1-4: quartz = -62.6, carbonate = -68.4; KAN 3-8: quartz = -36.4, carbonate = -94.0; all values in ‰ V-SMOW) reflecting the overall dataset, in which there is no correlation between carbonate samples (only heated to 400 ℃) and heavier δD values. The hydrogen data still remain significantly fractionated towards lighter values even if a 30 ‰ fractionation were taken into account, supporting the interpretation that a further explanation is required to explain this effect.

Hydrocarbons, coals and kerogens show isotopic signatures significantly depleted in deuterium, particularly natural methane, typically <-100 ‰ (Burruss and Laughrey, 2010; Fekete et al., 2011; Li et al., 2001; Redding, 1978; Schoell, 1980; Schoell and Redding, 1978). Shales also show light δD signatures, -55 to -87 ‰ (Savin and Epstein, 1970). It is clear that oxidation of organic material plays a role in the generation of light isotope signatures for δ^{13}C, and the light δD signatures may also reflect this process. Since hydrocarbons are predominantly composed of C and H over O, this represents a process capable of generating the heterogeneous and light δD signatures with very little variation in $\delta^{18}O_{fluid}$ reported here. Many workers have implicated the role of hydrocarbons

as a fluid reductant for ore genesis in the Copperbelt (Heijlen et al., 2008; McGowan et al., 2006; Selley et al., 2005), as well as for other sediment-hosted stratiform copper systems around the world (Hitzman et al., 2005). Multiple studies report the presence of hydrocarbons within fluid inclusion assemblages, for example at Kansanshi (Speiser et al., 1995), Chambishi (Greyling et al., 2005) and Kipushi (Heijlen et al., 2008) in the form of methane, and at White Pine in the form of liquid petroleum (Mauk and Hieshima, 1992). Carbonates at Kipushi contain shungite (metamorphosed bitumen; Heijlen et al., 2008), whilst the presence of pyrobitumen in fracture-filling veins, and faults at White Pine records the migration of petroleum through the deposit (Mauk and Hieshima, 1992). Further empirical evidence for the role of hydrocarbons as a reductant is common across the Copperbelt in the form of arenite-hosted orebodies hosting mineralisation within structurally favourable sites for hydrocarbon accumulation (Hitzman et al., 2005; McGowan et al., 2006; Selley et al., 2005).

3.9 Conclusions

Host rocks for sediment-hosted stratiform copper deposits contain veins, which record physicochemical attributes of palaeofluid flow. This study suggests fluids were moderate to high temperature saline to highly saline brines in the Copperbelt, containing complex cation chemistries. Halogen ratios indicate these brines were generated through the evaporation of seawater. By investigation of pre- and post-kinematic veins we establish there is a broad temporal trend between earlier basinal fluids, dominated by chlorine-bromine ratios below that of modern seawater indicative of a significant component of residual evaporated seawater, and later fluids, which contain a component of halite dissolution shown by Cl/Br ratio >modern seawater values. Chlorine isotope data support a crustal source for chlorine, falling well within the field expected for seawater, evaporites and evaporite-derived brines. Variation in cation contents of the fluids are attributable to water-rock interaction, and are consistent with the extensive, basin-scale alteration assemblages present in the Copperbelt, and as such, are unlikely to be representative of seawater at this time. Halogen concentrations indicate evaporation conditions beyond the carnalite saturation point for most fluids, which also contained significant amounts of sulphate.

Isotopic evidence suggests that these fluids were derived from a seawater source, which has undergone strong evaporation and has begun to equilibrate with the country rocks. Early fluids showing low Cl/Br show the greatest amount of isotopic equilibration with oxygen, probably due to weaker evaporation and longer residence times in basins when

the region underwent stratigraphic and structural development. Later fluids are characterised by a component of halite dissolution (high Cl/Br), and isotopically lighter $\delta^{18}O_{fluid}$, suggesting less oxygen isotope equilibration with host rocks likely due to rapid cycling of fluids by compression and heat during orogenesis. δD signatures are lighter than would be expected if their source were meteoric fluid infiltration and flushing. Instead, these signatures may simply reflect the oxidation of organic matter, potentially hydrocarbons, during fluid reduction, accounting for the significant heterogeneity in δD for very little variation in $\delta^{18}O_{fluid}$.

Chapter 4

The geochemistry of sulphide mineralisation in the Zambian Copperbelt

4.1 Abstract

Rare earth element concentrations within sulphide minerals from the Copperbelt show a large range of concentrations, spanning up to ∼4 orders of magnitude. Rare earth element profiles are variable, showing LREE-enrichment, LREE-depletion and relatively flat profiles, typically with negative Eu anomalies. Variations in LREE concentration provide the main control over the shape of profiles. Sulphide mineralogy, or sulphide paragenesis does not control the shape of the profiles, instead profile shapes tend to be characteristic of the different mineralised deposits, whilst individual deposits may also show a variety of profile shapes. The most likely control on the variation in LREE concentrations is the development of the hydrothermal alteration assemblage, which includes phlogopite, muscovite and K-feldspar, as well as other minerals. Phlogopite, muscovite and K-feldspar are all LREE enriched, and so precipitation of these phases would leave the hydrothermal fluid progressively depleted in LREE, providing a mechanism to account for the extreme variation in LREE concentrations observed in Copperbelt sulphides. Hydrothermal K-feldspar also shows significant positive Eu anomalies, and so precipitation would leave the hydrothermal fluid with a negative Eu anomaly, similar to that seen in the sulphides in this study.

Copperbelt sulphides are enriched in Co compared to other transition metals, consistent with the Co enrichment in the Central African Copperbelt as a whole. The deposits on the Kafue Anticline, e.g. Nchanga and Konkola, are enriched in Co over the deposits in

the Domes Region. Variability in trace element concentrations in Copperbelt sulphides suggests that sulphide mineralogy does not play a strong role in controlling the trace element concentrations, instead suggesting that local effects at the different deposits, as well as potentially different timings of mineralisation are more important. For example, deposits thought to form during basin inversion and orogenesis contain sulphides relatively more enriched in Sn. Sulphides hosted in basement deposits contain higher mean concentrations of Total REE and Au. The local conditions responsible for variations in trace element concentrations in sulphides are most likely the trace element concentration of host rocks and variations in the original metal source scavenged by the hydrothermal fluids, i.e. variations in the metal contents of the basin redbed sediments and basement lithologies.

Sulphur isotope signatures from sulphides from across the Zambian Copperbelt and Domes Region show δ^{34}S >∼-10 ‰, with the majority of the data >0 ‰. This suggests that thermochemical sulphate reduction of seawater sulphate was the primary source and mechanism providing sulphide ions for mineralisation. A thermochemical sulphate reduction is consistent with the moderate to high temperature (>∼200 ℃) fluids identified as responsible for mineralisation in this study. Variation in δ^{34}S of sulphides is explicable by variation in background seawater sulphate δ^{34}S over the late Neoproterozoic period in which the Copperbelt deposits formed, when considering the long basin history and the potential different timings of deposit formation. Lighter δ^{34}S of mineralisation is most likely due to incorporation of preexisting sedimentary pyrite contained in the host sediments formed by bacterial sulphate reduction rather than a role for bacterial sulphate reduction during mineralisation itself, which occurred at temperatures too high for BSR to operate. Heavier values likely formed by closed system fractionation via thermochemical sulphate reduction.

Re concentrations in mainstage Cu sulphide mineralisation were too low for Re-Os dating to be performed. However, successful Re-Os dating on molybdenite samples from the Lumwana and Enterprise deposits was undertaken. Lumwana samples were dated at ∼535 to 525 Ma, consistent with available dates on uranium mineralisation at the deposit (Eglinger et al., 2013). The Enterprise deposit was dated at ∼523 Ma. These dates are broadly synchronous with other Re-Os data available for Copperbelt molybdenites (e.g. Kansanshi, Torrealday et al., 2000) as well as the later uranium event of Decrée et al. (2011), and reflect the importance of orogenesis for mineralisation in the Copperbelt and Domes Region.

4.2 Introduction

4.3 Sulphide samples and paragenesis

Sulphide samples were collected from a range of deposits, including the classic Copperbelt deposits of Nchanga, Konkola and Konkola North, basement hosted deposits of Lumwana and Samba, the late vein-hosted mineralisation at Kansanshi, and the exploration prospects of Kalumbila-Sentinel and Enterprise. This section gives a brief overview of the sulphide mineralogy of these orebodies.

4.3.1 Nchanga

Sampling for the Nchanga deposit was conducted from samples available at the University of Southampton from the Ph.D study of Ross McGowan (see McGowan et al., 2006). Nchanga is formed of two orebodies, a lower Cu orebody hosted within arkoses and shales (mostly altered to supergene mineralisation including malachite and copper oxides) and an upper Cu-Co orebody hosted within a feldspathic arenite (Fig. 4.1) and shales (McGowan et al., 2006). Disseminated 'stratiform' chalcopyrite, bornite, chalcocite and covellite from the upper orebody, massive chalcopyrite, bornite and chalcocite from a vein sample from the lower orebody, and late pyrite and chalcopyrite hosted in fracture zones and faults were sampled for this study.

FIGURE 4.1: Examples of sulphide mineralisation at the Nchanga deposit. Bornite, chalcopyrite and chalcocite stratiform mineralisation, Upper Orebody Feldspathic Quartzite (TFQ), Nchanga. For more examples of mineralisation at Nchanga see McGowan et al. (2006).

4.3.2 Konkola

The Konkola deposits are examples of argillite-hosted mineralisation within the Copperbelt Orebody Member. Whilst multiple different sulphide minerals are known at the orebody (Sweeney et al., 1986), the samples available for study contained disseminated pyrite and chalcopyrite within the 'Ore Shale' and pyrite and chalcopyrite recovered from quartz-carbonate veins in this unit (Fig. 4.2). The disseminated mineralisation is also hosted within or on the edges of mm to cm scale lenticular quartz-carbonate structures formed along laminations which may represent nodules similar to those of Muchez et al. (2008).

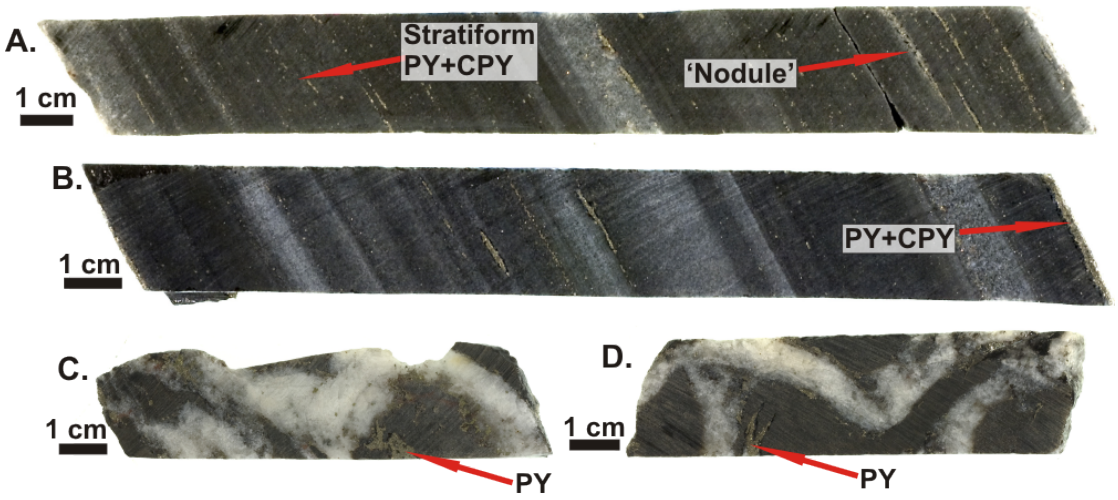

FIGURE 4.2: Examples of sulphide mineralisation at the Konkola deposit. A and B show stratiform pyrite and chalcopyrite mineralisation within the Copperbelt Orebody Member. Note strong local control by coarser laminae. Also note feature interpreted to possibly represent a flattened evaporite nodule pseudomorph similar to those of Muchez et al. (2008). C and D show pyrite and minor chalcopyrite hosted within, or disseminated close to quartz-carbonate veins within the Copperbelt Orebody Member.

4.3.3 Konkola North

Konkola North is similar to Konkola, with mineralisation hosted within the shales of the Copperbelt Orebody Member (Sutton and Maynard, 2005). However, in the drill cores sampled for this study, the mineralisation within the shales was essentially completely chalcocite. Chalcocite is not uncommon in Copperbelt orebodies, or indeed in the Konkola deposits (Selley et al., 2005; Sutton and Maynard, 2005; Sweeney et al., 1986). However, it is particularly difficult to identify whether the chalcocite at Konkola North is primary or an alteration product, since there is significant supergene mineralisation immediately underneath the Copperbelt Orebody Member caused by a conglomerate formation which allowed meteoric waters to percolate to depths of ~1400 m. This

conglomerate and other local units underlying the main orebody are characterised by extensive malachite and chrysocolla formation, and the chalcocite probably does not reflect the primary sulphide assemblage. Sampling recovered disseminated chalcocite, along with coarser chalcocite hosted in quartz-carbonate (± spectacular cobalt oxide mineralisation) veins (Fig. 4.3). Rare pyrite and chalcopyrite mineralisation was sampled from fractures, and structures morphologically similar to the nodules of Muchez et al. (2008) from slightly further up the sequence.

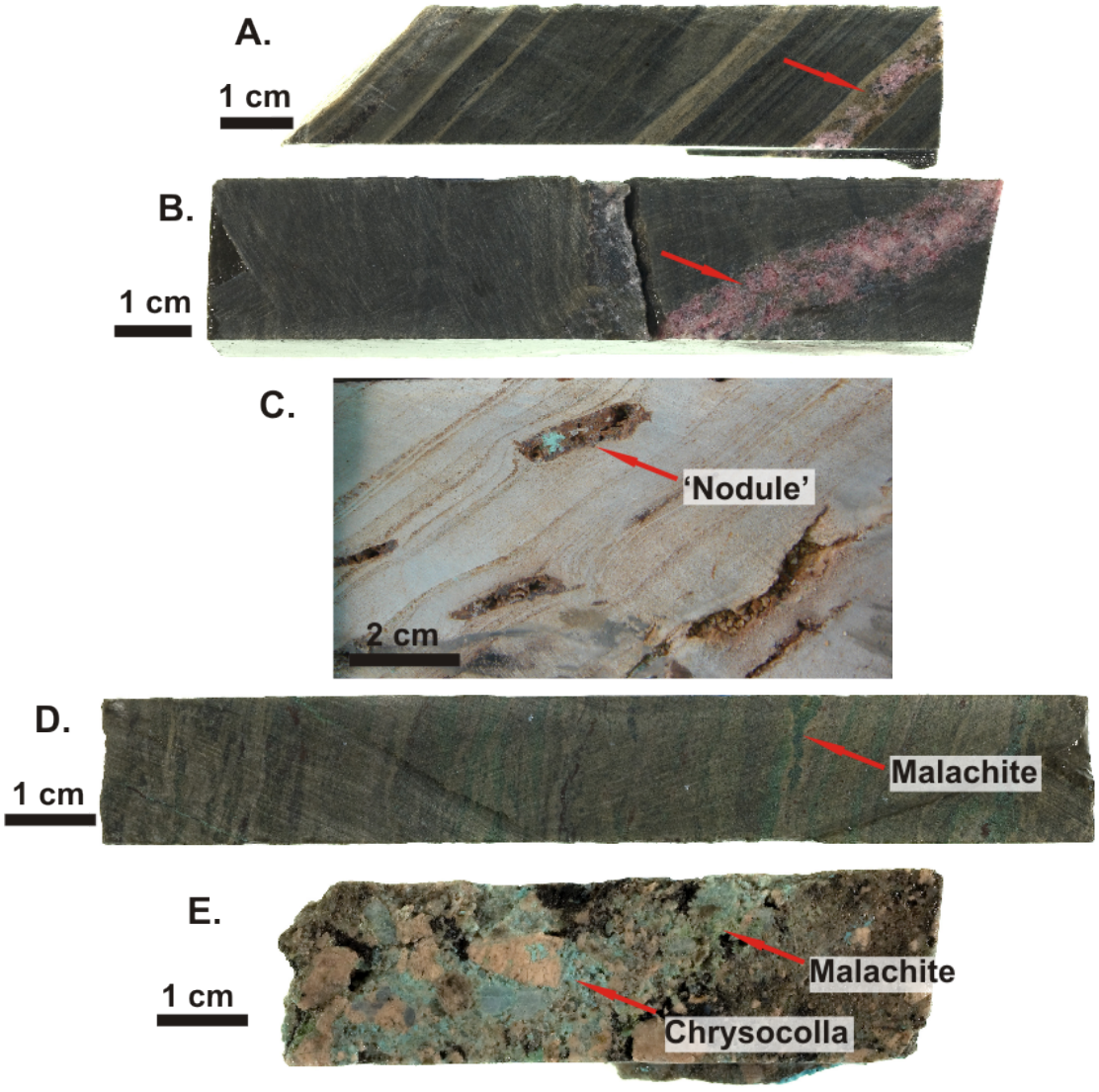

FIGURE 4.3: Examples of sulphide and oxide mineralisation at the Konkola North deposit. A) Fine chalcocite mineralisation in the Copperbelt Orebody member. Pink oxidised cobalt and chalcocite mineralisation exploits coarser laminae (red arrow). B) Oxidised cobalt and chalcocite vein cuts chalcocite-rich Copperbelt Orebody member (red arrow). C) Possible evaporite nodule pseudomorph (oxidised). D) Malachite-rich oxidised Copperbelt Orebody Member (1260.1 m depth). E) Malachite and chrysocolla mineralisation in conglomerate bed immediately underlying Copperbelt Orebody Member (1381.4 m depth).

4.3.4 Lumwana

The Lumwana deposits host Cu (± Co ± U) mineralisation within sheared basement at Mwombezhi Dome. Sulphide mineralisation is mostly chalcopyrite and bornite hosted within biotite-muscovite-quartz-kyanite schists ('Ore Schist') developed as shear zones in the granite gneiss of the basement dome (Bernau et al., 2013). Sulphide mineralisation pre-dates final movement on the shear zone, shown by sheared morphology and localisation into low strain areas such as the pressure shadows of kyanite porphyroblasts. Sulphide mineralisation is also locally hosted in discontinuous veins within the shear zone, interpreted to locally remobilise pre-existing disseminated sulphide mineralisation. Sampling included both shear zone and vein hosted bornite and chalcopyrite (Fig. 4.4) and molybdenite, while rare, was also recovered for Re-Os dating.

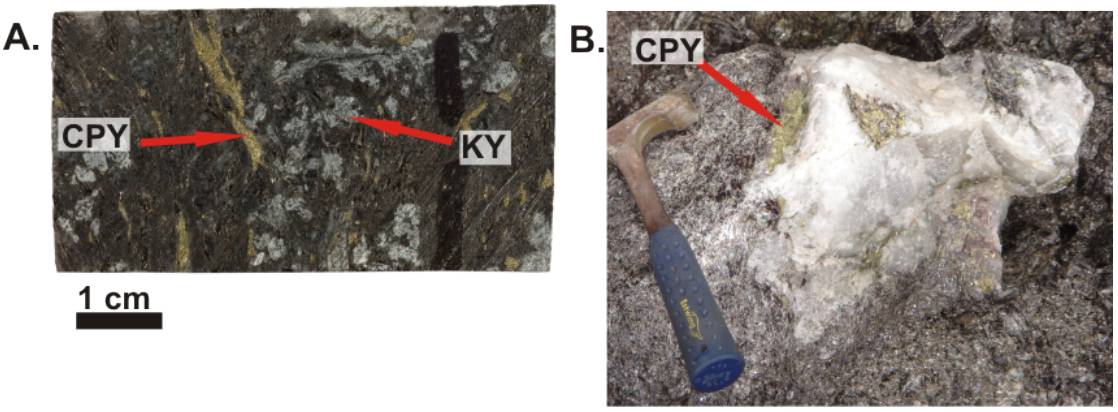

FIGURE 4.4: Examples of sulphide mineralisation at the Lumwana deposits. A) Sheared chalcopyrite in Malundwe Ore Schist, Lumwana. B) Chalcopyrite mineralisation in quartz veins, Lumwana open pit. For more examples of mineralisation at Lumwana see Bernau et al. (2013).

4.3.5 Samba

Samba is a deposit hosted within LS tectonites in the basement of the Kafue Anticline, west of Chambishi. The host rocks are metamorphosed igneous intrusives with rare relict extrusive/volcaniclastic textures, tentatively identified here as former lapilli tuffs (Wakefield, 1978). Wakefield (1978) interpreted this deposit as a metamorphosed porphyry, but recent work suggests it formed in a similar manner to Lumwana (Bernau et al., 2013). Host rocks include quartz-feldspar-biotite schists which show progressive feldspar destruction to quartz-biotite-muscovite schists. Biotite is present as both larger relict phenocrysts or early porphyroblasts/alteration phases, as well as fine-grained biotite aligned with schistosity along locally developed shear zones. Rarely amphibole is preserved, interpreted as relict phenocrysts. Sheared chalcopyrite ± minor bornite mineralisation is present within quartz-muscovite ± chlorite schists representing a sericite

± chlorite alteration assemblage (Fig. 4.5). Pyrite is common in these alteration zones. Further, later alteration occurs in the form of brown dolomite spotting which often pseudomorphs the earlier coarse biotite phases. The morphology of mineralisation indicates that the mineralisation event occurred prior to final shearing at the deposit. Sampling recovered chalcopyrite and pyrite from the mineralised zone.

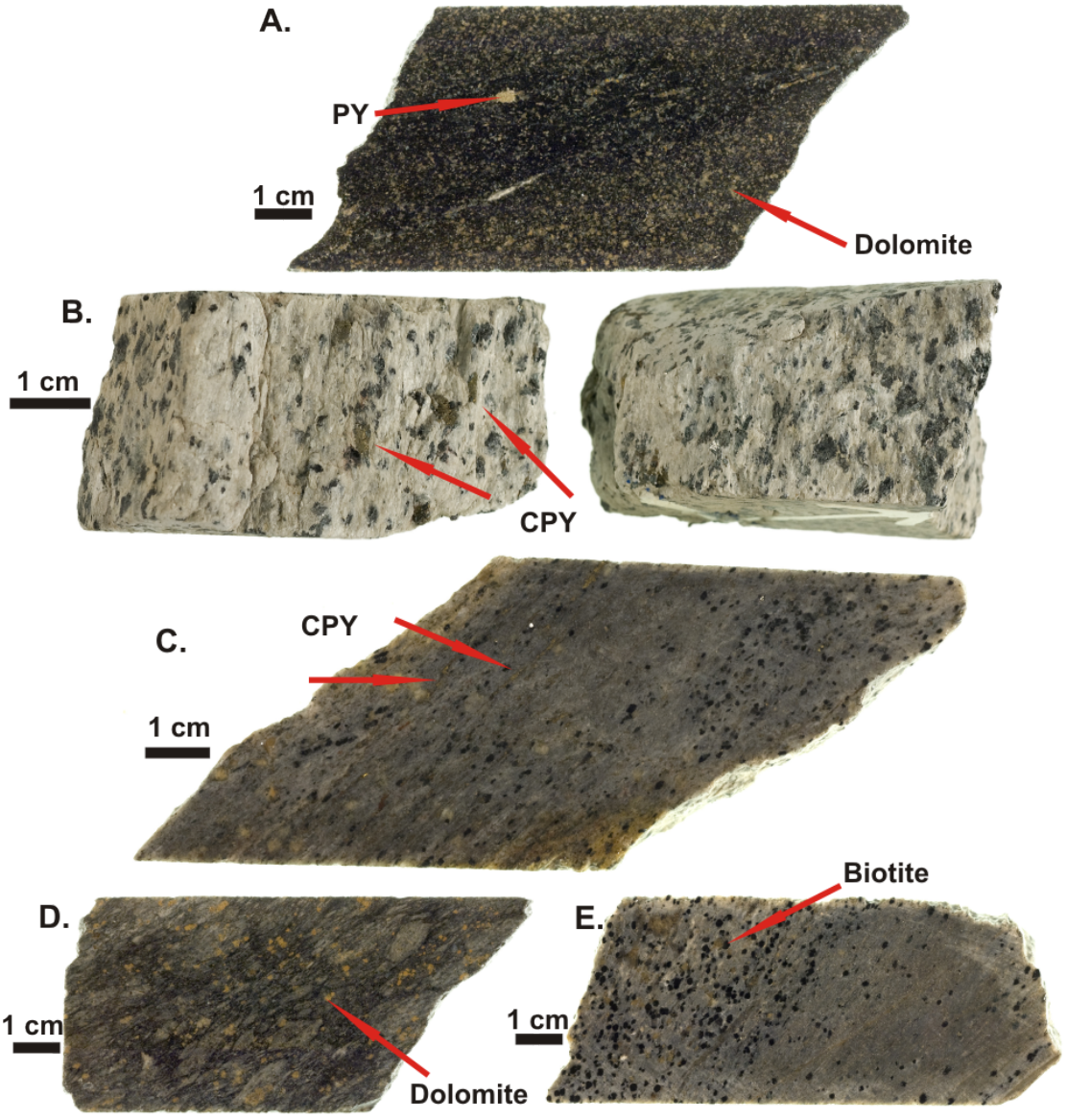

FIGURE 4.5: Examples of sulphide mineralisation at the Samba deposit. A) Biotite-chlorite-muscovite schist with dolomite spotting and minor pyrite. B and C) Sheared pyrite and chalcopyrite mineralisation within quartz-biotite-sericite-chlorite schist. D) Light brown dolomite spotting alteration in metavolcaniclastics. E). Quartz-muscovite-biotite schist with minor pyrite

4.3.6 Kansanshi

Kansanshi is a post-kinematic vein-hosted deposit near Solwezi Dome, comprising massive chalcopyrite and pyrite mineralisation (± molybdenite) within metre to tens-of-metres scale quartz-carbonate veins. Disseminated mineralisation locally extends into the host rocks around these veins (Broughton et al., 2002; Torrealday et al., 2000). Sampling undertaken at Kansanshi included pyrite and chacopyrite from the veins and disseminated mineralisation (Fig. 4.6). The host rocks for Kansanshi have been correlated as part of the Mwashia subgroup (Broughton et al., 2002).

4.3.7 Kalumbila-Sentinel

The Kalumbila prospect, currently named Sentinel by First Quantum Minerals (FQM), contains Cu (± Ni ± Co) mineralisation within a folded phyllite situated on the edge of the Kabompo Dome. Stratigraphic correlations are uncertain, but it has been suggested that this phyllite represents a metamorphosed stratigraphic equivalent of the Copperbelt Orebody Member (Steven and Armstrong, 2003). Sampling was conducted on recent drill cores from a copper-rich part of the orebody. Sulphide mineralisation is hosted as minor disseminations and within pre-kinematic carbonate (± quartz ± muscovite) veins which are typically oriented along the fabric of the phyllite, and are folded in a similar manner. These veins show a striking similarity to the veining described at Nkana by Brems et al. (2009). This mainstage mineralisation also cuts the host rock fabric, associated with bleaching ± carbonate-muscovite alteration, suggesting remobilisation of early mineralisation, or that the mineralisation event continued during compression. Minor coarse post-kinematic quartz-carbonate veining which cut the deposit, also shows sulphide mineralisation. Sulphide mineralisation is typically chalcopyrite and pyrite, with rare pyrrhotite (Fig. 4.7).

4.3.8 Enterprise

Enterprise is a post-kinematic vein-hosted deposit containing nickel sulphide mineralisation with minor Cu sulphides at Kabompo Dome. At the time of sampling, drilling of the deposit was only beginning (4 drill holes), and so limited material was available. Sulphide sampling was undertaken from veins and masses of mineralisation found in clots and alteration zones, comprising nickeliferous pyrite, vaesite and a single sample of molybdenite for Re-Os dating (Figs. 4.8). Since sampling was undertaken, millerite and other rare nickel sulphide phases have been identified, but were not available for this study (First Quantum Minerals Enterprise Nickel Prospect geological summary).

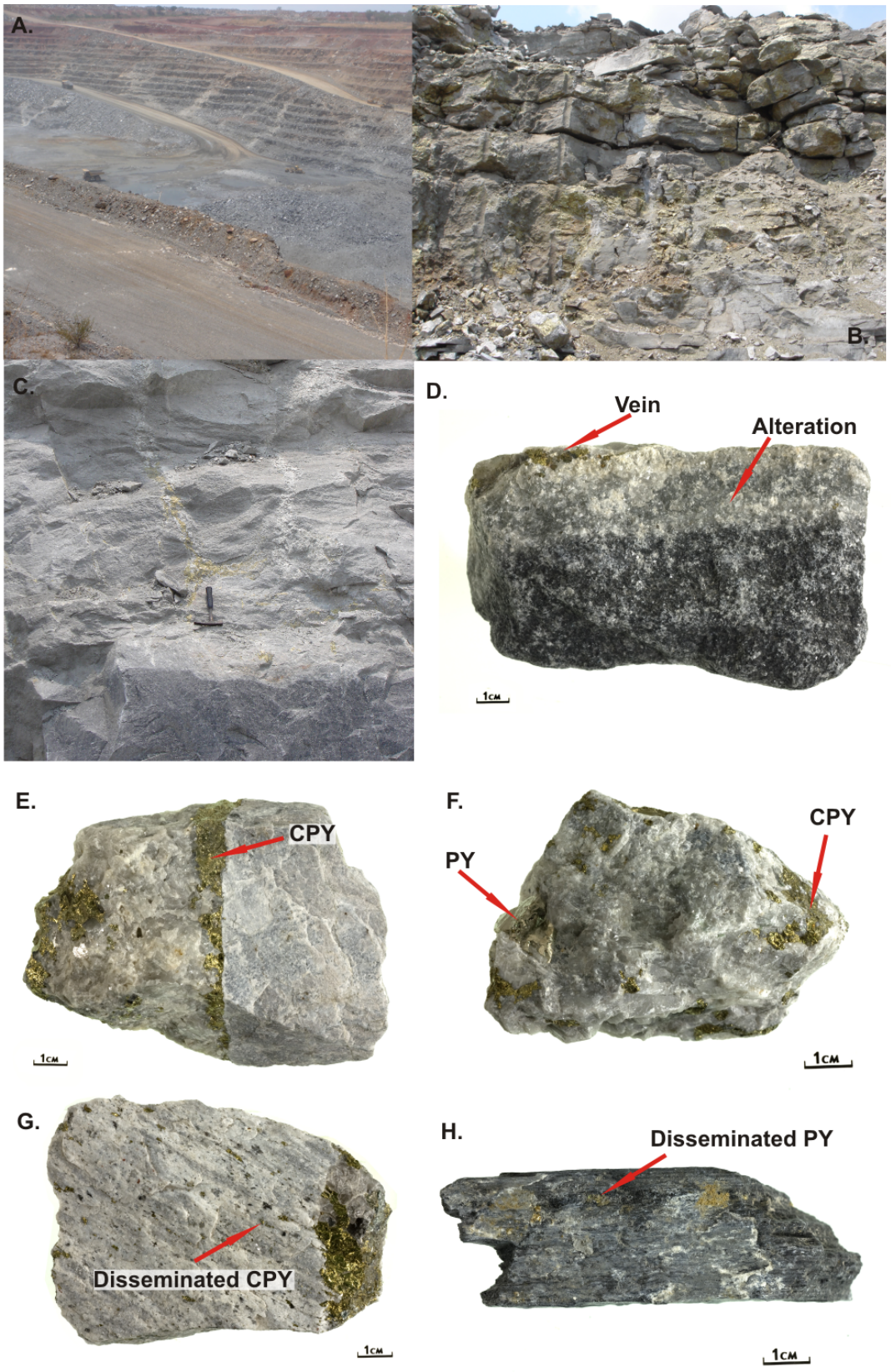

FIGURE 4.6: Examples of sulphide mineralisation at the Kansanshi deposit. A) Subvertical post-kinematic veins hosting mineralisation at Kansanshi open pit. B) Heavily chalcopyrite mineralised pit face (Field of view ~6 m). C) Local mineralised discordant quartz-carbonate vein cuts host rock. D) Bleaching and albite alteration in host marble on edge of vein. E) Quartz-carbonate vein hosts chalcopyrite. F) Pyrite and chalcopyrite mineralisation in quartz-carbonate vein. G) Disseminated chalcopyrite mineralisation in alteration zone on edge of vein. H) Disseminated pyrite mineralisation in host siltstone.

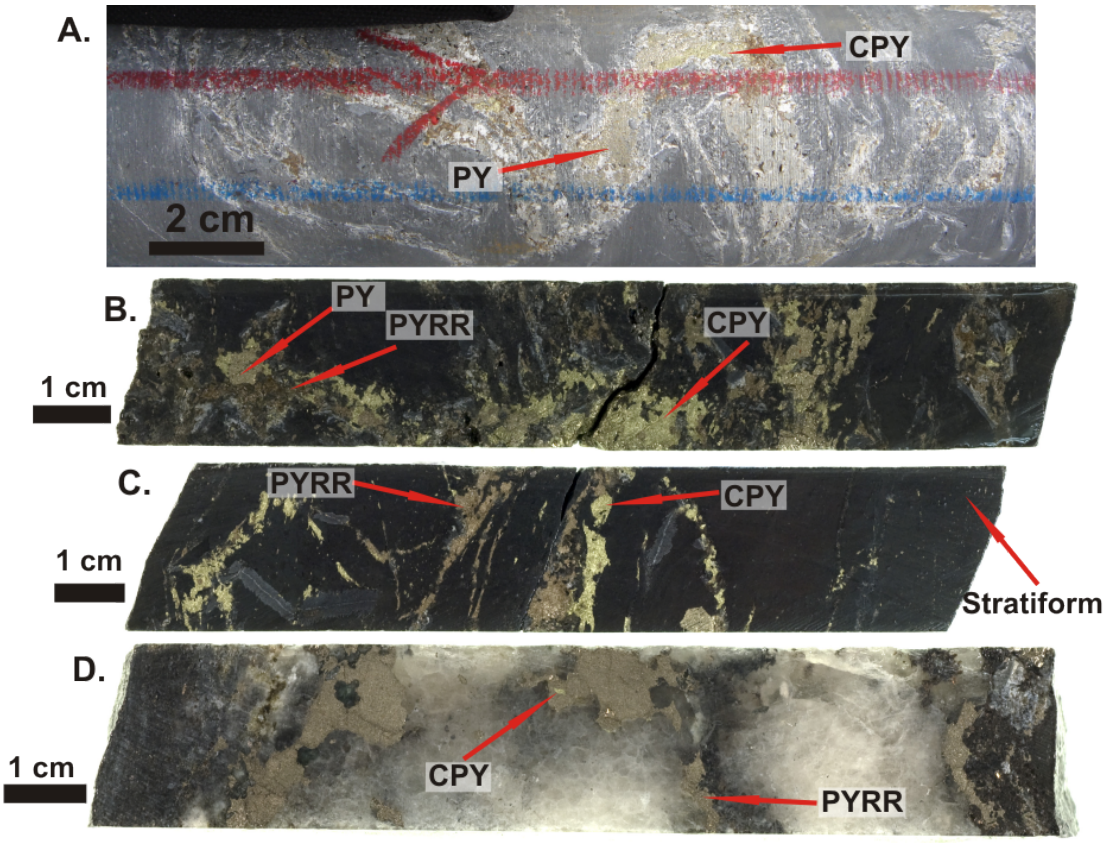

FIGURE 4.7: Examples of sulphide mineralisation at the Kalumbila-Sentinel prospect. A) Mainstage pyrite-chalcopyrite mineralisation in pre-kinematic carbonate veins, carbonaceous phyllite. B) Mainstage chalcopyrite-pyrite-pyrrhotite mineralisation associated with discordant bleaching ± carbonate-muscovite alteration in carbonaceous phyllite. C) Mainstage chalcopyrite and pyrrhotite mineralisation associated with bleaching ± carbonate-muscovite alteration in carbonaceous phyllite, minor stratiform mineralisation. D) Pyrrhotite mineralisation with minor chalcopyrite hosted by post-kinematic quartz vein.

Extremely pervasive alteration around the veins makes identification of lithology difficult, but the majority of mineralisation occurs in veins or alteration zones within black shales and more rarely carbonates. These units are part of the Katangan Sequence, and have been variably tentatively correlated with the Lower Roan or Mwashia Subgroup (First Quantum Minerals Enterprise Nickel Prospect geological summary). The deposit shows significant spacial correlation with mafic units in the sequence (highly altered), perhaps accounting for its nickel-rich mineralogy. The veining which hosts the mineralisation consists of quartz-kyanite ± talc veins, with similar alteration assemblages also containing magnesite. Nickel grades locally reach up to 14.5 %. Phlogopite is a common alteration product up to tens of metres around veins (First Quantum Minerals Enterprise Nickel Prospect geological summary).

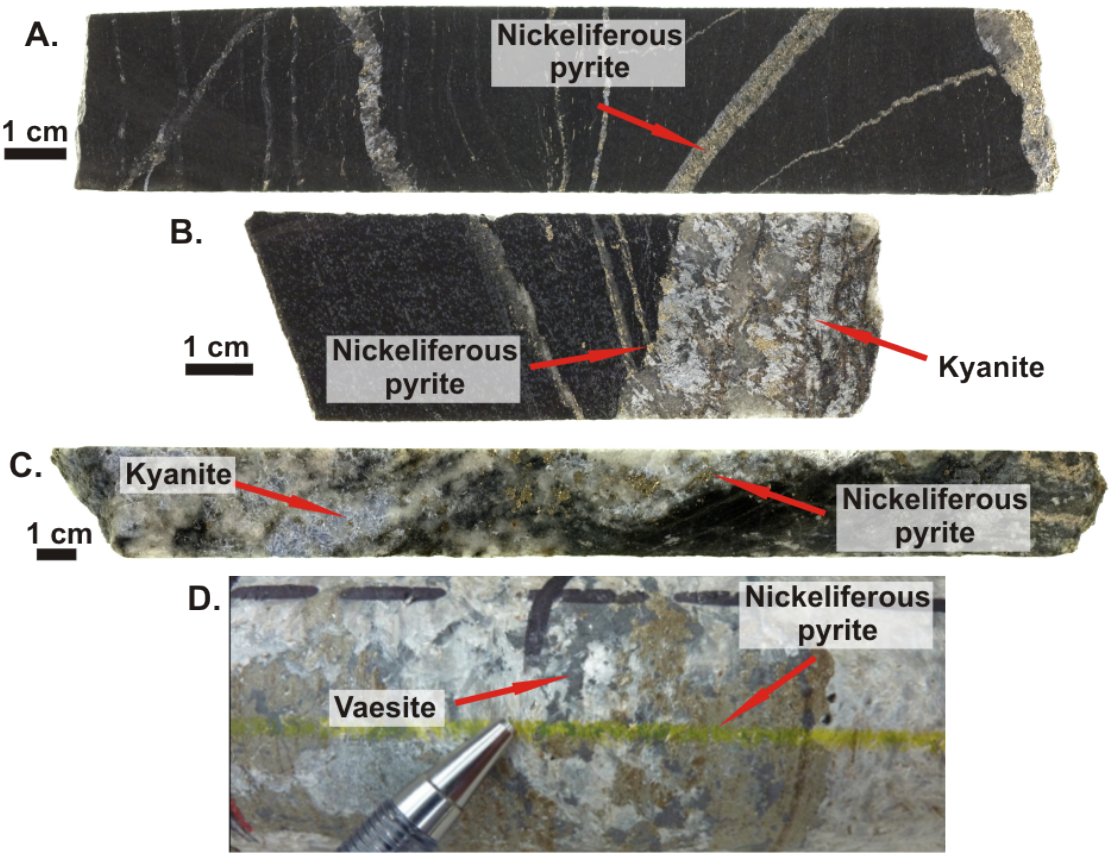

FIGURE 4.8: Examples of sulphide mineralisation at the Enterprise prospect. A) Nickeliferous pyrite in quartz-kyanite-talc veins cutting black shale. B) Nickeliferous pyrite in quartz-kyanite-talc veins exploiting and cutting black shale foliation. C) Nickeliferous pyrite in quartz-kyanite-talc vein in heavily altered black shale. D) Nickeliferous pyrite and vaesite in talc-kyanite vein and alteration zone.

4.4 Rare earth and trace elemental compositions of sulphides

Rare earth element (REE) profiles and trace elemental compositions of rocks and minerals can be useful in characterising samples as well as revealing information about formational and post-formational processes that have affected the samples. This section presents (to the author's knowledge) the first examples of trace element and REE data obtained from a suite of sulphide samples from the Central African Copperbelt (shown in tables 4.1 to 4.16).

TABLE 4.1: Elemental data for Konkola pyrite samples (ppm)

	KON149A 1412.65	KON149A 1412.80	KON149A 1420.65	KON149A 1421.20	KON149A 1421.30
Mineralogy	PY	PY	PY	PY	PY
Setting	Nodule	Stratiform	Stratiform	Stratiform	Vein
Na	101	107	164	107	152
Mg	718	825	1510	1010	470
Al	327	460	618	455	202
K	236	299	447	375	181
Ca	1110	1050	2180	1290	680
Sc	0.348	0.27	0.41	0.150	0.092
Ti	22.3	24.2	40.4	28.5	14.4
V	6.3	4.8	7.6	6.3	5.3
Cr	0.75	0.686	1.5	0.48	0.22
Mn	22.0	21.3	49	34.9	24.0
Co	3500	3850	5800	13700	17700
Ni	157	143	130	59.7	1020
Zn	6.5	3.9	11.7	249	43.4
Ga	0.248	0.259	0.35	0.19	0.14
Ge	3.88	3.7	3.56	3.7	3.53
As	118	131	165	569	750
Se	6.6	5.69	6.1	50	60.7
Sr	4.41	3.9	5.37	3.42	1.57
Zr	8.1	5.47	6.45	10.0	12.8
Nb	0.10	0.058	0.09	0.130	0.08
Mo	5.7	4.08	8.66	4.93	8.08
Ag	0.101	0.123	0.111	0.26	0.12
Cd	0.014	0.011	0.012	0.25	0.05
Sn	0.149	0.119	0.189	0.159	0.20
Sb	0.63	0.92	0.71	0.57	0.381
La	18.2	26.1	23.3	3.29	0.63
Ce	36.4	53.6	47.0	4.39	0.91
Nd	15.1	22.0	19.5	1.48	0.376
Sm	2.54	3.59	3.33	0.229	0.082
Eu	0.249	0.330	0.326	0.029	0.0124
Gd	1.42	1.81	1.89	0.201	0.096
Tb	0.138	0.163	0.184	0.031	0.018
Dy	0.607	0.627	0.805	0.204	0.131
Ho	0.098	0.086	0.122	0.042	0.032
Er	0.260	0.20	0.309	0.135	0.114
Yb	0.247	0.176	0.265	0.161	0.161
Lu	0.042	0.030	0.041	0.031	0.029
Hf	0.299	0.202	0.241	0.364	0.442
W	0.036	0.027	0.037	0.105	0.293
Re	0.008	0.008	0.046	0.035	0.038
Au	0.06	0.07	0.08	0.10	0.09
Pb	7.83	11.4	9	5.3	2.92
Bi	6.80	8.8	7.1	4.35	2.84
Th	9.98	6.87	11.1	8.8	8.10
U	1.44	1.13	1.94	1.10	1.07

TABLE 4.2: Elemental data for Konkola chalcopyrite samples (ppm)

	KON149A 1420.65	KON149A 1421.20	KON149A 1421.30
Mineralogy	CPY	CPY	CPY
Setting	Stratiform	Stratiform	Vein
Na	46	31	36
Mg	940	470	1230
Al	500	77	304
K	570	148	284
Ca	1360	900	1950
Sc	0.202	0.044	0.16
Ti	24.1	5.5	20.3
V	28	29	7.46
Cr	0.69	0.23	0.55
Mn	36.1	26.9	64.1
Co	3170	8200	3540
Ni	43.5	28.4	28.4
Zn	217	69	112
Ga	0.36	0.86	1.09
Ge	6.7	7.68	4.2
As	65	321	148
Se	18	129	203
Sr	1.87	2.05	2.30
Zr	4.22	3.86	4.16
Nb	0.169	0.19	0.088
Mo	4.61	2.82	1.19
Ag	1.46	1.30	2.00
Cd	0.261	0.10	0.17
Sn	17.8	5.07	8.33
Sb	0.300	0.353	0.248
La	1.89	0.33	14.9
Ce	3.72	0.529	28.1
Nd	1.66	0.24	12.1
Sm	0.33	0.055	2.09
Eu	0.040	0.011	0.221
Gd	0.28	0.071	1.28
Tb	0.040	0.013	0.102
Dy	0.37	0.6	0.5
Ho	0.056	0.070	0.046
Er	0.119	0.063	0.12
Yb	0.109	0.097	0.072
Lu	0.019	0.017	0.012
Hf	0.170	0.15	0.014
W	0.054	0.10	0.216
Re	0.134	0.123	0.005
Au	0.75	0.79	0.38
Pb	2.4	3.0	4.7
Bi	2.5	4	3.6
Th	10.2	0.575	5.18
U	2.46	0.155	0.197

TABLE 4.3: Elemental data for Konkola North pyrite and chalcopyrite samples (ppm)

	KN103 821.30	KN103 938.7	KN103 821.30	KN103 928.5
Mineralogy	PY	PY	CPY	CPY
Setting	Stratiform	Late Fracture	Stratiform	Stratiform
Na	69	97	27	37
Mg	790	232	517	129
Al	406	560	308	219
K	320	240	260	320
Ca	1410	58	840	23.5
Sc	0.280	0.46	0.16	0.081
Ti	9.5	17.8	7.8	13
V	2.44	14.5	3.00	31.8
Cr	0.76	0.8	0.54	0.46
Mn	54.0	4.3	32.1	0.97
Co	272000	27400	37000	21600
Ni	390	97	220	84
Zn	39.5	8.4	42.3	9.8
Ga	0.387	0.68	0.369	0.172
Ge	0.98	4.4	3.55	8.4
As	109	418	164	321
Se	3.5	39	4.2	43
Sr	2.17	0.64	1.03	0.105
Zr	8.6	4.2	5.8	5.59
Nb	0.020	0.078	0.012	0.200
Mo	14.6	3.6	3.7	1.11
Ag	1.31	1.07	0.72	1.44
Cd	0.05	0.076	0.03	BD
Sn	1.17	0.16	3.77	0.59
Sb	2.00	0.19	0.28	0.17
La	2.59	0.625	2.19	2.38
Ce	5.68	1.22	4.81	4.76
Nd	2.56	0.64	2.10	2.12
Sm	0.48	0.184	0.37	0.469
Eu	0.058	0.043	0.049	0.065
Gd	0.31	0.26	0.26	0.48
Tb	0.0361	0.050	0.029	0.07
Dy	0.203	0.37	0.150	0.54
Ho	0.040	0.0763	0.025	0.077
Er	0.118	0.236	0.077	0.146
Yb	0.160	0.244	0.098	0.135
Lu	0.0281	0.043	0.016	0.022
Hf	0.351	0.140	0.208	0.248
W	0.066	0.036	0.029	0.036
Re	0.003	0.199	0.003	0.19
Au	0.220	0.19	0.531	0.55
Pb	260	17	20.0	0.9
Bi	1.38	31.3	0.89	2.52
Th	1.47	2.55	1.15	2.49
U	0.269	19.1	0.241	1.06

TABLE 4.4: Elemental data for Konkola North chalcocite samples (ppm)

	KN103 928.5	KN54-191 1368.7	KN54-191 1372.5
Mineralogy	CCC	CCC	CCC
Setting	Stratiform	Vein	Vein
Na	35	66	124
Mg	215	334	251
Al	459	365	480
K	467	360	410
Ca	20	322	276
Sc	0.156	0.158	0.27
Ti	24.1	52	143
V	29	64	106
Cr	0.78	2.5	2.0
Mn	1.32	12.3	8.8
Co	12000	1800	29.8
Ni	61	1.31	0.57
Zn	9.7	8.3	9.9
Ga	0.26	0.26	0.67
Ge	5.76	2.9	3.36
As	234	BD	3.4
Se	158	15.8	129
Sr	0.148	2.57	14.5
Zr	5.5	5.6	11.0
Nb	0.121	0.209	0.88
Mo	1.43	20.8	35.0
Ag	7.1	2.70	5.90
Cd	0.003	0.014	0.026
Sn	0.873	0.377	0.452
Sb	0.16	0.50	0.648
La	2.45	0.94	0.67
Ce	4.83	1.73	1.14
Nd	2.11	0.73	0.54
Sm	0.39	0.150	0.14
Eu	0.051	0.021	0.025
Gd	0.30	0.114	0.152
Tb	0.038	0.014	0.024
Dy	0.61	0.55	0.43
Ho	0.082	0.06	0.053
Er	0.117	0.034	0.088
Yb	0.121	0.029	0.083
Lu	0.021	0.005	0.014
Hf	0.251	0.175	0.30
W	0.035	0.594	0.47
Re	0.34	0.060	0.045
Au	0.70	0.06	0.30
Pb	6.1	97	14
Bi	3.00	35.1	97
Th	2.5	2.82	9.4
U	0.992	3.64	9.37

TABLE 4.5: Elemental data for Nchanga chalcopyrite samples (ppm)

	NOP108 TFQ	NOP109 TFQ	NOP124 TFQ	NOP128 TFQ	BH7-741 TFQ
Mineralogy	CPY	CPY	CPY	CPY	CPY
Setting	Stratiform	Stratiform	Stratiform	Vein	Vein
Na	25	25.3	83	18	28
Mg	498	469	76.4	220	7.20
Al	72	48.8	252	111	12.8
K	77.4	75.6	153	91.4	37.3
Ca	1000	1160	178	681	155
Sc	0.303	0.275	0.135	0.115	0.229
Ti	1.0	0.374	3.06	2.93	0.203
V	3.04	6.17	9.78	6.93	4.53
Cr	0.58	0.23	1.20	0.284	0.201
Mn	29.4	29.4	3.94	17.2	48.0
Co	12.5	101	19.6	1630	1460
Ni	0.31	0.65	0.278	6.18	1.14
Zn	5.1	47.6	14.9	48.3	1110
Ga	1.59	4.46	0.253	1.92	10.41
Ge	3.22	5.16	3.15	4.73	4.69
As	BD	BD	BD	BD	0.002
Se	0.6	1.38	BD	12.6	6.30
Sr	1.05	2.17	0.391	3.58	2.53
Zr	0.96	1.23	1.41	0.454	0.163
Nb	0.009	0.017	0.016	0.019	0.011
Mo	2.55	5.56	6.97	1.24	8.52
Ag	10.9	7.24	0.79	7.61	4.87
Cd	0.057	0.234	0.078	0.304	8.18
Sn	35.2	95.1	45.5	105	102
Sb	0.66	0.94	0.160	0.960	0.218
La	1.13	0.67	0.488	0.087	0.043
Ce	2.32	1.46	1.02	0.211	0.111
Nd	0.96	0.625	0.494	0.136	0.078
Sm	0.159	0.119	0.166	0.054	0.027
Eu	0.017	0.014	0.031	0.007	0.005
Gd	0.089	0.090	0.253	0.066	0.045
Tb	0.009	0.013	0.053	0.011	0.008
Dy	0.048	0.074	0.397	0.078	0.070
Ho	0.008	0.013	0.088	0.015	0.016
Er	0.019	0.034	0.269	0.050	0.056
Yb	0.023	0.033	0.316	0.054	0.077
Lu	0.003	0.005	0.066	0.008	0.012
Hf	0.033	0.034	0.063	0.01	0.003
W	0.020	0.004	0.034	0.003	0.006
Re	BD	0.014	BD	0.021	0.011
Au	0.21	0.058	0.188	0.026	0.042
Pb	3.9	3.61	3.04	6.85	4.98
Bi	56	38.1	0.360	39.4	0.140
Th	0.95	0.189	0.58	0.20	0.20
U	0.227	0.086	0.128	0.460	0.468

TABLE 4.6: Elemental data for Nchanga chalcopyrite and bornite samples (ppm)

	BH14	Lower Orebody Arkose	NOP99 TFQ
Mineralogy	CPY	CPY	BN
Setting	Late fracture	Vein	Stratiform
Na	41.6	39.8	29.0
Mg	266	4.93	17.7
Al	267	22.8	69.7
K	108	31	39.9
Ca	546	BD	24.3
Sc	0.169	0.014	0.247
Ti	2.47	BD	2.24
V	10.4	7.9	9.02
Cr	2.09	0.14	0.414
Mn	3.72	0.20	14.3
Co	55800	13.3	15.3
Ni	3710	0.17	0.542
Zn	9.56	22.8	5.56
Ga	1.07	1.20	0.183
Ge	3.89	3.4	1.88
As	10.6	1.2	3.75
Se	188	42	5.22
Sr	5.81	0.0422	0.073
Zr	7.87	0.036	0.334
Nb	0.022	0.033	0.011
Mo	2.59	0.089	4.32
Ag	0.718	5.6	149
Cd	0.103	0.072	0.036
Sn	8.81	8.0	25.5
Sb	5.33	0.09	11.8
La	3.50	0.015	0.424
Ce	5.26	0.025	0.883
Nd	2.18	0.016	0.442
Sm	0.406	0.005	0.103
Eu	0.073	0.001	0.015
Gd	0.291	0.006	0.106
Tb	0.033	0.001	0.016
Dy	0.158	0.021	0.125
Ho	0.023	0.003	0.027
Er	0.053	0.007	0.077
Yb	0.052	0.004	0.080
Lu	0.010	0.001	0.014
Hf	0.228	0.002	0.015
W	0.008	0.014	0.128
Re	0.014	0.003	0.013
Au	0.222	0.10	0.017
Pb	4.79	2.83	17.3
Bi	24.3	59	243
Th	2.10	0.062	0.07
U	0.83	0.051	1.64

TABLE 4.7: Elemental data for Nchanga pyrite, carrolite and chalcocite samples (ppm)

	BH105	NOP108 TFQ	NOP123 TFQ	NOP124 TFQ	Lower Orebody Arkose
Mineralogy	PY	CARR	CARR	CARR	CCC
Setting	Late fracture	Stratiform	Stratiform	Stratiform	Vein
Na	166	90	109	59.0	31.8
Mg	12.8	161	840	115	13.3
Al	273	302	350	310	261
K	17.0	270	265	240	46.6
Ca	69	740	1170	850	22.2
Sc	1.83	0.32	0.62	0.22	0.14
Ti	3.53	2.7	19.4	4.71	1.41
V	13.8	6.10	10.3	27.6	10.3
Cr	0.21	1.37	2.6	1.84	0.077
Mn	16.1	10.3	30.0	10.9	0.570
Co	4330	336000	310000	736000	8.29
Ni	314	3930	107	417	0.244
Zn	88.5	7.1	10.3	41.6	2.53
Ga	1.07	0.19	0.601	0.174	0.991
Ge	4.33	0.31	0.57	1.10	0.376
As	85	7.4	32	101	1.02
Se	BD	0.9	7.5	1.61	56.4
Sr	0.238	0.91	5.59	11.4	4.06
Zr	1.18	4.63	6.90	6.25	0.157
Nb	0.085	0.005	0.023	0.008	0.003
Mo	0.97	36.3	30.0	27.3	0.520
Ag	1.56	12.8	2.57	1.24	134
Cd	0.008	0.114	0.044	0.798	0.012
Sn	0.39	5.27	1.15	7.57	7.12
Sb	0.191	21.7	8.21	44.5	1.18
La	3.90	3.97	2.80	1.56	1.32
Ce	6.97	8.69	6.14	3.21	2.13
Nd	3.41	4.23	2.90	1.36	1.13
Sm	1.10	0.92	0.675	0.250	0.233
Eu	0.462	0.091	0.101	0.032	0.027
Gd	1.31	0.840	0.66	0.237	0.237
Tb	0.200	0.129	0.098	0.031	0.034
Dy	1.26	0.83	0.595	0.490	0.244
Ho	0.255	0.158	0.110	0.060	0.042
Er	0.77	0.45	0.309	0.090	0.096
Yb	0.745	0.39	0.27	0.095	0.066
Lu	0.108	0.056	0.040	0.018	0.009
Hf	0.0282	0.225	0.273	0.219	0.00584
W	0.121	0.031	0.020	0.006	0.064
Re	0.007	0.011	0.027	0.034	0.018
Au	0.20	0.24	0.03	0.156	0.287
Pb	4.5	660	12	267	4.66
Bi	1.46	119	2.03	4.44	1130
Th	0.229	1.87	6.2	0.84	0.26
U	12.6	1.25	2.82	0.233	2.66

TABLE 4.8: Elemental data for Lumwana chalcopyrite samples (ppm)

	SP-002	SP-006	LUM0287 71.05	MLW0291 27.14	MLW0291 28.00
Mineralogy	CPY	CPY	CPY	CPY	CPY
Setting	Sheared	Sheared	Sheared	Sheared	Vein
Na	23	20.5	35	15.5	25
Mg	670	103	1120	661	710
Al	660	330	1680	750	840
K	18	75	750	340	540
Ca	114	21	27	13.2	2.2
Sc	0.027	0.157	0.44	0.111	0.113
Ti	0.87	7.6	72	25.3	43
V	4.0	11.5	8.1	7.6	10.6
Cr	0.36	0.24	3.6	1.02	1.4
Mn	3.1	5.1	5.1	5.49	6.3
Co	70	1220	500	710	490
Ni	29	118	5100	153	292
Zn	94	282	171	45	13.4
Ga	1.02	2.39	2.9	0.577	0.62
Ge	2.56	4.3	3.3	3.3	3.5
As	BD	BD	BD	BD	BD
Se	6.7	10.4	7.4	2.1	16.9
Sr	0.33	0.38	0.154	0.398	0.173
Zr	4.1	1.03	5.9	0.38	0.122
Nb	0.013	0.052	0.17	0.053	0.114
Mo	12.8	0.26	0.215	0.274	7.5
Ag	2.61	0.45	2.34	3.79	2.94
Cd	0.50	0.20	0.33	0.33	0.252
Sn	27.6	23.4	25.3	11.6	9.0
Sb	0.26	0.08	0.105	0.822	0.87
La	7.8	80	0.111	172	37.8
Ce	17.2	140	0.37	393	80
Nd	7.1	50.4	0.17	166	32.0
Sm	1.67	7.2	0.049	29.8	6.0
Eu	0.332	0.320	0.007	0.97	0.563
Gd	1.67	5.14	0.063	22	4.89
Tb	0.287	0.451	0.011	2.00	0.638
Dy	1.90	1.71	0.078	7.34	3.30
Ho	0.356	0.189	0.015	0.84	0.515
Er	0.97	0.270	0.05	1.21	1.17
Yb	0.62	0.078	0.031	0.26	0.58
Lu	0.077	0.015	0.005	0.040	0.064
Hf	0.121	0.044	0.195	0.042	0.017
W	0.023	0.027	0.047	0.063	0.049
Re	0.010	0.007	0.002	0.068	0.571
Au	0.039	0.09	0.17	8.1	0.37
Pb	4.9	6.70	12.2	25	19
Bi	12.6	0.69	0.951	7.64	20.5
Th	34.2	2.85	2.55	1.11	0.38
U	9.10	0.884	8.62	0.415	167

TABLE 4.9: Elemental data for Lumwana bornite samples (ppm)

	MLW0291 27.14	MLW0291 28.00	EQMAL083 94.43
Mineralogy	BN	BN	BN
Setting	Sheared	Vein	Vein
Na	19	1	4.2
Mg	56	5.35	450
Al	76	23.0	440
K	74	15	28
Ca	BD	BD	1110
Sc	0.017	0.010	0.10
Ti	1.48	0.6	2.5
V	18.2	2.6	5.98
Cr	0.16	0.07	0.6
Mn	0.90	0.21	4.7
Co	80	8.1	142
Ni	16.8	5.6	20.1
Zn	20.8	6.5	3.5
Ga	0.064	0.026	0.236
Ge	2.6	1.31	1.42
As	BD	0.1	7.8
Se	2.4	11.5	231
Sr	0.063	0.030	0.660
Zr	0.34	0.089	0.231
Nb	0.035	0.006	0.009
Mo	0.14	0.06	336
Ag	5.3	7.4	4.07
Cd	0.91	0.86	1.40
Sn	5.19	3.54	4.38
Sb	0.24	0.024	0.074
La	23.5	13.0	0.71
Ce	55.4	22.5	1.84
Nd	24.2	9.05	1.28
Sm	4.31	1.51	0.56
Eu	0.138	0.089	0.169
Gd	3.09	1.26	0.73
Tb	0.294	0.142	0.119
Dy	1.26	0.66	0.69
Ho	0.147	0.098	0.125
Er	0.194	0.199	0.33
Yb	0.052	0.086	0.22
Lu	0.011	0.009	0.030
Hf	0.0209	0.00456	0.00733
W	0.030	0.015	0.311
Re	0.036	0.007	0.401
Au	9.4	0.033	10.9
Pb	19.7	30	51
Bi	18.8	34.8	12.4
Th	0.41	0.37	0.10
U	0.099	0.468	11.2

TABLE 4.10: Elemental data for Samba sulphide samples (ppm)

	SAM001 105.30	SAM004A 74.60	SAM004A 74.60
Mineralogy	PY	PY	CPY
Setting	Main ore zone	Main ore zone	Main ore zone
Na	100	620	53
Mg	460	670	191
Al	620	920	196
K	211	160	130
Ca	1120	1730	95
Sc	0.65	0.74	0.38
Ti	204	25.6	3.2
V	3.0	30	34
Cr	0.60	0.29	0.28
Mn	29.1	32.3	3.54
Co	440	4.51	11300
Ni	58	5.9	32.6
Zn	7.0	118	9.46
Ga	0.232	0.377	0.120
Ge	4.0	7.24	11.8
As	9.4	BD	52.3
Se	88	21	21.4
Sr	4.08	2.89	0.173
Zr	63.1	35.1	48.3
Nb	0.71	0.23	0.31
Mo	1.32	0.124	1.19
Ag	1.09	1.21	0.69
Cd	0.12	3.80	0.06
Sn	0.12	3.86	0.7
Sb	0.61	0.35	0.41
La	12.5	33.2	4.41
Ce	25.5	78	13.3
Nd	11.4	29.5	9.71
Sm	2.39	5.07	4.74
Eu	0.542	0.781	1.7
Gd	2.16	3.41	8.2
Tb	0.315	0.433	1.72
Dy	1.89	2.58	12.3
Ho	0.365	0.453	2.30
Er	1.10	1.20	5.53
Yb	1.11	0.98	2.74
Lu	0.189	0.168	0.373
Hf	1.94	1.16	1.71
W	0.133	0.13	0.56
Re	BD	0.058	0.14
Au	1.47	1.61	1.91
Pb	220	2.33	2.98
Bi	6.19	2.22	9.35
Th	8.10	22.1	9.64
U	1.96	9.3	459

TABLE 4.11: Elemental data for Kalumbila-Sentinel pyrite and pyrrhotite samples (ppm)

	KAL0195 76.6	KAL0195 88.7	KAL0195 113.0	KAL23 445.8
Mineralogy	PY	PY	PYRR	PYRR
Setting	Mainstage	Mainstage	Mainstage	Vein
Na	78	90	46	84.8
Mg	440	690	107	544
Al	420	640	91.0	568
K	152	163	58	436
Ca	58	215	34.2	396
Sc	0.039	0.055	0.032	0.25
Ti	6.8	6.6	2.18	45.0
V	2.7	5.10	3.7	6.9
Cr	0.47	0.54	0.21	1.7
Mn	6.7	10.8	10.4	39.9
Co	730	1180	2870	438
Ni	690	340	1760	695
Zn	49	83	7.6	4.35
Ga	1.41	1.48	0.19	0.24
Ge	3.8	3.8	5.7	5.9
As	30.6	46	1.3	BD
Se	13.9	14.9	16.1	8.3
Sr	1.04	1.87	0.176	0.206
Zr	3.1	1.07	3.70	0.044
Nb	0.025	0.029	0.034	0.117
Mo	0.87	1.06	1.52	0.55
Ag	0.46	0.51	0.52	0.033
Cd	0.068	0.14	0.017	BD
Sn	10.2	10.0	0.42	0.071
Sb	0.94	0.71	0.22	0.012
La	0.614	1.74	0.413	4.24
Ce	1.34	3.78	0.89	8.2
Nd	0.618	1.77	0.43	3.74
Sm	0.135	0.399	0.089	0.65
Eu	0.022	0.063	0.012	0.080
Gd	0.10	0.34	0.085	0.57
Tb	0.014	0.040	0.013	0.059
Dy	0.066	0.21	0.074	0.265
Ho	0.009	0.027	0.014	0.038
Er	0.022	0.059	0.037	0.079
Yb	0.025	0.035	0.042	0.042
Lu	0.005	0.005	0.007	0.007
Hf	0.122	0.043	0.124	0.002
W	0.30	0.211	0.219	0.027
Re	BD	0.002	0.009	0.0064
Au	0.07	0.04	0.06	0.064
Pb	3.9	6.5	2.9	0.43
Bi	3.55	3.40	2.54	0.482
Th	0.21	0.587	0.769	0.101
U	0.116	0.45	0.64	0.106

TABLE 4.12: Elemental data for Kalumbila-Sentinel chalcopyrite samples (ppm)

	KAL0195 52.3	KAL0195 88.7	KAL0195 113.0	KAL23 204.0
Mineralogy	CPY	CPY	CPY	CPY
Setting	Mainstage	Mainstage	Mainstage	Mainstage
Na	17	53	14	33
Mg	254	470	219	2380
Al	288	440	161	1420
K	38	131	92	54
Ca	24	38	47	1450
Sc	0.026	0.037	0.030	0.152
Ti	1.66	5.6	4.4	1.7
V	2.35	3.3	3.7	5.3
Cr	0.19	0.36	0.25	0.38
Mn	29.1	9.9	43.1	74
Co	1810	950	503	5000
Ni	430	444	248	2200
Zn	390	86	737	500
Ga	6.3	1.51	10.6	4.0
Ge	4.2	4.7	3.9	4.1
As	8.7	33.9	0.4	62
Se	12.5	15.4	13	7.4
Sr	0.078	1.61	0.56	4.66
Zr	3.2	0.333	3.14	0.95
Nb	0.012	0.014	0.015	0.015
Mo	0.29	0.37	0.36	0.03
Ag	3.30	0.58	6.8	5.99
Cd	0.32	0.144	1.33	0.67
Sn	98	10.2	99	61
Sb	0.084	0.37	0.22	0.47
La	3.36	0.70	1.83	0.60
Ce	7.1	1.42	3.89	0.95
Nd	3.06	0.59	1.75	0.326
Sm	0.57	0.10	0.35	0.070
Eu	0.064	0.015	0.044	0.018
Gd	0.41	0.064	0.27	0.091
Tb	0.042	0.006	0.028	0.018
Dy	0.187	0.021	0.12	0.112
Ho	0.026	0.002	0.016	0.020
Er	0.045	0.004	0.034	0.051
Yb	0.023	0.002	0.023	0.044
Lu	0.003	BD	0.004	0.007
Hf	0.089	0.016	0.099	0.04
W	0.047	0.060	0.054	0.066
Re	0.001	BD	BD	0.002
Au	1.93	0.16	1.0	4.6
Pb	1.79	6.1	4.9	11.7
Bi	2.34	2.66	7.91	6.72
Th	2.61	0.176	1.04	0.30
U	5.04	0.255	0.337	8.8

TABLE 4.13: Elemental data for Enterprise sulphide samples (ppm)

	ENT0003 74.22	ENT0003 80.5	ENT0004 62.29	ENT0004 69.80
Mineralogy	PY	VAES	PY	PY
Setting	Vein	Vein	Vein	Vein
Na	203	66	184	121
Mg	384	145	167	18.4
Al	141	490	166	109
K	29	41	41	53
Ca	700	181	232	82
Sc	0.180	0.35	0.24	0.13
Ti	43	44.2	11.0	7.6
V	27.1	27.8	13.7	17.1
Cr	0.98	1.2	0.38	0.45
Mn	31.7	2.49	13.0	7.1
Co	1920	1560	780	1340
Ni	17800	379000	3550	5860
Zn	9.3	3.8	2.54	2.1
Ga	0.214	0.36	0.250	0.515
Ge	4.6	0.51	4.8	4.5
As	18.5	43.4	135	287
Se	69	31	80	84
Sr	2.31	0.79	1.93	2.44
Zr	13.3	25.0	8.40	1.23
Nb	0.208	0.25	0.048	0.023
Mo	0.20	14.2	0.35	1.38
Ag	0.058	0.036	0.013	0.005
Cd	0.107	0.018	0.007	0.003
Sn	0.052	0.062	0.045	0.038
Sb	0.18	0.025	0.036	0.034
La	0.065	1.40	0.802	1.05
Ce	0.140	3.16	1.68	2.26
Nd	0.049	0.93	0.46	0.74
Sm	0.008	0.15	0.074	0.185
Eu	0.005	0.023	0.018	0.023
Gd	0.010	0.14	0.061	0.189
Tb	0.002	0.020	0.009	0.032
Dy	0.017	0.137	0.062	0.186
Ho	0.006	0.318	0.015	0.030
Er	0.036	0.125	0.057	0.065
Yb	0.088	0.191	0.101	0.032
Lu	0.020	0.039	0.021	0.004
Hf	0.39	0.85	0.278	0.075
W	0.162	0.19	0.034	0.054
Re	BD	0.058	0.003	0.001
Au	0.043	0.034	0.07	0.04
Pb	2.9	1.8	2.8	2.4
Bi	0.320	0.029	0.121	0.081
Th	0.062	1.45	0.146	0.18
U	0.222	0.943	0.250	0.140

TABLE 4.14: Elemental data for Kansanshi chalcopyrite samples (ppm)

	KAN 1-4	KAN 1-7	KAN 2-1	KAN 2-2	KAN 3-9
Mineralogy	CPY	CPY	CPY	CPY	CPY
Setting	Vein	Vein	Vein	Vein	Vein
Na	61	43	68	40.3	38.5
Mg	26.5	11.5	243	6.6	14.9
Al	19.1	4.49	6.15	0.46	0.25
K	28	27	26	29	34.1
Ca	1030	478	702	1340	563
Sc	0.166	0.053	0.209	0.016	0.041
Ti	0.21	0.3	0.12	0.10	0.13
V	5.1	7.4	3.5	3.9	5.6
Cr	0.14	0.12	0.13	0.06	0.05
Mn	6.51	3.10	9.00	5.22	3.01
Co	66.5	740	0.10	1.89	3.6
Ni	1410	97	68	127	291
Zn	73.7	31.8	80.5	26.8	48.4
Ga	5.24	1.67	7.15	4.26	4.52
Ge	4.1	3.7	3.45	4.0	4.3
As	21	18	13.9	60.1	58.6
Se	480	410	346	1430	1380
Sr	2.41	0.54	2.22	11.0	2.58
Zr	0.773	0.038	0.077	0.016	0.033
Nb	0.018	0.036	0.010	0.015	0.018
Mo	84.7	0.10	92.4	1.23	0.215
Ag	6.18	3.10	6.12	4.72	7.01
Cd	0.40	0.13	0.391	0.115	0.211
Sn	101	68	141.8	175	218
Sb	0.198	0.046	0.169	0.105	0.197
La	1.61	1.19	0.009	0.028	0.073
Ce	2.58	2.27	0.018	0.071	0.172
Nd	0.958	0.78	0.012	0.055	0.117
Sm	0.249	0.128	0.00463	0.0275	0.0340
Eu	0.043	0.019	0.002	0.008	0.009
Gd	0.254	0.085	0.008	0.046	0.043
Tb	0.047	0.013	0.002	0.009	0.008
Dy	0.338	0.087	0.012	0.077	0.059
Ho	0.066	0.018	0.003	0.020	0.014
Er	0.191	0.060	0.009	0.067	0.045
Yb	0.173	0.077	0.012	0.065	0.056
Lu	0.023	0.013	0.002	0.009	0.009
Hf	0.019	0.001	0.002	0.001	0.001
W	0.125	0.016	0.131	0.003	0.002
Re	0.048	0.002	0.039	0.006	0.008
Au	0.236	0.087	0.050	0.149	0.082
Pb	10.2	0.36	3.47	0.90	1.99
Bi	1.18	0.074	1.30	0.19	2.15
Th	0.40	0.019	0.006	0.001	0.001
U	46.7	1.05	0.03	0.051	0.19

TABLE 4.15: Elemental data for Kansanshi chalcopyrite and pyrite samples (ppm)

	KAN 1-5	KAN 2-6	KAN 2-9	KAN 3-1
Mineralogy	CPY	CPY	PY	PY
Setting	Disseminated	Disseminated	Vein	Vein
Na	99.5	84	24.6	34.3
Mg	13.8	175	32.3	29.4
Al	69.8	81	7.2	6.6
K	69.3	38	20.3	42.0
Ca	1330	1550	2310	746
Sc	0.275	0.254	0.143	0.046
Ti	1.92	4.0	0.113	0.309
V	18.3	11.3	3.05	8.58
Cr	1.26	0.34	0.113	0.106
Mn	6.30	11.6	12.6	3.36
Co	3270	682	16400	5840
Ni	763	2050	1700	689
Zn	72.7	62.9	11.7	48.8
Ga	3.72	2.08	0.39	3.29
Ge	4.05	4.02	5.34	5.03
As	123	27.4	29.5	55.7
Se	406	147	404	817
Sr	3.72	2.75	11.5	2.33
Zr	31.8	57	0.035	1.76
Nb	0.047	0.092	0.012	0.027
Mo	42.2	3.69	0.181	0.14
Ag	1.71	1.57	0.623	3.49
Cd	0.412	0.23	0.045	0.21
Sn	75.2	71.2	12.7	89.9
Sb	0.195	0.178	0.049	0.088
La	0.424	47.6	0.178	1.67
Ce	1.14	93.5	0.378	3.01
Nd	0.884	31.2	0.182	1.07
Sm	0.301	4.98	0.053	0.162
Eu	0.042	0.63	0.018	0.023
Gd	0.402	3.02	0.067	0.117
Tb	0.066	0.306	0.012	0.013
Dy	0.419	1.24	0.096	0.068
Ho	0.080	0.162	0.025	0.014
Er	0.233	0.35	0.086	0.049
Yb	0.234	0.33	0.127	0.065
Lu	0.044	0.069	0.025	0.011
Hf	0.818	2.44	0.001	0.043
W	0.177	0.094	0.003	0.004
Re	0.066	0.016	0.007	0.010
Au	0.37	1.68	0.09	0.04
Pb	39.4	2.2	0.95	1.06
Bi	4.29	0.675	0.869	0.195
Th	0.54	9.71	0.005	0.073
U	24.7	3.27	0.30	0.16

TABLE 4.16: Elemental data for miscellaneous sulphide samples (ppm)

	WS1 NKANA	WS4 CHAM	WS5 CHIB	WS6 CHIB
Deposit	Nkana	Chambishi	Chibuluma	Chibuluma
Mineralogy	CPY	BN	CPY	CPY
Setting				
Na	10	1.8	24	30
Mg	513	410	85	380
Al	311	324	110	390
K	280	330	40	104
Ca	830	630	116	30
Sc	0.072	0.077	0.169	0.122
Ti	13.3	30	1.47	3.0
V	6.05	4.3	3.9	5.9
Cr	0.40	0.54	0.61	1.0
Mn	45.2	65	3.5	1.63
Co	483	7.6	100000	1970
Ni	3.8	1.08	3370	195
Zn	1220	3.2	4.5	5.4
Ga	1.69	0.23	0.77	0.783
Ge	3.17	1.32	2.5	3.62
As	2	39	169	0.2
Se	59	1050	730	11.7
Sr	0.85	0.73	0.51	0.24
Zr	0.61	1.34	2.7	3.73
Nb	0.062	0.140	0.010	0.018
Mo	0.57	1.24	2.6	8.9
Ag	23.2	213	2.05	2.83
Cd	3.7	0.20	0.156	0.060
Sn	8.53	1.61	0.39	5.82
Sb	0.19	0.18	35.4	0.71
La	0.059	1.46	0.120	19.3
Ce	0.131	2.99	0.19	31.8
Nd	0.086	1.33	0.085	12.0
Sm	0.031	0.24	0.017	1.92
Eu	0.002	0.028	0.003	0.242
Gd	0.042	0.173	0.018	1.02
Tb	0.008	0.021	0.003	0.079
Dy	0.044	0.136	0.020	0.230
Ho	0.007	0.023	0.005	0.022
Er	0.018	0.069	0.012	0.030
Yb	0.017	0.059	0.020	0.024
Lu	0.002	0.090	0.004	0.005
Hf	0.018	0.038	0.10	0.125
W	0.054	0.011	0.014	0.022
Re	0.004	BD	0.001	0.002
Au	0.67	5.8	2.85	3.4
Pb	2.9	380	40	12.4
Bi	29.5	2250	6.85	36.6
Th	0.25	0.53	0.17	2.28
U	0.52	3.44	0.957	0.299

4.4.1 Rare earth element profiles

While sulphide minerals are not a preferred repository for REEs (e.g. Morgan and Wandless, 1980), the concentrations in most of the samples analysed were high enough to generate REE profiles for the sulphide mineral sample suite available from the Central African Copperbelt, including examples of pyrite, chalcopyrite, bornite, chalcocite, carrolite and vaesite. North American Shale Composite (NASC) was used for normalisation of the dataset, since many of the well mineralised deposits are hosted by the Copperbelt Orebody Member, or 'Ore Shale'.

The dataset as a whole shows variation in the shapes of the profiles, from patterns showing relative light REE enrichment over the heavy rare earths, to relatively flat profiles and profiles showing LREE depletion (Figs. 4.9, 4.10). The REE concentrations show significant variation, up to ~4 orders of magnitude, between profiles. In many examples, most notably the datasets for Konkola, Enterprise, Kansanshi and Lumwana, the LREE show much greater variations in concentration than the HREE, to the extent that the overall shape of the combined profiles for these deposits is controlled by the variation in the LREE concentrations. With only a few exceptions the dataset shows negative Eu anomalies.

The different deposits show subtly different profile shapes from one another, and many of the samples within the deposit show consistent profile shapes. Part of the Konkola dataset, the Kalumbila-Sentinel dataset and the majority of the Lumwana dataset show LREE enrichment (Figs. 4.9, 4.10). The other part of the Konkola dataset and the Konkola North dataset show relatively flat profiles. The Nchanga deposit shows flat to slightly LREE depleted profiles, whilst the Kansanshi dataset shows a variation from slightly LREE enriched to slightly LREE depleted profiles which are generally relatively flat. Smaller datasets from Enterprise and Samba are less consistent. The two pyrite samples from Samba show a relatively flat profile and one showing LREE enrichment, whilst the chalcopyrite profile shows striking LREE depletion and MREE enrichment (Fig. 4.10). The Enterprise samples show relatively flat profiles, with a trend towards HREE enrichment, with the vaesite sample showing essentially no difference (Fig. 4.10). The small number of available samples from Chambishi, Nkana and Chibuluma show some similarities to the rest of the dataset. One Chibuluma sample shows a relatively flat profile and the other exhibits a profile showing LREE enrichment, the Chambishi sample shows slight LREE enrichment and the Nkana sample shows LREE depletion (Fig. 4.11).

The dataset as a whole shows little effect from sulphide mineralogy on the shapes of the profiles, with profiles from different mineralogies frequently exhibiting similar shapes,

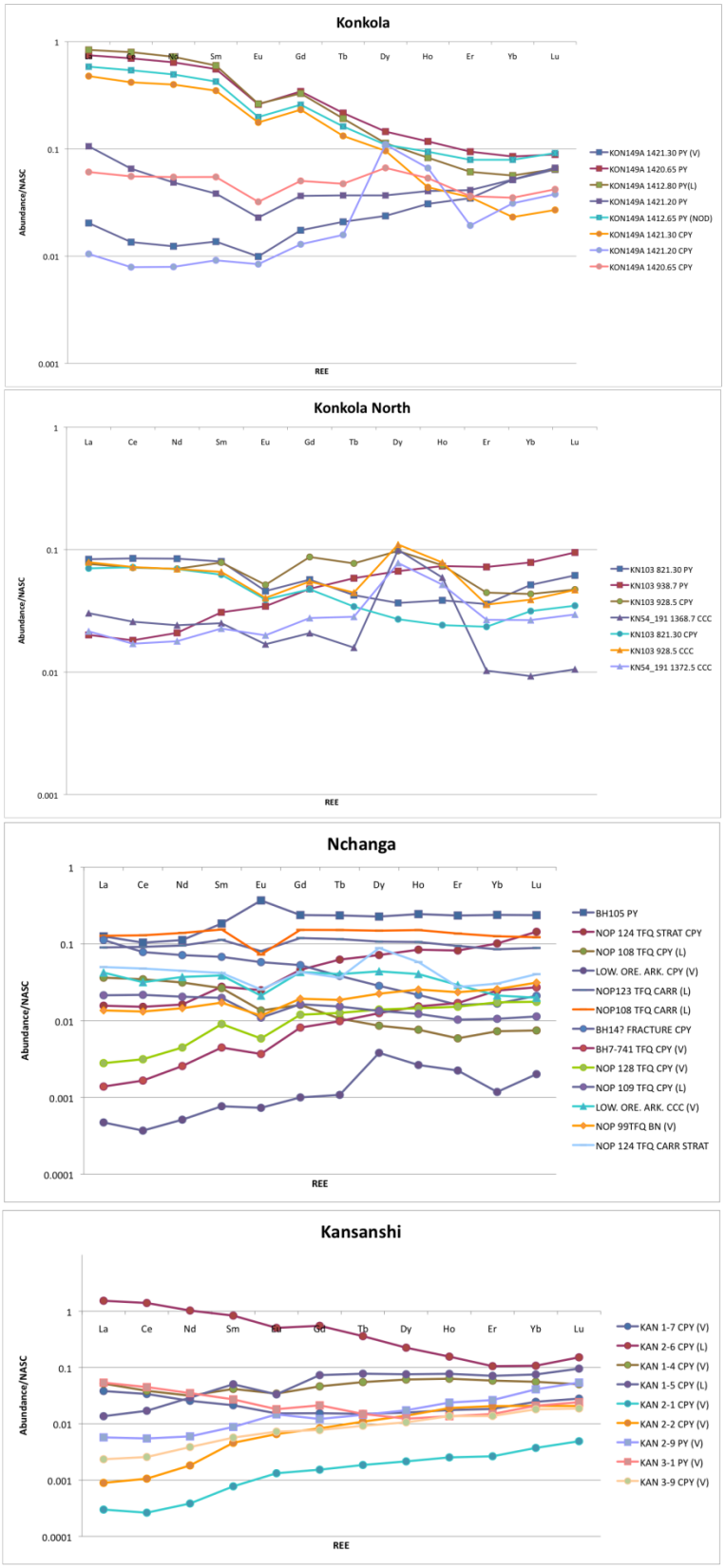

FIGURE 4.9: Composite REE profiles for sulphides from Konkola, Konkola North, Nchanga and Kansanshi, normalised to NASC.

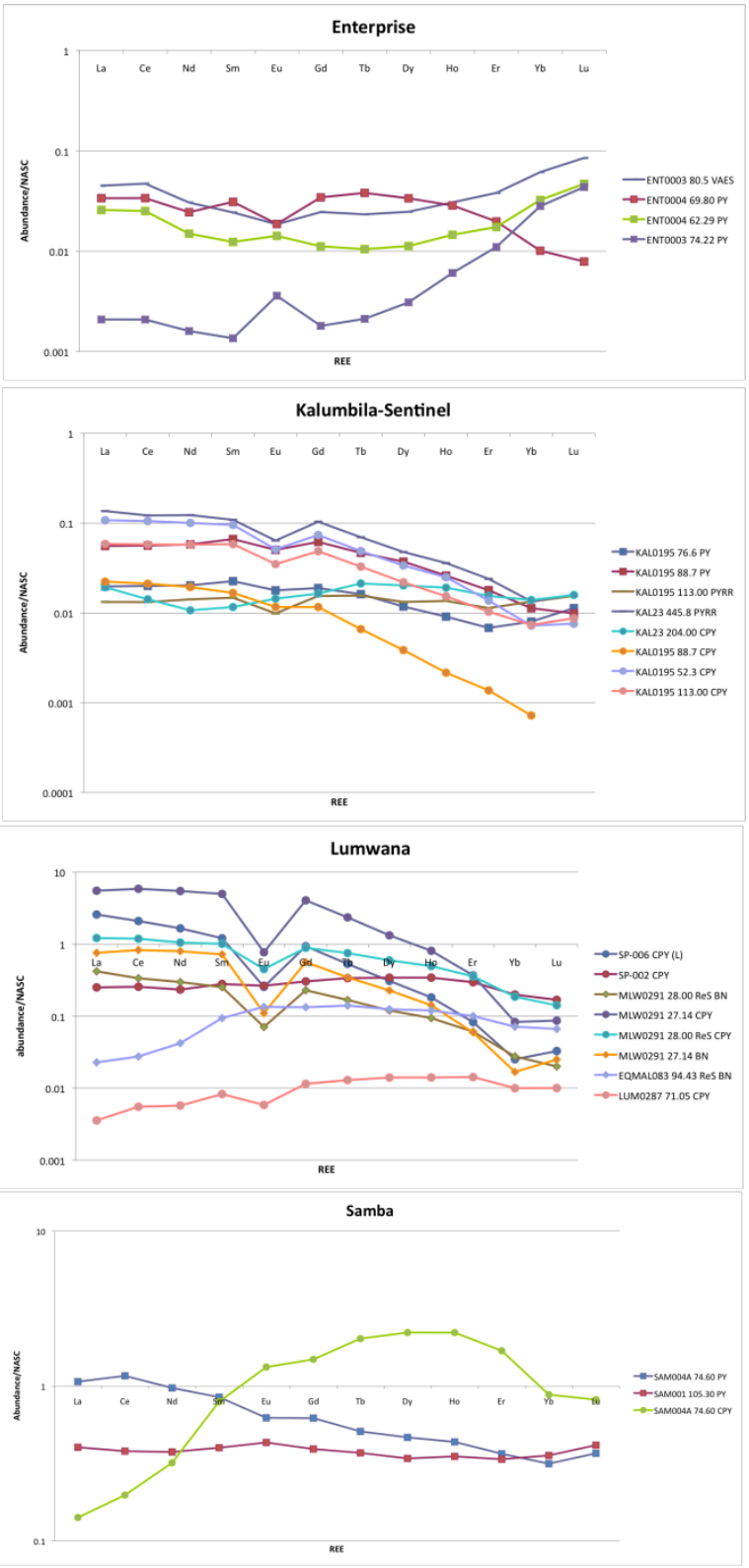

FIGURE 4.10: Composite REE profiles for sulphides from Enterprise, Kalumbila-Sentinel, Samba and Lumwana, normalised to NASC.

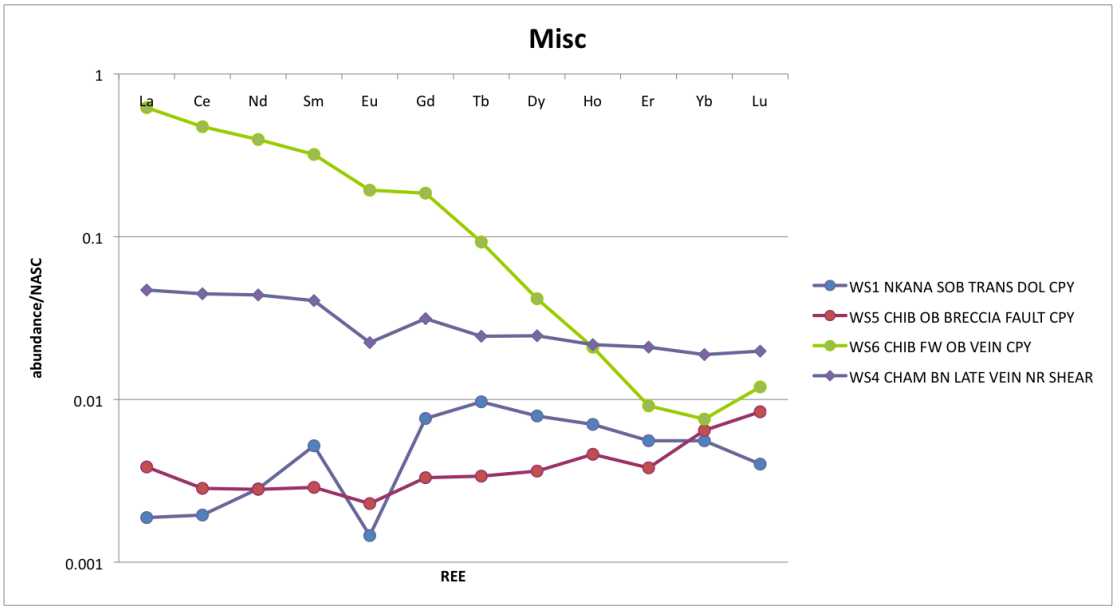

FIGURE 4.11: Composite REE profiles for sulphides from Nkana, Chambishi and Chibuluma, normalised to NASC.

and profiles of the same mineralogy capable of showing radically different shaped profiles. Clear examples of this include Konkola pyrite and chalcopyrite (Fig. 4.12), Kalumbila-Sentinel pyrite, chalcopyrite and pyrrhotite (Fig. 4.13) and Lumwana bornite and chalcopyrite (Fig. 4.14). There is also no clear effect on profile shape from different sulphide settings. Profiles of stratiform mineralisation and vein hosted mineralisation at Nchanga are similar in shape, as are sheared Ore Schist sulphides and vein sulphides at Lumwana (Fig. 4.15).

Several profiles which are otherwise similar to the majority of the data for their respective deposits show anomalously high Dy and Ho values, notably chalcocite samples from Konkola North (Fig. 4.12), a chalcopyrite sample from Konkola North (Fig. 4.9), a chalcopyrite sample from Konkola (Fig. 4.12), a vein-hosted chalcopyrite sample from the lower orebody at Nchanga, and a carrolite sample from the upper orebody at Nchanga (Fig. 4.9). This anomaly is not a mineralogical effect, occurring in a diverse suite of sulphide minerals, and occurs in both stratiform and vein-hosted sulphides. A single chalcopyrite profile from Samba shows MREE enrichment inconsistent with the shapes of most profiles, along with a single similarly shaped profile in a Lumwana bornite sample (Fig. 4.10).

4.5 Trace element data

Plots of transition metals show depletion of Sc, Ti, V, Cr and Mn in Copperbelt sulphides compared to NASC. In contrast, Co and Ni are typically enriched (Fig. 4.16). These

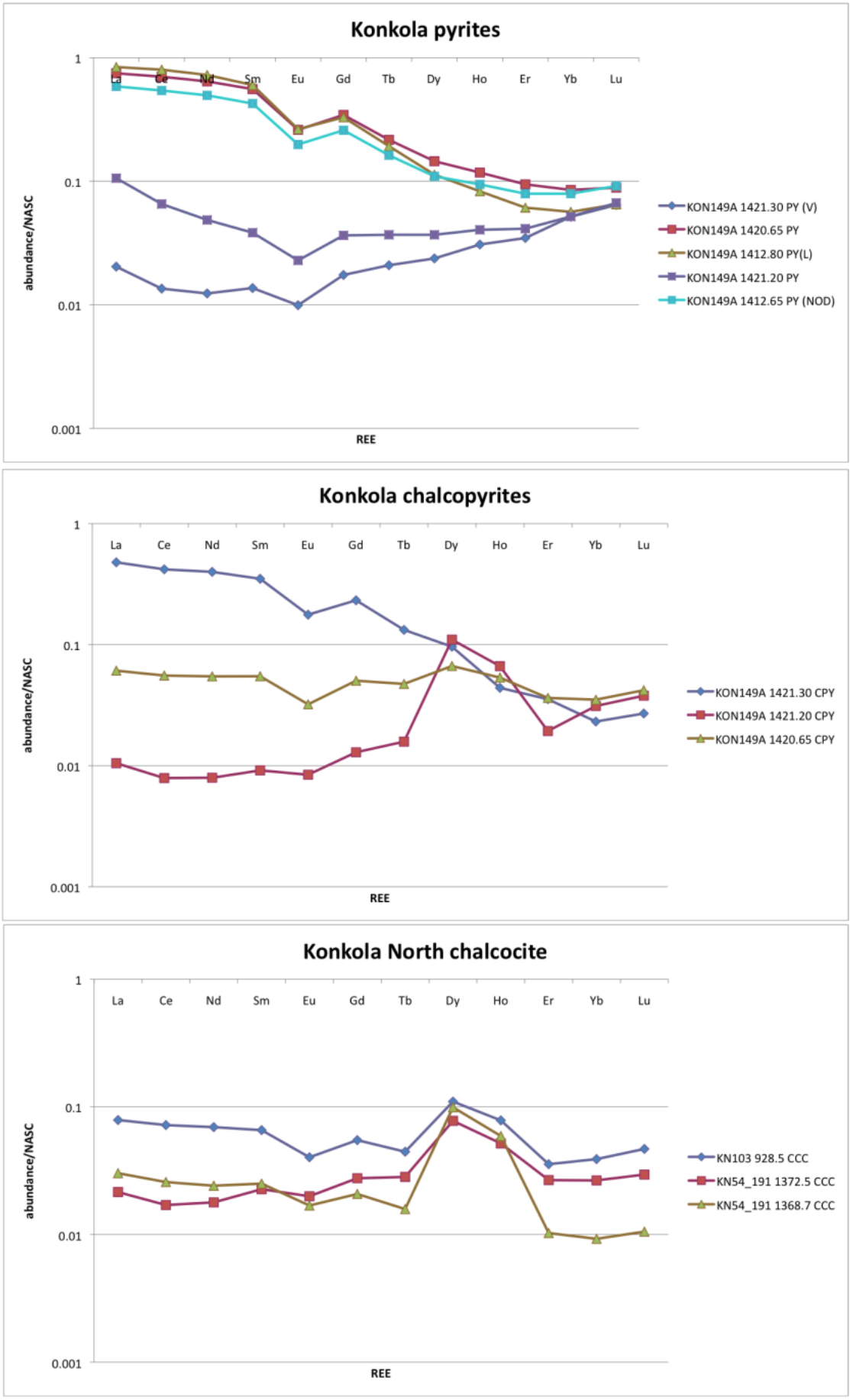

FIGURE 4.12: REE profiles for pyrite and chalcopyrite from Konkola, and chalcocite from Konkola North, normalised to NASC.

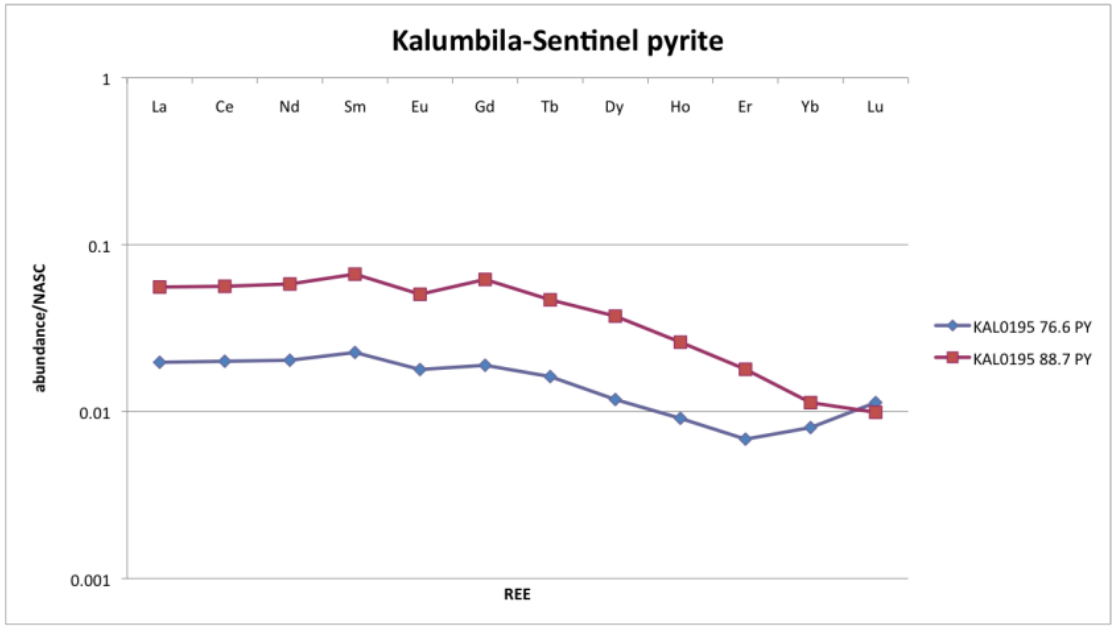

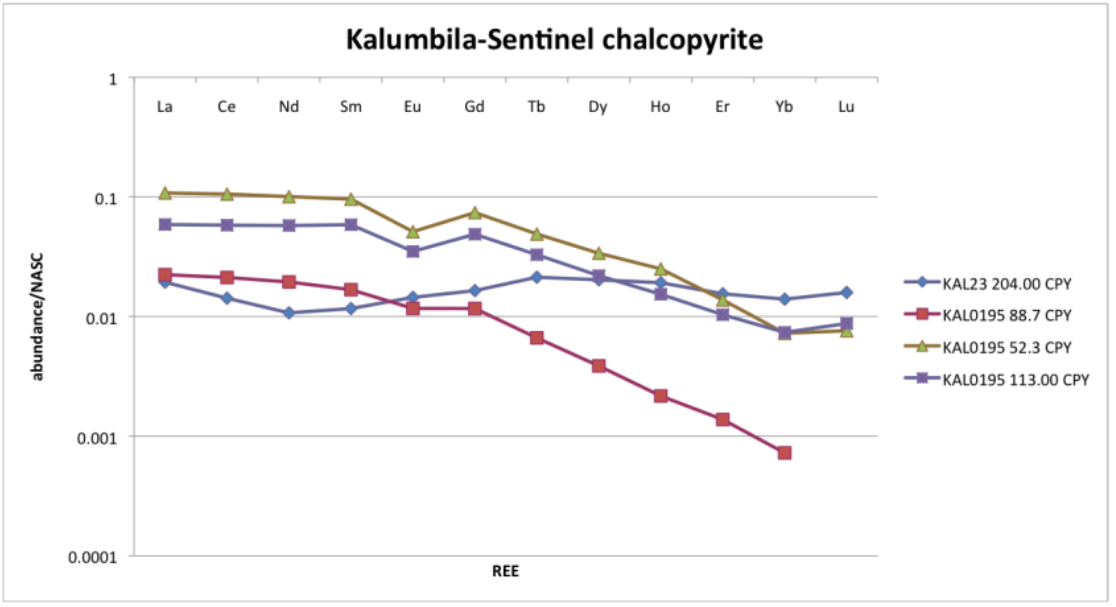

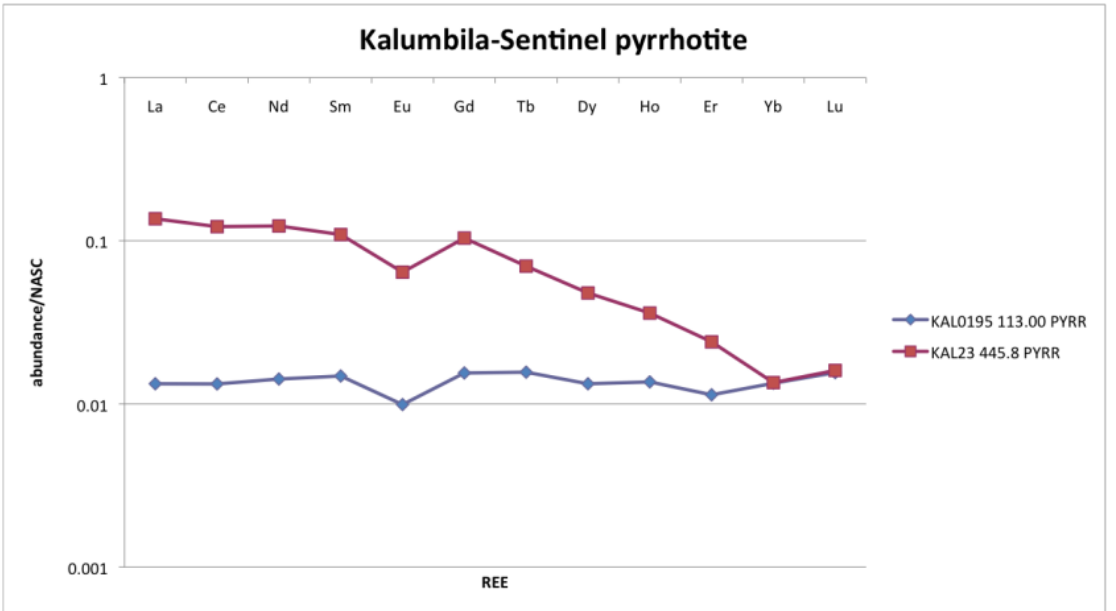

FIGURE 4.13: REE profiles for pyrite, chalcopyrite and pyrrhotite from Kalumbila-Sentinel, normalised to NASC.

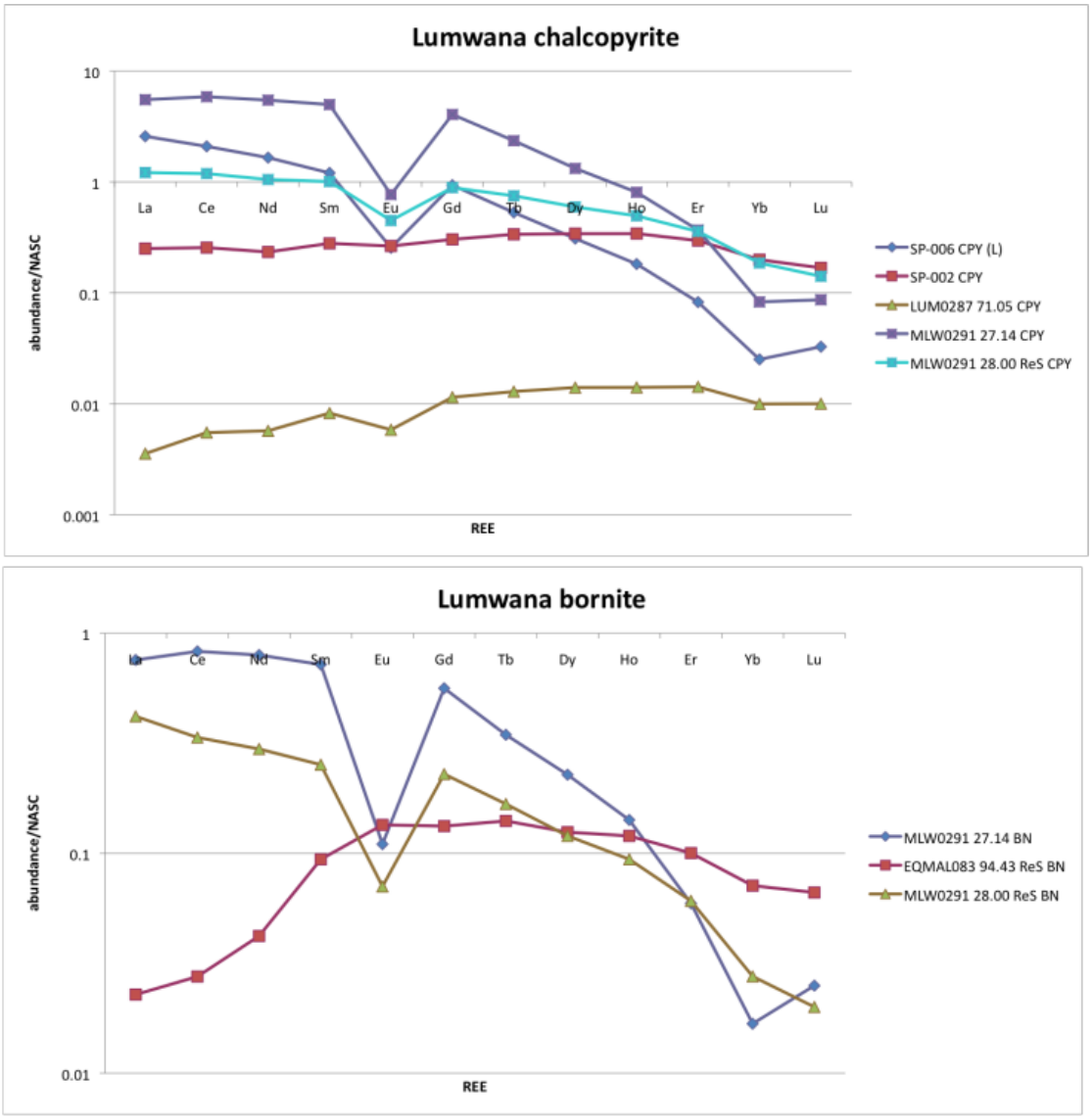

FIGURE 4.14: REE profiles for chalcopyrite and bornite from Lumwana, normalised to NASC.

plots show very consistent, characteristic shapes with low Sc, Ti, Cr and Mn, and with Ni, while generally enriched, lower than Co in most samples except for the Enterprise deposit, in which Ni is the primary economic mineralisation. While generally enriched in sulphides relative to NASC, cobalt content can be very variable, up to ∼5 orders of magnitude for the Nchanga and Kansanshi samples (Fig. 4.16). Ni content is also highly variable in Nchanga sulphides with differences up to ∼4 orders of magnitude. Carrolite from Nchanga contains the highest Co contents observed in the study.

Mean Na, K, Al, Ca, and Mg concentrations for the sulphides at the different deposits are very variable (Fig. 4.17). Mean Co and Ni contents for sulphides from the different deposits suggest that with the exception of the Enterprise deposit the sulphides in the Copperbelt are cobalt enriched compared to Ni, with the Nchanga, and Konkola deposits

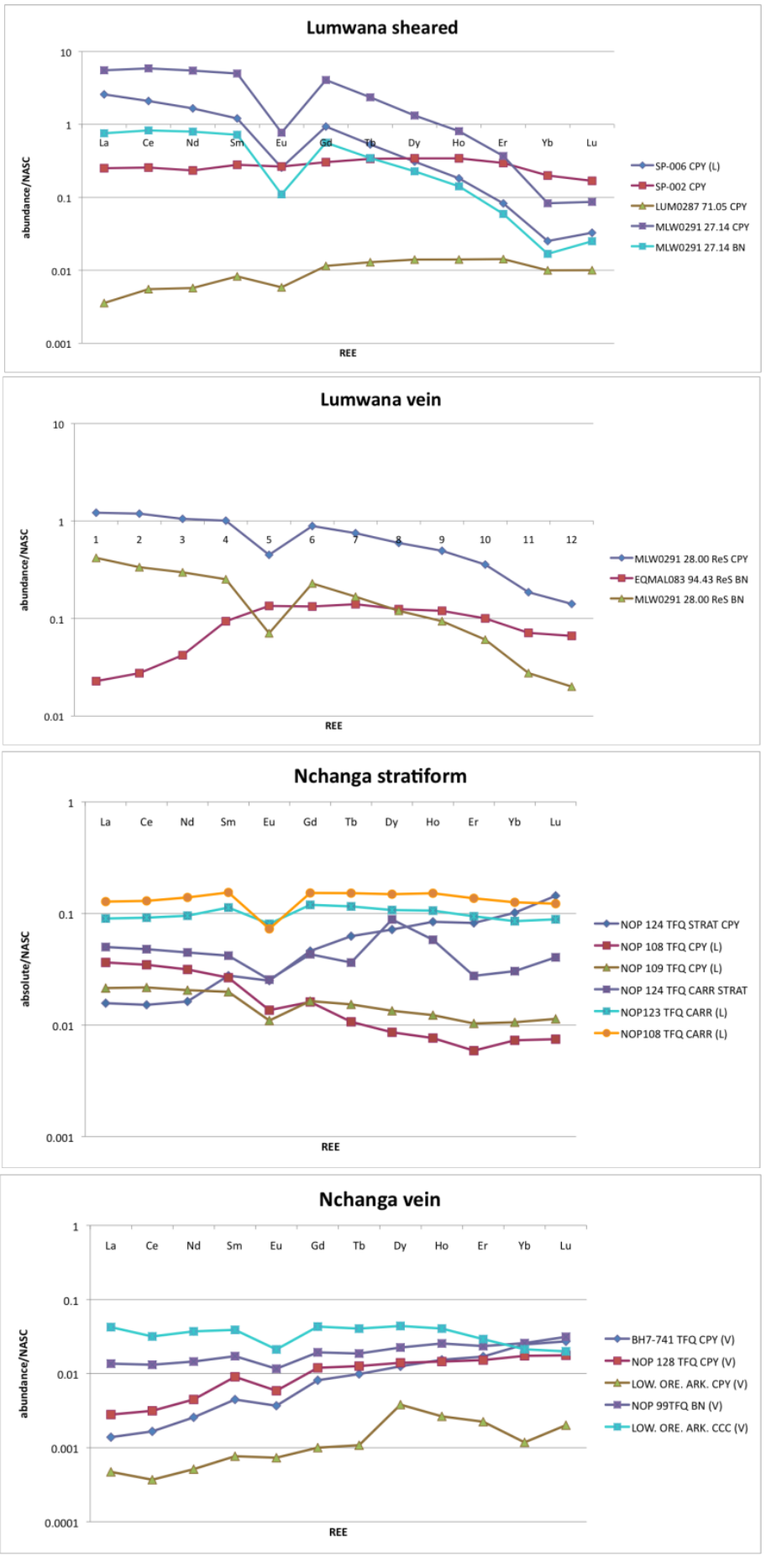

FIGURE 4.15: Composite REE profiles for stratiform and vein hosted sulphides at Nchanga and sheared and vein hosted sulphides at Lumwana, normalised to NASC.

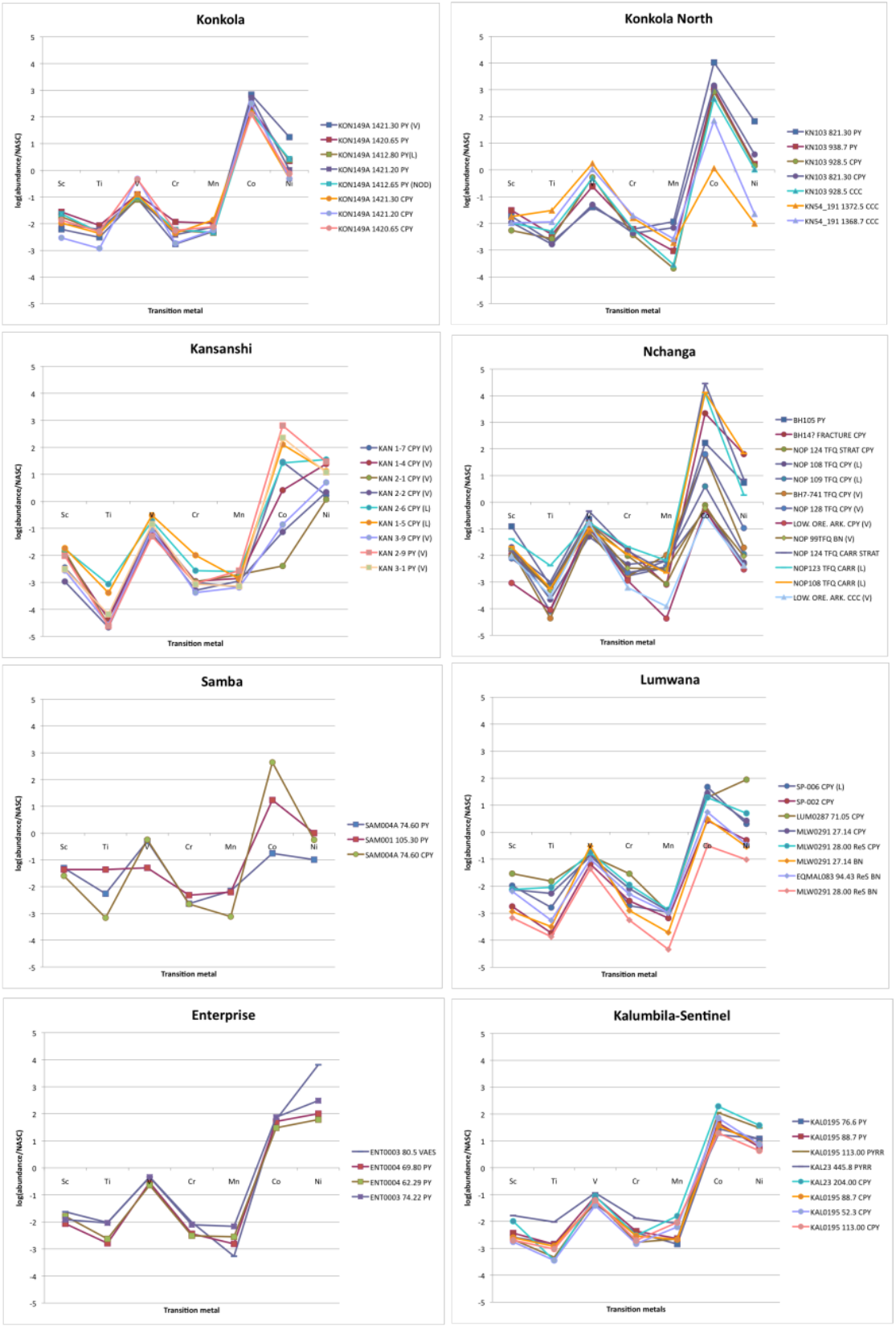

FIGURE 4.16: Composite transition metal profiles profiles for Copperbelt sulphides (NASC normalised).

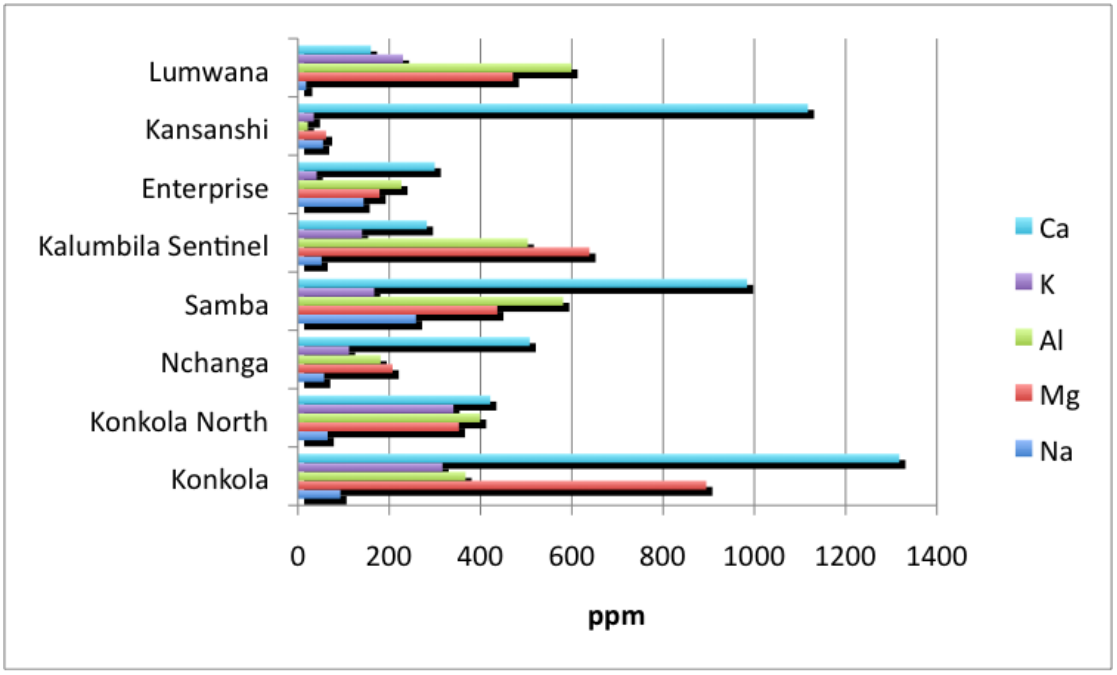

FIGURE 4.17: Na, K, Al, Ca, Mg concentrations for sulphides from the deposits sampled, calculated as a mean of all sulphide mineralogies in ppm.

in the traditional mining district of the Kafue Anticline the most Co enriched (Fig. 4.18). Note that the mean Co content for Nchanga and the mean Ni content for Enterprise are very high due to the inclusion of Carrolite and Vaesite in the means respectively. Mean Pb and Zn content of sulphides from the different deposits are very variable throughout the district, and with the exception of Kalumbila-Sentinel average <100 ppm (Fig. 4.18). Average Au and Ag contents for sulphides in the deposits are <5 ppm with the exception of Ag at Nchanga. Mo concentrations are highest in sulphides from Lumwana and Kansanshi, whilst the other deposits show values <~10 ppm. Mean total REE contents are highest in sulphides from the Lumwana and Samba deposits, with U also being high at Samba. Sulphides from the other deposits show U and total REE contents <50 ppm (Fig. 4.18). Other minor trace elements are very variable across the different deposits studied, though notably mean Se content in sulphides from the Kansanshi deposit is much higher than the others at >600 ppm (Fig. 4.19), mean As contents of Konkola and Konkola North sulphides are >150 ppm (Fig. 4.19), mean sulphide Bi content at Nchanga is much higher than the other deposits at >100 ppm (Fig. 4.19), and mean sulphide Sn content at Kansanshi is much higher than the other deposits at >100 ppm (Fig. 4.19).

Trace elements show some control by host sulphide mineralogy, as well as by different deposit. As a specific cobalt sulphide, carrolite from the upper orebody at Nchanga shows the highest cobalt concentrations (Table 4.7). Cobalt contents of pyrites and chalcopyrite from Nchanga, pyrite at Kansanshi, chalcopyrite at Samba are also enriched (Fig. 4.20).

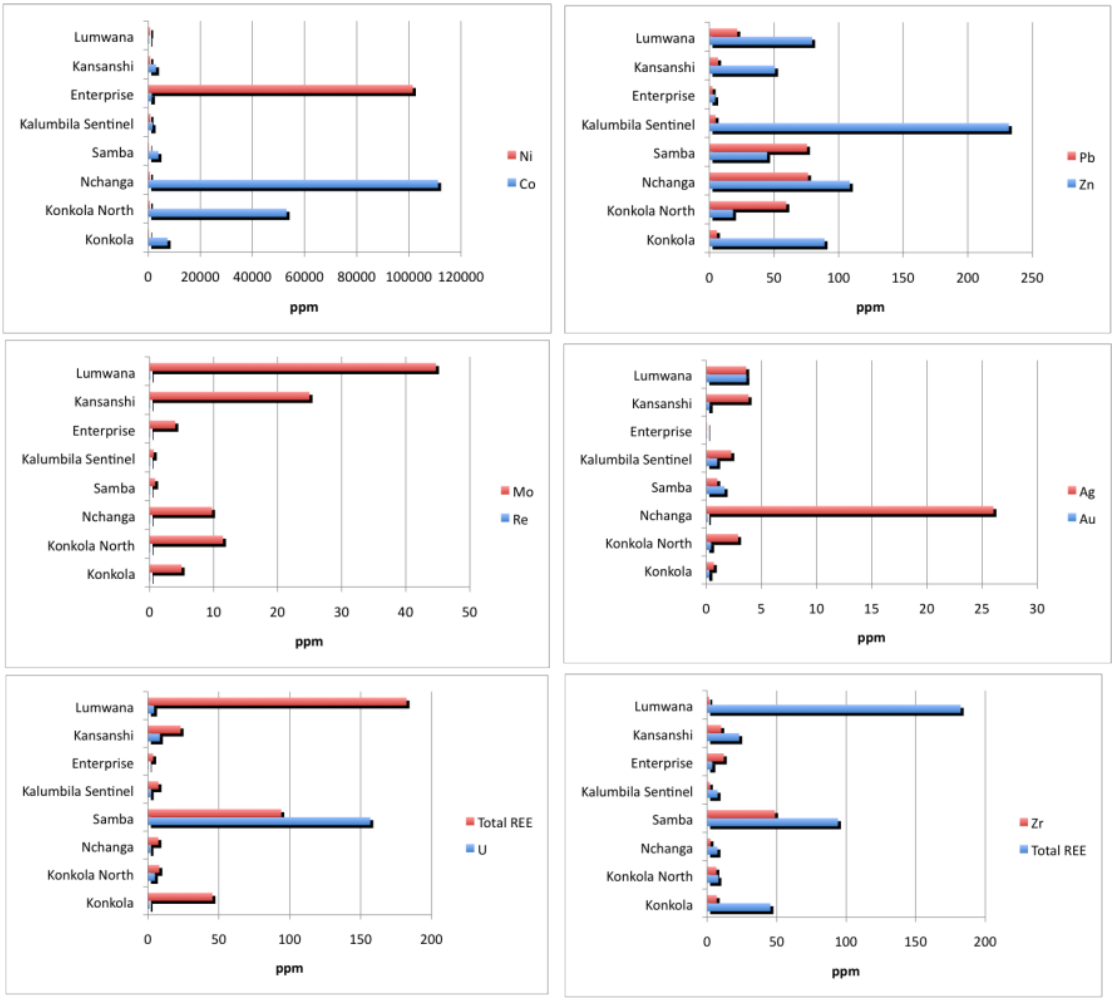

FIGURE 4.18: Co, Ni, Pb, Zn, Mo, Re, Ag, Au, U and Total REE concentrations for sulphides from the deposits sampled, calculated as a mean of all sulphide mineralogies in ppm.

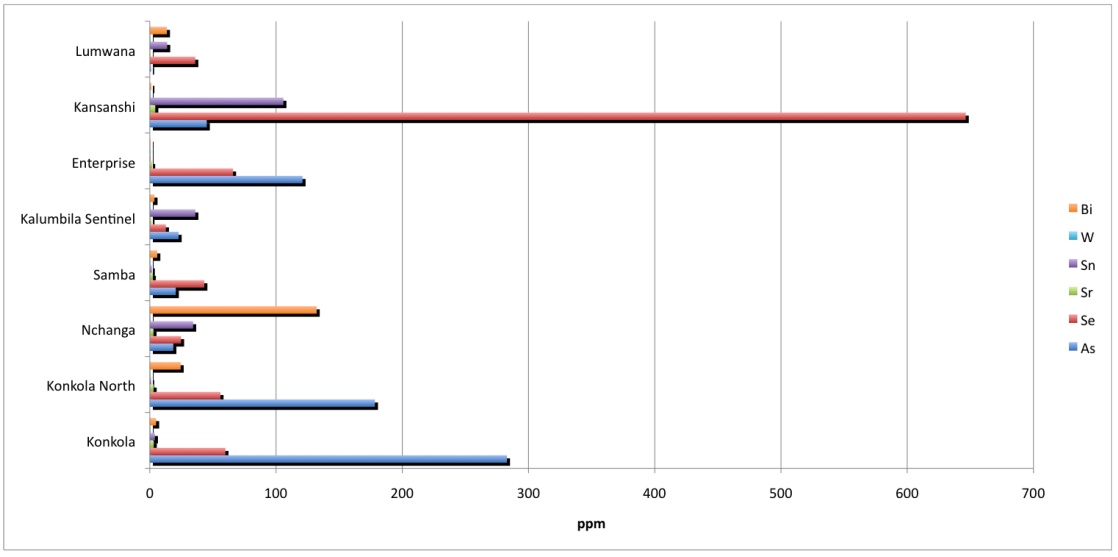

FIGURE 4.19: Bi, W, Sn, Sr, Se, As concentrations for sulphides from the deposits sampled, calculated as a mean of all sulphide mineralogies in pm.

Sulphides from the Konkola deposit as a whole are enriched in Co, particularly pyrite and chlacopyrite from Konkola North, where concentrations may reach up to ∼150,000 ppm (Fig. 4.20). Ni concentrations are highest in specific Ni sulphide phases, in this case vaesite from Enterprise (Table 4.13). Ni concentrations are also very high in pyrite from Enterprise (>9000 ppm) as well as being relatively enriched (>500 ppm) in carrolite at Nchanga, pyrite at Konkola North, pyrite and chalcopyrite from Kansanshi, chalcopyrite at Lumwana, and pyrite, chalcopyrite and pyrrhotite at Kalumbila-Sentinel (Fig. 4.20). Ag concentrations are highest at Nchanga within chalcocite and bornite (Fig. 4.21). Au concentrations are high (>1 ppm) in Lumwana bornite and chalcopyrite, Samba pyrite and chalcopyrite and Kalumbila chalcopyrite (Fig. 4.21). Sn concentrations are highest in Kansanshi chalcopyrite and pyrite, Nchanga bornite and chalcopyrite, Kalumbila-Sentinel chalcopyrite and Lumwana chalcopyrite (Fig. 4.22). Total REE concentrations are highest in Lumwana chalcopyrite and bornite, Samba chalcopyrite and pyrite and pyrite at Konkola (Fig. 4.22). Re concentrations are generally low in all sulphides at <0.15 ppm (Fig. 4.23).

4.6 Discussion of REE and trace element analysis

REE patterns in sulphides are controlled by the REE pattern of the hydrothermal fluid they are precipitating from and the partition coefficients between the sulphide mineral phase and the fluid. Additionally, part or all of the REE contents may be derived from fluid inclusions within the sulphides, or from crystal defect sites (Zhao and Jiang, 2007). Partition coefficients between REE and sulphide minerals are poorly understood, as is the general behaviour of REE in hydrothermal systems (Lottermoser, 1992) . Therefore, it is generally assumed that REE patterns in sulphides reflect that of the parent hydrothermal fluid although typically containing much lower concentrations, and this has been shown to be the case in active hydrothermal vent sites such as TAG and the Rainbow hydrothermal field at the Mid Atlantic Ridge (Barrett et al., 1990; Marques et al., 2006; Mills and Elderfield, 1995).

The REE concentrations reported here for sulphide minerals are similar to those of sulphides forming in active seafloor hydrothermal systems such as TAG black smokers though the patterns differ (Barrett et al., 1990; Mills and Elderfield, 1995). Seafloor hydrothermal systems typically show LREE enriched profiles with positive Eu anomalies (Bau and Dulski, 1999; Klinkhammer et al., 1994; Marques et al., 2006; Michard, 1989; Michard and Albarède, 1986; Mills and Elderfield, 1995). Fluid samples from geothermal systems hosted in sediments in Italy and brines from the Salton Sea show similar patterns. Hydrothermal fluids from Tibet and from granitic basement in Bulgaria however,

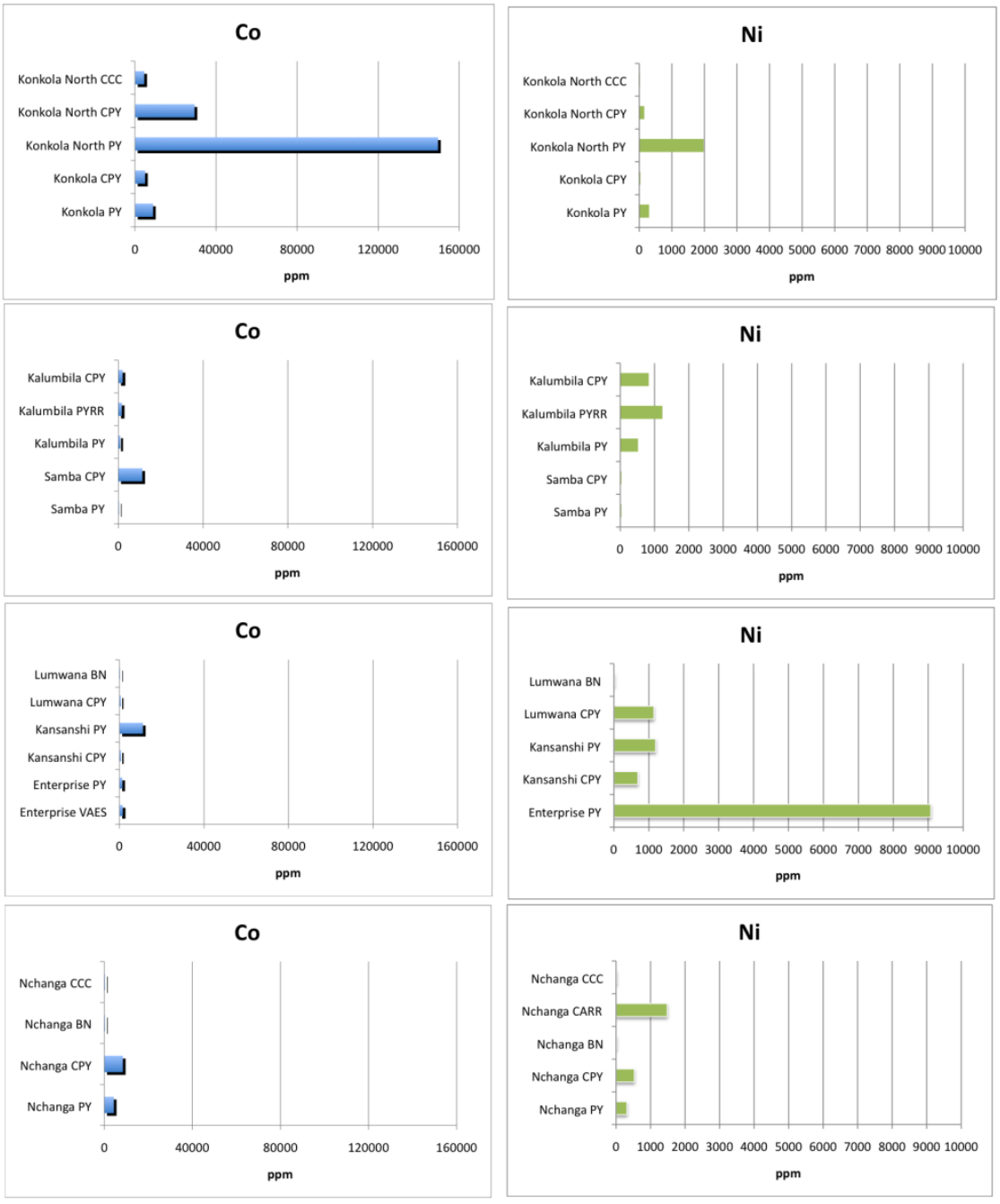

FIGURE 4.20: Co and Ni concentrations for different sulphide mineralogies from the deposits sampled, calculated as a mean of each particular sulphide mineralogy in ppm. This excludes carrolite for Co and vaesite for Ni as these metals form a major component in these sulphides.

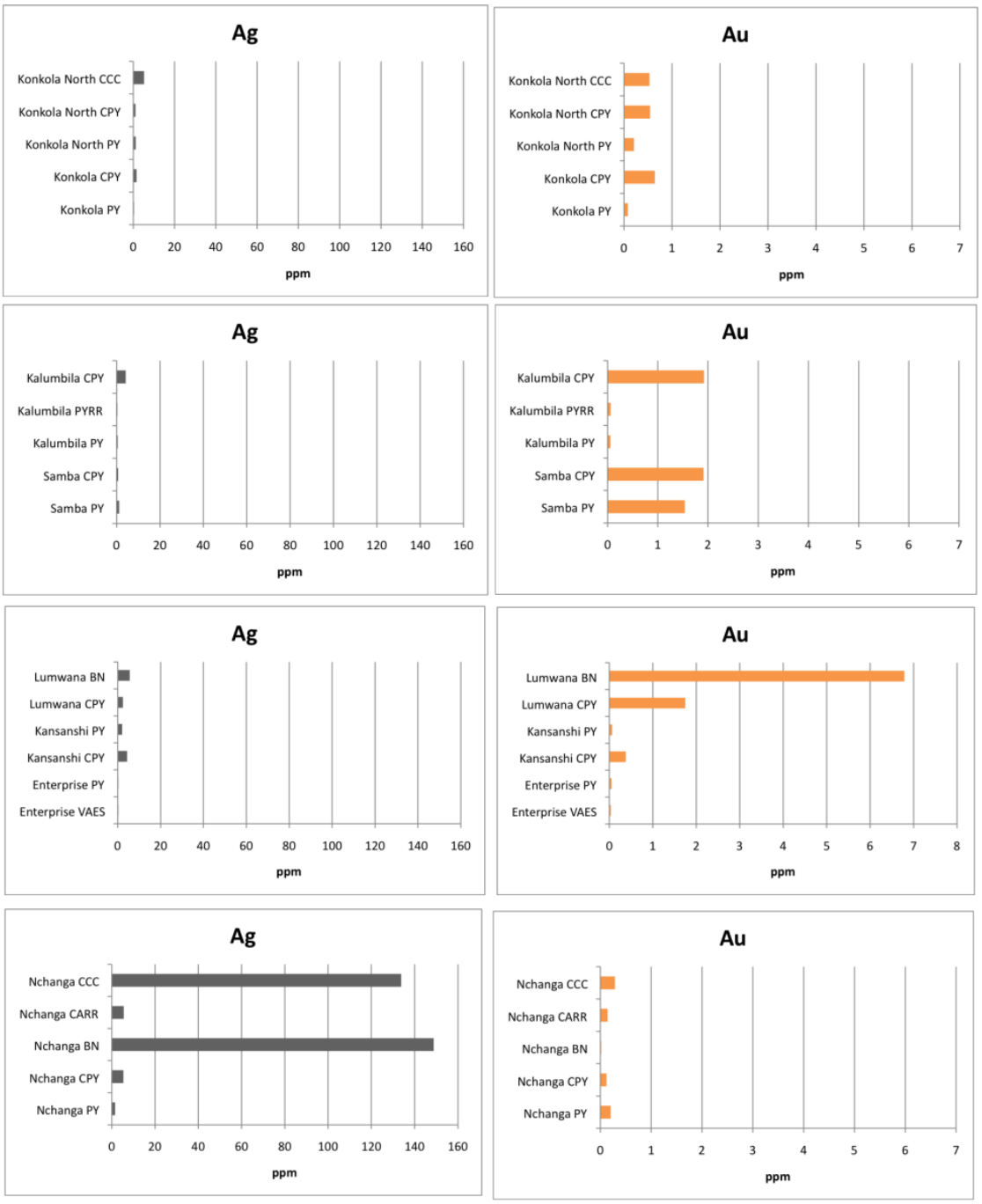

FIGURE 4.21: Ag and Au concentrations for different sulphide mineralogies from the deposits sampled, calculated as a mean of each particular sulphide mineralogy in ppm.

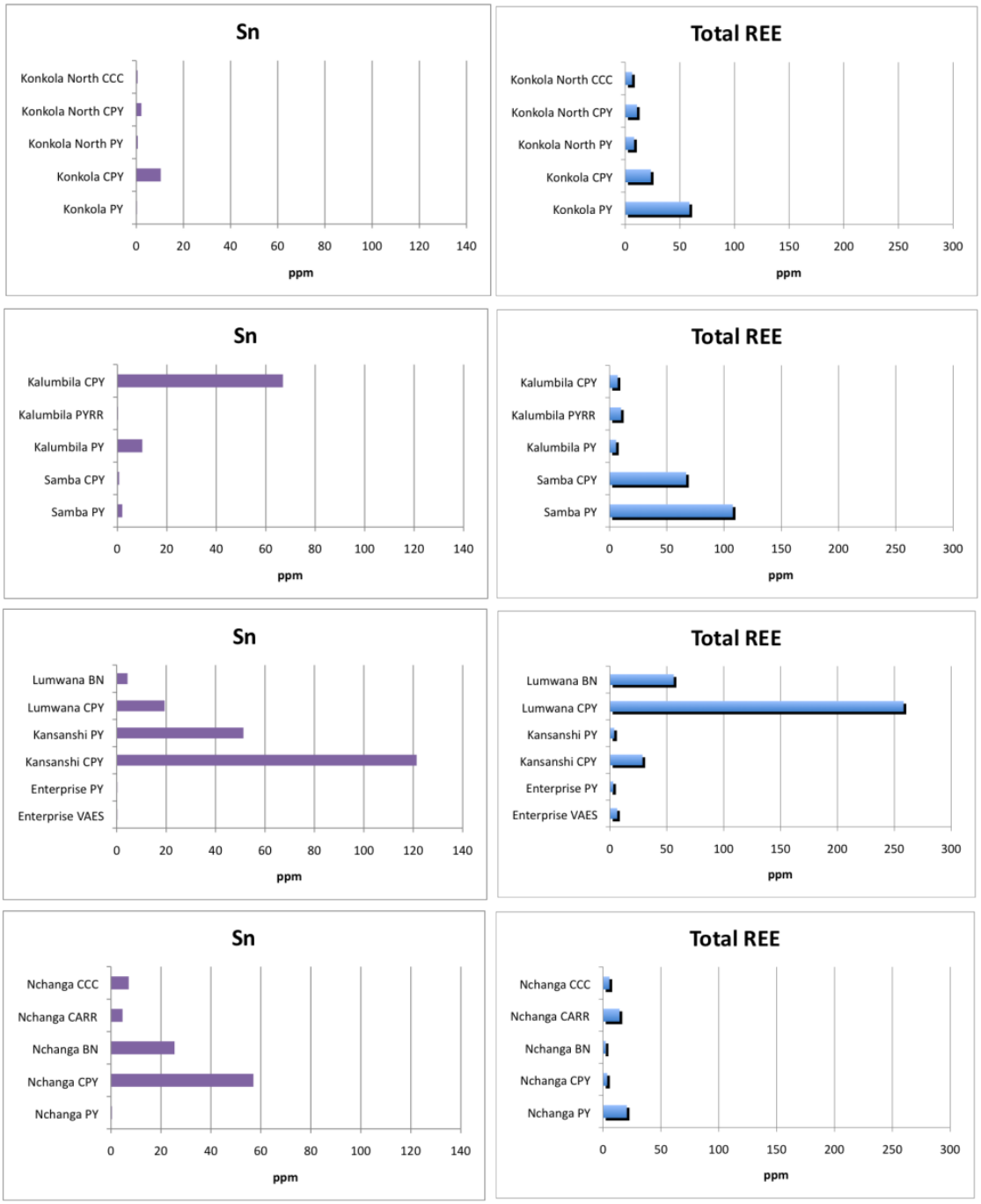

FIGURE 4.22: Sn and total REE concentrations for different sulphide mineralogies from the deposits sampled, calculated as a mean of each particular sulphide mineralogy in ppm.

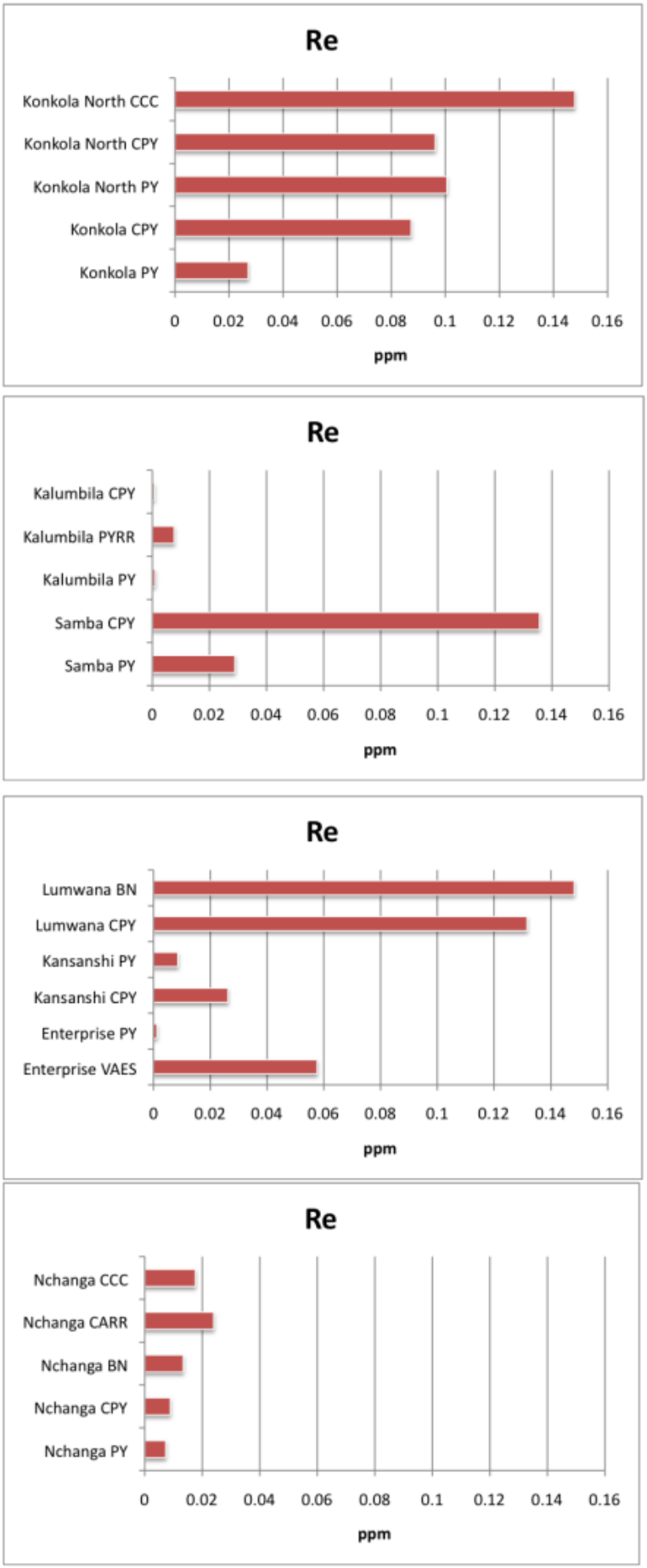

FIGURE 4.23: Re concentrations for different sulphide mineralogies from the deposits sampled, calculated as a mean of each particular sulphide mineralogy in ppm.

show flatter patterns with significant negative Eu anomalies (Michard and Albarède, 1986), broadly similar to the data presented for sulphides here, and it is worth noting that much of the Copperbelt contains a granite or granite gneiss basement. Overall however, there is very little data available on REE contents and patterns in continental fluid systems.

Eu anomalies are often controlled by redox conditions and the development of feldspars, since Eu^{2+} is compatible in plagioclase and K-feldspar, whereas REE^{3+} are not. Crystallisation of feldspars will preferentially remove Eu from the residual fluid or magma, resulting in a negative Eu anomaly (Rollinson, 1993). The hydrothermal fluids identified at black smoker sites are highly reduced, and show positive Eu anomalies, due to alteration and leaching of plagioclase-rich lithologies. Fluids which form SHSC mineralisation are generally thought to be oxidised (Hitzman et al., 2005), with reduction of these fluids causing precipitation of sulphides and development of orebodies. As such, while they may share some similar characteristics with deep sea hydrothermal fluids such as moderate to high temperatures, the oxidation state and host rocks are very different, with the host rocks for Copperbelt fluids typically felsic-derived sediments or felsic basement material compared to the basic rocks present in the ocean crust. Granites and fluids related to granites may show significant to moderate LREE-enrichment and significant Eu anomalies (e.g. Banks et al., 1994; Michard and Albarède, 1986; Zhao and Jiang, 2007), and so fluids in contact with this material may share a similar signature.

An alternative control on REE patterns of sulphide minerals may be small inclusions of other mineral phases. Alteration minerals such as phlogopite and muscovite generated by Copperbelt mineralisation are commonly finely intergrown with sulphides, whilst other mineral inclusions such as zircons which contain high concentrations of REEs could also contribute strongly to the REE content of bulk sulphide samples. It is unlikely that zircon inclusions have contributed significantly to the REE content, since zircons show very steep patterns of HREE enrichment and LREE depletion (Murali et al., 1983) which contrasts with the flat profiles and LREE-enriched profiles shown by sulphides in this study. Biotite and muscovite show LREE enriched patterns, with biotite in particular showing negative Eu anomalies (Laul and Lepel, 1987). These patterns are similar to the steeper LREE-enriched patterns shown by sulphides in this study, and inclusions of micas within the sulphides could be responsible for some of the REE patterns, though cannot explain all of the patterns observed, such as those showing MREE enrichment. An alternative explanation is that development of significant micaceous alteration assemblages would preferentially sequester LREEs within the micas, leaving the remaining fluid progressively comparatively LREE-depleted. Hydrothermal K-feldspar also shows LREE enrichment with a pronounced positive Eu anomaly (Bi et al., 2002), and development of K-feldspar, which is a widespread alteration product in the Copperbelt, would

leave the hydrothermal fluid further depleted in LREE, and with significant negative Eu anomalies. This, when combined with the development of other alteration phases such as feldspars, may provide a mechanism for explaining the significant variation in LREE concentrations seen in Copperbelt sulphides and within individual deposits. A similar interpretation was proposed to explain the negative Eu anomalies and LREE depletion shown by hydrothermal gangue carbonate minerals at the Nchanga deposit (Roberts et al., 2009). REE profiles from Copperbelt uranium minerals are variable, showing relatively flat profiles with LREE depletion and negative Eu anomalies, flat profiles with slight REE enrichment to LREE depletion and Eu anomalies, with a significant variation in LREE concentration as seen in sulphides in this study, and profiles with MREE enrichment and a 'bell curve' pattern (Eglinger et al., 2013), with variations likely caused by variability in oxidation and temperature conditions.

Studies of REE contents of sulphide minerals are rare. Aside from the studies of black smoker sulphide chimneys, which generally reflect the fluid they precipitated from, there are data available for some other types of sulphide ore deposits (Zhao and Jiang, 2007; Zhou et al., 2011). While sulphides from skarn deposits show similar patterns to the related granites, stratiform sulphides are found to be much more variable in REE concentration, with slight LREE enrichment and negative Eu anomalies, similar to profiles shown by some of the sulphides in this study (Zhao and Jiang, 2007). Sphalerite and pyrite from a sediment-hosted Pb-Zn deposit show variably shaped profiles. These ranging from LREE-depleted with negative Eu anomalies to flat profiles and LREE-enriched profiles with negative Eu anomalies, generally showing more significant variation within the LREE concentrations than HREE, similar to the observations made here on Copperbelt sulphides (Zhou et al., 2011).

Ultimately it seems likely that the REE patterns recorded by Copperbelt sulphides reflect a combination of the REE concentration of the mineralising fluid, which in turn may reflect the REE concentrations of host rocks, and the results of the precipitation of alteration assemblage minerals, which are likely to contain much higher concentrations of REEs than sulphides and so are capable of changing the REE budget of the fluid during the process of alteration, as suggested by Roberts et al. (2009).

It is clear from the trace element analysis that sulphides in the Copperbelt are enriched in Co and Ni. The high Co concentrations reflect the Co enrichment in the mineralised district as a whole. This study confirms that deposits formed in the traditional mining area of the Kafue Anticline (Nchanga and Konkola) typically show higher Co concentrations than the deposits from the Domes Region. Whilst particular sulphide mineralogies such as carrolite and pyrite tend to show the highest Co concentrations, concentrations from Nchanga and particularly Konkola are generally higher than the same mineralogies

from other deposits, suggesting that location or specific conditions at these deposits are the most important controls on Co distribution on a regional scale. Even when cobalt is sequestered into specific Co sulphide phases such as carrolite in the Nchanga Upper Orebody, pyrites and chalcopyrites still generally show higher concentrations of Co than equivalent mineralogies at other deposits in the Domes Region. The high Ni concentrations in sulphides at Enterprise and the geographically close Kalumbila-Sentinel deposit on the Kabompo Dome also suggest that local conditions were likely important for supplying the Ni content. The Nchanga deposit shows by far the highest Ag concentrations, particularly in chalcocite and bornite, whereas Au concentrations are highest within bornite and chalcopyrite from Lumwana, and the sulphides from Samba, suggesting differences in the distribution of the noble metals, again indicating that local conditions were probably important, with gold particularly showing affiliation with deposits hosted in basement rocks. Similarly, total REE concentrations were highest in sulphides from the basement-hosted deposits at Samba and Lumwana. Sn concentrations were highest at Kansanshi, and were also relatively enriched in sulphides at Nchanga and Lumwana. This may again be evidence of the importance of specific local conditions, or may also reflect timing of mineralisation in the basin. The Kansanshi and Nchanga deposits have been correlated with post-peak orogenesis and basin inversion, suggesting formation late in the basin history (McGowan et al., 2006; Torrealday et al., 2000). Similarly, mineralisation on the Lumwana shear zones has also been dated as late in the basin history (Eglinger et al., 2013, this study, see section 4.8). Re concentrations are generally very low in main stage sulphides from all the deposits studied, making Re-Os dating difficult (see section 4.8). Other anomalies such as the high Bi concentrations in sulphides from the Nchanga deposit, the As concentrations in the Konkola deposits and the Se concentrations within sulphides at Kansanshi may also reflect local conditions. Concentrations of Al, Ca, Mg, Na and K are highly variable among different sulphide mineralogies and deposits, and are likely a function of slight contamination of sulphide minerals by small inclusions of gangue alteration minerals and host rocks.

REE patterns and trace element concentrations tend to vary more as a function of different deposits than different sulphide mineralogies, indicating local conditions were very important. This study, as well as previous work has suggested that at a gross scale, the mechanisms involved in forming sediment-hosted stratiform sulphide deposits are relatively similar, with oxidised metalliferous saline fluids at moderate to high temperatures intersecting a favourable site for reduction to occur, precipitating metals as copper sulphides. As such, local differences in conditions which would result in different trace element concentrations are most likely primarily a function of chemical variations in host rocks, or variations in the original source of metals, i.e. different fluid pathways

tapped slightly different source areas, allowing for the scavenging of subtly different trace metals.

4.7 Sulphur isotopes

Sulphur isotopes are an excellent, well-understood tool for characterising processes related to sulphide deposition (Faure, 1986). As such, there is a wealth of data available for the Copperbelt from the comprehensive study of Dechow and Jensen (1965) to more recent studies focusing on individual deposits or aspects of mineralisation in great detail (e.g. McGowan et al., 2006; Muchez et al., 2008).

4.7.1 Background theory

Sulphur has four stable isotopes (^{32}S, ^{33}S, ^{34}S, ^{36}S), of which the most important are ^{32}S (95.02 %) and ^{34}S (4.21 %). The sulphur isotope ratio (δ^{34}S) is defined as :

$$\delta^{34}S = \frac{(^{34}S/^{32}S)_{sample} - (^{34}S/^{32}S)_{standard}}{(^{34}S/^{32}S)_{standard}} * 10^3 \quad (4.1)$$

where the standard is Canyon Diablo Troilite (V-CDT), a meteorite with a sulphur isotope ratio similar to that of the mantle (Thode, 1991).

Sulphur isotope ratios are controlled by two main factors, the δ^{34}S of the sulphur source, and any subsequent fractionation processes. Figure 4.24 shows ranges of δ^{34}S for some common substances (and likely sulphur sources) in nature.

There are a number of important processes which affect sulphur isotope ratios. An overview is compiled here from Faure (1986) and Thode (1991):

- Mantle sulphur has δ^{34}S ~0 ‰. Volcanic processes may modify this slightly through outgassing, dependent upon the oxygen fugacity and the sulphate/sulphide ratio.
- Bacterial reduction of seawater sulphate to form pyrite fractionates strongly in favour of the lighter isotope. This results in sedimentary sulphides being negative and the residual seawater δ^{34}S being positive (Fig. 4.25).
- Evaporation does not fractionate strongly, with δ^{34}S of sulphate in evaporite sequences similar to the seawater it was derived from.
- Contamination of magmas by assimilation of intruded sediments drives δ^{34}S towards that of the country rock (sulphurisation).

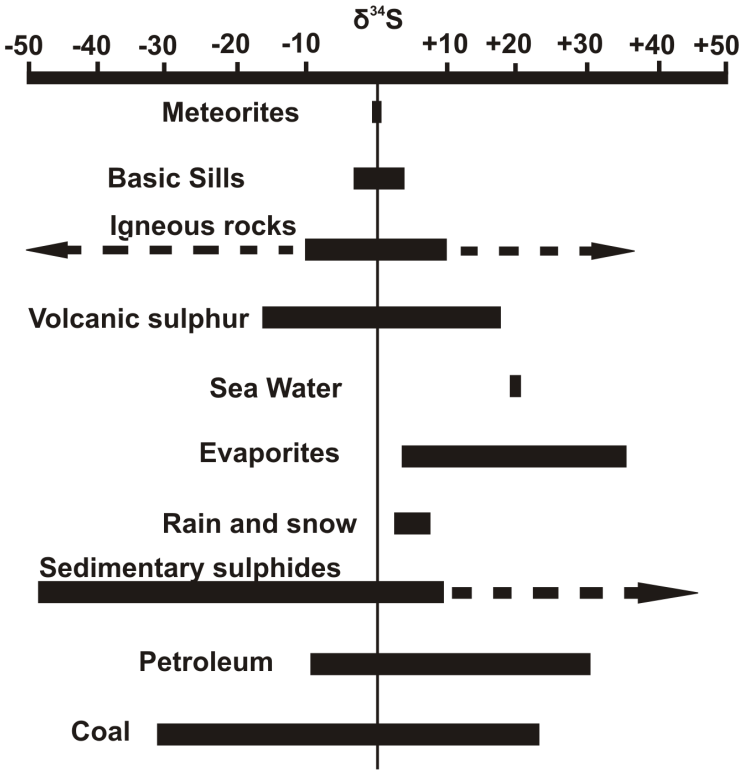

FIGURE 4.24: Variation of δ^{34}S typically found in a selection of common natural substances (after Thode, 1991)

- δ^{34}S of hydrocarbons initially reflects that of the source rock, but typically trends towards more positive values with greater maturity (Orr, 1974).
- δ^{34}S in hydrothermal sulphides is controlled by a variety of factors, including pH, incorporation of pre-existing sulphides and temperature, but a major factor is thermochemical sulphate reduction (TSR), which fractionates in favour of the lighter isotope, but not as strongly as bacterial sulphate reduction (BSR).

Igneous processes have long been ruled out as significant in the formation of SHSC mineralisation. Since these deposits are currently viewed as forming from basin brines, with important roles for dissolution of evaporites, seawater and hydrocarbons, sulphur isotope ratios in these deposits will likely reflect the δ^{34}S of these potential sources, as well as any fractionation effects. The current formation model suggests that mineralisation may occur during late diagenesis, as well as later in the basin history. Therefore, both BSR and TSR may be important in fractionating sulphur isotopes in these deposits, though with increasing temperatures after burial, BSR will cease occur. Figure 4.25 shows the difference in magnitude of fractionation by these two mechanisms. δ^{34}S of seawater has been variable over time (Claypool et al., 1980; Walter et al., 2000), and poor constraints on this can make it difficult to reliably estimate a starting point for δ^{34}S, considering seawater is the most likely initial source of sulphur in a SHSC system.

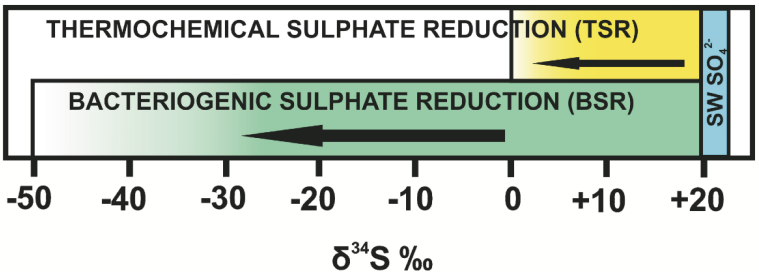

FIGURE 4.25: Schematic showing the difference in magnitude of fractionation between bacterial sulphate reduction (up to ∼-75 ‰) and thermochemical sulphate reduction (up to ∼-20 ‰) of seawater sulphate at modern seawater values.

4.7.2 Results

Table 4.17 contains the results of the sulphur isotope study. As far as the author is aware, this is the first regional study of δ^{34}S on the Zambian Copperbelt since those of Dechow and Jensen (1965) and Selley et al. (2005), and expands the dataset available for the Domes Region. There is significant variability in this dataset, with a range from -7.7 to +42.3 ‰.

Basement deposits sampled (Lumwana and Samba) show a broad range of values from -7.5 to +14.8 ‰ (Fig. 4.26). The range for Samba is -7.5 to -2.7, with a mean of -5.5 ‰. The data from the Malundwe deposit (Lumwana) are generally heavier, ranging from -1.5 to +14.8 with a mean of +9.3 ‰. This data expands the range for Malundwe to slightly lower values than the study of Bernau et al. (2013), and are similar to the data for Lumwana reported by Dechow and Jensen (1965).

Post-kinematic vein deposits (Enterprise and Kansanshi) show δ^{34}S -1.4 to +9.3 ‰ (Fig. 4.26). The data from Enterprise provide the highest and lowest values, with a mean of +3.2 ‰. The Kansanshi data are closely grouped, with a range from -1.2 to +5.1, and a mean of +3.1 ‰. The outlier (-1.2 ‰) in the Kansanshi dataset is disseminated pyrite in the host sediment, and may reflect pyrite with a sedimentary origin. The rest of the disseminated data fall within the same range as the vein-hosted sulphides. All the Kansanshi data fall within the range reported for the deposit by Dechow and Jensen (1965).

Deposits hosted in argillite or arenite show a very broad range of data in this study, from -7.7 to +42.3 ‰ (Fig. 4.26). Konkola and Konkola North show very similar data ranges, -5.0 to +5.8 with a mean of +0.3 ‰ for Konkola, and -7.7 to +3.5 with a mean of -3.2 ‰ for Konkola North. These data fall within the range reported by Sweeney and Binda (1989). The samples from Nchanga show a range from +3.7 to +19.7 and essentially replicate the findings of McGowan et al. (2006), with progressively heavier values from the Lower Orebody to the Upper Orebody, with the heaviest reported value

TABLE 4.17: Table of sulphur isotope data. (v) indicates vein sample, (f) indicates late fracture-hosted, (d) indicates disseminated, (n) indicates nodule-hosted, (km) indicates mainstage mineralisation at Kalumbila, associated with pre to syn-kinematic carbonate-quartz veins and alteration. All other data is 'stratiform'. PY is pyrite, CPY is chalcopyrite, BN is bornite, CCC is chalcocite, VAES is vaesite, CARR is carrolite, PYRR is pyrrhotite

Sample	Deposit	Mineralogy	$\delta^{34}S$
LUM0287-71.05	Malundwe	CPY	+6.5
LUM0287-71.05	Malundwe	CPY	+7.5
MLW0291-27.14	Malundwe	BN	+14.4
MLW0291-27.14	Malundwe	BN	+14.7
MLW0291-27.14	Malundwe	CPY	+14.8
MLW0291-28.00	Malundwe (v)	CPY	+13.9
MLW0291-28.00	Malundwe (v)	BN	+13.1
EQMAL083-94.43	Malundwe	BN	+6.8
SP-002	Malundwe	CPY	+14.3
SP-006	Malundwe	CPY	-1.4
SP-006	Malundwe	CPY	-1.5
ENT0004-62.29	Enterprise	PY	+9.3
ENT0004-69.80	Enterprise	PY	+0.5
ENT0003-74.22	Enterprise	PY	+4.5
ENT0003-80.5	Enterprise	VAES	-1.4
SAM004A-74.60	Samba	PY	-7.5
SAM004A-76.60	Samba	CPY	-6.4
SAM001-67.00	Samba	CPY	-5.3
SAM001-105.50	Samba	PY	-2.7
WS1 NKANA	Nkana	CPY	+10.1
WS4 CHAM	Chambishi	BN	-1.4
WS5 CHIB	Chibuluma	CPY	+5.3
WS6 CHIB	Chibuluma	CPY	+7.2
Low. OB Arkose	Nchanga	CPY	+3.7
Low. OB Arkose	Nchanga	CCC	+3.9
NOP99-TFQ	Nchanga (v)	BN	+12.3
NOP109-TFQ	Nchanga	CPY	+15.9
NOP123-TFQ	Nchanga	CARR	+12.5
NOP124-TFQ	Nchanga	CPY	+13.5
NOP124-TFQ	Nchanga	CARR	+13.8
NOP128-TFQ	Nchanga (v)	CPY	+14
BH7-741-TFQ	Nchanga (v)	CPY	+13.1
BH14	Nchanga (f)	CPY	+7.4
BH105	Nchanga (f)	PY	+19.7
KAN 1-4	Kansanshi (v)	CPY	+4.8
KAN 1-5	Kansanshi (d)	CPY	+5.1
KAN 1-7	Kansanshi (v)	CPY	+2.8
KAN 2-1	Kansanshi (v)	CPY	+3.8
KAN 2-2	Kansanshi (v)	CPY	+2.7
KAN 2-6	Kansanshi (d)	CPY	+3.7
KAN 2-7	Kansanshi (d)	PY	-1.2
KAN 2-9	Kansanshi (v)	PY	+3.4
KAN 3-1	Kansanshi (v)	PY	+4.1
KAN 3-5	Kansanshi (d)	PY	+2.2
KAN 3-9	Kansanshi (v)	CPY	+3.3
KAL23-204.00	Kalumbila (km)	CPY	+20.7
KAL23-445.8	Kalumbila (v)	PYRR	+11.7
KAL0195-52.3	Kalumbila (km)	CPY	+29.4
KAL0195-76.6	Kalumbila (km)	PY	+37.4
KAL0195-88.7	Kalumbila (km)	CPY	+37.8
KAL0195-88.7	Kalumbila (km)	PY	+42.3
KAL0195-113.0	Kalumbila (km)	PYRR	+36.3
KAL0195-113.0	Kalumbila (km)	CPY	+37.4
KN103-821.30	Konkola North	CPY	+3.3
KN103-821.30	Konkola North	PY	+3.5
KN103-928.5	Konkola North	CPY	-5.1
KN103-928.5	Konkola North	CCC	-6.0
KN103-928.5	Konkola North (n)	PY	-4.4
KN103-938.7	Konkola North (f)	PY	-1.9
KN54-191-1368.7	Konkola North (v)	CCC	-7.1
KN54-191-1372.5	Konkola North (v)	CCC	-7.7
KON149A-1412.65	Konkola (n)	PY	+3.7
KON149A-1412.80	Konkola	PY	+4.1
KON149A-1420.65	Konkola	CPY	+5.8
KON149A-1420.65	Konkola	PY	-0.5
KON149A-1421.20	Konkola	CPY	-4.9
KON149A-1421.20	Konkola	PY	+0.3
KON149A-1421.30	Konkola (v)	CPY	-5.0
KON149A-1421.30	Konkola (v)	PY	-0.8

from a late fracture hosted pyrite. The Kalumbila-Sentinel data show a very broad range from +11.7 to +42.3 with a mean of +31.6 ‰. This is by far the heaviest data reported from the Copperbelt, and is significantly heavier than the data for Kalumbila reported by Dechow and Jensen (1965).

Limited data are available on samples from Nkana, Chambishi and Chibuluma, which fall within the range of the rest of the data (Table 4.17).

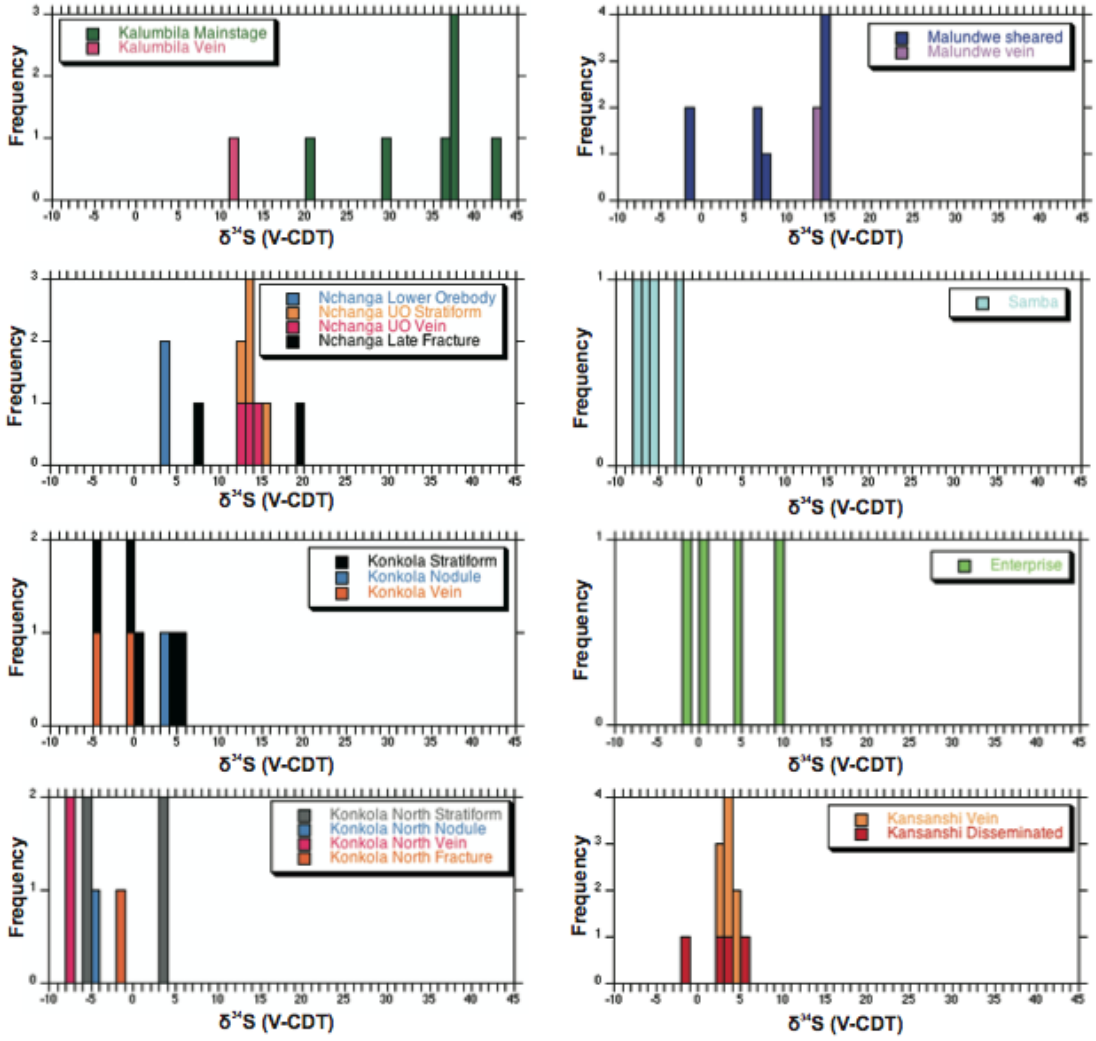

FIGURE 4.26: Stacked histograms of sulphur isotope data segregated by deposit.

At most deposits δ^{34}S does not significantly vary between different sulphide minerals in the same specimens (Table 4.17). At Konkola, where there is some variation between pyrite and chalcopyrite, there is no consistency of one sulphide phase to be lighter or heavier than the other. Sulphides hosted in veins almost always show similar values to the rest of the sulphide mineral assemblage. Sulphides from structures showing morphological similarities to pseudomorphs of evaporite nodules (see Muchez et al., 2008) also show similar values to the rest of the sulphide assemblage.

4.7.3 Implications

The study of Dechow and Jensen (1965) showed that δ^{34}S values have a significant range in the Copperbelt. Although the majority of data fall between ~0 and +10 ‰, supported by this study, in which only Konkola North and Samba show mean δ^{34}S <0 ‰. The data for Kalumbila-Sentinel are significantly heavier. This study and recent work such as Muchez et al. (2008) suggest that the source of sulphur for mineralisation in the Copperbelt was originally seawater, in the form of seawater-derived hydrothermal fluids such as basin brines, sulphate minerals in evaporite sequences or sedimentary pyrite derived from reduction of seawater sulphate. Sulphur incorporated from hydrocarbons may have also played a role. Evaporites show broadly similar values of δ^{34}S to the seawater they precipitated from, however sedimentary pyrite will often have much lighter values due to the fractionation effect of BSR (4.25). While organic-derived carbon can have a wide range of δ^{34}S (Fig. 4.24), coal is not found in the Copperbelt, indicating any sulphur derived from organic material would be from oil or gas in the form of H_2S. From this, it is clear that the only source likely to have an initial δ^{34}S significantly more negative than ~0 ‰ is sedimentary sulphides, and that the rest of the sulphur sources are likely to have much heavier ratios.

The BSR and TSR mechanisms of sulphide formation where sulphides can be formed from sulphate; both fractionate in favour of the lighter isotope (Fig. 4.25). The δ^{34}S of bacteriogenic pyrite depends on the δ^{34}S of seawater sulphate, whether the system is open or closed and kinetic isotope effects, but the mechanism of bacterial sulphate reduction typically averages $\Delta_{sulphate-sulphide}$ 40 ‰ (Ohmoto, 1986) and may reach values up to ~75 ‰ (Faure, 1986). Thermochemical sulphate reduction at temperatures 100–300 ℃ may reach $\Delta_{sulphate-sulphide}$ up to ~20 ‰ (Harrison and Thode, 1957; Kiyosu and Krouse, 1990; Machel et al., 1995; Ohmoto and Rye, 1979). Bacterial reduction of sulphate only occurs at temperatures <80 ℃ (Ohmoto and Rye, 1979). As such, any evidence of BSR in the form of light δ^{34}S would reflect formation of sulphides during 'early' diagenesis, or an incorporation of isotopically light sulphur from pre-existing sedimentary pyrite. In contrast, heavier values are much more likely to reflect only limited isotopic fractionation via the mechanism of TSR. This then represents a mechanism to identify 'early, diagenetic' mineralisation from epigenetic mineralisation occurring later in the basin history at higher temperatures, assuming no isotopic homogenisation has occurred.

Dechow and Jensen (1965) suggested that isotopic homogenisation occurring during metamorphism could account for the generally heavy δ^{34}S signatures prevalent across most Copperbelt orebodies. However, δ^{34}S characteristic of BSR is preserved in shales

at Nchanga, whilst orebody sulphides at the deposit preserve evidence of TSR, indicating that no significant isotopic homogenisation has occurred (McGowan et al., 2006, 2003). Additionally the host rocks at Nchanga have not achieved the upper amphibolite metamorphic grades usually associated with isotopic homogenisation (e.g. Crowe et al., 1990). In this study, the samples from Kalumbila, Konkola and Konkola North have also not been subjected to these metamorphic grades. Mineralisation at Kansanshi occurred after peak metamorphism, shown by the post-kinematic veining and Re-Os dating (Torrealday et al., 2000) and so metamorphism is unlikely to have caused isotopic homogenisation at this deposit either. Kyanite is present in the mineral assemblage of both Lumwana and Enterprise, suggesting that these deposits may have suffered a higher grade of metamorphism, with the basement rocks at Lumwana in particular thought to have been subjected to high pressures (John et al., 2004). Metamorphic grade is difficult to identify at Samba, but as a basement-hosted deposit, this also may have been subjected to significant metamorphism. Lumwana, Enterprise and Samba may all have reached metamorphic grades high enough for isotopic homogenisation to occur. However, the range of δ^{34}S data at these deposits is no different to others in the study which underwent metamorphic grades no higher than greenschist facies. Additionally, the relatively wide range in values at Lumwana (-1.5 to +14.8 ‰, this study) suggests that no significant homogenisation of δ^{34}S has occurred for the deposit as a whole.

Whilst identification of BSR and TSR may give strong indications on whether mineralisation formed via diagenesis or not, it is critical to know the initial seawater sulphate value before fractionation occurs in order to correctly identify the mechanism of reduction. However, secular variation in δ^{34}S through time is poorly constrained, particularly in the Precambrian, due to lack of preservation of evaporite sequences to use as proxies. Figure 4.27 represents a recent reconstruction of seawater sulphate δ^{34}S during the Neoproterozoic. In addition to the poor constraints upon δ^{34}S, it is clear that there has been significant variation in the δ^{34}S of seawater sulphate through this time period, particularly during basin closure and orogenesis of the Lufilian Arc. The long basin history allows for multiple fluid events (this study) and it is likely that sulphate in the basin brines preserved different δ^{34}S based upon their age of formation, as well as any interaction with evaporites. McGowan et al. (2006) suggested that one possible explanation for the heavy δ^{34}S signatures of late pyrite at Nchanga was formation from fluids with an isotopically heavier initial seawater sulphate from later in the basin history. From the data available in this study, and historical data, it is reasonable to suggest that much of the variation in the data of the Copperbelt can be explained by this initial source heterogeneity. Much of the data available fall between ~0 to +10 ‰ (this study, Dechow and Jensen, 1965; McGowan et al., 2006; Selley et al., 2005), and thus are within the range expected for thermochemical reduction of seawater sulphate with an initial

δ^{34}S of +20 to +30. This range is broadly the range currently predicted over the history of the Copperbelt (Fig. 4.28). In addition, many deposits show evidence for multiple mineralisation events through their individual history (Nchanga; McGowan et al., 2006; Nkana; Brems et al., 2009; Muchez et al., 2010), and variable initial δ^{34}S may compound other factors such as closed system fractionation (e.g. Nchanga; McGowan et al., 2006) increasing heterogeneity.

It is notable in this study that the two well documented argillite hosted deposits (Konkola and Konkola North) show some of the lightest δ^{34}S signatures. Previous workers have suggested that this may reflect a role of bacterial formation during diagenesis (Sweeney et al., 1986). However, these signatures are not light enough to conclusively identify BSR of Neoproterozoic seawater sulphate. Previous studies providing light δ^{34}S as evidence for BSR had values as low as $\sim$ -16 ‰ for sedimentary pyrite at Nchanga (McGowan et al., 2006) and -14.2 ‰ for chalcopyrite at Luiswishi (Lerouge et al., 2005; Muchez et al., 2008). Instead, it seems more likely that these slightly lighter values are simply a reflection of incorporation of isotopically light sedimentary pyrite. These orebodies are hosted within shales, which are likely to have initially contained much more sedimentary pyrite than an arenite as they are formed under reducing conditions, and thus would be more prone to lighter δ^{34}S. Indeed, this mechanism may also account for the lighter δ^{34}S values at Luiswishi, and other argillite-hosted deposits (Fig. 19 in Selley et al., 2005).

The Lumwana and Enterprise data, while potentially having undergone isotopic homogenisation via metamorphism, show no evidence for BSR, instead falling well within the range expected for TSR of Neoproterozoic seawater sulphate, as do the data for Kansanshi. Whilst only limited data are available, the light δ^{34}S generated for samples from Samba, and the heavy data for sulphide mineralisation at Kalumbila-Sentinel are more difficult to explain. It is highly unlikely that bacterial sulphate reduction would have played a significant role (or any role at all) in the basement-hosted Samba deposit, particularly due to the fact that the host rocks are metamorphosed igneous and volcanic successions. The light values may reflect an isotopically light igneous source of sulphur, though most sulphur found in igneous rocks shows δ^{34}S $\sim$ +5 to -5 ‰ (Faure, 1986), which would put the Samba data on the lower end or just outside of this typical range. Whilst clearly a more thorough investigation is required into the sulphur isotope systematics of the Samba deposit, these data strongly suggest that light sulphur isotope ratios can be formed in the Copperbelt region without a role for BSR. The data presented here for the Kalumbila-Sentinel deposit are by far the heaviest recorded from the Copperbelt, and are difficult to reconcile with either mechanism of seawater sulphate reduction, with much of the data showing δ^{34}S $>$ δ^{34}S of seawater sulphate identified through the Neoproterozoic (Table 4.17; Fig. 4.28). The similarities in mineralisation style between the Kalumbila-Sentinel deposit and other Copperbelt mineralisation,

particularly Nkana (Brems et al., 2009) suggest that the ultimate mechanism of deposit formation is likely to be similar. The heavy data for Kalumbila-Sentinel may then be the result of closed-system fractionation processes, where ^{32}S is preferentially incorporated into early mineralisation, with the remaining supply of S becoming increasingly enriched in the heavier isotope, as suggested for the steadily heavier values at the Nchanga deposit (McGowan et al., 2006). However, the paucity of light data is difficult to explain with this mechanism. This may reflect a sampling bias, in which vein hosted samples were prioritised as they contained both sulphide and gangue mineralisation, as well as providing the best sulphide grades at the deposit and the majority of mineralisation.

4.7.4 Comparisons with other SHSC districts

$\delta^{34}S$ in the Central African Copperbelt typically shows values between ~0 to +10 ‰ (Dechow and Jensen, 1965), and the results of this study are consistent with these values. In contrast, other major SHSC districts record lighter $\delta^{34}S$. Sulphide mineralisation in the Kupferschiefer shows $\delta^{34}S$ -44.7 to -2 ‰ (Bechtel et al., 2001; Marowsky, 1969), with the majority of the data between ~-44 and -20 ‰. $\delta^{34}S$ at the White Pine deposit varies between -20 to +35 ‰, with the majority of the data between -15 and +20 ‰ (Burnie et al., 1972). The lightest data in these districts (particularly in the case of the Kupferschiefer) are consistent with BSR of seawater sulphate at time of formation (Claypool et al., 1980; Walter et al., 2000). These three districts show fundamental differences in the distribution of sulphur isotope values (Fig. 4.29). The strong skew towards light $\delta^{34}S$ in samples from the Kupferschiefer and paucity of heavier values is strongly indicative of fractionation via BSR. While timing of mineralisation in the Kupferschiefer remains unclear, data suggest timing from early Permian (end Cisuralian) to Late Triassic (Pašava et al., 2010). This time period shows a remarkable variation in $\delta^{34}S$ of seawater sulphate from the lightest values recorded in Earth history (~+12 ‰) up to +28.4 ‰ (Claypool et al., 1980; Newton et al., 2004; Walter et al., 2000). The light $\delta^{34}S$ recorded by Kupferschiefer mineralisation supports an early formation hypothesis with an important role for BSR (Fig. 4.27). In contrast, data from the Zambian Copperbelt typically show much heavier values (Fig. 4.29) more consistent with the TSR mechanism, and the trend towards heavier $\delta^{34}S$ occurring later in the basin history (Figs. 4.27; 4.28). Whilst many of sulphur isotope data for the CAC are consistent with the TSR mechanism, figure 4.28 shows that the average data for deposits reliably dated using the Re-Os technique are slightly lighter than expected (~5 ‰ or less) for TSR of seawater sulphate present at that time alone. In these cases, there may have been incorporation of light $\delta^{34}S$ from sedimentary pyrite, or simply the fluids involved were older, and spent a period of time residing in or migrating through

the basin. If these fluids were older, they would likely preserve an isotopically lighter seawater sulphate (Figs. 4.27; 4.28), and mean the TSR mechanism could achieve lighter values. This is highly likely, as it seems more realistic that palaeofluids were expelled during orogeny than a new influx of seawater entered the system during compression. Alternatively, if the sulphur source was not seawater, but instead being derived from evaporite sequences, these would also preserve a lighter δ^{34}S signature from when they were deposited earlier in the basin history.

The data for White Pine differ from both the Zambian Copperbelt and the Kupferschiefer data, having peaks at ∼-8 and ∼+18 ‰, and generally presenting a broad range of values (Fig. 4.29). This wide range is difficult to reconcile with solely BSR or TSR (especially considering the poor constraint on seawater sulphate δ^{34}S at the time of formation), perhaps reflecting both processes importance in the formation of the deposit. Best estimates of δ^{34} seawater sulphate at this time are ∼+16 to ∼+22 ‰ (Canfield, 1998; Canfield and Teske, 1996), suggesting that while BSR is responsible for the light δ^{34}S, many of the heavier data are more consistent with fractionation by TSR, or heavier than seawater altogether. Recent research has suggested the White Pine deposit formed as a one-pass fluid system driven by compaction caused by subsequent deposition (Swenson et al., 2004), and a single pass system would be more likely to cause Raleigh fractionation from a single initial batch of sulphur. It is interesting to note that all three of these districts formed around the same time as significant positive sulphur isotope excursions in seawater sulphate. These excursions are typically thought to indicate periods of ocean anoxia (Canfield, 1998; Newton et al., 2004; Walter et al., 2000), in some cases perhaps representing favourable burial conditions for organic matter useful as a reductant in these systems. However, the Copperbelt Orebody Member in the CAC was deposited before the Neoproterozoic excursion, and it is likely the Kupferschiefer was deposited before the the excursion in the late Permo-Triassic. It remains unclear whether this correlation has any significance.

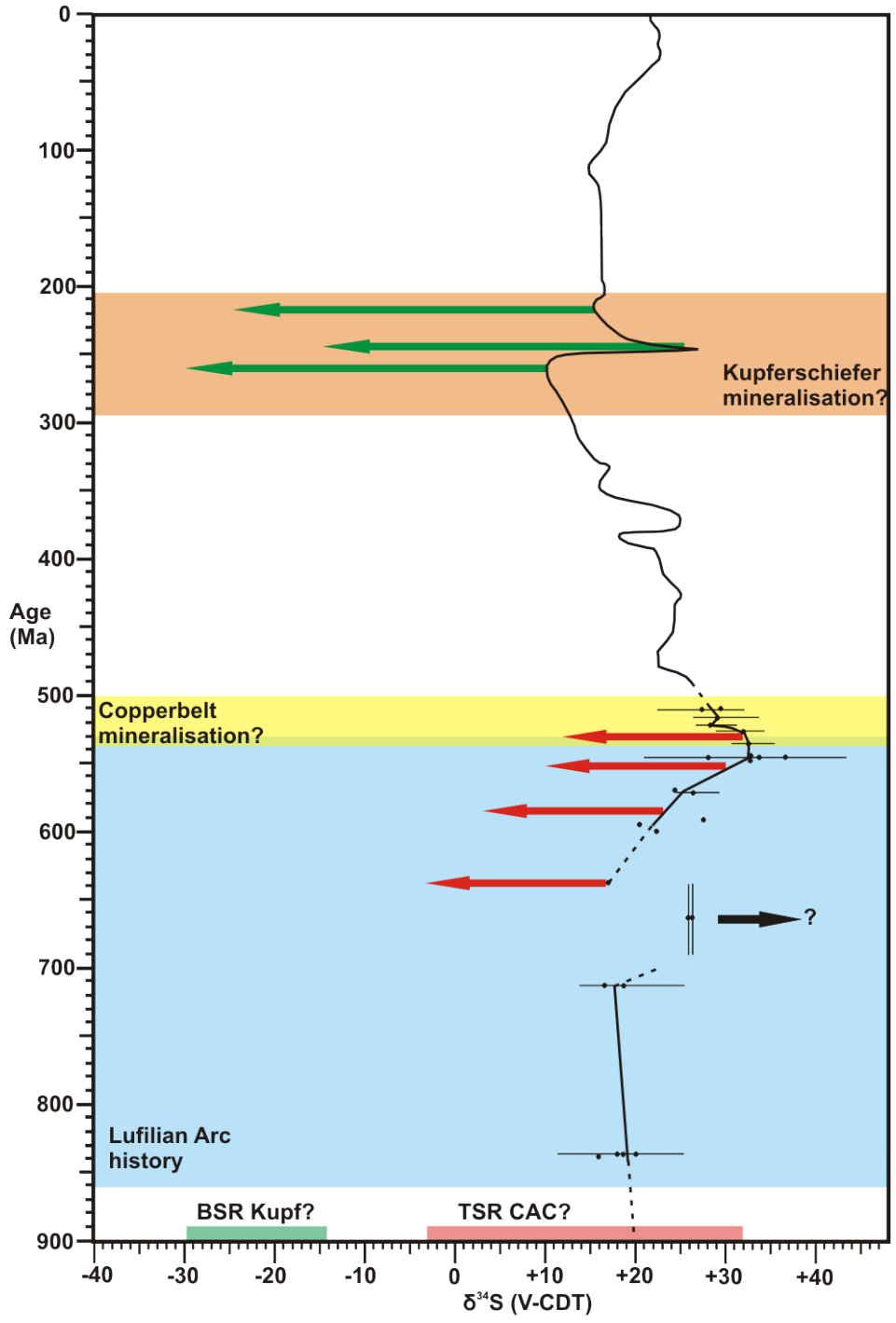

FIGURE 4.27: Variation in $\delta^{34}S$ through time and mechanisms of formation for the Kupferschiefer and the Central African Copperbelt. Orange area represents age constraints on Kupferschiefer mineralisation (Pašava et al., 2010). Yellow area represents age constraints on Copperbelt copper sulphide mineralisation (see 4.8). Blue area represents the lifetime of the Lufilian arc (see 1.3.4). Green arrows show average expected magnitude of fractionation via BSR of seawater sulphate (curve). Red arrows show maximum expected magnitude fractionation via TSR of seawater sulphate (curve). BSR is much more realistic for forming the range of $\delta^{34}S$ for Kupferschiefer, whilst TSR better explains the data for the Copperbelt (see Fig. 4.29). Adapted from Walter et al. (2000).

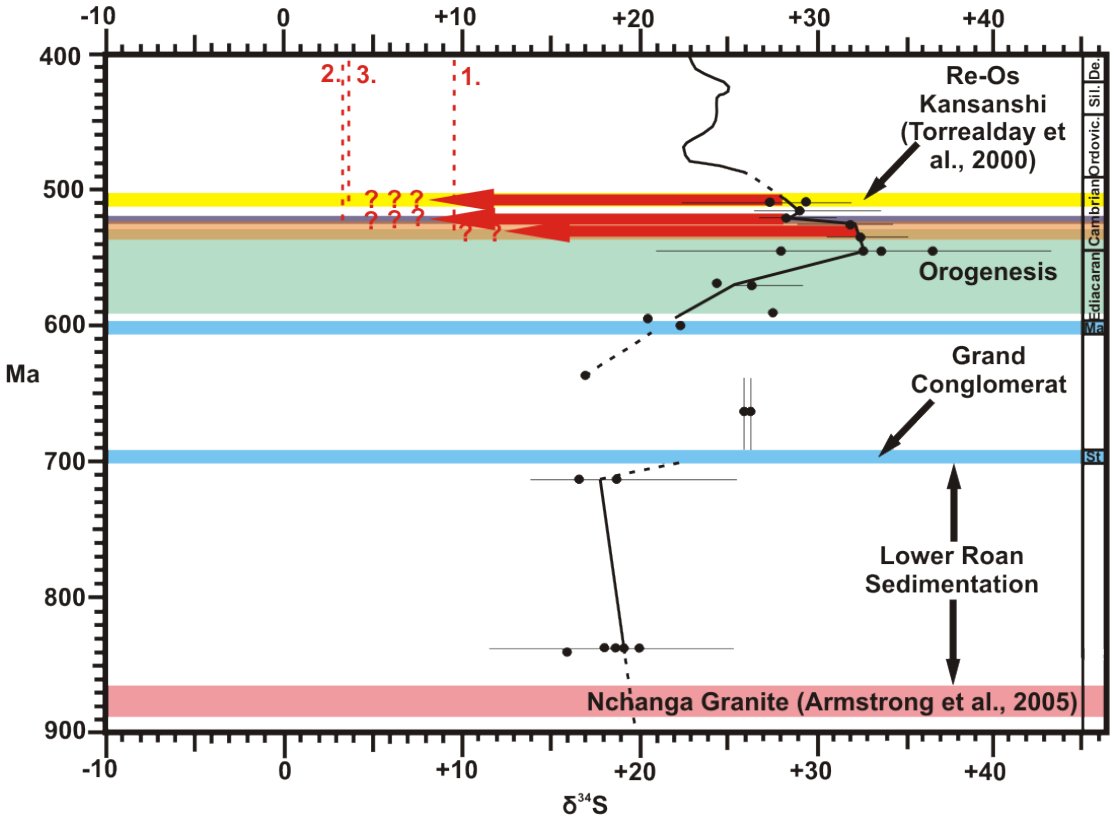

FIGURE 4.28: Variation in δ^{34}S through time and mechanisms of formation for the Copperbelt Horizontal bars show age constraints for the Copperbelt and mineralisation. Red shows the Nchanga granite, and maximum age of Roan sedimentation, with sedimentation constrained by the development of glacial diamictites (blue). Green shows the estimated range of basin inversion and orogenesis. In orange and purple are the Re-Os constraints on mineralisation at Lumwana and Enterprise (this study, see 4.8) and in yellow the constraints for the Kansanshi deposit. The red arrows show the maximum fractionation effect of TSR from seawater sulphate at the time of mineralisation. Numbered vertical dotted lines show the average δ^{34}S for 1) Lumwana, 2) Enterprise, 3) Kansanshi obtained in this project. Average δ^{34}S for these deposits is slightly lighter than would be expected from TSR of seawater of those ages. Adapted from Walter et al. (2000).

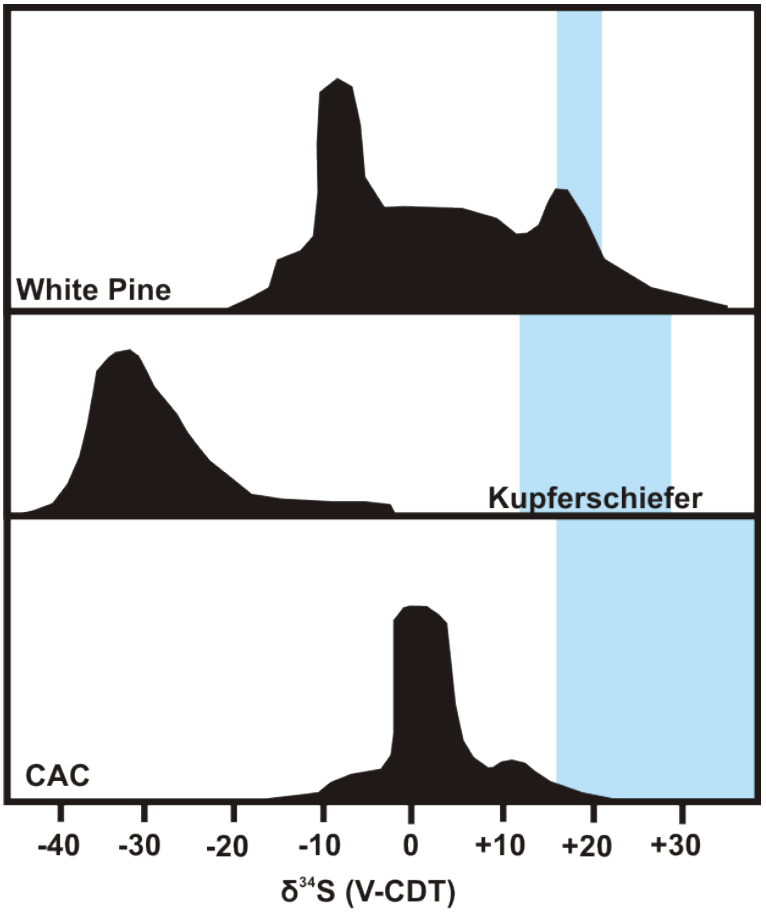

FIGURE 4.29: Distribution of sulphur isotope data for different SHSC districts (black) and range of δ^{34}S for seawater sulphate over the possible times of deposit formation (blue). Adapted from Burnie et al. (1972).

4.8 Rhenium-Osmium dating

Understanding the absolute timing of copper and cobalt sulphide mineralisation in the Central African Copperbelt (and in SHSCs in general) remains perhaps a significant challenge. There are constraints placed on relative timing by large-scale events, such as the onset of sedimentation and the formation of post-kinematic veins defining the closure of the basin (see Chapter 1), and the sulphide paragenesis is relatively well understood for the region (Selley et al., 2005) and at many deposits (e.g. Annels, 1989; Brems et al., 2009; McGowan et al., 2006; Sweeney et al., 1986). However, reliable absolute dates on mineralisation are restricted to uranium phases and associated mineralisation (Decrée et al., 2011; Eglinger et al., 2013; Richards et al., 1988b,a), sulphides from Pb-Zn deposits (Kamona et al., 1999; Kampunzu et al., 2009; Schneider et al., 2007), and a single Re-Os study at Kansanshi (Torrealday et al., 2000).

The Re-Os dating technique provides a powerful mechanism for the dating of sulphide minerals, since these minerals (particularly molybdenite) are commonly enriched in Re (Stein et al., 2001). Dates of 816 ± 62 Ma (Konkola) and 576 ± 41 Ma (for a number of samples of different mineralogies and from different deposits, Nkana, Chibuluma and Nchanga) obtained using the Re-Os technique are frequently cited from the unpublished work of Barra et al. (2004) (e.g. Selley et al., 2005). Since these data were generated, there has been further work undertaken to improve the robustness of the Re-Os technique and attempt to understand the factors controlling the distribution of Re and Os in sulphide minerals. Even individual grains of molybdenite can be extremely heterogeneous in Re and Os concentration (Selby and Creaser, 2004) and other sulphides may show extreme variation in Re and Os geochemistry even at a hand specimen scale (Morelli et al., 2004, 2010). As such, blends of different sulphide mineralogies as utilised in the study of Barra et al. (2004) are now regarded as unlikely to produce a reliable age. Additionally it is unrealistic to use data from different deposits which may not have formed in the same manner or at the same time to generate an isochron and expect it to give a reliable age, particularly considering multiple stages of mineralisation are identified at these deposits (Brems et al., 2009; McGowan et al., 2006; Muchez et al., 2010). The correlation (or lack thereof) in timing of mineralisation is the key question, so to utilise these different samples to generate a single age seems fundamentally flawed.

This section presents precise Re-Os dates obtained from molybdenite samples collected from the Domes Region of the Zambian Copperbelt, and evaluates these new data in conjunction with the data from Kansanshi (Torrealday et al., 2000), and the other geochronological constraints on the history of the Copperbelt.

4.8.1 Samples selected for dating

A large suite of samples was available for this study, consisting of pyrite, chalcopyrite, bornite, chalcocite, carrollite and molybdenite from numerous different deposits and settings (see section 4.3). However, since sulphides other than molybdenite often contain low concentrations of Re, only larger non-molybdenite samples were tested for Re concentrations. Unfortunately, only the molybdenite samples were regarded as containing enough Re to be likely to give accurate dates.

In total, 5 samples containing molybdenite mineralisation were available for testing, four from the Lumwana deposit, and one from the Enterprise prospect (Fig. 4.30). The sample from Enterprise was obtained from a friable heavily-altered talc and muscovite zone within the stockworked vein area. The four samples from Lumwana came from different sections within the orebodies. Two samples were obtained from the Malundwe open pit, one showing coarse molybdenite mineralisation within a pegmatitic section of granite gneiss on the edge of a quartz vein, and the second showing sheared mineralisation similar to main-stage sulphide mineralisation at the deposit. The samples from Chimiwungo were from coarse mineralisation in a pegmatite, and in RC chips from an intersection also containing significant glassy quartz, interpreted as representing a late-stage coarse quartz vein.

4.8.2 Re-Os concentrations and geochronological data

The results of the geochemical testing and dating of the 5 samples are presented in Table 4.18:

TABLE 4.18: Rhenium and Osmium concentrations of molybdenite and model ages with uncertainties.

	CHI-132	ZA-196981	ZA-196982	ZA-196983	ENT0004 82.28
Deposit	Lumwana (Chi)	Lumwana (Chi)	Lumwana (Mal)	Lumwana (Mal)	Enterprise
Lithology	Glassy quartz vein	Granite gneiss pegmatite	Sheared in granite gneiss	Pegmatite vein	Talc-musc alteration
Re (ppm) $\pm 2\sigma$	1048.5 2.71	251.9 0.65	527.0 1.36	741.2 1.92	91.6 0.24
^{187}Re (ppb) $\pm 2\sigma$	659037 1705.1	158300 409.6	331222 857.0	465869 1205.3	57586 149.2
^{187}Os (ppb) $\pm 2\sigma$	5799.4 4.16	1415.6 1.00	2908.7 2.04	4164.6 2.94	503.9 0.36
Total common Os (pg)	10.3	13.2	106.2	7.7	31.7
Model Age (Ma) $\pm 2\sigma$ (Ma)	525.9 2.2	534.4 2.2	524.8 2.2	534.2 2.2	522.9 2.1

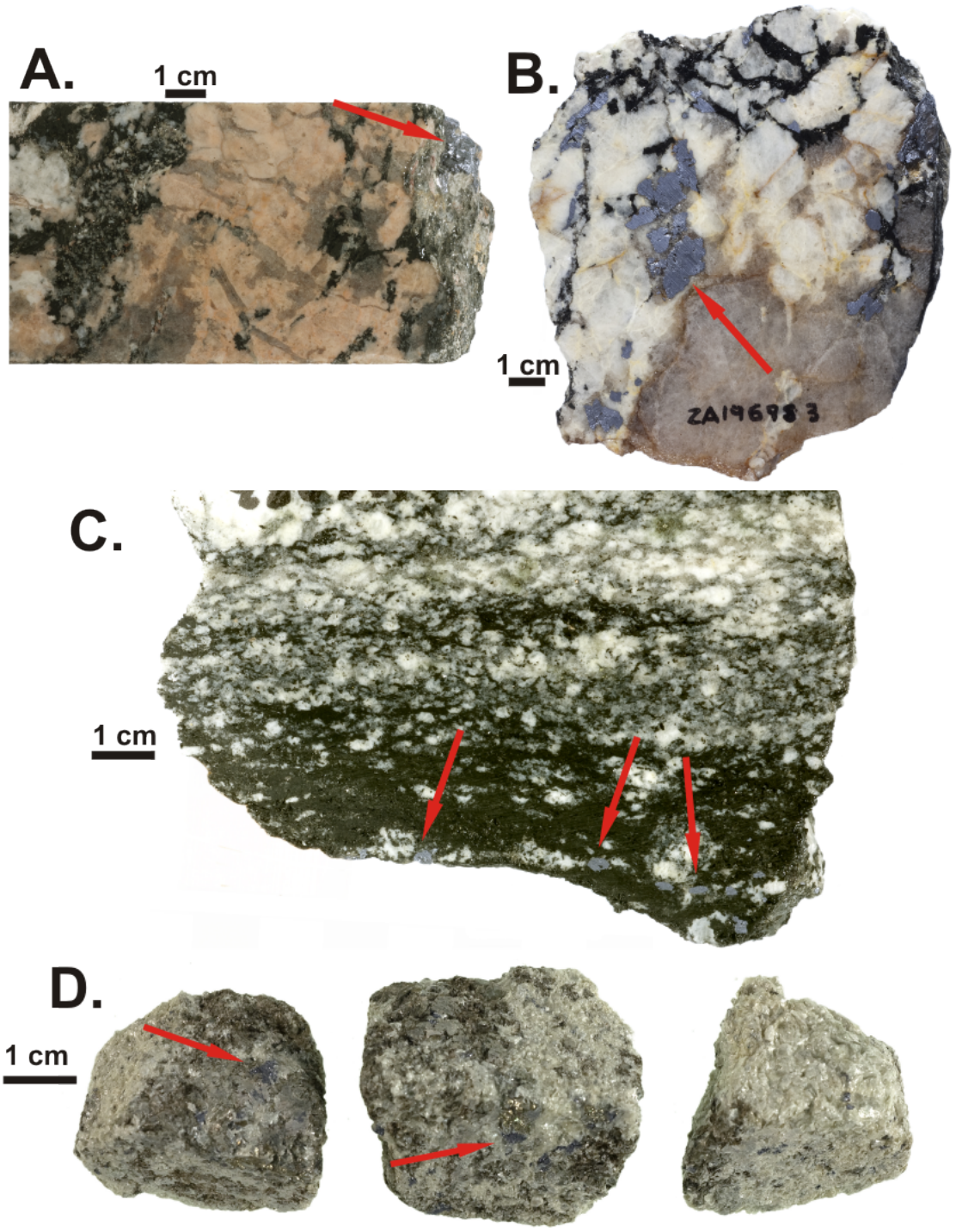

FIGURE 4.30: Molybdenite samples for Re-Os dating. A) ZA-196981: Sample from Lumwana (Chimiwungo) showing coarse mineralisation hosted in pegmatite vein. B) ZA-196983: Sample from Lumwana (Malundwe) with coarse mineralisation hosted in pegmatite on the edge of quartz vein. C) ZA-196982: Sample from Lumwana (Malundwe) showing sheared mineralisation hosted in biotite-rich section of granite gneiss. D) ENT0004 82.28: Sample from Enterprise showing mineralisation in friable talc-muscovite alteration zone. Red arrows show molybdenite mineralisation.

4.8.3 Implications for mineralisation and understanding of the basin history

This new suite of Re-Os dates significantly expands the dataset for mineralisation in the Copperbelt, previously limited to Kansanshi (Torrealday et al., 2000) and Kipushi (Schneider et al., 2007). Whilst a significant deposit, mineralisation at Kipushi is not typical of the Copperbelt, forming on a large fault, and containing primarily Zn and Pb, as well as significant unusual by-product metals such as Ge. Schneider et al. (2007) dated Kipushi using two independent radiogenic dating techniques (Re-Os and Rb-Sr), resulting in an age ~451 Ma. This age is significantly younger than the closure of the basin (Fig. 4.32), and is likely unrelated to the other Re-Os dates available. The remaining Re-Os data span a range ~535–500 Ma, representing multiple occurrences of molybdenite mineralisation from multiple deposits across a number of different basement inliers of the Domes Region (Fig. 4.31). This temporal range of emplacement for molybdenite mineralisation is closely synchronous with estimates on the timing of peak metamorphism in the Lufilian Arc (John et al., 2004) and the shift towards post-orogenic cooling (Cosi et al., 1992; John et al., 2004; Selley et al., 2005; Fig. 4.32). The earlier dates at Enterprise and Lumwana are also synchronous with the later uranium event of Decrée et al. (2011), whilst the earlier dates of emplacement for the Kansanshi veins occur at a similar time to the late hydrothermal event at Musoshi (Richards et al., 1988a; Torrealday et al., 2000).

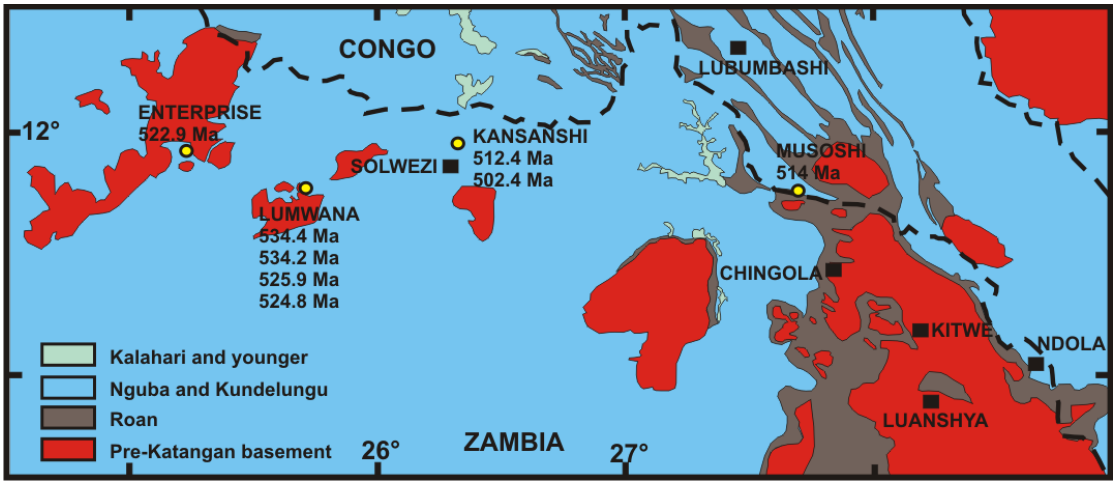

FIGURE 4.31: Map of the Copperbelt showing the deposit with reliably dated mineralisation. Enterprise and Lumwana dated via Re-Os of molybdenite (this study). Kansanshi dated via Re-Os dating of molybdenite (Torrealday et al., 2000). Musoshi hydrothermal event dated via U-Pb of rutile (Richards et al., 1988a). Map adapted from Cailteux et al. (2005a)

Whilst the Cu sulphide mineralisation at Lumwana remains undated, the Re-Os constraints available for Malundwe and Chimiwungo deposits may be interpreted in multiple

ways. The excellent precision of the Re-Os technique allows for individual mineralising events to be identified, even when they are temporally closely related, for example the two distinct mineralising events at ∼512 and ∼502 Ma at Kansanshi (Torrealday et al., 2000). On the basis of this precision, the data available for Lumwana can be grouped into two pairs, at ∼534 and ∼525 Ma, and may be interpreted as representing two phases of mineralisation. However, with this small dataset, this may not be significant, and more data are required to fully interrogate this hypothesis. The mineralisation age of ∼534 Ma supports the age of uranium mineralisation reported for Lumwana (∼530 Ma) by Eglinger et al. (2013). These data suggest that mineralisation took place on the Lumwana shear zones from ∼535–525 Ma. Additionally, from the limited data set available, mineralisation at both Malundwe and Chimiwungo appears to have occurred concurrently, and since the sulphides and uranium mineralisation are sheared along with the host rocks, movement on the shear zones clearly persisted until this time as well.

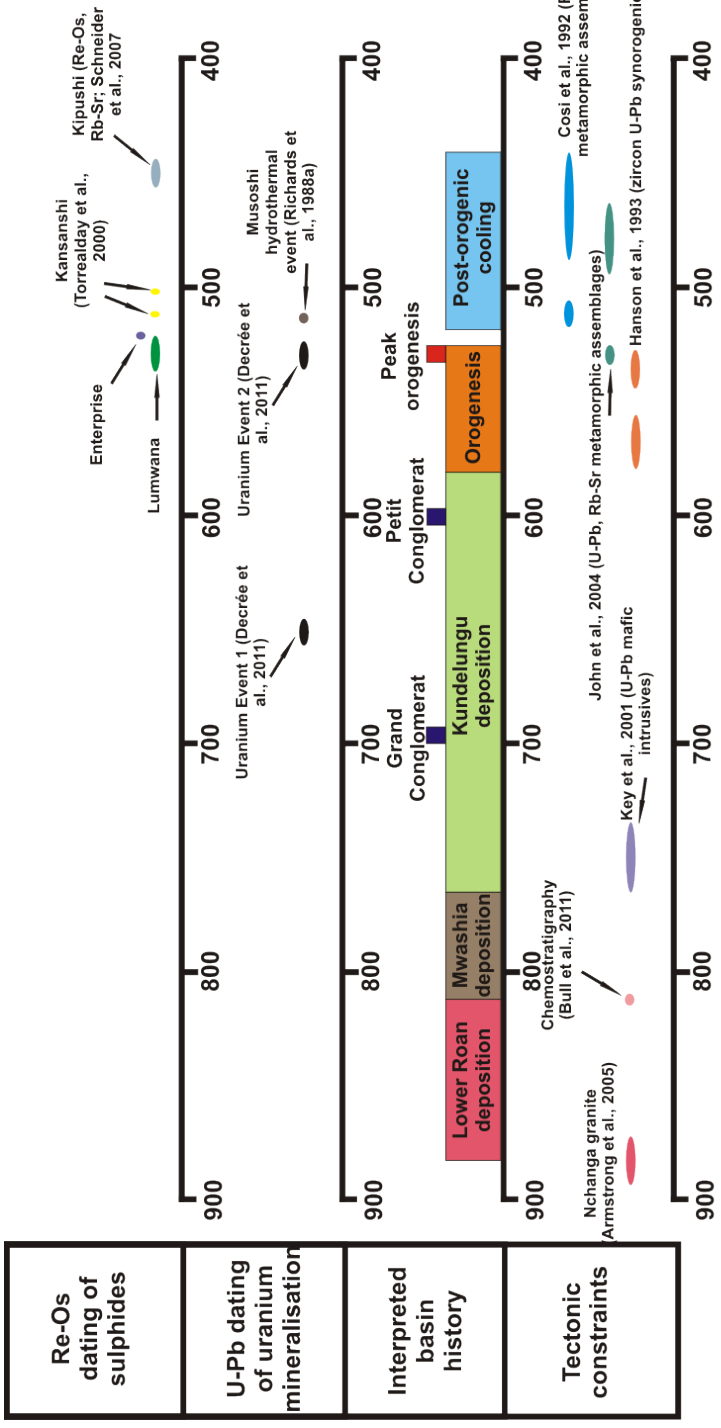

FIGURE 4.32: A selection of dating constraints for the Copperbelt and the evolution of the Lufilian Arc, including the new data presented here. Grand and Petit Conglomérat data from Walter et al. (2000)

The expanded Re-Os dataset indicates a molybdenum mineralising event across the Domes Region broadly contemporaneous with peak metamorphism and the waning stages of orogenesis in the Lufilian Arc. This event is also generally contemporaneous with the late uranium event of Decrée et al. (2011) and other hydrothermal events occurring during orogenesis. It is highly unlikely that the Re-Os ages reflect metamorphic resetting, as the Re-Os geochronometer is extremely robust (Raith and Stein, 2000; Stein et al., 2001). Whilst this late event has been recognised for many years (e.g. Richards et al., 1988a), recent research suggests it is becoming increasingly significant. Whilst there is still vigourous debate over the timing and introduction of sulphide mineralisation, studies by Brems et al. (2009); McGowan et al. (2006); Muchez et al. (2010); Torremans et al. (2013) emphasise that at the very least, orogenesis and related fluid events play a significant role in remobilising and concentrating ores, controlling their distribution and grade on a deposit scale. Other workers go further, suggesting that stratiform mineralisation may have been formed during orogenesis (Sillitoe et al., 2010). In the case of the Domes Region, it is now clear that the two major economic deposits so far discovered (Kansanshi, Lumwana) and one of the current exploration prospects (Enterprise) were also formed during this event. This has important implications for exploration in the Domes Region, suggesting that structures of this age are viable targets for exploration and have proven potential to host economic tonnages. Structures of this age are likely to be more common, larger and more well-developed in the Domes Region, which has undergone more significant metamorphism than the Kafue Anticline and the External Fold and Thrust Belt.

It is perhaps unsurprising that the Re-Os data for the Copperbelt indicate formation and mineralisation late in the history of the basin, since these molybdenite samples are all associated with late-forming structures. Kansanshi and Enterprise represent post-kinematic vein sets, whilst Lumwana represents a shear zone interpreted to have undergone motion during basin inversion and/or orogenesis (Bernau et al., 2013). Additionally it must be stated that molybdenite is not a common mineral in the main sulphide paragenesis of the Copperbelt (Selley et al., 2005), which has hindered the application of the Re-Os technique. However, these data represent the only directly applied absolute temporal constraint available on sulphide mineralisation in the district, aside from estimates on Zn-Pb deposits (e.g. Kamona et al., 1999; Schneider et al., 2007). As such, until an earlier date is generated, the temporal constraints available simply highlight the importance of orogenesis on mineralisation, particularly in the Domes Region.

Whilst Re-Os dating has been applied to the Kupferschiefer in a number of studies, applied to both mineralisation, and the host black shales, much of this work is not peer reviewed. The available data suggest a range of timings for mineralisation from syngenetic to epigenetic (see Pašava et al., 2010 for a review of the available dates).

Re-Os data for the Tangdan SHSC deposit in China also indicate multiple stages of mineralisation over a protracted period (Huang et al., 2013). These studies support the hypothesis that SHSC deposits can form throughout the history of the host basins.

4.9 Conclusions

REE concentrations in Copperbelt sulphides, as well as stratiform sulphides in general are variable at both a regional and deposit scale. These profiles show LREE enrichment, LREE depletion and relatively flat profiles, typically with negative Eu anomalies and the shape of the profile controlled by variations in concentrations of LREE rather than HREE. There is little to no control on REE profile shapes by different sulphide mineralogies, though sulphides associated with supergene alteration of orebodies may show anomalously high Dy and Ho. There is no consistent control on REE profile shape by remobilisation of sulphides into veins. The lack of a positive Eu anomaly shows fundamental differences from sulphides produced by black smoker fluids, which reflect the source hydrothermal fluid. Instead, the profiles of these sulphides reflect the formation of a fluid formed in different, more oxidised conditions contained in a fundamentally different host rock sequence. Sulphides contain low concentrations of REE and so any microinclusions of other mineral phases may contribute disproportionately to the REE budget of the sample. Many profiles exhibit similar shapes to that of biotite, and phlogopite is a common alteration phase intergrown with sulphides in the Copperbelt. Development of common alteration minerals such as phlogopite, muscovite and K-feldspar would leave the the fluid LREE depleted with negative Eu anomalies, and progressive alteration may explain the high variability in LREE concentrations and negative Eu anomalies observed in Copperbelt sulphide samples.

Trace element concentrations in Copperbelt sulphides typically show enriched levels of Co compared to other transition metals, as would be expected for one of the world's most enriched Cobalt districts, with deposits from the Kafue Anticline such as Nchanga and Konkola the most Co rich. Other trace element concentrations suggest that variation in trace elements within Copperbelt sulphides is more strongly controlled by different deposits more than different sulphide mineralogies, similar to the observations about REE profiles. This suggests that diversity in local conditions, probably a combination of host rocks and the differences in the original source rocks for the metals are responsible for the differences in trace element concentrations in sulphides. Timing of deposit formation may also play a role in controlling the trace element budget of sulphides. Other element concentrations such as Al, Na, K, Ca and Mg are likely a function of slight contamination of sulphides by small inclusions of host rock and alteration assemblages.

Sulphur isotope data generated in this study suggest that thermochemical sulphate reduction of seawater sulphate was the primary source of sulphide for mineralisation. The variations in the sulphur isotope dataset can be readily explained via the significant variation in seawater sulphate values during the late Neoproterozoic in which the Central African Copperbelt was formed. Lighter data may be explained by incorporation of preexisting sedimentary pyrite from the host succession formed by bacterial sulphate reduction. Bacterial sulphate reduction was unlikely to have played a role in the formation of the ore deposits themselves.

Re-Os dating of 5 molybdenite samples from the Lumwana and Enterprise deposits records dates from $\sim$ 535 to 523 Ma, suggesting molybdenite mineralisation occurred late in the basin history during orogenesis. The data for the Lumwana shear zone are synchronous with dates reported for uranium mineralisation on the shear zone (Eglinger et al., 2013), and these data highlight the importance of orogenesis in forming mineralisation in the Domes Region and the Copperbelt as a whole.

Chapter 5

Uranium mineralisation and remobilisation at the Lumwana Copper (Co-U) Deposits, Zambia

5.1 Abstract

Uranium is a common accessory element in many copper-cobalt deposits of the Zambian Copperbelt. At the Lumwana Cu-Co deposits of the Domes Region, northwest Zambia, significant uranium mineralisation (>500 ppm) occurs within a Cu-Co bearing quartz-mica-kyanite schist (Ore Schist), and in particular at the boundaries between the Ore Schist and the host granite gneiss sequences. The most extensive uranium mineralisation and highest uranium grades occur at the boundary between the Ore Schist and the Footwall Gneiss. Three contrasting settings of uranium mineralisation are recognised: 1) Coarse uraninite and brannerite, developed within the Ore Schist, typically enclosed within phyllosilicates and sulphides, and associated with hydrothermal rutile, ilmenite, zircon, REE-rich carbonates and phosphates with the sulphide and uranium minerals enclosed and tectonised within a flat lying (S_1) fabric; 2) Coarse centimetre-scale uraninite and brannerite mineralisation hosted in syn-kinematic quartz-carbonate veins variably oriented and deformed by the prevailing S_1 fabric. 3) Uraninite and coffinite which are remobilised along mica cleavage planes and phyllosilicate grain boundaries and enclosed within retrograde chlorite often associated with post-kinematic veining.

There is evidence that brannerite, which formed as Type 1 mineralisation, is progressively leached, with the removal of uranium from grain margins resulting in rims enriched in relatively immobile titanium (rutile) with local reprecipitation of the uranium as coffinite. These observations suggest that initial uranium mineralisation (brannerite

± uraninite predates sulphide precipitation and peak metamorphism and is then subsequently remobilised during a later phase of hydrothermal activity characterised by the discordant quartz (± chlorite) veins, which cut the deposit. These observations in part may explain the variable age dates reported for uranium mineralisation across the Copperbelt.

5.2 Introduction

This chapter describes the nature and relative timing of the uranium mineralisation at the Lumwana Mine in the Domes region of Zambia, west of the classic Copperbelt district of the Kafue Anticline. Lumwana Mine consists of two deposits, one currently exploited (Malundwe) with a second (Chimiwungo) being prepared for production. Whilst these deposits are primarily copper-bearing with minor cobalt (e.g. at Chimiwungo), they locally contain significant uranium mineralisation. A series of additional prospects in the region are being drilled at the time of writing, and contain similar styles of mineralisation.

The Lumwana deposits do not conform to the conventional historic model of Copperbelt ore formation (Cu-Co orebodies located at the boundary between an arkosic sandstone package and a series of shale formations), instead containing sulphide ore within a biotite-phlogopite-muscovite-quartz-kyanite schist shear zone developed within a host basement granite-gneiss sequence (Bernau et al., 2013).

5.3 Uranium mineralisation in the Copperbelt

Uranium is part of a suite of elements commonly associated with sedimentary copper deposits which in addition to Cu include: Co, Ag, Zn, Pb, Fe, and V (Hitzman et al., 2005; Oszczepalski, 1999). A Cu-U association within the Central African Copperbelt has long been recognised, with localised uraniniferous zones reported for many of the Zambian deposits e.g. at Nkana, Chibuluma, and Luanshya (Garlick and Gane, 1961; Mendelsohn, 1961c; Meneghel, 1981) and in the Congolese Copperbelt at Shinkolobwe, Swango, Kalongwe, Musonoi, Kambove and Kamoto (Meneghel, 1981). The uranium mineralisation is characterised by disseminated pitchblende within weakly Cu-mineralised quartz-argillites, with accessory uraninite, brannerite and coffinite e.g. at Mindola (Jordaan, 1961) and Musoshi (Lefèbvre and Tshauka, 1986; Richards et al., 1988b), with a second phase of brannerite, uraninite, chalcopyrite and bornite mineralisation within cross-cutting calcite (± quartz ± feldspar ± anhydrite) veins (Jordaan, 1961). Elsewhere, uranium mineralisation, without associated Cu-Co mineralisation, occurs e.g. at

Kawanga and Mikutukulu in the Domes Region of Zambia (Meneghel, 1981). Multiple generations of uranium mineralisation are preserved across the Domes Region, associated with a series of tectono-thermal events during basin inversion and the subsequent decompression and unroofing of the Lufilian arc (Cosi et al., 1992; Meneghel, 1981). Previous exploration and research on the uranium of the Lumwana deposits recognised several styles of uranium mineralisation in the region including fine-grained disseminated brannerite in association with ilmenite, rutile, titanomagnetite and coarse-grained uraninite occurring in massive aggregates and veins which crosscut an F_1 foliation, but are subsequently deformed by later deformation phases (Cosi et al., 1992). Recent work by Decrée et al. (2011) argues for two distinct uranium mineralisation events across the Copperbelt. The first at 652.3 ± 7.8 Ma suggests that initial uranium concentration and mineralisation predates the onset of orogenesis in the Lufilian arc, likely initiated at 592 ± 22 Ma (Rainaud et al., 2005), with a second event at 530.1 ± 5.9 Ma consistent with estimates of Lufilian peak metamorphism (John et al., 2004).

This section describes in detail the location, setting and relative timing of the uranium mineralisation at Lumwana in order to better understand the relationship between copper mineralization and uranium mineralisation. The uranium distribution within the Malundwe Ore Body is reported and a detailed petrographic and SEM study of the uranium mineralisation showing remobilisation of the primary uranium assemblage by a secondary event is provided.

5.3.1 Geological Background

Cu-Co (± U) mineralisation in the Mwombezhi Dome (Fig. 5.1A) was initially discovered in the 1920s and following a long and sporadic history of exploration drilling that finally resulted in the opening of the Lumwana Mine and the Malundwe open pit in 2009. Initial descriptions of the geology of the Lumwana deposits interpreted the ores as syngenetic, subsequently metamorphosed (Benham et al., 1976; McGregor, 1964). However, Benham et al. (1976) recognised that metamorphism of lower Roan material was unlikely to produce the mineral assemblages present at Lumwana. Bernau et al. (2013) provide a current view on ore formation at Lumwana, interpreting the deposits as the result of a shear zone development within pre-Katangan basement lithologies.

The Lumwana Mine consists of two deposits, one currently exploited (Malundwe) with a second (Chimiwungo) in preparation for production. Although these deposits are primarily copper-bearing with minor cobalt (e.g. at Chimiwungo), locally they contain significant uranium mineralisation. Furthermore, the Lumwana deposits do not conform to the conventional historic model of Copperbelt ore formation, i.e. Cu-Co orebodies

located at the boundary between an arkosic sandstone package and a series of shale formations. The Lumwana deposits are tabular, with disseminated Cu-(Co) sulphide ore bodies located within the basement inlier complex of the Mwombezhi Dome. The host rocks are a series of quartz-feldspar ± muscovite ± biotite ± haematite ± amphibole gneisses, with occasional quartz-feldspar ± biotite schist units (Bernau et al., 2013). Schist units are interpreted to represent shear zones, and typically show gradational boundaries with surrounding gneiss units. Localised gneiss units are also occasionally incorporated into the shear zone and surrounded by schists (Fig. 5.1C), and this process can be seen on a smaller scale with the presence of boudinaged quartz veins (Bernau et al., 2013). The sulphide mineral assemblage is contained within a biotite-muscovite-quartz-kyanite schist (Ore Schist), though also extends locally into internal gneiss units (Bernau et al., 2013). Kinematic indicators show a top to the north shear sense consistent with the overall sense of motion on the Lufilian Arc. Gneiss and schist preserve a flat lying planar fabric (S_1), which is overprinted by a later parallel fabric defined by muscovite (S_2) and a N-S orientated stretching lineation. Sulphides are deformed by the S_1 fabric and are often concentrated in pressure shadows of kyanite, indicating mineralisation occurred syn- or pre-peak metamorphism (Bernau et al., 2013).

5.4 Uranium mineralisation

Uranium mineralisation is variably distributed within the Malundwe and Chimiwungo deposits although is much less evident at Chimiwungo. The gross distribution of uranium mineralisation in the Malundwe pit is well illustrated using the grade control data from the Vulcan mine database (Fig. 5.1B - G). The copper and uranium orebodies trend north-south (Fig. 5.1B), aligned within a N-S gently dipping stretching lineation (L_1) with copper grades being higher towards the centre of the Ore Schist. However, in contrast to the relatively consistent shape and grade of the copper ore body, the uranium mineralisation shows a variable morphology at the deposit scale. The main bodies of uranium mineralisation are discontinuous, with a lack of continuity at a scale of tens to hundreds of metres between the various sections through the ore body (Fig 5.1B). Although generally constrained within the Ore Schist, the uranium-mineralised zones show a strong affinity for the boundaries with the hanging wall and particularly the footwall gneiss units (Fig. 5.1C; D and F). Uranium ore grades are relatively poor around gneiss units entrained within the ore schist (Fig. 5.1C). Uranium mineralisation outside of the Ore Schist typically shows low grades (Fig. 5.1C; D and F) related to post-kinematic sub-vertical quartz carbonate veins cross-cutting the deposit.

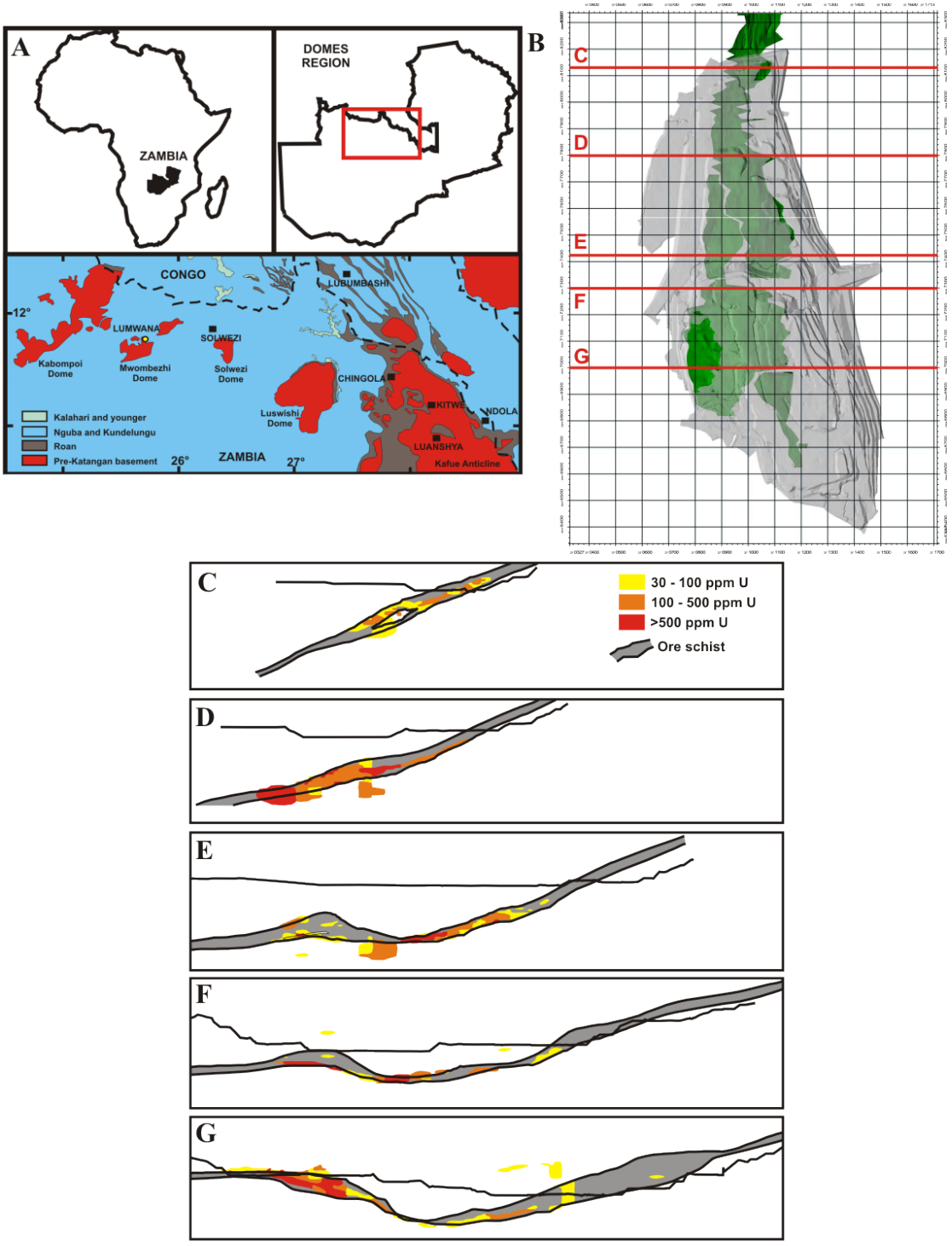

FIGURE 5.1: Gross distribution of uranium mineralisation in Malundwe open pit, Lumwana Mine. A) Maps showing the location of the Lumwana deposits B) Plan view of pit shell (as of November 2009) and uranium orebodies (green) oriented along the north south stretching lineation present at Malundwe. Red lines show position of block model cross sections C-G (scale in ppm). C) Mineralisation on boundaries of ore schist with gneissic units, including a giant gneiss boudin. D) Mineralisation within the ore schist, and on the footwall gneiss contact. E) Mineralisation at the footwall and hanging wall contacts of the ore schist and gneisses, and within the ore schist. F) Mineralisation at the contact of ore schist and footwall gneiss. G) Mineralisation at footwall contact and within the ore schist.

There are three main settings for the uranium mineralisation: Type 1) Coarse-grained millimetre to centimetre scale brannerite and uraninite aggregates, often surrounded by halos of secondary uranium minerals (Fig. 5.2A, B, C) and rare chlorite; Type 2) Coarse centimetre scale uranium mineralisation hosted in quartz-carbonate veins, typically oriented similarly to schistosity, often boudinaged and typically overprinted by the late muscovite fabric (Fig. 5.2D). These veins show evidence of reaction with the host schist and are overprinted by the late muscovite fabric. These veins are texturally analogous to quartz veins within the ore schist, which locally remobilise sulphide minerals; Type 3) Disseminated uranium mineralisation associated with post-kinematic discordant quartz veins, often with associated retrogressive chlorite alteration (Fig. 5.2E).

Coarse, tectonised uraninite and brannerite aggregates, characteristic of Type 1 mineralisation, are found throughout the Ore Schist, although tend to be predominantly located at or near the footwall and hangingwall contacts between the Ore Schist and the gneiss units in which the shear zone is developed (Fig. 5.1B-F). Uraninite occurs as disseminations and larger grains within a quartz and phyllosilicate assemblage, which defines the schistosity (Fig. 5.3A-C), and is frequently associated with rutile (Fig. 5.3D, E) and ilmenite, as well as phosphates (Fig. 5.33E) and rarely REE-rich carbonates. Uraninite is locally enclosed in sulphide phases (Fig. 5.3F) as well as rarely within brannerites.

Brannerite forms large grains (often greater than 100 μm) and aggregates typically hosted within biotite (Fig. 5.4A-D). Brannerite is commonly enclosed by sulphide minerals, typically chalcopyrite, but also bornite (Fig. 5.3G-H), which are frequently partially oxidised to iron oxides. Galena occurs as small, discrete crystals around the edges, and more rarely within the centre of brannerite crystals and aggregates (Fig. 5.4A, B, D). Brannerite grains and aggregates frequently show rims of rutile. In contrast brannerites enclosed by sulphide minerals tend not to show the U-depleted rims. Brannerite is rarely also contained within apatite (Fig. 5.3E).

Fine-grained uraninite and coffinite are commonly identified within chlorite (Fig. 5.4E-G), and are often located within the cleavage planes and along grain boundaries of phyllosilicates (Fig. 5.4H), forming Type 3 mineralisation. Chlorite at Luwmana exists as radial aggregates overprinting the main fabric (Fig. 5.2E) and individual grains replacing other phyllosilicates (Fig. 5.4E, F), formed during retrograde metamorphism, and is often associated with late discordant veining which cuts the deposit.

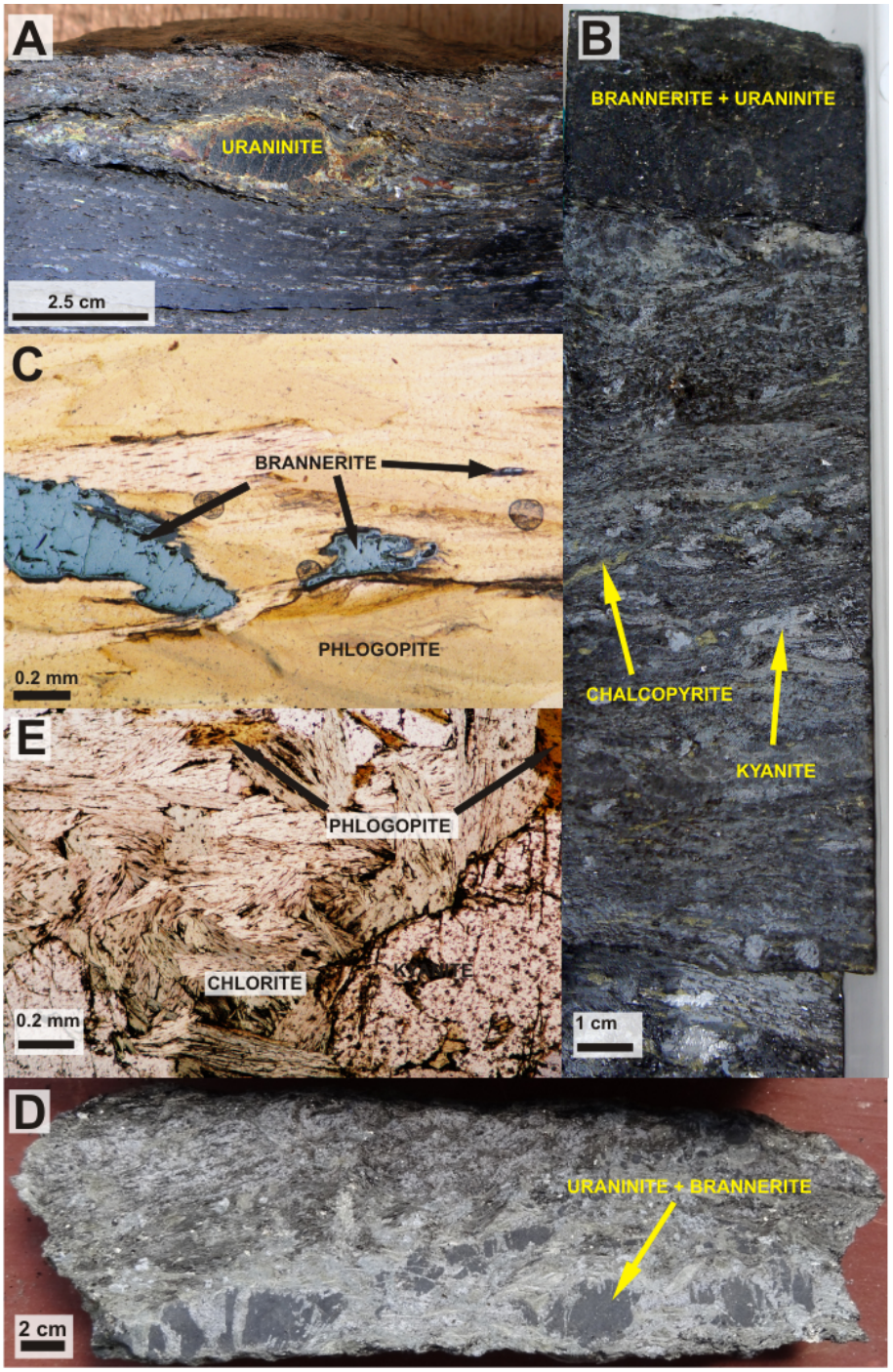

FIGURE 5.2: Textural relationship between uranium mineralisation, and the metamorphic fabric. A) Coarse uraninite enclosed within the dominant schistosity. B) Coarse slug of uranium mineralisation enclosed within the schistosity. A side view of the drill core is similar to relationship illustrated by (A). C) Reflected light microscopy and plane polarised light image of coarse brannerite aggregates enclosed within biotite showing S_1 fabric. D) Boudinaged quartz-carbonate vein containing coarse uranium mineralisation becoming overprinted by late muscovite fabric. E) Plane polarised light image of retrogressive radiating chlorite replacing biotite of S_1 fabric.

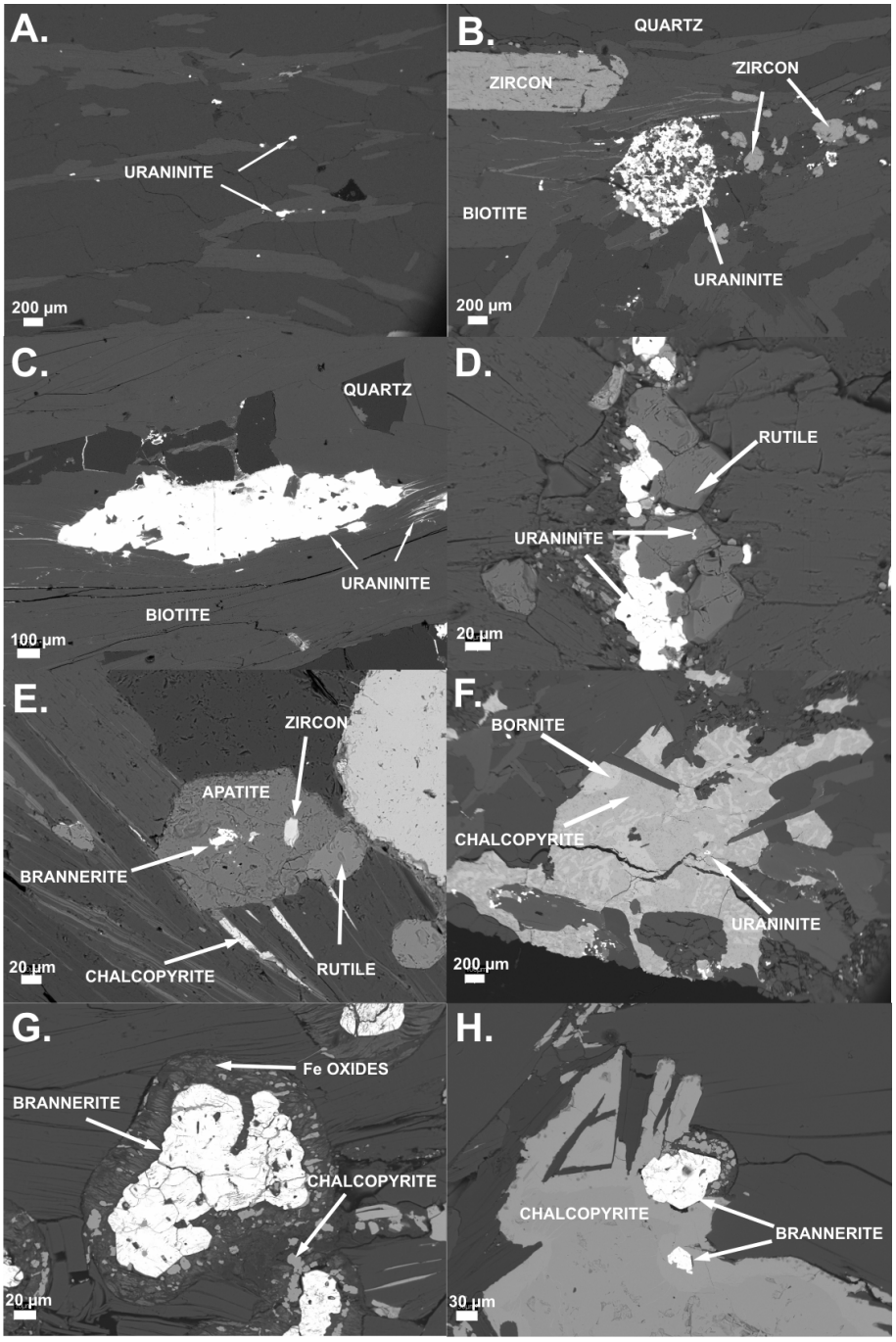

FIGURE 5.3: SEM images illustrating relationship between uranium and the metamorphic fabric and sulphides. A) Uraninite enclosed within quartz and biotite as part of the metamorphic fabric. B) Uranium mineralization as an aggregate, enclosed within phyllosilicates of the metamorphic fabric. The aggregate contains uraninite, zircon and REE-rich carbonate. C) Coarse deformed uraninite mass enclosed within the metamorphic fabric. D) Uraninite intergrown with rutile. E) Brannerite and zircon contained in apatite and rutile, in turn enclosed within phyllosilicates with chalcopyrite mineralisation. F) Uraninite grain enclosed by sulphide mineralisation. G) Brannerites enclosed by sulphides (partially altered to oxides), in turn enclosed by the metamorphic fabric. H) Brannerite contained within chalcopyrite.

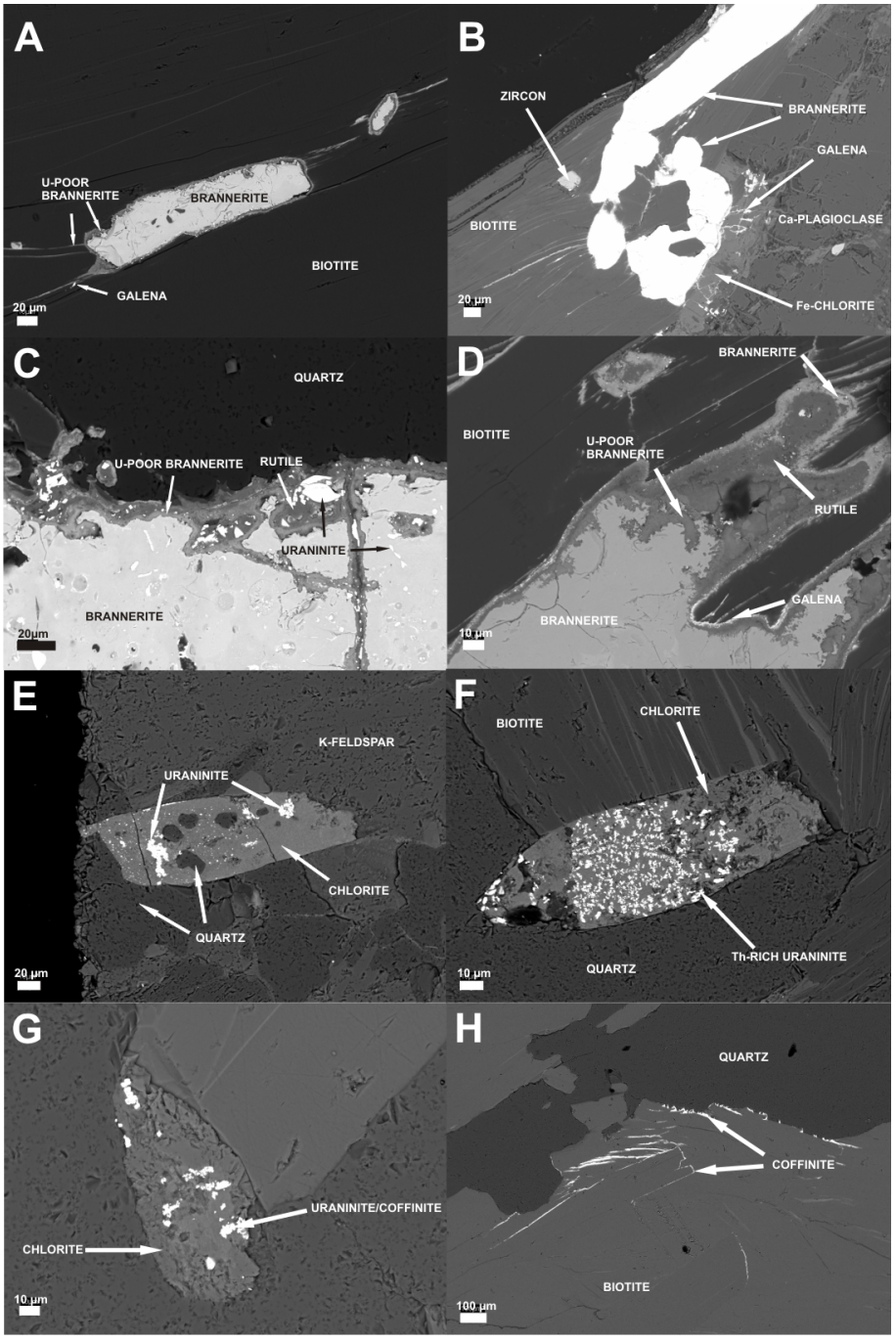

FIGURE 5.4: SEM images illustrating remobilisation of pre-existing uranium at Lumwana. A) Brannerite in biotite groundmass shows uranium depletion at rims, particularly at mica cleavages. B) Brannerite aggregate shows uranium mobility away from edges down mica cleavages. C and D) Coarse brannerite grains show progressive uranium leaching towards the rim, eventually leaving rutile with minor galena. In D, uranium mobility is strongest through mica cleavages. E, F and G) Uraninite (sometimes Th enriched) and rare coffinite form in retrogressive chlorite. H) Coffinite Forms in mica cleavages and on grain boundaries.

5.5 U-Pb dating

A sample of uraninite hosted within a carbonate vein from Malundwe was selected to attempt U-Pb dating via LA-ICP-MS. This was considered a good initial sample to test, as it had a high volume of uranium mineralisation, and was uraninite rather than brannerite, meaning it would contain an insignificant amount of common Pb. If this procedure worked, then other, finer material hosted in the groundmass would be tested (e.g. material similar to Figs. 5.3 and 5.4).

TABLE 5.1: U-Pb ages from LA-ICP-MS analysis of a carbonate vein-hosted uraninite sample from the Malundwe orebody.

Raster No.	Age (Ma)	$\pm$ 2σ (Ma)
1	3660	850
2	4490	1000
3	4190	920
4	2500	670
5	2390	630
6	2010	550
7	1900	500
8	1730	440
9	1456	370
10	1660	380
11	822	230
12	1008	280
13	1010	280
14	779	220
15	758	210
16	747	210
17	833	230
18	717	200
19	718	200
20	703	200
21	960	270
22	964	260

At the μm scale, the uraninite was intergrown with carbonate from the vein, making large spot sizes unreliable. Whilst the zircon standard produced reliable ages (section 2.4), U-Pb dating on the uraninite produced very inconsistent age data with large errors, ranging from 4490 to 703 Ma (Table 5.1). The wide range of dates span ages much older than the host rocks (impossible), to ages closer to the age of uranium mineralising events for the Copperbelt identified by Decrée et al. (2011), and that previously established for uranium mineralisation at the Malundwe orebody ($\sim$ 530 Ma) by Eglinger et al. (2013). This extreme variation in ages, towards very old dates suggests an open system, with a comparative increase in ^{206}Pb concentration compared to ^{238}U. This is consistent with the evidence presented in this chapter for uranium remobilisation and loss in the Malundwe samples, suggesting that any dates obtained from this suite of samples would be unreliable and inaccurate.

5.6 Discussion

The location and textural setting of the coarse, tectonised uranium mineralisation contained within the prevailing fabric are indicative of a pre-kinematic uranium formation

event, whereas the depletion of uranium on rims of brannerite and formation of rutile along with uraninite and coffinite located within phyllosilicate cleavages provide clear evidence of a subsequent remobilisation event in the Lumwana deposits.

Uraninite and brannerite enclosed within phyllosilicates and sulphides suggest that the initial U mineralising event predates peak metamorphism and sulphide mineralisation within the shear zone. In addition, the association of the uranium mineralisation with common hydrothermal phases such as rutile and ilmenite, REE carbonates and phosphates supports a hydrothermal origin. The Lumwana data are consistent with the hydrothermal introduction of uranium during formation or reactivation of a shear zone with uranium precipitation predominantly occurring at the boundaries between the ore schist and host gneiss. Continued development of the shear zone led to the deformation of the pre-existing uranium oxide aggregates, and shearing of the Lumwana deposits into the north-south orientation they currently display. This origin of the mineralisation is consistent with observations at multiple scales within the deposit including centimetre to decimetre-scale quartz boudins and metre to many metre-scale tectonised giant gneiss blocks incorporated within the shear zone (Fig. 5.1B). The shear zone at Lumwana underwent volume loss through the breakdown of feldspar and subsequent mica growth (Bernau et al., 2013). The heterogeneous nature of shear zone development may in part explain variations in the distribution of the uranium mineralisation within the ore schist (Fig. 5.1). The initial concentration of uranium mineralisation at the boundary between the Ore Schist and footwall gneisses may reflect a redox boundary between these units. The development of the shear zone at Malundwe resulted in the formation of significant amounts of biotite within the ore schist, along with the destruction of feldspar, leading to increased modal abundance of biotite (Bernau et al., 2013). Biotite contains ferrous iron, and thus may provide a reducing environment within the shear zone to facilitate mineralisation.

The difference in the distribution and textural associations between copper and uranium mineralisation within the Ore Schist implies some variation in their respective depositional and preservation mechanisms or timing. Sulphide minerals commonly enclose uraninite and brannerite, indicating the uranium mineralisation occurred prior to copper mineralisation. It is unclear whether the uranium and copper mineralisation occurred as individual events, or as a series of stages with uranium introduced before copper. If the uranium and copper formed from a continuous event with multiple stages, and assuming a redox-type model for mineralisation, it is likely that uranium would precipitate first, since oxidised fluids at near neutral pH containing uranium and copper when subjected to reducing conditions are suggested to precipitate uraninite before exiting the field of copper solubility (Metcalfe et al., 1994). Uranium minerals surrounded by sulphides do not show remobilised rims. Uraninite and brannerite unenclosed by sulphides often show

significant remobilisation textures, suggesting that the remobilisation event postdates sulphide mineralisation.

The distribution of the uranium mineralisation at Lumwana is strikingly similar to shear zone hosted uranium mineralization at the Jaduguda deposit in the Singhbhum shear zone (India) which contains brannerite and uraninite with associated ilmenite and other Ti minerals along with Cu sulphides. The uranium mineralisation is located on the hangingwall and footwall boundaries of a biotite schist unit (Pal et al., 2010). The Nabarlek deposit of the Alligator Rivers uranium field in Northern Territory, Australia shows similar uranium mineral assemblages and accessory minerals to Lumwana, with primary uraninite (± brannerite) occurring with chlorite and muscovite alteration as veins and breccia (Wilde and Wall, 1987). Other phases associated with mineralisation include rutile, as well as minor sulphides which post-date uranium mineralisation such as chalcopyrite, galena, pyrite, chalcocite, bornite and rare arsenopyrite and cobaltite (Wilde and Wall, 1987). Secondary uranium mineralisation is present in the form of coffinite associated with white mica alteration. The deposit was formed from multiple fluid events within a fault/shear zone in muscovite-quartz-biotite schists and amphibolite (Polito et al., 2004). Multiple fluids have been identified in the deposit, with those thought to be responsible for U mineralization typically saline (generally >25 wt% NaCl equiv.) fluids at temperatures ~165-270 ℃ (Polito et al., 2004). The Nabarlek deposit is thought to have formed in a similar manner to unconformity-type U deposits, in this case where brines infiltrated a reactivated shear zone in the basement (Polito et al., 2004). Eglinger et al. (2013) noted similar geochemical characteristics between Copperbelt U occurrences (based on REE profiles, e.g. Mercadier et al., 2011) and unconformity-type U deposits, though they interpreted the Malundwe mineralization to be more similar to 'metamorphic' uranium mineralisation, drawing parallels with the Mistamisk deposit. The Mistamisk U occurrences comprise uraninite-albite-quartz veins with minor chlorite and dolomite formed from saline solutions during metamorphism (Kish and Cuney, 1981). The differences in REE profile shapes between deposits in the Copperbelt classified as metamorphic and those classified as 'unconformity type' are minor (Eglinger et al., 2013), suggesting that this distinction may not be obvious. However, the formation of mineralisation at, or near the time of peak orogenesis is consistent with both the U-Pb age of 530 Ma available for the deposit (Eglinger et al., 2013) and the textural observations of this study.

5.6.1 Subsequent remobilisation of uranium mineralisation

Abundant textural evidence is presented for local remobilisation of uranium from the early, coarse uraninite and brannerite mineralisation. The residual lead content at the

edges of these brannerites may facilitate the formation of galena. Alternatively, galena formed within uranium minerals can develop due to the release of radiogenic lead, as observed in uraninites in the Athabasca basin (Alexandre et al., 2005). The widespread alteration of brannerite suggests the former is the most prevalent cause.

Remobilisation of pre-existing uranium minerals by later fluid events is a common feature of many uranium deposits due to the high relative mobility of U, with secondary uraninite phases and coffinite often common. For example, similar leaching of U from brannerite is noted by Alexandre (2010) at the Aricheng South uranium occurrence, Guyana, and coffinite forming in cleavage planes of phyllosilicates reported at the Rozna U deposit, Czech Republic (Kříbek et al., 2009).

Chlorite alteration is frequently associated with ore formation in a wide variety of uranium deposits. For example, at the Henry Basin, Utah (Northrop et al., 1990), the Xiazhuang uranium ore field in China (Zhang et al., 2009), across the Athabasca Basin (Alexandre et al., 2005) and other unconformity-type uranium deposits (Beaufort et al., 2005), and deposits associated with Na-metasomatism (Alexandre, 2010; Polito et al., 2009). Chlorite is known to have an affinity for uranium (Singer et al., 2009), and secondary remobilisation events affecting pre-existing uranium deposits into secondary structures are also associated with chlorite in the Athabasca basin (Cloutier et al., 2011). It is likely that the fluids forming pre-syn kinematic and post-kinematic veins often associated with chlorite alteration were responsible for the remobilisation of the earlier Type 1 uranium assemblage into Type 2 and Type 3 mineralisation settings.

Whilst similarities exist with other types of uranium deposits, the metal content (Cu ± Co ± U) suggests that it is likely that the source of mineralising fluids that formed the assemblage at Lumwana were similar to others in the Copperbelt. The presence of mineralised basement lithologies underlying large stratiform deposits in the Copperbelt is well known (Cailteux et al., 2005a; Selley et al., 2005), and suggests that the fluid processes which formed the majority of copper mineralisation were also capable of depositing sulphides in the basement. Where related to stratiform deposits, basement mineralisation immediately underlies mineralised strata, exploiting permeable features such as weathering cracks on the basement-cover unconformity (Cailteux et al., 2005a; Mendelsohn, 1961d; Selley et al., 2005). In other cases, e.g. Samba (Wakefield, 1978), basement mineralisation occurs unrelated to stratiform deposits, but also occurs within a permeable conduit, in this case a shear zone (Bernau et al., 2013). Brines are commonly regarded as an important fluid source for metal transport in sedimentary copper systems (Hitzman et al., 2005; Jowett, 1986; Selley et al., 2005). Fluid modelling work has illustrated the possibilities of brines penetrating the basement whilst supporting the idea of basement acting as a source of metals (Koziy et al., 2009). The shear zones

represented by the ore schist in the Lumwana deposits preserve evidence for large scale conduits in the basement in which significant fluid flow has taken place (Bernau et al., 2013). Mineralisation is thought to have occurred throughout the history of the basin, indicated by early diagenetic mineralisation in much of the Congo (e.g. Muchez et al., 2008), through to basin inversion (McGowan et al., 2006) and postdating basin inversion (Broughton et al., 2002; Torrealday et al., 2000). This study suggests mineralisation of the Lumwana shear zones occurred during orogenesis, with metals deposited by the reduction of brines transporting Cu ± Co ± U, which were present throughout the history of the Copperbelt.

5.7 Conclusions

Two main stages of uranium mineralisation are present at Lumwana, a primary introduction which has subsequently been remobilised. The initial uranium mineralisation occurred relatively early in the formation of the shear zone, shown by the tectonised nature of coarse grains and aggregates of uranium minerals enclosed within the dominant S_1 fabric, and, at a larger scale, the orientation and geometry of the orebodies. This initial U mineralisation was deposited on the boundaries between the ore schist and surrounding gneiss units, predominantly on the footwall contact, possibly due to a difference in redox conditions between the ore schist and gneiss. Continued development and volume loss on the shear zone subsequently physically reworked early mineralisation from the boundaries into the centre of the ore schist. The uranium mineralisation event probably predated that of the copper sulphides, demonstrated by common enclosure of brannerite and uraninite by chalcopyrite and bornite, as well as rarely pyrite.

A secondary hydrothermal event locally remobilised uranium into mica cleavages, grain boundaries and chlorites formed by retrograde metamorphism and late discordant veins. This event is characterised by the loss of mobile U from the edges of brannerite grains leaving behind immobile Ti in the form of rutile rims.

Chapter 6

Conclusions

6.1 Summary

Circulation of oxidised hydrothermal fluids within sedimentary basins and the underlying basement is known to be important in the liberation, transport and deposition of metals to form sediment-hosted stratiform copper deposits throughout the basin history of the Central African Copperbelt, as well as for the development of SHSCs in general (Hitzman et al., 2005; Jowett, 1986; McGowan et al., 2006; Muchez et al., 2010; Selley et al., 2005). Fluid inclusions hosted in vein minerals preserve a record of past fluid flow events. This thesis presents constraints on the physicochemical characteristics of these fluids, as well as using their chemistries combined with textural analysis as a mechanism to distinguish between temporal fluid events within the regional basin history of the Zambian Copperbelt. Chemistries and stable isotope characteristics of fluids and host mineral assemblages were used to further understand fluid processes including water-rock interaction and the development of hydrothermal alteration assemblages associated with mineralisation. The geochemistry and stable isotope composition of the sulphide minerals also provides information into the development of mineralisation, whilst radiogenic isotope compositions and textural analysis of both sulphide and uranium oxide minerals provides both absolute and relative information on the timing of mineralisation. This chapter summarises the main conclusions of the thesis.

6.2 Conclusions

Vein minerals in the Domes Region and the Zambian Copperbelt investigated in this study preserve saline to highly saline brines of up to ~50 wt% NaCl equiv., typically

30–40 wt% NaCl equiv.. These brines have diverse and complex salt chemistries including NaCl, $MgCl_2$, $CaCl_2$, $FeCl_2$ and KCl, as well as often containing CO_2 and CH_4. These fluids typically formed at ∼200-400 ℃. Chlorine isotope analysis indicates that the ultimate source of salinity in these brines was seawater. By analysing the halogen contents of fluid inclusion leachates it is possible to identify different fluids derived from seawater evaporation processes, both residual bittern brines and fluids generated with a component of dissolved halite. By combining this data with the textural settings of pre and post-kinematic vein sets within the deposits, it is possible to identify changes in the source of halogens generating brines through basin history. This study a progression of fluid generation events in the Zambian Copperbelt and Domes Region. An initial fluid reservoir formed mainly by bittern brines was generated by the evaporation of seawater and deposition of evaporite sequences. Post-kinematic veins record an increasing input of fluids generated by the dissolution of the evaporite sequences in the basin later in the basin history. Halogen concentrations indicate evaporation occurring beyond the carnalite saturation point for most fluids. The cation concentrations in fluid inclusion leachates are highly variable, are attributable to water-rock interaction and are consistent with the generation of the extensive, basin-scale alteration assemblages present in the Copperbelt. Therefore the cation concentrations are not likely to be representative of seawater at the time of development. Similarly, sulphate concentrations are much higher than modern seawater values, and are probably derived from the dissolution of anhydrite preserved within the host sedimentary sequence. Oxygen isotope evidence indicates that fluids were initially derived from seawater which partially equilibrated with the country rocks. Early fluids show the greatest amount of isotopic equilibration due to long residence times. Later fluids show less equilibration with the host rocks indicating shorter residence times associated with fast fluid cycling during orogenesis. Carbon isotope data is consistent with oxidation of organic matter or buffering by Neoproterozoic marine carbonates. Hydrogen isotope evidence is anomalously lighter than would be expected for infiltration of meteoric waters into the basin. These signatures are consistent with isotope data for hydrocarbons, and provides further evidence for the role of a mobile organic reductant in the formation of these ore deposits.

The pilot micro-CT study undertaken as part of this project was able to image fluid inclusions successfully within vein carbonate. This method presents a technique able to identify fluid inclusion assemblages within a sample in three dimensions. This technique can be used to complement the standard visual techniques, and provides a potentially powerful mechanism to interrogate spatial distribution of inclusions.

Concentrations of rare earth elements in Copperbelt sulphides are typically low, and the shapes of the profiles are variable at both the regional and deposit scale, showing LREE-enrichment, LREE depletion and relatively flat profiles, typically with negative

Eu anomalies. The variation in profile shape is generally controlled by differences in LREE concentrations. This is similar to the limited data available for sulphides in other stratiform ore deposits. The negative Eu anomaly contrasts with the positive Eu anomalies shown by sulphides derived from hydrothermal fluids from submarine vent systems, as well as other examples of hydrothermal fluids such as brines from the Salton Sea. It is suggested here that the shape of these profiles is controlled by the formation of common alteration minerals such as phlogopite, muscovite and K-feldspar, which are LREE-enriched, and in the case of K-feldspar show significant positive Eu anomalies. Generating these alteration assemblages would leave the residual fluid increasingly LREE depleted and with a negative Eu anomaly, providing a mechanism which could cause the variation in LREE concentrations and the observed sulphide REE profile shapes. The potential importance of the role of alteration minerals in controlling the REE patterns of mineralising hydrothermal fluids and subsequently formed sulphide minerals supports the conclusions of the analysis of the fluid inclusion leachates, which suggested an important role for the development of alteration assemblages in controlling the cation budgets of the mineralising fluids.

Trace element concentrations of sulphides are enriched in Co, and to a lesser extent Ni compared to other transition metals, confirming the importance of the Copperbelt as a Co repository. In particular, the deposits formed on the Kafue Anticline such as Nchanga and Konkola show the most enriched Co concentrations. Other trace element concentrations in sulphides are very variable, with little consistency between similar sulphide mineralogies at different deposits, suggesting that instead, local conditions at the different deposits were more important for controlling the trace element budgets of sulphide phases. This study and other work (e.g. Hitzman et al., 2005) have suggested that mineralising fluids in the Copperbelt and sulphide deposition mechanisms were broadly similar, as well as being similar to other SHSC mineralised districts. This implies that the most likely local control on the trace element budget of sulphides is the host rock sequence or the original metal source, which in the Copperbelt is probably the basin sedimentary sequence and the basement rocks.

Sulphur isotope data provides a method to understand mechanisms of sulphide formation and sources of sulphur. The data reported here from the Zambian Copperbelt and Domes Region are generally indicative of formation via thermochemical sulphate reduction of seawater sulphate, rather than bacterial sulphate reduction which would result in lighter values than those reported here. A thermochemical sulphate reduction mechanism of seawater sulphate is consistent with the results of the fluid geochemistry survey conducted as part of this thesis, which reported fluid temperatures above those for which bacterial sulphate reduction can take place. Variations in sulphur isotope ratios include

very heavy values which can be explained by closed system isotopic fractionation. Alternatively, light values may be explained by the incorporation of an earlier phase of sedimentary sulphides formed by bacterial sulphate reduction during diagenesis. Variation in sulphur isotope values between different SHSC districts can be explained by variations in the seawater sulphate δ^{34}S curve through time.

Re-Os dating of molybdenite from the Lumwana and Enterprise deposits in the Domes Region is very consistent, between ~525 to 535 Ma. This age of mineralisation is consistent with formation during peak orogenesis, basin closure and post-orogenic cooling. It is also closely synchronous with the later uranium mineralisation event of Decrée et al. (2011) in the region, the specific age of ~530 Ma reported by Eglinger et al. (2013) for uranium mineralisation at Lumwana, and the age of the molybdenite mineralisation at Kansanshi (Torrealday et al., 2000). These dates continue to support the conclusion that mineralisation in the Copperbelt continued throughout basin inversion and orogenesis. Since the mineralisation at Lumwana is sheared, it also provides a youngest age for final movement on the Lumwana shear zones.

The textural study on uranium mineralisation in the Lumwana orebodies identified two main stages of mineralisation, an initial introduction of uranium into the shear zone which was tectonically reworked by shear zone movement and then subsequently remobilised by a later fluid event. The development of the shear zone controls the distribution of the majority of uranium mineralisation, evidenced by the tectonised nature of uranium mineral aggregates incorporated and aligned with the S_1 fabric, and at a larger scale the orientation and geometry of the ore bodies. The uranium mineralisation was deposited on the edges of the shear zone, possibly due to difference in redox potential between the gneiss and the relatively reduced, biotite-rich Ore Schist. Uranium mineralisation pre dates sulphide mineralisation in the shear zone evidenced by the inclusion of uraninite and brannerite within sulphide phases. A secondary hydrothermal event remobilised the uranium into mica cleavages grain boundaries and retrogressive chlorite alteration. This event is characterised by loss of uranium from the edge of brannerite aggregates leaving behind less mobile titanium as rutile rims. The uranium mineralisation age provided by Eglinger et al. (2013) for Lumwana is synchronous with that generated by Re-Os dating of molybdenite in this study, suggesting that the Lumwana shear zone formed during orogenesis.

6.3 Further work

The results of this study suggest further work investigating the following areas would be beneficial:

- Kansanshi veins
- Micro-CT of fluid inclusions
- Further δD studies
- Further trace and rare earth element work, including radiogenic dating.

The Cl/Br data at Kansanshi show a bimodality, suggesting the presence of both bittern brines and brines derived from the dissolution of evaporite sequences. Whilst multiple fluid inclusion assemblages are known to be present at Kansanshi, both the numerical and volumetric majority were of a single type, suggesting that bulk leachate extraction processes for anion and cation analysis, as well as δD would be representative of that particular fluid. Textural analysis and field relationships of the veins at Kansanshi suggest that the veins likely formed from a single pass system. It is then difficult to reconcile the textural relationships with the results of the Cl/Br study. A scanning electron cathodoluminescence (SE-CL) study may prove useful in identifying different generations of quartz and carbonate growth within the veins, potentially explaining the bimodality in the dataset.

The success of the pilot micro-CT study in imaging inclusions suggests that with further work it would be possible to obtain volumetric data on fluid content in samples, as well as analyse the distribution and orientation of fluid inclusions in a numerical manner. Using standards of known density may allow for the density of inclusions within the sample to be identified. Eventually this technique may be able to identify between different types of fluids using differences in density, orientations, distributions and volumes, aiding in the categorisation of fluid inclusion assemblages. A further short study on samples with multiple inclusion assemblages of different types, preferably highly saline and very weakly saline, or liquid-rich and vapour-rich inclusions could further investigate the possible uses of the micro-CT technique for the analysis of fluid inclusions.

Whilst a relatively common technique in the analysis of geofluids in many settings, and despite the understanding of the fundamental role of basin fluid processes in their formation, there is a paucity of hydrogen isotope data available for sediment-hosted stratiform copper deposits. Further δD data from both the Central African Copperbelt and other sediment-hosted copper deposits such as those in the Kupferschiefer would be helpful in corroborating the results of this study, as well as improving the understanding of the local basin fluid histories and their potential role in the formation of stratiform copper mineralisation.

The results of the trace and rare earth element study of sulphide minerals conducted here suggest that many of the samples contain measurable contents of the rare earth

elements Sm and Nd, as well as containing variable ratios of Sm to Nd. This suggests that it may be possible to utilise the Sm-Nd radiogenic dating technique to directly date the sulphide mineralisation formed in the Copperbelt. Similarly, the Sr concentrations of some of the samples may also be high enough to attempt Rb-Sr dating. Direct dating of sulphide mineralisation via Re-Os dating was one of the original goals of this study, but it was found that most of the samples didn't contain high enough Re and Os concentrations. Sm-Nd and Rb-Sr provide powerful and complementary dating techniques which may then be combined with the available Re-Os and U-Pb data from the Copperbelt in order to further investigate the timing of mineralisation, which remains one of the largest unresolved challenges in the field. This study has highlighted variability within REE patterns and trace element distributions between different Copperbelt deposits and settings. Further data and additional data from other districts such as the Kupferschiefer would be very useful as a comparator, particularly when understanding the mechanisms which control variability in the distribution of minor economic elements such as Co, Ag, Au and the platinum group elements in SHSCs remains incomplete. REE analysis of sulphides undertaken in this project has suggested that the formation of the alteration assemblage may affect the REE patterns of sulphides, as well as carbonates (Roberts et al., 2009). Additional REE analysis of alteration minerals such as K-feldspars and micas from the Copperbelt would help to further investigate and test this hypothesis.

Appendix A

Appendix A: Sample lists and descriptions

Lists of the samples collected for use in this project in the 2009 and 2010 field seasons. Additional samples were used from the projects of McGowan and Bernau, as well as some Musoshi samples kindly provided by J.P. Richards (University of Alberta). Most samples available were from drill core, and the sample numbers follow the naming pattern of Drill Hole Number followed by depth, e.g. MLW0294 54.7 is from the drill hole MLW0294 and the depth of 54.7m.

TABLE A.1: Table of Lumwana orebody drillcore samples

Sample	Description
MLW0294 54.7	Large glassy quartz vein cuts hangingwall pegmatite dyke
MLW0294 60.4	Qtz boudin in hangingwall gneiss
MLW0294 62.76	Qtz boudins in micaceous ore schist
MLW0294 80.06	Qtz vein on ore schist footwall boundary
MLW0294 99.8	Qtz vein cuts footwall
LUM0287 59.75	Qtz vein with recrystallised sulphides within ore schist, cpy and py
LUM0287 68.25	Qtz vein cuts ore schist rich in musc
LUM0287 71.05	Cpy rich ore schist
LUM0287 80.1	Qtz vein in footwall aligned with fabric
LUM0287 80.82	Massive barren boudinaged qtz veins in footwall
LUM0287 87.79	Micaceous biotite-chlorite footwall gneiss
MLW0291 27.14	Ore schist, bn and cpy veinlets and disseminations
MLW0291 28.00	Qtz vein in ore schist, bn–cpy–musc
MLW0291 31.78	Qtz vein in ore schist, barren
MLW0291 35.00	Qtz boudin in ore schist
MLW0291 35.30	Glassy qtz vein in ore schist
MLW0291 35.7	Remnants of glassy qtz vein in ore schist
MLW0291 38.34	Glassy qtz veins, chlorite alteration in ore schist
MLW0291 42.05	Glassy qtz vein in footwall biot–plag gneiss
MLW0291 44.65	Qtz vein (weathered?) biotite-chlorite halo, footwall
MLW0291 50.85	Glassy late qtz vein with chlorite/biot alteration, footwall
MLW0291 52.9	Qtz boudins and fabric parallel vein, footwall
EQMAL084 66.6	Late glassy qtz vein, biot halo in hanging wall schist
EQMAL084 91.3	Glassy qtz vein in ore schist
EQMAL084 98.93	Boudins in ore schist
EQMAL084 106.84	Qtz boudins in footwall biot schist
EQMAL083 18.04	Glassy qtz vein with biot halo, hanging wall schist
EQMAL083 24.83	Qtz vein cuts schistosity in hanging wall
EQMAL083 31.1	Qtz boudins in hangingwall schist
EQMAL083 45.37	Qtz boudins in hangingwall schist
EQMAL083 46.82	Qtz boudin, hangingwall schist
EQMAL083 53.3	Qtz boudins in hangingwall schist
EQMAL083 71.2	Qtz boudins in hangingwall gneiss
EQMAL083 94.43	Glassy quartz vein with recrystallised cpy and bn
EQMAL083 102.56	Qtz vein in biotite rich ore schist
EQCHI062 37.8	Large qtz vein in hanging wall gneiss
EQCHI062 40.13	Large late qtz vein in hanging wall
EQCHI062 49.48	Qtz boudins in hanging wall biotite schist
EQCHI062 90.68	Qtz boudin with biot halo in hanging wall schist with pegmatitic bands
EQCHI062 124.59	Qtz boudins in hanging wall schist
EQCHI062 130.24	40cm thick barren discordant qtz vein in hanging wall
EQCHI062 135.79	Qtz + plag boudins in biotitic hangingwall schist
EQCHI062 153.11	30cm thick barren discordant qtz vein in kyanite ore schist with cpy
EQCHI062 171.75	Glassy discordant qtz vein with musc halo cuts locally barren ore schist
EQCHI062 174.4	Glassy qtz vein cuts ore schist with mica alteration
EQCHI062 181.1	Cpy rich micaceous ore schist with schistosity parallel qtz vein containing recrystallised cpy
EQCHI062 190.27	Ore schist with large qtz vein containing recrystallised sulphides and musc
EQCHI062 211.33	Boudinaged qtz veins in muscovitic ore schist containing bn
EQCHI062 271.43	Qtz boudins in cpy rich ore schist near footwall boundary
EQCHI062 278.18	Qtz boudin in ore schist with bn mineralisation in ore schist grading into footwall

TABLE A.2: Table of Lumwana orebody open pit samples

Sample	X	Y	Z	Dip	Strike	Type of Fabric	Description
SP-001	370860.045	8646854.83	1243.457	32	240	Schistosity	Musc-biot-qtz ore schist with cpy + bn
SP-002	370860.045	8646854.83	1243.457				Heavily silicified ore schist, coarse cpy-bn mineralisation
SP-003	370848.679	8646882.48	1244.073	30	271	Schistosity	Footwall biot-qtz schist
SP-004	370884.126	8646929.33	1244.665				Chrysocolla near weathered qtz vein
1E-001	370815.534	8647951.99	1290.78	20	086	Gneiss foliation	Hangingwall gneiss, qtz-biot-haem stained plag
1E-002	370815.534	8647951.99	1290.78	42	265	Vein dip/strike	Large discordant barren qtz vein cuts hanging wall (10-40cm thick)
1E-003	370915.534	8647951.99	1290.78	75	92	Vein dip/strike	Large bifurcating discordant barren qtz vein cuts hanging wall (2-25cm thick)
1E-004	370815.534	8647951.99	1290.78	90	115	Vein dip/strike	Large bifurcating discordant barren qtz vein cuts hanging wall (2-15cm thick)
1E-005	370803.268	8647903.85	1289.566	60	060	Vein dip/strike	Large discordant barren qtz vein cuts hanging wall (15-20cm thick)
1E-006	371016.482	8648012.4	1276.268	15	034	Schistosity	Barren footwall biot-qtz schist with minor musc
1E-007	371026.972	8647953.65	1277.824	23	300	Schistosity	Biot-musc-qtz ore schist with cpy + bn
1E-008	371026.972	8647953.65	1277.824				Boudinaged qtz vein in weathered ore schist with bn and cpy
1E-009	370827.455	8647963.03	1276.92	90	068	Vein dip/strike	Subvertical qtz vein cuts pink hanging-wall gneiss, 2-70cm in thickness, local specular haematite
SP-005	371313.767	8646754.64	1240.366				Unmineralised qtz boudin in weakly mineralised biot-qtz-garnet schist
SP-006	371315.583	8646715.27	1240.256				Musc-biot-qtz-(chlor) ore schist with cpy-bn

TABLE A.3: Table of Lumwana footwall/decollement samples

Sample	Lithology	Description
MAD56 74.70	Mottled schist	
MAD56 112.4	Mottled schist	Near fault zone at 114m
MAD56 123.56	Lower quartzite	Lower Roan
MAD56 151.08	Whiteschist	Decollement
MAD56 158.87	Whiteschist	Decollement
MAD56 171.61	Whiteschist	Decollement
MAD56 185.71	Whiteschist	Decollement
MAD56 196.64	Mafic	Sheared mafic intrusion in 'whiteschist' zone
MAD56 231.13	Mafic	Sheared mafic intrusion in 'whiteschist' zone
MAD56 243.55	Upper Roan breccia	
MAD56 251.40	Upper Roan quartzite	
MAD56 258.32	Mafic	Gabbroic fragment
MAD56 273.00	Phyllite	Metapelite with qtz-carb veins

TABLE A.4: Table of Kansanshi samples

Sample	Stratigraphy	Ore zone	Lithology	Description
KAN1-1	Lower marble	Sulphide	Biotite-rich marble	Dirty marble with biotite causing dark colour (after pelitics). Bi and carb crystals up to 7mm. Minor disseminated cpy, foliation picked out by biotite
KAN1-2	Lower marble	Sulphide	Biotite-rich marble with quartz vein	slightly bleached on vein edges, blebby cpy in vein
KAN1-3	Lower marble	Sulphide	Marble with qtz-carb vein	Carb + minor qtz vein cuts bleached/less dirty marble. Massive cpy in vein, mainly on margin. Py near biotitic zones in marble, and occasional cpy disseminated in marble
KAN1-4	Lower marble	Sulphide	Qtz-carb vein	Massive and blebby cpy, euhedral white carb up to 2cm, glassy anhedral qtz, qtz: carb 50:50
KAN1-5	Lower marble	Sulphide	Marble with qtz vein	Bleached/less biotitic. Cut by qtz-carb-cpy vein. Cpy blebs intrude into fabric of marble up to 5mm in size. Carb up to 2cm in vein
KAN1-6	Lower marble	Sulphide	Carb-qtz-cpy vein in marble	Carb 1mm to 9mm, glassy qtz up to 1.4cm. Massive cpy. Minor blebs of cpy in host, but no foliation
KAN1-7	Lower marble	Sulphide	Carbonate-cpy vein	Massive and blebby cpy in euhedral rhombic carbonate up to 2cm crystals. Off white to grey. Massive to blebby cpy, minor rare disseminated py
KANX-1	Middle mixed clastics	Transition/oxide	Oxidised phyllite	Protolith prob a pelite or siltstone. Foliation clear, at 30 degrees to bedding. Covered in malachite and chrysocolla with some Fe oxides. Oxidisation roughly follows foliation. Some botrioidal features
KANX-2	Unknown (loose boulder)	Transition	Qtz vein	Coarse glassy qtz with Fe-oxide around cpy and fractures. Coarse 2cm vug once contained cpy. Now mostly empty, with some prismatic malachite and pale chrysocolla Taken from dump zone, mixed oxide and sulphide

TABLE A.5: Table of Kansanshi samples continued

Sample	Stratigraphy	Ore zone	Lithology	Description
KAN2-1	Middle mixed clastics	Sulphide	Qtz-carb-cpy vein	2 pieces. 20 % qtz, 80 % carb, + cpy. Fairly dense. Carbonate sub to euhedral rhombs 1-5mm, qtz small and anhedral. Cpy massive, occassionally blebby up to 1cm
KAN2-2	Middle mixed clastics	Sulphide	Carb-cpy vein	Single euhedral crystal, rhombic, 4cm, massive cpy
KAN2-3	Middle mixed clastics	Sulphide	Massive cpy	2 pieces, massive cpy from within vein
KAN2-4	Middle mixed clastics	Sulphide	Qtz-carb-cpy vein	Smokey glassy coarse anhedral cm scale qtz. Cm scale euhedral white carb. Massive cpy on edge between qtz and carb zones. Cpy blebs (mm scale) in carb, disseminated sub mm cpy in qtz
KAN2-5	Middle mixed clastics	Sulphide	Qtz-carb-cpy vein	White carb up to 2.5cm. Blebby cpy to massive. Qtz not glassy, extremely finely disseminated sulphides sub mm scale in qtz
KAN2-6	Middle mixed clastics	Sulphide	Bleached phyllite	Finely laminated/foliated. Spotting (chiastolite?) beginning to appear. Remnant vein edge cuts fabric at high angle (coarse cpy). Protolith prob siltstone. Alligned biotite horizons were probably more argillacious. Small amounts of Biot align on foliations. Mainly cpy (minor py) formed on foliations, elongate, not necessarily flattened
KAN2-7	Middle mixed clastics	Sulphide	Phyllite	Host rock. Minor spotting - Baked. Strong fabric, riddled with py up to 5mm in length, elongate along foliations. Fairly dark, sooty looking, protolith a carbonaceous siltstone? No cpy
KAN2-8	Middle mixed clastics	Sulphide	Bleached phyllite	Bleached MMC phyllite. Minor cpy along foliation planes. Green alteration on foliations, micaceous, fuchsite? Cpy typically 1-3mm elongate blebs along fabric up to 12 mm
KAN2-9	Middle mixed clastics	Sulphide	Carb-qtz-cpy vein	Dirty euhedral carb up to 3cm. Minor Qtz. Minor blebby cpy, mostly py blebs. Blebs typically granular masses, but can also be coarse sub to euhedral. Individual sulphide crystals up to 1.5cm in size

TABLE A.6: Table of Kansanshi samples continued

Sample	Stratigraphy	Ore zone	Lithology	Description
KAN3-1	Middle mixed clastics	Sulphide	Carb-qtz-cpy vein	Mostly carb, minor anhedral qtz. Carb sub-euhedral up to 1mm in crystal size. Common blebs of cpy, and rare blebs of py (as a single crystal, sub-euhedral) up to 1.1cm in size
KAN3-2	Middle mixed clastics	Sulphide	Vein carbonate	6cm single euhedral rhombic carb crystal from vein. No visible sulphides
KAN3-3	Middle mixed clastics	Sulphide	Massive cpy	Massive cpy lump from vein. Shape mirrors carb rhomb. Replaced/pseudomorphed it. Very minor carb visible between cpy
KAN3-4	Middle mixed clastics	Sulphide	Bleached phyllite with carb-qtz-cpy vein	MMC phyllite with cpy blebs in parts of fabric. Vein almost completely carb, euhedral, 1-2cm in size typically. Cpy mostly forms on boundary with host rock. Vein both cuts and exploits fabric. Rare galssy vein qtz
KAN3-5	Middle mixed clastics	Sulphide	Phyllite	Darkish grey. Little bleaching. Minor py blebs along fabric, some spotting forming
KAN3-6	Middle mixed clastics	Sulphide	Qtz vein	Glassy, with some mm scale py and minor fe oxide staining
KAN3-7	Middle mixed clastics	Sulphide	Carb-cpy vein with phyllite	Coarse anhedral to subhedral carb, up to 1cm. Cuts bleached MMC phyllite, with only minor fabric still visible. Rare sub mm cpy on fabric remnants. Most cpy mineralisation massive, forming along vein phyllite contact
KAN3-8	Middle mixed clastics	Sulphide	Qtz-carb-cpy vein	Carb relatively dirty, up to 2cm crystals. Qtz glassy and anhedral. Massive cpy on boundary between qtz and carb
KAN3-9	Middle mixed clastics	Sulphide	Carb-cpy vein	Coarse euhedral rhombic carb up to 3cm with cpy
KAN3-10	Middle mixed clastics	Sulphide	Carb-cpy vein	Anhedral to euhedral calcite with minor cpy blebs. Carb varies from fine anhedral patches mm scale to up to 2cm euhedral rhombs

Table A.7: Table of Konkola samples

Sample	Lithology	Description
KON149A 1399.38	Shales with grits (hanging wall)	Gritty arkosic section of shales with haematite spotting after py
KON149A 1401.00	Shales with grits (hanging wall)	Shale-rich section of ore shale with grits and minor haematite spotting after py
KON149A 1408.42	Ore shale/hanging wall contact	Shale with lots of sandier bands, py + Fe-oxide bands
KON149A 1412.65	Ore shale	Py-rich, minor ccc, pseudonodules? Sandier horizons
KON149A 1412.80	Ore shale	Py-rich, minor ccc, pseudonodules? Sandier horizons
KON149A 1420.65	Ore shale	Sandy band, section full of py
KON149A 1421.20	Ore shale	Ore shale with quartz-carb veins containing py and cpy
KON149A 1421.30	Ore shale	Ore shale with quartz-carb veins containing py and cpy
KON149A 1424.65	Footwall conglomerate	Conglomerate with grits and shales (immediate footwall)

Table A.8: Table of Konkola North samples

Sample	Lithology	Description
KON149A 1399.38	Shales with grits (hanging wall)	Gritty arkosic section of shales with haematite spotting after py
KON149A 1401.00	Shales with grits (hanging wall)	Shale-rich section of ore shale with grits and minor haematite spotting after py
KON149A 1408.42	Ore shale/hanging wall contact	Shale with lots of sandier bands, py + Fe-oxide bands
KON149A 1412.65	Ore shale	Py-rich, minor ccc, pseudonodules? Sandier horizons
KON149A 1412.80	Ore shale	Py-rich, minor ccc, pseudonodules? Sandier horizons
KON149A 1420.65	Ore shale	Sandy band, section full of py
KON149A 1421.20	Ore shale	Ore shale with quartz-carb veins containing py and cpy
KON149A 1421.30	Ore shale	Ore shale with quartz-carb veins containing py and cpy
KON149A 1424.65	Footwall conglomerate	Conglomerate with grits and shales (immediate footwall)

Table A.9: Table of Samba samples

Sample	Lithology	Description
KN54 1359.8	Hanging wall/ore shale contact	Bleached ore shale, minor ccc above this, but grade drops off significantly
KN54 1361.7	Ore shale	Shale with bands of ccc and cobaltiferous py in permeable sections
KN54 1368.7	Ore shale	Vein and layered ccc mineralisation in shale
KN54 1372.5	Ore shale	Vein cuts ore shale, vein contains significant cobalt as pink oxide and ccc
KN54 1381.4	Footwall conglomerate	Conglomerate with malachite and ccc mineralisation in fractures and conglomerate matrix
KN54 1385.65	Footwall	Quartzites, minor arkoses with vugs and pink haematite staining
KN44 1248.9	Ore shale	Ore shale with coarse mineralised horizon (ccc, no Co)
KN44 1260.1	Ore shale	Ore shale with disseminated ccc mineralisation
KN103 821.30	Hanging wall (shale with grit)	Mixed shale and grit with py and pyrr
KN103 927.60	Ore shale	Ccc contains py surrounded by Fe oxides and malachite
KN103 928.50	Ore shale	Ore shale with coarse (cm scale) vug containing py on inner edge, with qtz
KN103 938.7	Ore shale	Py on probably late fracture in ore shale

Table A.10: Table of Kalumbila-Sentinel samples

Sample	Lithology	Description
KAL0200 31.1	Ore phyllite	Folded sheared phyllite
KAL0200 48.85	Ore phyllite	Massive pyrr and py in sheared phyllite
KAL0200 58.65	Ore phyllite	Py vein cuts phyllite fabric
KAL0200 89.80	Ore phyllite	Bleached phyllite with py
KAL0200 107.00	Ore phyllite	Bleached phyllite with phlogopite growth
KAL0200 119.8	Ore phyllite	Bleached phyllite with micaceous spotting
KAL0200 134.9	Ore phyllite	Bleached phyllite with talc alteration and blue dolomite spotting
KAL0200 139.85	Ore phyllite	Dol-phlog-talc-chlor altered phyllite
KAL0200 160.35	Ore phyllite	Massive quartz vein with dolomite and chlorite and talc alteration
KAL0195 51.85	Ore phyllite	Cpy, py mineralised phyllite
KAL0195 52.3	Ore phyllite	Cpy within qtz-carb vein in phyllite
KAL0195 60.35	Ore phyllite	Cpy, pyrr vein in phyllite
KAL0195 67.1	Ore phyllite	Massive cpy and py mineralisation in phyllite
KAL0195 76.6	Ore phyllite	Massive py and minor cpy in qtz-carb vein oriented with fabric
KAL0195 88.7	Ore phyllite	Cpy + py mineralisation in qtz-carb veins in phyllite
KAL0195 113.00	Ore phyllite	Pyrr and cpy in qtz-carb veins in phyllite
KAL0195 133.60	Ore phyllite	Folded quartz-carbonate veins in phyllite
KAL23 204.00	Ore phyllite	Qtz-carb-cpy vein in phyllite
KAL23 215.50	Ore phyllite	Qtz-carb-chlor-cpy vein in phyllite
KAL23 309.80	Ore phyllite	Qtz-carb vein in phyllite
KAL23 445.80	Ore phyllite	Silicified zone in phyllite with sulphides on edge
KAL23 493.60	Ore phyllite	Bleached phyllite with chlor-talc alteration on edge of qtz-carb vein

Table A.11: Table of Enterprise samples

Sample	Lithology	Description
KW1 92.83	Altered phyllite	Talc-haematite altered 'whiteschist'
ENT0004 62.29	Altered phyllite	(Comparatively weakly altered) qtz-ky-py-albite alteration
ENT0004 69.80	Altered phyllite	Phyllite relatively unaltered showing qtz-py-ky-musc veins
ENT0004 72.00	Altered phyllite	Massive veining vaesite-py-ky-qtz, weakly altered
ENT0004 82.28	Altered phyllite	Heavily altered, silica-phlog-musc with molybdenite
ENT0004 101.00	Altered phyllite	Massive talc alteration in bleached phyllite (qtz-rich, albitised)
ENT0003 74.22	Altered phyllite	Heavily veined (qtz-ky-py) bleached phyllite
ENT0003 76.00	Altered phyllite	Stockworked, bleached phyllite with qtz-ky veins and vaesite
ENT0003 80.50	Altered phyllite	Bleached, altered phyllite with massive vaesite mineralisation (very little veining)

Appendix B

Appendix B: Fluids in the crust

B.1 Fluid flow in sedimentary basins

Fundamentally, fluid flow in the upper continental crust is driven by energy from the sun or by heat from the Earth's interior. The sun's energy drives precipitation and evaporation, as well as wind, and in turn, sediment deposition, followed by burial and compaction and subsequent fluid processes. Heat from within the earth drives plate tectonics, and the igneous activity, extension and compression and associated pressure changes also act as key fluid drivers (Cathles and Adams, 2005). Fluid flow plays an important role in the development of mineral resources, through the scavenging and transport of metals and metal complexing ligands. Fluid flow in the crust can occur in very large scales, over long time periods, and may be steady-state and continuous or transient (Cathles and Adams, 2005). Understanding the physicochemical processes that generate and transport fluids through the Earth's crust, as well as determine their physical and chemical properties is essential in understanding how and where mineral deposits form.

Fluids from the hydrosphere penetrate the crust in a variety of ways, including direct infiltration into fractures and other conduits such as karstic terrain, however, the most important method is via burial (and subsequent subduction) of sediments. Sediments typically contain large volumes of water, either in pore space or in the form of hydrous mineral assemblages such as clays, initially derived from the waters depositing the sedimentary successions (typically seawater). Fluid transport within evolving basins holds particular importance for the development of SHSCs.

B.1.1 Controls on and mechanisms of fluid movement

The most critical constraint on fluid flow in sedimentary basins is the supply of fluids (Fig. B.1). This supply may be from external sources, or it may be derived internally and constrains the total time integrated flux (Bjørlykke, 1997). Other important constraints on fluid flow are the porosity, permeability and homogeneity of the host medium, and the properties of the fluid, which are primarily controlled by temperature, pressure and chemistry (Fetter, 2001).

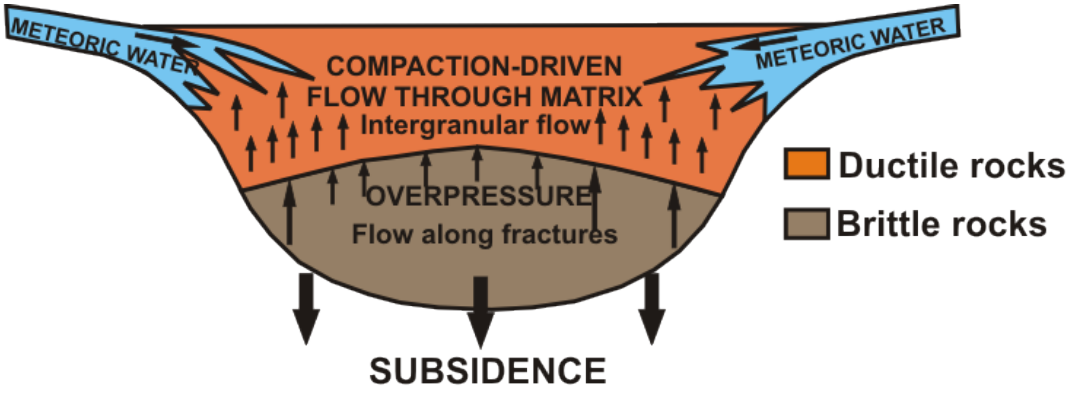

FIGURE B.1: Schematic illustration of fluid flow in a subsiding, partly overpressured basin. (Adapted from Bjørlykke, 1997).

B.1.1.1 Porosity

Porosity is void spaces within rocks, defined mathematically as:

$$n = \frac{100V_v}{V} \tag{B.1}$$

where (n) is the percentage porosity, (V_v) is the volume of void space in unit volume of earth material and (V) is the unit volume of earth material, the total volume of voids and solids (Fetter, 2001). The more important factor is (n_e), the effective porosity, is controlled by the size of the molecules being transported and the size of the passageways (pore throats) connecting the pores. It has been shown that even in lacustrine clays water molecules can still pass through pore throats (Fetter, 2001), and so for sedimentary rocks (n) is functionally equal to (n_e). Porosity is controlled by the sorting, packing and shape of grains within rocks. Mixed grain sizes typically result in lower porosities, as do highly spherical grains, which can be more tightly packed. The alignment of non-spherical grains also affects porosity (Fetter, 2001). Initial porosity in sediments is therefore controlled by transport and depositional processes, particularly compaction and diagenesis (Fig. B.2) which almost always result in lower porosities than the original sediments

(Fetter, 2001). The resultant porosity is known as primary porosity. Secondary porosity is created in sediments via fracturing or chemical dissolution (common in carbonates).

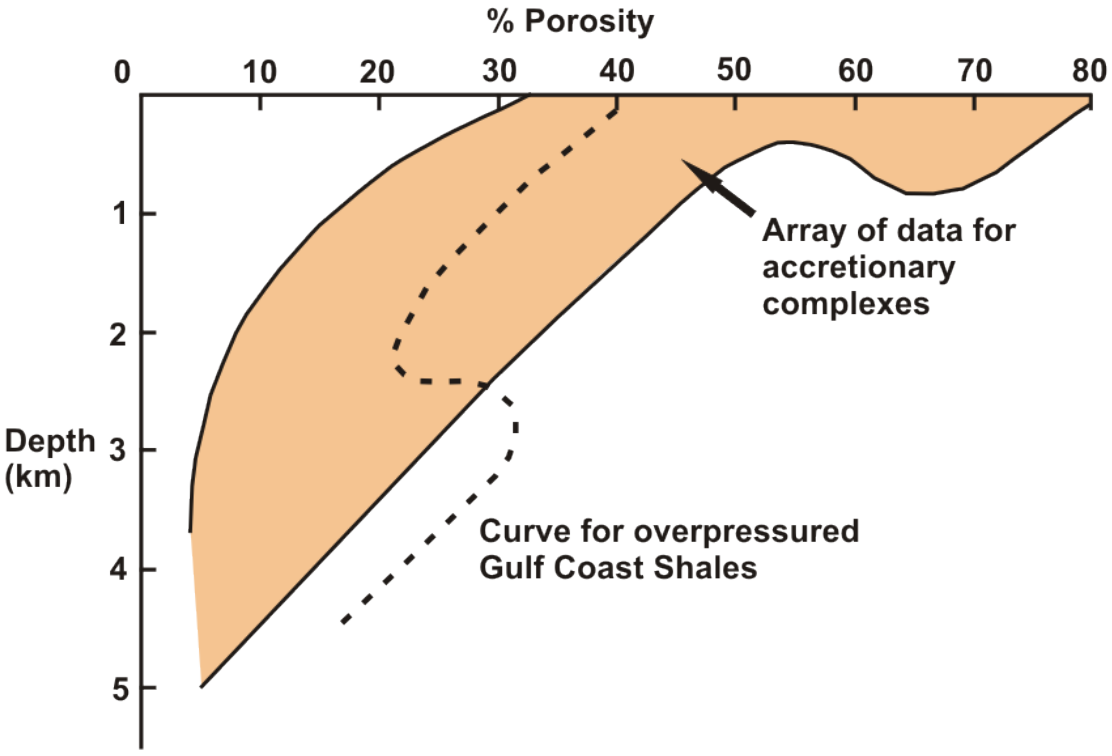

FIGURE B.2: Porosity variation with depth in modern sedimentary environments. The shaded field shows sample and seismic porosities from various accretionary complexes. The dashed line shows the porosity of shales from the Gulf Coast, with an overpressured zone below 2.5 km. (Adapted from Bonham, 1980; Bray and Karig, 1985; Yardley, 1997).

B.1.1.2 Permeability

Intrinsic permeability is a function of the size of a pore opening. The smaller the size, the greater the surface area the fluid contacts, and the greater the frictional resistance to flow (Fetter, 2001). As such, as average grain size increases, so does permeability due to the larger size of pore throats. Heterogeneous grain size reduces permeability as finer material fills voids and reduces pore throat size (Fetter, 2001). Secondary openings after rock formation are critical in determining permeabilities, with size of openings, volume of open space and degree of interconnectivity crucial. Secondary effects such as diagenesis, and subsequent mineral and cement formation can reduce permeability by constricting pore throats (Fetter, 2001). Hydraulic conductivity is a practical measure of permeability, and can be described using Darcy's Law:

$$Q = -KA\frac{dh}{dl} \tag{B.2}$$

where (Q) is discharge (or flow), (K) is a proportionality constant, (A) is the cross-sectional area and (dh/dl) is the hydraulic gradient (Fetter, 2001). The proportionality constant is a function of the properties of both the porous medium and the fluid, with key fluid properties being density, viscosity and the effects of gravity. Viscosity and density of fluids are partly controlled by temperature (Fetter, 2001).

B.1.1.3 Homogeneity

A fully homogeneous geological unit is one that has the same properties in all directions at all points, and so has the same ability to transmit fluids in any direction, at any point. Heterogeneous units have properties which vary spatially, and so the hydraulic properties of the unit vary, giving the unit anisotropic characteristics. Typical examples of heterogeneity in a unit include:

- Change in thickness of the unit.
- Layers with different hydraulic properties (vertical facies changes).
- Lateral changes in hydraulic properties (commonly facies changes).
- Different amounts and sizes of solution cavities or fractures acting as conduits

As such, it is rare to find truly homogenous rock formations, and the degree of isotropy has significant implications for fluid flow. Heterogeneity also occurs on small scales. If the geometry of voids within a unit is uniform in all directions intrinsic permeability will also be the same, and the unit is described as isotropic. If the geometry of voids is not uniform, then there may be a direction in which the intrinsic permeability is greater, and the unit is described as anisotropic, and will conduct fluid flow in one direction preferentially to another (Fetter, 2001).

B.1.1.4 Source of fluids

Supply of fluids is related to the permeability and pressure gradients during the basin history:

$$Q = k\frac{(dP/dZ)}{\mu} \tag{B.3}$$

Where (Q) represents the flux, (dP/dZ) represents the potentiometric pressure gradient, (k) represents permeability and (μ) represents viscosity (Darcy equation). In most cases, the flux is relatively constant over time as it is limited by the supply of fluids (Bjørlykke, 1997). The main types of fluids in sedimentary basins are:

- Pore waters formed from meteoric water.
- Pore waters derived from seawater.
- Fluids generated from solids (via dehydration of minerals or petroleum generated from kerogens).
- CO_2 and other non-aqueous, non-hydrocarbon fluids.

Meteoric water flow is limited by the rate of infiltration into the groundwater, with the flow rate in the subsurface controlled by groundwater head and the orientation and lateral continuity of aquifers (Bjørlykke, 1997). This flow may be focussed by aquifers, but the flux generally decreases away from the area of recharge (Bjørlykke, 1997). Pore waters derived from seawater are driven out of sediments by mechanical and chemical compaction developed by increasing overburden and are discussed in detail below. Tectonic stresses can also increase compaction. Fluids may be generated by the breakdown of solids, for example derivation of petroleum and CO_2 from solid kerogens. Diagenetic reactions may lead to fluid release such as dehydration of clay minerals. Dehydration of gypsum to anhydrite may release up to 60 % water by volume at shallow depths (~1 km; Bjørlykke, 1997). Fluids generated in this manner may lead to overpressuring (Bjørlykke, 1997).

B.1.1.5 Deposition, burial and extension

During deposition and burial fluid flow in sediments is primarily driven by compaction caused by increasing overburden (Bjørlykke, 1997, 2006). Compaction processes result in a reduction of porosity and an increase in rock density. The amount of compaction is controlled by the nature and magnitude of stresses upon the rock or sediment and the physical properties of the rock. Compaction occurs mechanically, as a function of effective stress (σ_e):

$$\sigma_e = \sigma_t - P_f \tag{B.4}$$

where (σ_t) is total stress (generally the weight of overburden) and (P_f) is pore fluid pressure (Bjørlykke, 2006). Volume changes in the solid parts of the rock are negligible due to the low compressibility of mineral phases, and so change in rock volume is essentially due to reduction in porosity. Fluids must then be expelled due to this porosity reduction. In subsiding sedimentary basins, mechanical compression normally occurs under increasing effective stress. These sediments are then normally consolidated and have ductile properties, meaning open fractures do not exist. Subsequent uplift and

erosion may then reduce the effective vertical stress, causing the sediments to be over-consolidated and brittle, likely leading to deformation and fracture formation (Bjørlykke, 2006).

Chemical compaction also occurs as a function of diagenesis, and involves dissolution of grains at load-bearing grain contacts, along with precipitation of cements in open pores where there is no effective stress. These processes are controlled by thermodynamic stability of the mineral phases and the kinetics of the reactions (Bjørlykke, 2006). The volume of cement precipitated (V_c) is:

$$V_c = Ft(\Delta T)\alpha_T \rho^{-1} \tag{B.5}$$

where (F) is the vertical component of fluid flux, (t) is time, (ΔT) is the geothermal gradient, (α_T) is the solubility/temperature gradient of the mineral phase, and (ρ) is the mineral density (Bjørlykke, 1994). Distribution of cement is in most cases controlled by local diffusion rather than advective transport, except for at the near surface and along permeable faults (Bjørlykke, 2006). In some situations, chemical processes may reduce the volume of the solid phase. Dissolution and dehydration of mineral phases reduce solid volume, as does the conversion of solid kerogens to hydrocarbons (Bjørlykke, 2006). Chemical compaction dominates in the deeper parts of basins ($>$ 80–100 °C). These processes reduce rock volume (Bjørlykke, 2006). Quartz dissolution and cementation is the main process in silicious sediments, but clay and feldspar dissolution/precipitation may also contribute. The rate of chemical compaction is related to temperature and the surface area of grains available for cementation, as well as time. Quartz dissolution rates in water increase by a factor of 10^5 over the temperature interval 20–100 °C (Palandri and Kharaka, 2004). Similarly, surface controlled precipitation rates increase by a factor of 10^7 over a similar temperature range (Giles, 1997). In mudstones, mechanical compaction is dominant at temperatures up to 80 °C. From 80–110 °C smectite becomes thermally unstable and opal A and opal CT dissolve and reprecipitate as quartz. Mineral composition (particularly smectite content) is an important control on the compaction of mudstones, as is the presence of carbonate cement (Nygård et al., 2004).

Carbonate compaction is more sensitive to stress and less to temperature than that of silicious sediments (Giles, 1997). Carbonate mineral dissolution and precipitation is relatively fast, even at low temperatures. Increased effective stress along grain contacts or stylolites increases the solubility of carbonate minerals. Clay minerals also increase the dissolution rate of carbonates and become consolidated along stylolites where much of the dissolution takes place. Overall, chemical compaction is controlled by thermodynamics and kinetics, whereas mechanical compaction occurs as a result of effective stress and rock strength (Bjørlykke, 2006).

In subsiding sedimentary basins, water is expelled upwards at an average rate constrained by the porosity loss of the underlying sediment (caused by mechanical and chemical compaction). Rates of subsidence may cause the net movement of fluids to be downward in relation to the sea floor, even though average water flow is upwards (Bjørlykke, 1994). Absolute flow rates depend on the permeability of the sedimentary sequences.

Faulting and fracturing are important control on fluid flow, and faults can act as both barriers and conduits depending upon their permeability. The permeability of faults is controlled by mechanical shearing and damage and deformation, as well as diagenetic reactions (Bjørlykke, 2006). The type of fracturing depends upon the magnitude and distribution of the effective shear stresses, and the shear strength of the lithology. Shear deformation in soft uncemented sediments at shallow depths typically causes negative dilation (compaction), whereas well-cemented rocks tend to develop dilation and increased permeability (Bjørlykke, 2006). Style of shearing is also dependent upon mineralogy and texture, with well-sorted sands producing a dense interlocking grain fabric when sheared resulting in strain hardening and reduced permeability before the onset of grain crushing (Wong et al., 1997). Strain hardening then causes the zone of shear deformation to shift, developing a broad zone of deformation without a well-defined shear plane, and generally prevents the development of clay smear (Bjørlykke, 2006). Diagenetic reactions including quartz cementation cause a reduction in porosity and permeability as a function of time and temperature during burial (Bjørlykke, 2006). The porosity of the shear zone when quartz cementation begins is important in determining the final porosity and permeability characteristics (Fisher et al., 2003). Diagenetic healing of faults can change their properties over time, and fractured grains provide good nucleation sites for quartz overgrowth since fault zones often have more quartz cement than matrix (Bjørlykke, 2006). Thus, in sandy sediments, faults are less likely to be reactivated since the fault plane then has a higher shear strength than the surrounding rocks. often resulting in new faults adjacent to old ones (Bjørlykke, 2006). Permeable faults and fractures formed in sediments during burial are rarely filled with cement precipitated from advecting water, since quartz cementation requires temps above 70-100 ℃ and much higher fluid fluxes than are realistic, and calcite will dissolve when upward flowing water is cooled (Bjorlykke and Egeberg, 1993). Fractures are more likely to be filled by crystal growth via diffusion from adjacent rocks (Egeberg and Saigal, 1991; Hesthammer et al., 2002). Clay rich sediments may develop a clay smear along fault planes resulting in strain softening and subject to easy reactivation, due to a shift from random to alligned clay minerals along the shear zone (Bjørlykke, 1997, 2006). However, at increased depth and temperatures, recrystallisation of the clay may result in increased shear strength, resulting in a stronger plane than the matrix (Bjørlykke, 2006). Hydrofracturing is an important process and occurs when the pore fluid pressure exceeds the least principal stress. In

subsiding sedimentary basins, this is normally the horizontal stress (plus the tensional strength, generally assumed to be small compared to horizontal stress Bjørlykke, 1997, 2006):

$$P_f = \sigma_h + \tau \tag{B.6}$$

where (P_f) is pore fluid pressure, (σ_h) is horizontal stress, and (τ) is tensile strength. Hydrofracturing is a common effect of overpressure, which occurs when compression due to sediment loading occurs faster than fluids can be expelled via porosity reduction. This is a common feature in fine grained mudstones during high sedimentation rates. Examples of hydrofracturing are common in the Copperbelt in the form of layer parallel veins, particularly in the Copperbelt Orebody Member (Greyling et al., 2005; Selley et al., 2005).

In most cases, faults formed during the deposition and burial of sediments are less permeable than the sediments themselves. Faulting becomes increasingly important for permeability the more consolidated and lithified the sediments become.

Extensional faulting due to rifting is often associated with uplift and the erosion of a margin, stopping mechanical compaction due to decreased effective stress, and reducing the rate of chemical compaction by quartz cementation. Therefore little porosity reduction occurs, and little compaction drives fluid flow to fill fractures (Bjørlykke, 2006). The increase in porosity due to fracturing may then lower pore pressure below hydrostatic levels and cause drawdown fluids from above (Bjørlykke, 1999). This effect, when combined with the high density of residual fluids from the evaporation of seawater potentially represents an effective mechanism for transporting brines to depth.

Ultimately, in subsiding sedimentary basins, two distinct hydrological regimes are recognised (Powley, 1990). In the upper part of basins, fluid pressures are near hydrostatic, with fluids able to migrate throughout the basin in response to topographic, tectonic or thermally-induced gradients in hydraulic head. In the deeper sections of basins compaction has rendered some layers highly impermeable, resulting in fluids present in discrete compartments confined by impermeable rocks without significant interconnection (Yardley, 1997).

In mature sedimentary basins, compaction is completed, and uplift has begun, with fluid flow primarily driven by hydraulic gradients caused by the water table configuration, which reflects basin topography (Garven and Freeze, 1984a). Fluid flow occurs from areas of high topography to low topography, with brines typically driven towards basin margins (Fig. B.3). Gravity driven flow, aided by temperature and salinity gradients, leads to the development of a steady state system, providing a mechanism where fluids can be transported great distances through basins (Garven and Freeze, 1984a,b). On

local scales, this regional flow is controlled by the distribution of lithologies with different hydrogeological characteristics.

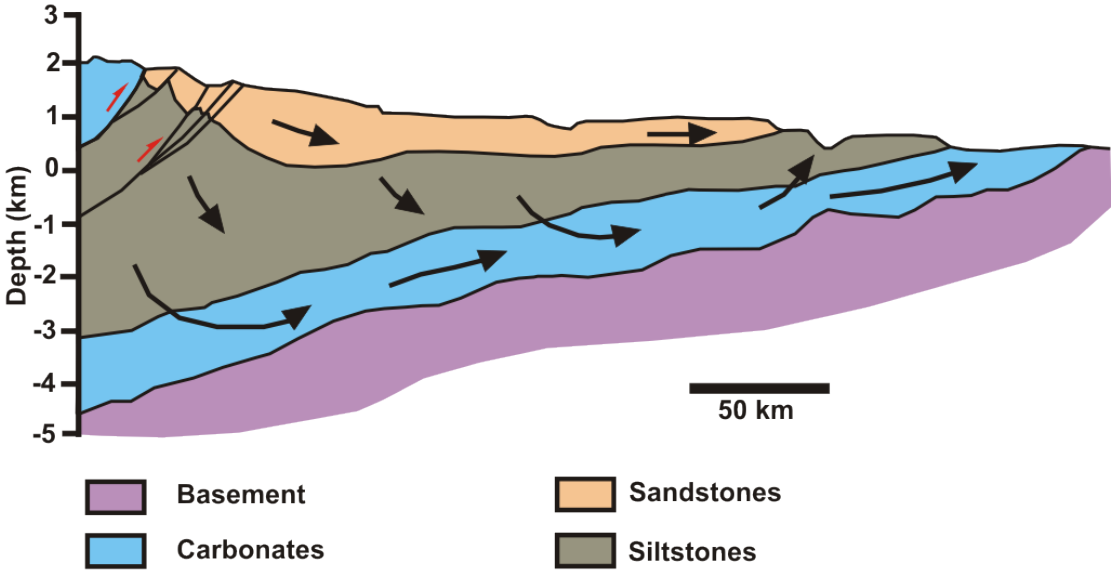

FIGURE B.3: Conceptual model of gravity-driven fluid flow in evolving sedimentary basins. The major driving mechanism for flow is the sloped water table caused by the variation in topography. Lithologies locally control the flow with their porosity and permeability characteristics. (Adapted from Garven and Freeze, 1984a).

B.1.2 Fluid chemistry

Fluid chemistry in sedimentary basins is dominantly controlled by the chemistry of the pore fluids (typically seawater) and that of the host sediments. Ultimately, with time, chemical interactions between pore fluids and and minerals within the host sediments cause fluid chemistries to evolve towards equilibrium with the host sediments (e.g. Davisson et al., 1994; Hanor, 1994; Land, 1995). Cation exchange reactions are the most common, but solvent content can change, as can addition of ligands from the surrounding rocks (Yardley, 1997). Solvent content may vary through dehydration of hydrous mineral phases or hydration of anhydrous phases, as well as decarbonation (or mixed-volatile) reactions involving diagenetic, authigenic and detrital minerals, as well as methanogenesis of organic matter (Yardley, 1997). Solute content may be modified by leaching of chloride from detrital minerals, dissolution of halite or gypsum, or the release of sulphate via oxidation of sulphides (Yardley, 1997).

In sedimentary basins and passive continental margin environments, mineral dehydration reactions are common with increasing depth. Theoretically, this should lead to dilution of fluids (Yardley, 1997). However, fluids at depth in sedimentary basins are typically highly saline, leading many workers to suggest that evaporation-derived bittern brines

and dissolution of evaporites play a very important role in determining fluid salinities and chemistries (Yardley, 1997). In accretionary zones and oceanic settings, pore waters may become less saline with depth, potentially reflecting up-flow and dilution by metamorphic waters (Yardley, 1997). This contrasts with the evidence from passive margin sequences, and is likely due to the lack of evaporite sequences in marine sediment packages.

B.2 Fluid flow in lithified rocks during orogenesis and metamorphism

Whilst much of the fluid history of the Copperbelt is likely to have been dominated by sedimentary and basin processes, modern workers recognise that mineralisation occurred at multiple times through basin evolution, and that individual deposits often show evidence for multiple phases of fluid flow, associated with mineralisation or remobilisation of ore (e.g. Nkana; Muchez et al., 2010). Economic deposits may also form after peak orogenesis, for example Kansanshi, hosted in post-kinematic veins (Broughton et al., 2002; Torrealday et al., 2000). As such, it is also important to assess the conditions which control the properties and distribution of fluids in these environments. 'Metamorphic' fluids in these environments are ultimately sourced from sediment pore waters and hydrous assemblages. These fluids become modified physically and chemically due to the changing temperature and pressure conditions during metamorphism (Yardley, 1997). Since igneous fluids have long been discounted in the generation of SHSCs, this section will focus purely on fluids of metamorphic origin. Yardley (1997) make a distinction between fluids hosted by metamorphic or other crystalline rocks, irrespective of origin (termed crustal fluids) and those fluids derived in part from the devolatilisation of minerals (termed metamorphic fluids). This nomenclature will be followed in this section.

B.2.1 Mechanisms of fluid movement

The shift from burial and diagenesis to metamorphism is transitional and likely involves further porosity loss, particularly in sandstones. It is typically assumed that lithostatic fluid pressures are normal during metamorphism due to evidence from extensional veining (Ague, 1995) and estimates of P-T conditions from fluid-present and fluid-absent equilibrium (Yardley, 1997). Essentially, initially sediments are in hydrostatic equilibrium where rigid grains contain an interconnecting network of pores and fractures in which fluid pressure is dictated by the weight of the overlying water column (Yardley,

1997). As pressure and temperature increases, the interconnected network of pores becomes cut off, and lithostatic equilibrium is achieved, where a plastic rock compacts pores until fluid pressure is equal to lithostatic pressure, leaving low permeability. In relatively weak metamorphic rocks (e.g. schists) during metamorphism, the fluid pressure cannot exceed lithostatic pressure by a significant amount, meaning permeability and porosity maintain values allowing metamorphic fluid to escape at the same rate that it is generated. Since devolatilisation reactions are endothermic, heat supply effectively controls permeability in metamorphism (Yardley, 1997). Fluid flow in crustal rocks can be described as either pervasive or focussed. Pervasive flow is the movement of fluids around individual mineral grains, whereas focussed flow occurs along conduits with enhanced permeability, such as faults, shear zones and lithological contacts (Oliver, 1996).

Large changes in isotopic values, bulk rock chemistry and the presence of metamorphic veins have often been taken to indicate areas which have been subjected to significant flow of fluids. In reality, in most cases metamorphosing rocks are subject to very low permeabilities and contain small amounts of fluid at near lithostatic pressures which constantly leak away at similar rates to that which they are generated (i.e. pervasive flow; Yardley, 1997). When higher permeability pathways are created (allowing focussed flow) to regions of lower hydraulic head by deformation or porosity enhancing reactions (Yardley and Lloyd, 1995) extensive fluid drainage will occur down that pathway until it becomes of similar permeability to the surrounding areas or it is cut off from the areas of lower head (Yardley, 1997). This is likely to be a rapid process, as these high permeability zones will drain the metamorphic fluid faster than it can be generated, and so will collapse and be compressed as the fluid pressure drops (Yardley, 1997). Evidence of significant fluid flow in metamorphic environments thus likely represent fluid conduits transporting fluids with a significant source at depth to account for the longevity of flow (Yardley, 1997). In pervasive flow conditions, fluid pathways are strongly controlled by anisotropy, with inequidimensional minerals (particularly sheet silicates) causing variation in permeabilities $\sim$10 times greater parallel to foliation than perpendicular to it (Huenges et al., 1997; Zhang et al., 2001). Oriented fracture sets may also cause anisotropy (Ague, 2004).

Many minerals created at high temperatures and pressures have the potential to react with fluid during cooling on the retrograde metamorphic path. Pore fluids from peak metamorphism are then consumed by hydration and carbonation of high PT phases (Yardley, 1997). The general lack of retrograde features in many metamorphic rocks suggests that most metamorphic fluid has been lost by diffusion and flow before the rocks are uplifted and unroofed. Initially, after peak metamorphism, these rocks become fluid sinks liable to incorporate metamorphic fluids still available from the prograde

metamorphic path (Yardley, 1997). Eventually, cooling occurs fluid pressures drop from lithostatic to hydrostatic. After fluids drop below hydrostatic pressure, the metamorphic rocks become highly impermeable and cannot lose fluid to flow, but are closed to any external inputs. Finally, deep penetrating fractures permit the influx of fluid from above to react with the dry metamorphic rocks (Yardley, 1997). Since most prograde fluids are removed during the prograde path, or taken up in the early part of the retrograde path, retrograde fluids are typically externally derived, and disassociated and unrelated to fluids formed earlier on in the metamorphic cycle.

B.2.2 Fluid chemistry

Chemical compositions of fluids during metamorphism is strongly dependent upon the composition of the sedimentary pile, including the proportions of clays, carbonates and degraded organic matter (Yardley, 1997). Constraining compositions of crustal fluids during the metamorphic cycle is challenging, as samples often record both the prograde and retrograde metamorphic paths.

Many examples of what are thought to be prograde fluids are relatively saline with halogen signatures similar to oilfield brines (Banks et al., 1991; Grant et al., 1990). Other examples of high salinity fluids (in this case derived from evaporites) surviving into low grade metamorphism are provided by emerald deposits (Guiliani et al., 1995). Lower salinity fluids may also be preserved (Yardley, 1997). Sequences with more volcaniclastic material may develop more saline pore fluids with time through hydration of volcanic material (Yardley, 1997).

Identification and isolation of examples of peak-metamorphic crustal fluids from medium to high grade metamorphic rocks is difficult, but examples from the alps are moderately saline (5–15 wt% NaCl equiv.) with increasing salinities in proximity to evaporites with gas chemistries reflecting metamorphic grade (Yardley, 1997). Other studies from metamorphosed continental margin sequences report fluids more saline than seawater, but below halite saturation, indicating dilution of brines by metamorphic fluid (Hollister and Burruss, 1976; Yardley, 1997). Highly saline waters may be associated with granulites, but may record dissolution of water into anatectic melt phases rather than original fluid compositions (Yardley, 1997). Fluids derived from highly metamorphosed ocean margin rocks are of low salinity, as are fluids preserved in metabasite minerals, suggesting high salinity fluids do not develop during metamorphism unless already present, or until the onset of anatexis (Hay and Craw, 1993; Yardley, 1982). The concentrations of conservative ligands at the point of diagenesis persist through most metamorphic conditions.

Salinity also helps to control non-conservative ion chemistry, particularly through cation exchange reactions, normally involving Na and Ca. These exchange reactions may favour equilibrium states with mineral phases (e.g. paragonite, albite and quartz) containing hydroxide groups in equilibrium with a fluid rich in Na^+. Changes in salinity may then favour the formation of the H^+ ion, causing pH to vary with changing salinities, e.g.:

$$3NaAlSi_3O_8 + 2H^+ = NaAl_3Si_3O_{10}(OH)_2 + 6SiO_2 + 2Na^+ \tag{B.7}$$

Such reactions, where calcic phases are present also increase Ca content and Ca/Na (Yardley, 1997). Minor ligands such as F^-, HCO_3^- and SO_4^{2-} often form Ca minerals, and so Ca content often defines maximum concentrations those ligands attain (Yardley, 1997).

Other important components of fluids in metamorphic conditions are CH_4, CO_2 and NH_4^+, developed by the breakdown of organic material (typically occurring after initial loss of porosity) and carbonate minerals (Ague, 2004; Pitcairn et al., 2005; Yardley, 1997). Sulphur may also be released by progressive heating of pyrite to form pyrrhotite (Pitcairn et al., 2010). Pure water is miscible with CO_2 and CH_4 by greenschist facies temperatures, and methane is generally immiscible under the conditions it forms. During greenschist facies, carbonate minerals begin to breakdown and form CO_2, and if carbonates are a significant part of the sequence, CO_2 generation may be a significant new source of fluid by the time amphibolite facies is reached (Cooper, 1972; Yardley, 1997). At low temperatures during diagenesis aqueous phases are likely immiscible with CH_4 and CO_2. Saline fluids increase the immiscibility gap to high temperatures, which may cause decoupling between aqueous fluids and CO_2 (Yardley and Bottrell, 1988).

B.3 Evaporites and brine generation

Evaporites are frequently cited as being critical for the formation of a number of different ore deposit types, SHSCs included (Warren, 2000). Evaporites play three major roles in ore deposit formation:

1. Evaporites provide a source of Cl-rich brines (± other anions) highly effective at complexing and transporting metals.

2. Evaporites can provide a source of sulphur for the formation of sulphide mineralisation.

3. Evaporites provide numerous effective mechanisms for channeling and focussing fluid flow.

Whilst transient features in many sedimentary basins, evaporite formations are a rich source of saline brines at multiple stages of their life cycle. During the formation of evaporite deposits, dense Br-rich bittern brines form as Na and Cl are partitioned from seawater into halite. Over their stable life, evaporite sequences are known to discharge significant volumes of brines due to compaction, dewatering and metamorphic recrystallisation (e.g. Fontes and Matray, 1993). Complete dissolution of evaporite sequences through halokinesis is common, and provides a major source of Cl-rich brines in basins. All of these brines are dense, and typically flow downward into the underlying stratigraphy (Warren, 2000). Evaporites also contain easily soluble sulphate minerals useful as a source of SO_4^{2-} ready for reduction and the formation of sulphide minerals common across a suite of deposit types. Evaporite sequences have very low permeabilities, and are highly capable of channeling fluids around and along and under their margins. This impermeability may focus fluids under margins or entire underbellies of salt bodies and through faults in the salt bodies themselves, and these locations may be suitable for the development of brine convection cells (Warren, 2000). Aside from providing brines, halokinesis may also dramatically increase permeability in surrounding stratigraphy through the formation of dissolution breccias, faults and salt weld structures (Warren, 2000).

B.4 Variation in seawater chemistry through time

Ultimately, whilst fluid compositions may be modified by a number of processes throughout deposition, burial, diagenesis and metamorphism, initial pore fluid composition provides a strong control over the fluid chemistry. Since most pore waters are derived from seawater, it is important to understand past seawater chemistry in order to relate to the likely initial fluid compositions within the Katangan Supergroup and the basins of the Copperbelt.

The chemical composition of seawater has varied over geological timescales (Canfield, 1998; De Ronde et al., 1997; Lowenstein et al., 2003; Lyons et al., 2009). Cation concentrations (especially Ca) in seawater are thought to be significantly variable throughout geological time (De Ronde et al., 1997; Gutzmer et al., 2003), particularly in the Phanerozoic (Brennan et al., 2004; Hardie, 1996; Horita et al., 1996, 2002; Kovalevich et al., 1998; Lowenstein et al., 2003, 2001). In contrast, the halogens act relatively conservatively in seawater (Fontes and Matray, 1993; You et al., 1994), and so are less likely to have been as variable through time. Attempts to reconstruct seawater chemistry in the Phanerozoic are based around examining fluid inclusions within halite in evaporite sequences (Brennan et al., 2004; Horita et al., 1996, 2002; Kovalevich et al.,

1998; Lowenstein et al., 2003, 2001). Due to lack of preservation of evaporite sequences in deep geological time, attempts to reconstruct seawater chemistry in the Archaean and Proterozoic involve investigating fluid inclusions hosted in hydrothermal quartz and carbonate preserved in pillow basalt sequences (Channer et al., 1997; De Ronde et al., 1997; Foriel et al., 2004; Gutzmer et al., 2003). Reconstructions for the Archaean using samples from the Barberton greenstone belt (South Africa) suggest that chlorine concentrations were higher than in modern seawater by ∼165 %, and that Br^- and I^- concentrations were also higher at ∼3.2 Ga (De Ronde et al., 1997). It is suggested that sulphate concentrations were lower than modern day values, and that Ca was higher (De Ronde et al., 1997). Estimations of halogen ratios suggest that they are within error of the bulk earth, and that at this time, chlorine and bromine were controlled by mantle buffering, giving chlorine-bromine ratios ∼409, lower than modern values (Channer et al., 1997; De Ronde et al., 1997). Estimates from pillow basalts in Western Australia provide a different view, indicating seawater at North Pole showed chlorine-bromine ratios ∼630, similar to modern values, with low sulphate concentrations, controlled by organic sedimentation (Foriel et al., 2004). Other fluids at North Pole are interpreted as hydrothermal in nature, and show chlorine-bromine ratios lower than modern seawater (∼350 and ∼390), close to the value of the bulk earth (∼420) suggesting hydrothermal fluids at this locality were buffered by the mantle (Foriel et al., 2004). However, the basin at North Pole may have been restricted, potentially allowing fractionation between Br and Cl to occur by the formation of organic material in this region, which may not have been the case for the oceans as a whole (Foriel et al., 2004).

Reconstructions of estimated seawater chemistry in the Palaeoproterozoic were made from quartz veins and pods hosted in hydrothermally altered 2.2 Ga basaltic andesites, South Africa (Gutzmer et al., 2003). Increases in Ca in this case are attributed to water-rock interaction, but Cl/Br values remain similar to those suggested for a mantle-buffered ocean by De Ronde et al. (1997), indicating that the marine system still lacked enough organic material to fractionate Br and Cl at this time (Gutzmer et al., 2003). In modern systems, bromine is typically enriched compared to seawater values in marine planktonic organisms, whilst chlorine is depleted (Price and Calvert, 1977; Romankevich, 1990). Bromine is released from organic matter in sediments into pore fluids at depth (Martin et al., 1993), but the majority of these pore fluids are not returned to the ocean system, instead being trapped and recycled below the sediment-water interface (Wakefield and Elderfield, 1985). Thus, burial of organic material represents a mechanism for increasing Cl/Br above that of the bulk earth, towards modern values.

Reconstructed estimates for seawater chemistry in the Phanerozoic suggest an oscillation between periods with relatively high Mg^{2+}/Ca^{2+} ratios and Na^+ concentrations during parts of the Late Precambrian (544–543 Ma), Permian (258–251 Ma) and Tertiary to

present (40–0 Ma; Lowenstein et al., 2001). In contrast, lower Mg^{2+}/Ca^{2+} ratios and lower Na^{+} concentrations occurred during parts of the Cambrian (540–520 Ma), Silurian (440–418 Ma) and Cretaceous (124–94 Ma; Lowenstein et al., 2001). In both these scenarios, absolute concentrations of the Cl^{-} anion were higher (Lowenstein et al., 2001). It is suggested that these periods where seawater is Ca-rich are responsible for the generation of $CaCl_2$-rich basinal brines (Lowenstein et al., 2003), which also show low $SO_4{}^{2-}$ concentration and enrichment in Cl^{-} concentrations above modern seawater values (Horita et al., 2002; Kovalevich et al., 1998). These oscillations occur in step with long-term changes in seafloor spreading rates, variations in global sea level and changes between 'greenhouse and 'icehouse conditions, all controlled by plate tectonics (Horita et al., 2002; Lowenstein et al., 2001). Changes in Phanerozoic seawater chemistry may then be controlled by factors including fluxes at Mid Ocean Ridges, dolomitisation of carbonate sediments and biologic evolution over this period (Horita et al., 2002).

Significant issues exist with attempts to constrain past seawater chemistry by preservation of fluid inclusions. In addition to lack of data, Archaean estimates are reconstructed from quartz veins formed in hydrothermal systems at much higher temperatures than seawater, and attempts must be made to deconvolve hydrothermal signals from that of seawater (e.g. De Ronde et al., 1997; Foriel et al., 2004). Some of the available data are from deposits identified as having formed in restricted basins (Foriel et al., 2004) and thus may not fully reflect global seawater chemistry. Additionally, there is doubt whether the deposits sampled by De Ronde et al. (1997) and Channer et al. (1997) actually represent Archaean seafloor hydrothermal systems at all (Lowe and Byerly, 2003). For Phanerozoic measurements, it is necessary to very carefully understand the nature of the evaporite sequence itself in order to avoid restricted basin deposits (e.g. Lowenstein and Hardie, 1985) and even then, fluids trapped in evaporite halite are likely to have undergone some degree of evaporation (as discussed by Horita et al., 2002). However, these represent our best estimates at constraining a particularly difficult problem.

Appendix C

Appendix C: Supplementary data

This is an electronic appendix containing spreadsheets of all the fluid inclusion microthermometric data, fluid leachate chemistry data, and trace and rare earth data of sulphides obtained during this project. See attached CD-ROM.

Bibliography

Ague, J., 1995. Deep crustal growth of quartz, kyanite and garnet into large-aperture, fluid-filled fractures, north-eastern Connecticut, USA. Journal of Metamorphic Geology 13, 299–314.

Ague, J., 2004. Fluid flow in the deep crust, in: Rudnick, R., Holland, H., Turekian, K. (Eds.), Treatise on geochemistry Vol. 3: The Crust. Elsevier, London, pp. 195–228.

Alexandre, P., 2010. Mineralogy and geochemistry of the sodium metasomatism-related uranium occurrence of Aricheng South, Guyana. Mineralium Deposita 45, 351–367.

Alexandre, P., Kyser, K., Polito, P., Thomas, D., 2005. Alteration mineralogy and stable isotope geochemistry of Paleoproterozoic basement-hosted unconformity-type uranium deposits in the Athabasca Basin, Canada. Economic Geology 100, 1547–1563.

Annels, A., 1984. The geotectonic environment of Zambian copper-cobalt mineralization. Journal of the Geological Society 141, 279–289.

Annels, A., 1989. Ore genesis in the Zambian Copperbelt, with particular reference to the northern sector of the Chambishi Basin, in: Boyle, R., Brown, A., Jefferson, C., Jowett, E., Kirkham, R. (Eds.), Sediment-hosted stratiform copper deposits. Geological Association of Canada Special Paper 36, Ontario, pp. 427–452.

Annels, A., Vaughan, D., Craig, J., 1983. Conditions of ore mineral formation in certain Zambian Copperbelt deposits with special reference to the role of cobalt. Mineralium Deposita 18, 71–88.

Armstrong, R., Master, S., Robb, L., 2005. Geochronology of the Nchanga Granite, and constraints on the maximum age of the Katanga Supergroup, Zambian Copperbelt. Journal of African Earth Sciences 42, 32–40.

Banks, D., Da Vies, G., Yardley, B., McCaig, A., Grant, N., 1991. The chemistry of brines from an Alpine thrust system in the Central Pyrenees: an application of fluid inclusion analysis to the study of fluid behaviour in orogenesis. Geochimica et Cosmochimica Acta 55, 1021–1030.

Banks, D., Giuliani, G., Yardley, B., Cheilletz, A., 2000. Emerald mineralisation in Colombia: fluid chemistry and the role of brine mixing. Mineralium Deposita 35, 699–713.

Banks, D., Yardley, B., Campbell, A., Jarvis, K., 1994. Ree composition of an aqueous magmatic fluid: a fluid inclusion study from the Capitan Pluton, New Mexico, USA. Chemical Geology 113, 259–272.

Barra, F., Broughton, D., Ruiz, J., Hitzman, M., 2004. Multi-stage mineralization in the Zambian Copperbelt based on Re-Os isotope constraints (abs.). Geological Society of America Abstracts with Program 36, 516.

Barrett, T.J., Jarvis, I., Jarvis, K.E., 1990. Rare earth element geochemistry of massive sulfides-sulfates and gossans on the Southern Explorer Ridge. Geology 18, 583–586.

Bateman, A., 1930. Ores of the Northern Rhodesian Copperbelt. Economic Geology 25, 365–418.

Batumike, M., Cailteux, J., Kampunzu, A., 2007. Lithostratigraphy, basin development, base metal deposits, and regional correlations of the Neoproterozoic Nguba and Kundelungu rock successions, central African Copperbelt. Gondwana Research 11, 432–447.

Batumike, M., Kampunzu, A., Cailteux, J., 2006. Petrology and geochemistry of the Neoproterozoic Nguba and Kundelungu Groups, Katangan Supergroup, southeast Congo: Implications for provenance, paleoweathering and geotectonic setting. Journal of African earth sciences 44, 97–115.

Bau, M., Dulski, P., 1999. Comparing yttrium and rare earths in hydrothermal fluids from the Mid-Atlantic Ridge: implications for Y and REE behaviour during near-vent mixing and for the Y/Ho ratio of Proterozoic seawater. Chemical Geology 155, 77–90.

Beaufort, D., Patrier, P., Laverret, E., Bruneton, P., Mondy, J., 2005. Clay alteration associated with proterozoic unconformity-type uranium deposits in the East Alligator Rivers uranium field, Northern Territory, Australia. Economic Geology 100, 515–536.

Bechtel, A., Sun, Y., Püttmann, W., Hoernes, S., Hoefs, J., 2001. Isotopic evidence for multi-stage base metal enrichment in the Kupferschiefer from the Sangerhausen Basin, Germany. Chemical Geology 176, 31–49.

Benham, D., Greig, D., Vink, B., 1976. Copper occurrences of the Mombezhi Dome area, northwestern Zambia. Economic Geology 71, 433–442.

Bernau, R., Roberts, S., Richards, M., Nisbet, B., Boyce, A., Nowecki, J., 2013. The geology and geochemistry of the Lumwana Cu (±Co±U) deposits, NW Zambia. Mineralium Deposita 48, 137–153.

Bi, X., Cornell, D., Hu, R., 2002. Ree composition of primary and altered feldspar from the mineralized alteration zone of alkaline intrusive rocks, western Yunnan Province, China. Ore Geology Reviews 19, 69–78.

Binda, P., Van Eden, J., 1972. Sedimentological evidence on the origin of the Precambrian Great Conglomerate (Kundelungu tillite), Zambia. Palaeogeography, Palaeoclimatology, Palaeoecology 12, 151–168.

Binda, P.L., 1994. Stratigraphy of Zambian copperbelt orebodies. Journal of African earth sciences 19, 251–264.

Bjørlykke, K., 1994. Fluid flow and diagenesis in sedimentary basins, in: Parnell, J. (Ed.), Geofluid: Origin, migration and evolution of fluids in sedimentary basins. Geological Society Special Publication 78, London, pp. 127–140.

Bjørlykke, K., 1997. Lithological control on fluid flow in sedimentary basins, in: Jamtveit, B., Yardley, B. (Eds.), Fluid flow and transport in rocks: Mechanisms and effects. Chapman and Hall, London, pp. 15–34.

Bjørlykke, K., 1999. An overview of factors controlling rates of compaction and fluid flow in sedimentary basins, in: Jamveit, B., Meakin, P. (Eds.), Growth, dissolution and pattern formation in geological systems. Kluwer Akademic Publishers, pp. 381–404.

Bjørlykke, K., 2006. Effects of compaction processes on stresses, faults, and fluid flow in sedimentary basins: examples from the Norwegian margin, in: Buiter, S., Schreurs, G. (Eds.), Analogue and numerical modelling of crustal-scale processes. Geological Society Special Publication 253, London, pp. 359–380.

Bjorlykke, K., Egeberg, P., 1993. Quartz cementation in sedimentary basins. AAPG Bulletin 77, 1538–1548.

Bodiselitsch, B., Koeberl, C., Master, S., Reimold, W.U., 2005. Estimating duration and intensity of Neoproterozoic snowball glaciations from Ir anomalies. Science 308, 239–242.

Bonham, L., 1980. Migration of hydrocarbons in compacting basins. AAPG Bulletin 64, 549–567.

Brandt, R., Burton, C., Maree, S., Woakes, M., 1961. Mufulira, in: Mendelsohn, F. (Ed.), The Geology of the Northern Rhodesian Copperbelt. MacDonald, London, pp. 410–461.

Bray, C., Karig, D., 1985. Porosity of sediments in accretionary prisms and some implications for dewatering processes. Journal of Geophysical Research 90, 768–778.

Brems, D., Muchez, P., Sikazwe, O., Mukumba, W., 2009. Metallogenesis of the Nkana copper–cobalt South Orebody, Zambia. Journal of African Earth Sciences 55, 185–196.

Brennan, S.T., Lowenstein, T.K., Horita, J., 2004. Seawater chemistry and the advent of biocalcification. Geology 32, 473–476.

Broughton, D., Hitzman, M., Stephens, A., 2002. Exploration history and geology of the Kansanshi Cu(-Au) deposit, Zambia, in: Goldfarb, R., Nielson, R. (Eds.), Integrated Methods for Discovery: Global Exploration in the 21st Century. Society of Economic Geologists Special Publication 9, London, pp. 141–153.

Brown, A.C., 1971. Zoning in the White Pine copper deposit, Ontonagon County, Michigan. Economic Geology 66, 543–573.

Bull, S., Selley, D., Broughton, D., Hitzman, M., Cailteux, J., Large, R., McGoldrick, P., 2011. Sequence and carbon isotopic stratigraphy of the neoproterozoic roan group strata of the zambian copperbelt. Precambrian Research 190, 70–89.

Burnie, S., Schwarcz, H.P., Crocket, J., 1972. A sulfur isotopic study of the White Pine Mine, Michigan. Economic Geology 67, 895–914.

Burruss, R., Laughrey, C., 2010. Carbon and hydrogen isotopic reversals in deep basin gas: Evidence for limits to the stability of hydrocarbons. Organic Geochemistry 41, 1285–1296.

Cailteux, J., Binda, P., Katekesha, W., Kampunzu, A., Intiomale, M., Kapenda, D., Kaunda, C., Ngongo, K., Tshiauka, T., Wendorff, M., 1994. Lithostratigraphical correlation of the Neoproterozoic Roan Supergroup from Shaba (Zaire) and Zambia, in the central African copper-cobalt metallogenic province. Journal of African earth sciences 19, 265–278.

Cailteux, J., Kampunzu, A., Batumike, M., 2005b. Lithostratigraphic position and petrographic characteristics of RAT (Roches Argilo-Talqueuses) Subgroup, Neoproterozoic Katangan Belt (Congo). Journal of African Earth Sciences 42, 82–94.

Cailteux, J., Kampunzu, A., Lerouge, C., 2007. The Neoproterozoic Mwashya–Kansuki sedimentary rock succession in the central African Copperbelt, its Cu–Co mineralisation, and regional correlations. Gondwana research 11, 414–431.

Cailteux, J., Kampunzu, A., Lerouge, C., Kaputo, A., Milesi, J., 2005a. Genesis of sediment-hosted stratiform copper–cobalt deposits, central African Copperbelt. Journal of African earth sciences 42, 134–158.

Canfield, D., 1998. A new model for Proterozoic ocean chemistry. Nature 396, 450–453.

Canfield, D.E., Teske, A., 1996. Late Proterozoic rise in atmospheric oxygen concentration inferred from phylogenetic and sulphur-isotope studies. Nature 382, 11.

Carpenter, A., 1978. Origin and chemical evolution of brines in sedimentary basins. Oklahoma Geological Circular 79, 60–77.

Cathles, L., Adams, J., 2005. Fluid flow and petroleum and mineral resources in the upper (<20-km) continental crust. Economic Geology 100th Anniversary Edition , 77–110.

Channer, D.D., De Ronde, C., Spooner, E., 1997. The Cl^--Br^--I^- composition of ∼3.23 Ga modified seawater: implications for the geological evolution of ocean halide chemistry. Earth and Planetary Science Letters 150, 325–335.

Chi, G., Savard, M.M., 1997. Sources of basinal and Mississippi Valley-type mineralizing brines: mixing of evaporated seawater and halite-dissolution brine. Chemical Geology 143, 121–125.

Claypool, G.E., Holser, W.T., Kaplan, I.R., Sakai, H., Zak, I., 1980. The age curves of sulfur and oxygen isotopes in marine sulfate and their mutual interpretation. Chemical Geology 28, 199–260.

Clayton, R., Friedman, I., Graf, D., Mayeda, T., Meents, W., Shimp, N., 1966. The origin of saline formation waters. Journal of Geophysical Research 71, 3869–3882.

Cloutier, J., Kyser, K., Olivo, G.R., Brisbin, D., 2011. Geochemical, isotopic, and geochronologic constraints on the formation of the Eagle Point basement-hosted uranium deposit, Athabasca Basin, Saskatchewan, Canada and recent remobilization of primary uraninite in secondary structures. Mineralium Deposita 46, 35–56.

Cooper, A., 1972. Progressive metamorphism of metabasic rocks from the Haast Schist Group of southern New Zealand. Journal of petrology 13, 457–492.

Cosi, M., De Bonis, A., Gosso, G., Hunziker, J., Martinotti, G., Moratto, S., Robert, J., Ruhlman, F., 1992. Late Proterozoic thrust tectonics, high-pressure metamorphism and uranium mineralization in the Domes Area, Lufilian Arc, northwestern Zambia. Precambrian Research 58, 215–240.

Crowe, D.E., Valley, J.W., Baker, K.L., 1990. Micro-analysis of sulfur-isotope ratios and zonation by laser microprobe. Geochimica et Cosmochimica Acta 54, 2075–2092.

Davisson, M.L., Presser, T., Criss, R., 1994. Geochemistry of tectonically expelled fluids from the northern Coast ranges, Rumsey Hills, California, USA. Geochimica et Cosmochimica Acta 58, 1687–1699.

De Ronde, C.E., Channer, D.M.d., Faure, K., Bray, C.J., Spooner, E.T., 1997. Fluid chemistry of Archean seafloor hydrothermal vents: Implications for the composition of circa 3.2 Ga seawater. Geochimica et Cosmochimica Acta 61, 4025–4042.

Dechow, E., Jensen, M., 1965. Sulfur isotopes of some central African sulfide deposits. Economic Geology 60, 894–941.

Decrée, S., Deloule, É., De Putter, T., Dewaele, S., Mees, F., Yans, J., Marignac, C., 2011. SIMS U–Pb dating of uranium mineralization in the Katanga Copperbelt: Constraints for the geodynamic context. Ore Geology Reviews 40, 81–89.

Dewaele, S., Muchez, P., Vets, J., Fernandez-Alonzo, M., Tack, L., 2006. Multiphase origin of the Cu–Co ore deposits in the western part of the Lufilian fold-and-thrust belt, Katanga (Democratic Republic of Congo). Journal of African Earth Sciences 46, 455–469.

Donnelly, T., Waldron, S., Tait, A., Dougans, J., Bearhop, S., 2001. Hydrogen isotope analysis of natural abundance and deuterium-enriched waters by reduction over chromium on-line to a dynamic dual inlet isotope-ratio mass spectrometer. Rapid Communications in Mass Spectrometry 15, 1297–1303.

Eastoe, C., Long, A., Land, L.S., Kyle, J.R., 2001. Stable chlorine isotopes in halite and brine from the Gulf Coast Basin: brine genesis and evolution. Chemical Geology 176, 343–360.

Eastoe, C., Peryt, T., Petrychenko, O.Y., Geisler-Cussey, D., 2007. Stable chlorine isotopes in Phanerozoic evaporites. Applied Geochemistry 22, 575–588.

Eastoe, C.J., Long, A., Knauth, L.P., 1999. Stable chlorine isotopes in the Palo Duro Basin, Texas: Evidence for preservation of Permian evaporite brines. Geochimica et cosmochimica acta 63, 1375–1382.

Egeberg, P.K., Saigal, G.C., 1991. North Sea chalk diagenesis: cementation of chalks and healing of fractures. Chemical geology 92, 339–354.

Eglinger, A., André-Mayer, A.S., Vanderhaeghe, O., Mercadier, J., Cuney, M., Decrée, S., Feybesse, J.L., Milesi, J.P., 2013. Geochemical signatures of uranium oxides in the Lufilian belt: From unconformity-related to syn-metamorphic uranium deposits during the Pan-African orogenic cycle. Ore Geology Reviews 54, 197–213.

El Desouky, H.A., Muchez, P., Cailteux, J., 2009. Two Cu–Co sulfide phases and contrasting fluid systems in the Katanga Copperbelt, Democratic Republic of Congo. Ore Geology Reviews 36, 315–332.

El Desouky, H.A., Muchez, P., Dewaele, S., Boutwood, A., Tyler, R., 2008a. Postorogenic origin of the stratiform Cu mineralization at Lufukwe, Lufilian foreland, Democratic Republic of Congo. Economic Geology 103, 555–582.

El Desouky, H.A., Muchez, P., Tyler, R., 2008b. The sandstone-hosted stratiform copper mineralization at Mwitapile and its relation to the mineralization at Lufukwe, Lufilian foreland, Democratic Republic of Congo. Ore Geology Reviews 34, 561–579.

Faure, G., 1986. Principles of isotope geology (second ed.). John Wiley and Sons, New York.

Faure, K., 2003. δD values of fluid inclusion water in quartz and calcite ejecta from active geothermal systems: do values reflect those of original hydrothermal water? Economic Geology 98, 657–660.

Fekete, J., Sajgó, C., Demeny, A., 2011. Hydrogen isotope type-curves of very hot crude oils. Rapid Communications in Mass Spectrometry 25, 191–198.

Fetter, C., 2001. Applied hydrogeology (fourth ed.). Prentice Hall, New Jersey.

First Quantum Minerals Enterprise Nickel Prospect geological summary, 2011.

Fisher, Q.J., Casey, M., Harris, S.D., Knipe, R.J., 2003. Fluid-flow properties of faults in sandstone: the importance of temperature history. Geology 31, 965–968.

Fontes, J.C., Matray, J., 1993. Geochemistry and origin of formation brines from the Paris Basin, France: 1. Brines associated with Triassic salts. Chemical Geology 109, 149–175.

Foriel, J., Philippot, P., Rey, P., Somogyi, A., Banks, D., Ménez, B., 2004. Biological control of Cl/Br and low sulfate concentration in a 3.5–Gyr-old seawater from North Pole, Western Australia. Earth and Planetary Science Letters 228, 451–463.

Garlick, W., 1961. Structural evolution of the Copperbelt, in: Mendelsohn, F. (Ed.), The Geology of the Northern Rhodesian Copperbelt. MacDonald, London, pp. 89–105.

Garlick, W., Gane, P., 1961. Exploration—Geophysics, in: Mendelsohn, F. (Ed.), The Geology of the Northern Rhodesian Copperbelt. MacDonald, London, pp. 178–187.

Garven, G., Freeze, R.A., 1984a. Theoretical analysis of the role of groundwater flow in the genesis of stratabound ore deposits; 1, Mathematical and numerical model. American Journal of Science 284, 1085–1124.

Garven, G., Freeze, R.A., 1984b. Theoretical analysis of the role of groundwater flow in the genesis of stratabound ore deposits; 2, Quantitative results. American Journal of Science 284, 1125–1174.

Giles, M.R., 1997. Diagenesis: a quantitative perspective. Kluwer Academic Publishers Dordrecht.

Gleeson, S., Roberts, S., Fallick, A., Boyce, A., 2008. Micro-Fourier Transform Infrared (FT-IR) and¡ i¿ δD¡/i¿ value investigation of hydrothermal vein quartz: Interpretation of fluid inclusion¡ i¿ δD¡/i¿ values in hydrothermal systems. Geochimica et Cosmochimica Acta 72, 4595–4606.

Gleeson, S., Turner, W., 2007. Fluid inclusion constraints on the origin of the brines responsible for Pb–Zn mineralization at Pine Point and coarse non-saddle and saddle dolomite formation in southern Northwest Territories. Geofluids 7, 51–68.

Godon, A., Jendrzejewski, N., Eggenkamp, H.G., Banks, D.A., Ader, M., Coleman, M.L., Pineau, F., 2004. A cross-calibration of chlorine isotopic measurements and suitability of seawater as the international reference material. Chemical Geology 207, 1–12.

Grandia, F., Canals, À., Cardellach, E., Banks, D.A., Perona, J., 2003. Origin of ore-forming brines in sediment-hosted Zn-Pb deposits of the Basque-Cantabrian Basin, Northern Spain. Economic Geology 98, 1397–1411.

Grant, K., Gleeson, S.A., Roberts, S., 2003. The high-temperature behavior of defect hydrogen species in quartz: Implications for hydrogen isotope studies. American Mineralogist 88, 262–270.

Grant, N., Banks, D., McCaig, A., Yardley, B., 1990. Chemistry, source, and behaviour of fluids involved in Alpine thrusting of the Central Pyrenees. Journal of Geophysical Research: Solid Earth (1978–2012) 95, 9123–9131.

Greyling, L., Robb, L., Master, S., Boiron, M., Yao, Y., 2005. The nature of early basinal fluids in the Zambian Copperbelt: A case study from the Chambishi deposit. Journal of African Earth Sciences 42, 159–172.

Guiliani, G., Cheilletz, A., Arboleda, C., Carrillo, V., Rueda, F., Baker, J., 1995. An evaporitic origin of the parent brines of Colombian emeralds: fluid inclusion and sulphur isotope evidence. European Journal of Mineralogy 7, 151–165.

Gutzmer, J., Banks, D., Lüders, V., Hoefs, J., Beukes, N., Von Bezing, K., 2003. Ancient sub-seafloor alteration of basaltic andesites of the Ongeluk Formation, South Africa: implications for the chemistry of Paleoproterozoic seawater. Chemical geology 201, 37–53.

Haest, M., Muchez, P., Dewaele, S., Boyce, A.J., von Quadt, A., Schneider, J., 2009. Petrographic, fluid inclusion and isotopic study of the Dikulushi Cu–Ag deposit, Katanga (DRC): implications for exploration. Mineralium Deposita 44, 505–522.

Hanor, J., 1994. Origin of saline fluids in sedimentary basins, in: Parnell, J. (Ed.), Geofluids: origin, migration and evolution of fluids in sedimentary basins. Geological Society of London Special Publication 78, pp. 151–174.

Hanson, R.E., Wardlaw, M.S., Wilson, T.J., Mwale, G., 1993. U-Pb zircon ages from the Hook granite massif and Mwembeshi dislocation: Constraints on Pan-African deformation, plutonism, and transcurrent shearing in central Zambia. Precambrian Research 63, 189–209.

Hardie, L.A., 1996. Secular variation in seawater chemistry: An explanation for the coupled secular variation in the mineralogies of marine limestones and potash evaporites over the past 600 my. Geology 24, 279–283.

Harrison, A., Thode, H., 1957. The kinetic isotope effect in the chemical reduction of sulphate. Transactions of the Faraday Society 53, 1648–1651.

Hay, R., Craw, D., 1993. Syn-metamorphic gold mineralisation, Invincible vein, NW Otago Schist, New Zealand. Mineralium deposita 28, 90–98.

Haynes, D., 1986a. Stratiform copper deposits hosted by low-energy sediments; I, Timing of sulfide precipitation, an hypothesis. Economic Geology 81, 250–265.

Haynes, D., 1986b. Stratiform copper deposits hosted by low-energy sediments; II, Nature of source rocks and composition of metal-transporting water. Economic Geology 81, 266–280.

Heijlen, W., Banks, D.A., Muchez, P., Stensgard, B.M., Yardley, B.W., 2008. The nature of mineralizing fluids of the Kipushi Zn-Cu deposit, Katanga, Democratic Repubic of Congo: quantitative fluid inclusion analysis using laser ablation ICP-MS and bulk crush-leach methods. Economic Geology 103, 1459–1482.

Hesthammer, J., Bjorkum, P.A., Watts, L., 2002. The effect of temperature on sealing capacity of faults in sandstone reservoirs: Examples from the Gullfaks and Gullfaks Sor fields, North Sea. AAPG bulletin 86, 1733–1751.

Hitzman, M., 2000. Source basins for sediment-hosted stratiform Cu deposits: Implications for the structure of the Zambian copperbelt. Journal of African Earth Sciences 30, 855–863.

Hitzman, M., Kirkham, R., Broughton, D., Thorson, J., Selley, D., 2005. The sediment-hosted stratiform copper ore system. Economic Geology 100th Anniversary Edition , 609–642.

Hitzman, M.W., Selley, D., Bull, S., 2010. Formation of sedimentary rock-hosted stratiform copper deposits through Earth history. Economic Geology 105, 627–639.

Hoffman, P.F., 1999. The break-up of Rodinia, birth of Gondwana, true polar wander and the snowball Earth. Journal of African Earth Sciences 28, 17–33.

Hollister, L.S., Burruss, R.C., 1976. Phase equilibria in fluid inclusions from the Khtada Lake metamorphic complex. Geochimica et Cosmochimica Acta 40, 163–175.

Holser, W., 1979. Trace elements and isotopes in evaporites, in: Burns, R. (Ed.), Marine Minerals: Mineralogical Society of America Reviews in Mineralogy. Mineralogical Society of America. volume 6, pp. 295–346.

Horita, J., Weinberg, A., Das, N., Holland, H.D., 1996. Brine inclusions in halite and the origin of the Middle Devonian Prairie evaporites of western Canada. Journal of Sedimentary Research 66, 956–964.

Horita, J., Zimmermann, H., Holland, H.D., 2002. Chemical evolution of seawater during the Phanerozoic: Implications from the record of marine evaporites. Geochimica et Cosmochimica Acta 66, 3733–3756.

Hoy, L., Ohmoto, H., 1989. Constraints for the genesis of redbed-associated stratiform Cu deposits from sulphur and carbon mass-balance relations, in: Boyle, R., Brown, A., Jefferson, C., Jowett, E., Kirkham, R. (Eds.), Sediment-hosted stratiform copper deposits. Geological Association of Canada Special Paper 36, Ontario, pp. 151–172.

Huang, X.W., Zhao, X.F., Qi, L., Zhou, M.F., 2013. Re-Os and S isotopic constraints on the origins of two mineralization events at the Tangdan sedimentary rock-hosted stratiform Cu deposit, SW China. Chemical Geology 347, 9–19.

Huenges, E., Erzinger, J., Kück, J., Engeser, B., Kessels, W., 1997. The permeable crust: Geohydraulic properties down to 9101 m depth. Journal of Geophysical Research 102, 18255–18265.

Jackson, M., Warin, O., Woad, G., Hudec, M., 2003. Neoproterozoic allochthonous salt tectonics during the Lufilian orogeny in the Katangan Copperbelt, central Africa. Geological Society of America Bulletin 115, 314–330.

Jacobsen, S.B., Kaufman, A.J., 1999. The Sr, C and O isotopic evolution of Neoproterozoic seawater. Chemical Geology 161, 37–57.

John, T., Schenk, V., Haase, K., Scherer, E., Tembo, F., 2003. Evidence for a Neoproterozoic ocean in south-central Africa from mid-oceanic-ridge–type geochemical signatures and pressure-temperature estimates of Zambian eclogites. Geology 31, 243–246.

John, T., Schenk, V., Mezger, K., Tembo, F., 2004. Timing and PT evolution of whiteschist metamorphism in the Lufilian Arc–Zambezi Belt orogen (Zambia): implications for the assembly of Gondwana. The Journal of geology 112, 71–90.

Johnson, S.P., Rivers, T., De Waele, B., 2005. A review of the Mesoproterozoic to early Palaeozoic magmatic and tectonothermal history of south–central Africa: implications for Rodinia and Gondwana. Journal of the Geological Society 162, 433–450.

Jordaan, J., 1961. Nkana, in: Mendelsohn, F. (Ed.), The Geology of the Northern Rhodesian Copperbelt. MacDonald, London, pp. 297–328.

Jowett, E., 1991. The evolution of ideas about the genesis of stratiform copper-silver deposits. Economic Geology Monograph 8 , 117–132.

Jowett, E.C., 1986. Genesis of Kupferschiefer Cu-Ag deposits by convective flow of Rotliegendes brines during Triassic rifting. Economic Geology 81, 1823–1837.

Jowett, E.C., 1987. Formation of sulfide-calcite veinlets in the Kupferschiefer Cu-Ag deposits in Poland by natural hydrofracturing during basin subsidence. The Journal of Geology , 513–526.

Jowett, E.C., 1992. Role of organics and methane in sulfide ore formation, exemplified by Kupferschiefer Cu–Ag deposits, Poland. Chemical Geology 99, 51–63.

Kamona, A., Leveque, J., Friedrich, G., Haack, U., 1999. Lead isotopes of the carbonate-hosted Kabwe, Tsumeb, and Kipushi Pb-Zn-Cu sulphide deposits in relation to Pan African orogenesis in the Damaran-Lufilian fold belt of Central Africa. Mineralium Deposita 34, 273–283.

Kampunzu, A., Cailteux, J., 1999. Tectonic evolution of the Lufilian Arc (Central Africa Copper Belt) during Neoproterozoic Pan African orogenesis. Gondwana Research 2, 401–421.

Kampunzu, A., Cailteux, J., Kamona, A., Intiomale, M., Melcher, F., 2009. Sediment-hosted Zn–Pb–Cu deposits in the Central African Copperbelt. Ore Geology Reviews 35, 263–297.

Kampunzu, A., Tembo, F., Matheis, G., Kapenda, D., Huntsman-Mapila, P., 2000. Geochemistry and tectonic setting of mafic igneous units in the Neoproterozoic Katangan Basin, Central Africa: implications for Rodinia break-up. Gondwana Research 3, 125–153.

Kaufmann, R., Long, A., Bentley, H., Davis, S., 1984. Natural chlorine isotope variations. Nature 309, 338–340.

Key, R., Liyungu, A., Njamu, F., Somwe, V., Banda, J., Mosley, P., Armstrong, R., 2001. The western arm of the Lufilian Arc in NW Zambia and its potential for copper mineralization. Journal of African Earth Sciences 33, 503–528.

Kirkham, R., 1989. Distribution, settings and genesis of sediment-hosted stratiform copper deposits, in: Boyle, R., Brown, A., Jefferson, C., Jowett, E., Kirkham, R. (Eds.), Sediment-hosted stratiform copper deposits. Geological Association of Canada Special Paper 36, Ontario, pp. 3–38.

Kish, L., Cuney, M., 1981. Uraninite–albite veins from the Mistamisk Valley of the Labrador Trough, Québec. Miner Mag 44, 471–483.

Kiyosu, Y., Krouse, H.R., 1990. The role of organic acid in the abiogenic reduction of sulfate and the sulfur isotope effect. Geochemical Journal 24, 21–27.

Klinkhammer, G., Elderfield, H., Edmond, J., Mitra, A., 1994. Geochemical implications of rare earth element patterns in hydrothermal fluids from mid-ocean ridges. Geochimica et Cosmochimica Acta 58, 5105–5113.

Knauth, P., Epstein, S., 1975. Hydrogen and oxygen isotope ratios in silica from the JOIDES Deep Sea Drilling Project. Earth and Planetary Science Letters 25, 1–10.

Kovalevich, V.M., Peryt, T.M., Petrichenko, O.I., 1998. Secular variation in seawater chemistry during the Phanerozoic as indicated by brine inclusions in halite. The Journal of Geology 106, 695–712.

Koziy, L., Bull, S., Large, R., Selley, D., 2009. Salt as a fluid driver, and basement as a metal source, for stratiform sediment-hosted copper deposits. Geology 37, 1107–1110.

Kříbek, B., Žák, K., Dobeš, P., Leichmann, J., Pudilová, M., René, M., Scharm, B., Scharmová, M., Hájek, A., Holeczy, D., et al., 2009. The Rožná uranium deposit (Bohemian Massif, Czech Republic): shear zone-hosted, late Variscan and post-Variscan hydrothermal mineralization. Mineralium deposita 44, 99–128.

Land, L.S., 1995. Na—Ca—Cl saline formation waters, Frio Formation (Oligocene), south Texas, USA: Products of diagenesis. Geochimica et Cosmochimica Acta 59, 2163–2174.

Large, D., MacQuaker, J., Vaughan, D., Sawlowicz, Z., Gize, A., 1995. Evidence for low-temperature alteration of sulfides in the Kupferschiefer copper deposits of southwestern Poland. Economic Geology 90, 2143–2155.

Laul, J., Lepel, E., 1987. Rare earth element patterns in biotite muscovite and tourmaline minerals. Journal of Radioanalytical and Nuclear Chemistry 112, 461–471.

Lefebvre, J., 1989. Depositional environment of Copper-Cobalt mineralization in the Katangan sediments of Southeast Shaba, Zaire, in: Boyle, R., Brown, A., Jefferson, C., Jowett, E., Kirkham, R. (Eds.), Sediment-hosted stratiform copper deposits. Geological Association of Canada Special Paper 36, Ontario, pp. 401–426.

Lefèbvre, J., Tshauka, T., 1986. Altérations associées à la minéralisation uranifère de Musoshi (Shaba, Zaïre). Musée royal de l'Afrique centrale.

Lerouge, C., Cailteux, J., Kampunzu, A., Milesi, J., Fléhoc, C., 2005. Sulphur isotope constraints on formation conditions of the Luiswishi ore deposit, Democratic Republic of Congo (DRC). Journal of African Earth Sciences 42, 173–182.

Li, M., Huang, Y., Obermajer, M., Jiang, C., Snowdon, L.R., Fowler, M.G., 2001. Hydrogen isotopic compositions of individual alkanes as a new approach to petroleum correlation: case studies from the Western Canada Sedimentary Basin. Organic Geochemistry 32, 1387–1399.

Limaye, A., 2012. DRISHTI: volume exploration and presentation tool, in: SPIE Optical Engineering + Applications, International Society for Optics and Photonics. pp. 85060X–85060X.

Long, A., Eastoe, C., Kaufmann, R., Martin, J., Wirt, L., Finley, J., 1993. High-precision measurement of chlorine stable-isotope ratios. Geochimica Cosmochimica Acta 57, 2907–2912.

Lottermoser, B., 1992. Rare earth elements and hydrothermal ore formation processes. Ore Geology Reviews 7, 25–41.

Lowe, D.R., Byerly, G.R., 2003. Ironstone pods in the Archean Barberton greenstone belt, South Africa: Earth's oldest seafloor hydrothermal vents reinterpreted as Quaternary subaerial springs. Geology 31, 909–912.

Lowenstein, T.K., Hardie, L.A., 1985. Criteria for the recognition of salt-pan evaporites. Sedimentology 32, 627–644.

Lowenstein, T.K., Hardie, L.A., Timofeeff, M.N., Demicco, R.V., 2003. Secular variation in seawater chemistry and the origin of calcium chloride basinal brines. Geology 31, 857–860.

Lowenstein, T.K., Timofeeff, M.N., Brennan, S.T., Hardie, L.A., Demicco, R.V., 2001. Oscillations in Phanerozoic seawater chemistry: Evidence from fluid inclusions. Science 294, 1086–1088.

Lyons, T.W., Anbar, A.D., Severmann, S., Scott, C., Gill, B.C., 2009. Tracking euxinia in the ancient ocean: A multiproxy perspective and Proterozoic case study. Annual Review of Earth and Planetary Sciences 37, 507–534.

Macdonald, F.A., Schmitz, M.D., Crowley, J.L., Roots, C.F., Jones, D.S., Maloof, A.C., Strauss, J.V., Cohen, P.A., Johnston, D.T., Schrag, D.P., 2010. Calibrating the Cryogenian. Science 327, 1241–1243.

Machel, H., 2001. Bacterial and thermochemical sulfate reduction in diagenetic setting-sold and new insights. Sedimentary Geology 140, 143–175.

Machel, H.G., 1987. Saddle dolomite as a by-product of chemical compaction and thermochemical sulfate reduction. Geology 15, 936–940.

Machel, H.G., Krouse, H.R., Sassen, R., 1995. Products and distinguishing criteria of bacterial and thermochemical sulfate reduction. Applied Geochemistry 10, 373–389.

Markey, R., Stein, H.J., Hannah, J.L., Zimmerman, A., Selby, D., Creaser, R.A., 2007. Standardizing Re–Os geochronology: a new molybdenite reference material (Henderson, USA) and the stoichiometry of Os salts. Chemical Geology 244, 74–87.

Marowsky, G., 1969. Schwefel, kohlenstoff und sauerstoff isotopenuntersuchungen am Kupferschiefer als beitrag zur genetischen deutung. Contributions to Mineralogy and Petrology 22, 290–334.

Marques, A.F.A., Barriga, F., Chavagnac, V., Fouquet, Y., 2006. Mineralogy, geochemistry, and Nd isotope composition of the Rainbow hydrothermal field, Mid-Atlantic Ridge. Mineralium Deposita 41, 52–67.

Martin, J.B., Gieskes, J.M., Torres, M., Kastner, M., 1993. Bromine and iodine in Peru margin sediments and pore fluids: Implications for fluid origins. Geochimica et Cosmochimica Acta 57, 4377–4389.

Matsuhisa, Y., Goldsmith, J.R., Clayton, R.N., 1979. Oxygen isotopic fractionation in the system quartz-albite-anorthite-water. Geochimica et Cosmochimica Acta 43, 1131–1140.

Mauk, J.L., Hieshima, G., 1992. Organic matter and copper mineralization at White Pine, Michigan, USA. Chemical geology 99, 189–211.

McGowan, R.R., Roberts, S., Boyce, A.J., 2006. Origin of the Nchanga copper–cobalt deposits of the Zambian Copperbelt. Mineralium Deposita 40, 617–638.

McGowan, R.R., Roberts, S., Foster, R.P., Boyce, A.J., Coller, D., 2003. Origin of the copper-cobalt deposits of the Zambian Copperbelt: An epigenetic view from Nchanga. Geology 31, 497–500.

McGregor, J., 1964. The Lumwana copper project in Zambia. Unpublished Ph.D thesis, Rhodes University , 171 pp.

Meert, J., Torsvik, T., 2004. Palaeomagnetic constraints on Neoproterozoic 'Snowball Earth' continental reconstructions, in: Jenkins, G., McMenamin, M., Sohl, L., McKay, C. (Eds.), The extreme Proterozoic: geology geochemistry and climate. AGU Geophysical Monograph. volume 144, pp. 5–11.

Mendelsohn, F., 1961a. The geology of the Northern Rhodesian Copperbelt. MacDonald, London.

Mendelsohn, F., 1961c. Ore Deposits—General, in: Mendelsohn, F. (Ed.), The Geology of the Northern Rhodesian Copperbelt. MacDonald, London, pp. 124–129.

Mendelsohn, F., 1961d. Ore Genesis, in: Mendelsohn, F. (Ed.), The Geology of the Northern Rhodesian Copperbelt. MacDonald, London, pp. 130–165.

Meneghel, L., 1981. The occurrence of uranium in the Katanga System of northwestern Zambia. Economic Geology 76, 56–68.

Mercadier, J., Cuney, M., Lach, P., Boiron, M.C., Bonhoure, J., Richard, A., Leisen, M., Kister, P., 2011. Origin of uranium deposits revealed by their rare earth element signature. Terra Nova 23, 264–269.

Metcalfe, R., Rochelle, C., Savage, D., Higgo, J., 1994. Fluid rock interactions during continental red bed diagenesis. Implications of theoretical models of mineralisation in sedimentary basins. Geological Society of London Special Publications 78, 301–324.

Michard, A., 1989. Rare earth element systematics in hydrothermal fluids. Geochimica et Cosmochimica Acta 53, 745–750.

Michard, A., Albarède, F., 1986. The REE content of some hydrothermal fluids. Chemical Geology 55, 51–60.

Mills, R.A., Elderfield, H., 1995. Rare earth element geochemistry of hydrothermal deposits from the active TAG Mound, 26 N Mid-Atlantic Ridge. Geochimica et Cosmochimica Acta 59, 3511–3524.

Morelli, R., Creaser, R., Selby, D., Kelley, K., Leach, D., King, A., 2004. Re-Os sulfide geochronology of the Red Dog sediment-hosted Zn-Pb-Ag deposit, Brooks Range, Alaska. Economic Geology 99, 1569–1576.

Morelli, R.M., Bell, C.C., Creaser, R.A., Simonetti, A., 2010. Constraints on the genesis of gold mineralization at the Homestake gold deposit, Black Hills, South Dakota from rhenium–osmium sulfide geochronology. Mineralium Deposita 45, 461–480.

Morgan, J.W., Wandless, G.A., 1980. Rare earth element distribution in some hydrothermal minerals: evidence for crystallographic control. Geochimica et Cosmochimica Acta 44, 973–980.

Muchez, P., Brems, D., Clara, E., De Cleyn, A., Lammens, L., Boyce, A., De Muynck, D., Mukumba, W., Sikazwe, O., 2010. Evolution of Cu–Co mineralizing fluids at Nkana Mine, Central African Copperbelt, Zambia. Journal of African Earth Sciences 58, 457–474.

Muchez, P., Vanderhaeghen, P., El Desouky, H., Schneider, J., Boyce, A., Dewaele, S., Cailteux, J., 2008. Anhydrite pseudomorphs and the origin of stratiform Cu–Co ores in the Katangan Copperbelt (Democratic Republic of Congo). Mineralium Deposita 43, 575–589.

Munyanyiwa, H., Hanson, R.E., Blenkinsop, T.G., Treloar, P.J., 1997. Geochemistry of amphibolites and quartzofeldspathic gneisses in the Pan-African Zambezi belt, northwest Zimbabwe: evidence for bimodal magmatism in a continental rift setting. Precambrian Research 81, 179–196.

Murali, A., Parthasarathy, R., Mahadevan, T., Das, M.S., 1983. Trace element characteristics, REE patterns and partition coefficients of zircons from different geological environmentsa case study on Indian zircons. Geochimica et Cosmochimica Acta 47, 2047–2052.

Newton, R., Pevitt, E., Wignall, P., Bottrell, S., 2004. Large shifts in the isotopic composition of seawater sulphate across the Permo–Triassic boundary in northern Italy. Earth and Planetary Science Letters 218, 331–345.

Northrop, H.R., Goldhaber, M.B., Landis, G.P., Unruh, J.W., Reynolds, R.L., Campbell, J.A., Wanty, R.B., Grauch, R.I., Whitney, G., Rye, R.O., 1990. Genesis of the tabular-type vanadium-uranium deposits of the Henry Basin, Utah. Economic Geology 85, 215–269.

Nygård, R., Gutierrez, M., Høeg, K., Bjørlykke, K., 2004. Influence of burial history on microstructure and compaction behaviour of Kimmeridge clay. Petroleum Geoscience 10, 259–270.

Ohmoto, H., 1986. Stable isotope geochemistry of ore deposits, in: Valley, J., Taylor, H., O'Neil, J. (Eds.), Reviews in mineralogy 16: Stable isotopes and high temperature geological processes. Mineralogical Society of America, Washington D.C., pp. 460–491.

Ohmoto, H., Goldhaber, M., 1997. Sulfur and carbon isotopes. Geochemistry of hydrothermal ore deposits 3, 517–612.

Ohmoto, H., Rye, R., 1979. Isotopes of sulfur and carbon, in: Barnes, H. (Ed.), Geochemistry of hydrothermal ore deposits. John Wiley and Sons, New York., pp. 509–567.

Oliver, N., 1996. Review and classification of structural controls on fluid flow during regional metamorphism. Journal of Metamorphic Geology 14, 477–492.

Orr, W.L., 1974. Changes in sulfur content and isotopic ratios of sulfur during petroleum maturation–study of Big Horn basin Paleozoic oils. AAPG bulletin 58, 2295–2318.

Oszczepalski, S., 1999. Origin of the Kupferschiefer polymetallic mineralization in Poland. Mineralium Deposita 34, 599–613.

Pal, D.C., Trumbull, R.B., Wiedenbeck, M., 2010. Chemical and boron isotope compositions of tourmaline from the Jaduguda U (–Cu–Fe) deposit, Singhbhum shear zone, India: Implications for the sources and evolution of mineralizing fluids. Chemical Geology 277, 245–260.

Palandri, J., Kharaka, Y., 2004. A compilation of rate parameters of water–mineral interaction kinetics to geochemical modelling. U.S. Geological Survey Report , 2004–1068.

Pašava, J., Oszczepalski, S., Du, A., 2010. Re–Os age of non-mineralized black shale from the Kupferschiefer, Poland, and implications for metal enrichment. Mineralium Deposita 45, 189–199.

Paton, C., Hellstrom, J., Paul, B., Woodhead, J., Hergt, J., 2011. Iolite: Freeware for the visualisation and processing of mass spectrometric data. Journal of Analytical Atomic Spectrometry 26, 2508–2518.

Pitcairn, I.K., Olivo, G.R., Teagle, D.A., Craw, D., 2010. Sulfide evolution during prograde metamorphism of the Otago and Alpine Schists, New Zealand. The Canadian Mineralogist 48, 1267–1295.

Pitcairn, I.K., Teagle, D.A., Kerrich, R., Craw, D., Brewer, T.S., 2005. The behaviour of nitrogen and nitrogen isotopes during metamorphism and mineralization: evidence from the Otago and Alpine Schists, New Zealand. Earth and Planetary Science Letters 233, 229–246.

Polito, P.A., Kyser, T.K., Marlatt, J., Alexandre, P., Bajwah, Z., Drever, G., 2004. Significance of alteration assemblages for the origin and evolution of the Proterozoic Nabarlek unconformity-related uranium deposit, Northern Territory, Australia. Economic Geology 99, 113–139.

Polito, P.A., Kyser, T.K., Stanley, C., 2009. The Proterozoic, albitite-hosted, Valhalla uranium deposit, Queensland, Australia: a description of the alteration assemblage associated with uranium mineralisation in diamond drill hole v39. Mineralium Deposita 44, 11–40.

Porada, H., Berhorst, V., 2000. Towards a new understanding of the Neoproterozoic-Early Palaeozoic Lufilian and northern Zambezi Belts in Zambia and the Democratic Republic of Congo. Journal of African Earth Sciences 30, 727–771.

Powley, D., 1990. Pressures and hydrogeology in petroleum basins. Earth-Science Reviews 29, 215–226.

Price, N., Calvert, S., 1977. The contrasting geochemical behaviours of iodine and bromine in recent sediments from the Namibian shelf. Geochimica et Cosmochimica Acta 41, 1769–1775.

Rainaud, C., Master, S., Armstrong, R., Robb, L., 2005. Geochronology and nature of the Palaeoproterozoic basement in the Central African Copperbelt (Zambia and the Democratic Republic of Congo), with regional implications. Journal of African Earth Sciences 42, 1–31.

Raith, J., Stein, H., 2000. Re–Os dating and sulfur isotope composition of molybdenite from tungsten deposits in western Namaqualand, South Africa: implications for ore genesis and the timing of metamorphism. Mineralium Deposita 35, 741–753.

Ramsay, C., Ridgway, J., 1977. Metamorphic patterns in Zambia and their bearing on problems of Zambian tectonic history. Precambrian Research 4, 321–337.

Redding, C., 1978. Hydrogen and carbon isotopes in coals and kerogens, in: Zartmann, R. (Ed.), Short papers of the fourth international conference, geochronology, cosmochronology, isotope geology. USGS Open File Report 78-701, p. 348.

Richards, J., Cumming, G., Krstic, D., Wagner, P., Spooner, E., 1988b. Pb isotope constraints on the age of sulfide ore deposition and U-Pb age of late uraninite veining at the Musoshi stratiform copper deposit, Central Africa copper belt, Zaire. Economic Geology 83, 724–741.

Richards, J., Krogh, T., Spooner, E., 1988a. Fluid inclusion characteristics and U-Pb rutile age of late hydrothermal alteration and veining at the Musoshi stratiform copper deposit, Central African copper belt, Zaire. Economic Geology 83, 118–139.

Roberts, S., Palmer, M.R., Cooper, M.J., Buchaus, P., Sargent, D., 2009. REE and Sr isotope characteristics of carbonate within the Cu–Co mineralized sedimentary

sequence of the Nchanga Mine, Zambian Copperbelt. Mineralium Deposita 44, 881–891.

Robinson, B.W., Kusakabe, M., 1975. Quantitative preparation of sulfur dioxide, for sulfur-34/sulfur-32 analyses, from sulfides by combustion with cuprous oxide. Analytical Chemistry 47, 1179–1181.

Roedder, E., 1984. Reviews in Mineralogy volume 12: Fluid inclusions. Reviews in Mineralogy .

Rollinson, H., 1993. Using geochemical data. Evaluation, presentation, interpretation. John Wiley and Sons, New York.

Romankevich, E., 1990. Biogeochemical problems of living matter of the present-day biosphere, in: Ittekot, V., Kempe, S., Michaelis, W., Spitzy, A. (Eds.), Facets of moderm biochemistry. Springer, Berlin, pp. 39–51.

Rose, A., 1976. The effect of cuprous chloride complexes in the origin of red-bed copper and related deposits. Economic Geology 71, 1036–1048.

Rose, A., 1989. Mobility of copper and other heavy metals in sedimentary environments, in: Boyle, R., Brown, A., Jefferson, C., Jowett, E., Kirkham, R. (Eds.), Sediment-hosted stratiform copper deposits. Geological Association of Canada Special Paper 36, Ontario, pp. 97–110.

Rose, A.W., Bianchi-Mosquera, G.C., 1993. Adsorption of Cu, Pb, Zn, Co, Ni, and Ag on goethite and hematite; a control on metal mobilization from red beds into stratiform copper deposits. Economic Geology 88, 1226–1236.

Savin, S.M., Epstein, S., 1970. The oyxgen and hydrogen isotope geochemistry of ocean sediments and shales. Geochimica et Cosmochimica Acta 34, 43–63.

Sawlowicz, Z., Wedepohl, K., 1992. The origin of rhythmic sulphide bands from the Permian sandstones (Weissliegendes) in the footwall of the Fore-Sudetic Kupferschiefer (Poland). Mineralium Deposita 27, 242–248.

Schneider, J., Melcher, F., Brauns, M., 2007. Concordant ages for the giant Kipushi base metal deposit (DR Congo) from direct Rb–Sr and Re–Os dating of sulfides. Mineralium Deposita 42, 791–797.

Schoell, M., 1980. The hydrogen and carbon isotopic composition of methane from natural gases of various origins. Geochimica et Cosmochimica Acta 44, 649–661.

Schoell, M., Redding, C., 1978. Hydrogen isotopic composition of selected crude oils and their fractions, in: Zartmann, R. (Ed.), Short papers of the fourth international

conference, geochronology, cosmochronology, isotope geology. USGS Open File Report 78-701, pp. 384–385.

Selby, D., Creaser, R.A., 2004. Macroscale NTIMS and microscale LA-MC-ICP-MS Re-Os isotopic analysis of molybdenite: Testing spatial restrictions for reliable Re-Os age determinations, and implications for the decoupling of Re and Os within molybdenite. Geochimica et Cosmochimica Acta 68, 3897–3908.

Selley, D., Broughton, D., Scott, R., Hitzman, M., Bull, S., Large, R., McGoldrick, P., Croaker, M., Pollington, N., F, B., 2005. A new look at the geology of the Zambian Copperbelt. Economic Geology 100th Anniversary Edition , 965–1000.

Sharp, Z.D., 1990. A laser-based microanalytical method for the *in situ* determination of oxygen isotope ratios of silicates and oxides. Geochimica et Cosmochimica Acta 54, 1353–1357.

Shepherd, T., Rankin, A., Alderton, D., 1985. A practical guide to fluid inclusion studies. Blackie, London.

Sheppard, S., 1986. Characterization and isotopic variations in natural waters, in: Valley, J., Taylor, H., O'Neil, J. (Eds.), Mineralogical Society of America Reviews in Mineralogy vol. 16: Stable isotopes in high temperature geothermal processes. Mineralogical Society of America, pp. 165–184.

Shouakar-Stash, O., Alexeev, S., Frape, S., Alexeeva, L., Drimmie, R., 2007. Geochemistry and stable isotopic signatures, including chlorine and bromine isotopes, of the deep groundwaters of the Siberian Platform, Russia. Applied geochemistry 22, 589–605.

Sillitoe, R.H., Perelló, J., García, A., 2010. Sulfide-bearing veinlets throughout the stratiform mineralization of the Central African Copperbelt: temporal and genetic implications. Economic Geology 105, 1361–1368.

Simon, K., 2001. Does¡ i¿ δ¡/i¿D from fluid inclusion in quartz reflect the original hydrothermal fluid? Chemical Geology 177, 483–495.

Singer, D.A., 1995. World class base and precious metal deposits; a quantitative analysis. Economic Geology 90, 88–104.

Singer, D.M., Zachara, J.M., Brown Jr, G.E., 2009. Uranium speciation as a function of depth in contaminated Hanford sediments-A micro-XRF, micro-XRD, and micro-and bulk-XAFS study. Environmental science & technology 43, 630–636.

Speiser, A., Hein, U., Porada, H., 1995. The Kansanshi copper mine (Solwezi area, northwestern Zambia: Geology, wall-rock alteration and fluid inclusions, in: Pasava, J., Kribek, B., Zak, K. (Eds.), Mineral deposits: From their origin to their environmental impacts. A. A. Balkema, Rotterdam, pp. 389–392.

Stein, H., Markey, R., Morgan, J., Hannah, J., Scherstén, A., 2001. The remarkable Re–Os chronometer in molybdenite: how and why it works. Terra Nova 13, 479–486.

Steven, N., Armstrong, R., 2003. A metamorphosed proterozoic carbonaceous shale-hosted Co-Ni-Cu deposit at Kalumbila, Kabompo Dome: the Copperbelt ore shale in northwestern Zambia. Economic Geology 98, 893–909.

Sutton, S., Maynard, J., 2005. A fluid mixing model for copper mineralization at Konkola North, Zambian Copperbelt. Journal of African Earth Sciences 42, 95–118.

Sverjensky, D.A., 1987. The role of migrating oil field brines in the formation of sediment-hosted Cu-rich deposits. Economic Geology 82, 1130–1141.

Sweeney, M., Binda, P., 1989. The role of diagenesis in the formation of the Konkola Cu-Co orebody of the Zambian Copperbelt, in: Boyle, R., Brown, A., Jefferson, C., Jowett, E., Kirkham, R. (Eds.), Sediment-hosted stratiform copper deposits. Geological Association of Canada Special Paper 36, Ontario, pp. 499–518.

Sweeney, M., Turner, P., Vaughan, D., 1986. Stable isotope and geochemical studies in the role of early diagenesis in ore formation, Konkola Basin, Zambian copper belt. Economic Geology 81, 1838–1852.

Swenson, J., Person, M., Raffensperger, J., Cannon, W., Woodruff, L., Berndt, M., 2004. A hydrogeologic model of stratiform copper mineralization in the Midcontinent Rift System, Northern Michigan, USA. Geofluids 4, 1–22.

Taylor, H., 1997. Oxygen and hydrogen isotope relationships in hydrothermal mineral deposits, in: Barnes, H. (Ed.), Geochemistry of hydrothermal ore deposits. Wiley, New York, pp. 229–302.

Thode, H., 1991. Sulphur isotopes in nature and the environment: An overview, in: Krause, H., Grinenko, V. (Eds.), Stable isotopes: Natural and anthropogenic sulphur in the environment (Scope 43). John Wiley and Sons, New York, pp. 1–26.

Torrealday, H.I., Hitzman, M.W., Stein, H.J., Markley, R.J., Armstrong, R., Broughton, D., 2000. Re-Os and U-Pb dating of the vein-hosted mineralization at the Kansanshi copper deposit, northern Zambia. Economic Geology 95, 1165–1170.

Torremans, K., Gauquie, J., Boyce, A.J., Barrie, C.D., Dewaele, S., Sikazwe, O., Muchez, P., 2013. Remobilisation features and structural control on ore grade distribution at the Konkola stratiform Cu-Co ore deposit, Zambia. Journal of African Earth Sciences 79, 10–23.

USGS Mineral Commodities Summaries, 2012.

Wakefield, J., 1978. Samba: A deformed porphyry-type copper deposit in the basement of the Zambian Copperbelt. Transactions of the Institute of Mining and Metallurgy 87, 43–52.

Wakefield, S., Elderfield, H., 1985. Interstitial water iodine enrichments in sediments from the eastern Pacific. Journal of Marine Research 43, 951–961.

Walter, M., Veevers, J., Calver, C., Gorjan, P., Hill, A., 2000. Dating the 840–544 Ma Neoproterozoic interval by isotopes of strontium, carbon, and sulfur in seawater, and some interpretative models. Precambrian Research 100, 371–433.

Warren, J., 2000. Evaporites, brines and base metals: Low-temperature ore emplacement controlled by evaporite diagenesis. Australian Journal of Earth Sciences 47, 179–208.

Wassenaar, L.I., Koehler, G., 2004. On-line technique for the determination of the δ^{37}Cl of inorganic and total organic Cl in environmental samples. Analytical Chemistry 76, 6384–6388.

White, W.S., Wright, J.C., 1966. Sulfide-mineral zoning in the basal Nonesuch Shale, northern Michigan. Economic Geology 61, 1171–1190.

Wiedenbeck, M., Alle, P., Corfu, F., Griffin, W., Meier, M., Oberli, F., von Quadt, A., Roddick, J., Spiegel, W., 1995. Three natural zircon standards for U-Th-Pb, Lu-Hf, trace element and REE analyses. Geostandards Newsletter 19, 1–23.

Wilde, A., Wall, V., 1987. Geology of the Nabarlek uranium deposit, Northern Territory, Australia. Economic Geology 82, 1152–1168.

Wong, T.f., David, C., Zhu, W., 1997. The transition from brittle faulting to cataclastic flow in porous sandstones: Mechanical deformation. Journal of Geophysical Research: Solid Earth (1978–2012) 102, 3009–3025.

Yardley, B., 1997. The evolution of fluids through the metamorphic cycle, in: Jamtveit, B., Yardley, B. (Eds.), Fluid flow and transport in rocks: Mechanisms and effects. Chapman and Hall, London, pp. 99–121.

Yardley, B., Bottrell, S., 1988. Immiscible fluids in metamorphism: implications of two-phase flow for reaction history. Geology 16, 199–202.

Yardley, B.W., 1982. The early metamorphic history of the Haast Schists and related rocks of New Zealand. Contributions to Mineralogy and Petrology 81, 317–327.

Yardley, B.W., Lloyd, G.E., 1995. Why metasomatic fronts are really metasomatic sides. Geology 23, 53–56.

You, C.F., Butterfield, D., Spivack, A., Gieskes, J., Gamo, T., Campbell, A., 1994. Boron and halide systematics in submarine hydrothermal systems: effects of phase separation and sedimentary contributions. Earth and Planetary Science Letters 123, 227–238.

Zhang, S., Tullis, T.E., Scruggs, V.J., 2001. Implications of permeability and its anisotropy in a mica gouge for pore pressures in fault zones. Tectonophysics 335, 37–50.

Zhang, Z., Liu, S., Wu, J., 2009. Characteristics and the formation conditions of chlorite in the Xiazhuang uranium ore field, south China. Geochimica et Cosmochimica Acta 72, A1092.

Zhao, K.D., Jiang, S.Y., 2007. Rare earth element and yttrium analyses of sulfides from the Dachang Sn-polymetallic ore field, Guangxi Province, China: Implication for ore genesis. Geochemical Journal 41, 121–134.

Zheng, Y.F., 1999. Oxygen isotope fractionation in carbonate and sulfate minerals. GEOCHEMICAL JOURNAL-JAPAN- 33, 109–126.

Zhou, J., Huang, Z., Zhou, G., Li, X., Ding, W., Bao, D., 2011. Trace elements and rare earth elements of sulfide minerals in the Tianqiao Pb-Zn ore deposit, Guizhou Province, China. Acta Geologica Sinica-English Edition 85, 189–199.

Zielinski, R., Bloch, S., Walker, T., 1983. The mobility and distribution of heavy metals during the formation of first cycle red beds. Economic Geology 78, 1574–1589.